CHARGE TRANSPORT THROUGH ORGANIZED ORGANIC ASSEMBLIES IN CONFINED GEOMETRIES

A Dissertation

by

AMANDA EILEEN SCHUCKMAN

Submitted to the Office of Graduate Studies of
Texas A&M University
in partial fulfillment of the requirements for the degree of

DOCTOR OF PHILOSOPHY

May 2011

Major Subject: Chemistry

CHARGE TRANSPORT THROUGH ORGANIZED ORGANIC ASSEMBLIES IN CONFINED GEOMETRIES

A Dissertation

by

AMANDA EILEEN SCHUCKMAN

Submitted to the Office of Graduate Studies of
Texas A&M University
in partial fulfillment of the requirements for the degree of

DOCTOR OF PHILOSOPHY

Approved by:

Chair of Committee,	James D. Batteas
Committee Members,	David H. Russell
	D. Wayne Goodman
	Joseph H. Ross
Head of Department,	David H. Russell

May 2011

Major Subject: Chemistry

ABSTRACT

Charge Transport through Organized Organic Assemblies in Confined Geometries.

(May 2011)

Amanda Eileen Schuckman, B.S., Texas Lutheran University

Chair of Advisory Committee: Dr. James D. Batteas

Organic molecules such as porphyrins and alkanethiols are currently being investigated for applications such as sensors, light-emitting diodes and single electron transistors. Porphyrins are stable, highly conjugated compounds and the choice of metal ion and substituents bound to the macrocycle as well as other effects such as chemical surrounding and cluster size modulate the electronic and photonic properties of the molecule. Porphyrins and their derivatives are relatively non-toxic and their very rich photo- and electro-chemistry, and small HOMO-LUMO gaps make them outstanding candidates for use in molecularly-enhanced electronic applications.

For these studies, self-assembled tri-pyridyl porphyrin thiol derivatives have been fully characterized on Au(111) surfaces. A variety of surface characterization techniques such as Atomic Force Microscopy (AFM), Scanning Tunneling Microscopy (STM), FT-IR spectroscopy and X-ray photoelectron spectroscopy (XPS) have been implemented in order to obtain information regarding the attachment orientation based on the angle and physical height of the molecule, conductivity which is determined based on the apparent height and current-voltage (I-V) measurements of the molecule,

conductance switching behavior due to conformational or other effects as well as the stability of the molecular ensembles. Specifically, the transport properties of free base and zinc coordinated tri-pyridyl porphyrin thiol molecular islands inserted into a dodecanethiol matrix on Au(111) were investigated using STM and cross-wire inelastic electron tunneling spectroscopy (IETS). The zinc porphyrin thiol islands observed by STM exhibited reversible bias induced switching at high surface coverage due to the formation of Coulomb islands of ca. 10 nm diameter driven by porphyrin aggregation. Low temperature measurements (~ 4 K) from crossed-wire junctions verified the appearance of a Coulomb staircase and blockade which was not observed for single molecules of this compound or for the analogous free base. Scanning probe lithography via nanografting has been implemented to directly assemble nanoscale patterns of zinc porphyrin thiols and 16-mercapotohexadecanoic acid on Au surfaces. Matrix effects during nanopatterning including solvent and background SAMs have been investigated and ultimately ~ 10 nm islands of zinc porphyrins have been fabricated which is the optimal size for the observed switching effect.

DEDICATION

To my father, mother and brother, who have always been there for me

ACKNOWLEDGEMENTS

I would like to begin by thanking my advisor, Dr. James D. Batteas, for his support and guidance throughout the past five years. He has allowed me the opportunity to do research in emerging science in his laboratory as well as set up collaborations with researchers at other institutions, government and industrial laboratories. Without his continuous effort, I would have not had such a diverse graduate school experience. He has helped to shape my goals for the future by allowing me to make my own decisions regarding my research and intern/fellowship opportunities. I greatly appreciate his contribution to my development as an independent researcher and all of his advice concerning my future.

I am also grateful for the people at Texas A&M that have guided and helped me along the way. I would especially like to thank and acknowledge Ms. Kathryn Webb for her continuous devotion to research on this project for the past two years. She has made tremendous strides as an undergraduate researcher in our lab, and I wish her the best of luck in her future in industry. She has kept me sane this past year never turning down an opportunity for lunch or a movie to take a break from lab. I thank her for her genuine friendship as well. I would like to thank the rest of the Batteas group for all their suggestions and constructive criticism over the years. I thank Dr. Yang-Hsiang Chan for his helpful training when I joined the group. Mr. Ryan Jones has been a wonderful colleague and confidant always willing to listen when I was having a rough day or just needed someone to talk to. Mr. Brad Ewers has devoted countless hours to learning as a

graduate student and has been fully committed to our project which I greatly appreciate. Ms. Stacey Wark has been such an immense support and has contributed greatly to my success at A&M. She has always been there for me including the time she took care of me after my wisdom teeth removal. I thank her for always being someone I could talk to especially during the hard times of long hours and the overwhelming work load as a graduate student. Thank you for your empathy. I would also like to thank Dr. Stephanie Cologna and Dr. Meredith Mintzer for their friendship. I have spent many hours confiding in the each of them, and I thank them for all of their encouragement and support. I would especially like to acknowledge Dr. Lisa M. Pérez for all her help regarding the computational efforts on my research for the past 5 years. She has been tremendously helpful guiding me with her expertise in the field of theoretical investigations. She has always made time for me with her busy schedule, and I appreciate her kindness and advice throughout my time as a graduate student.

I am grateful for the CoreScience group at Huntsman for allowing me the opportunity to learn and grow in so many ways during my internship. Thank you to Dr. Rafael Camargo, Dr. Qiang Lan and Dr. Steve Diamanti for mentoring and teaching me about industry and polyurethane science. I also appreciate Ms. Tianshen Hu and Mr. Nyall Tavernier for helping me and working with me during my brief time in your lab. Thank you all for contributing to my success and for shaping my desire to continue to an industrial career.

I would like to thank Dr. Vasanth Coorg for his patience and kindness and especially his love. I admire his constant willingness to help others which is always the

person I strive to be. His positive attitude, sense of humor and endurance has kept me uplifted in times of weakness and despair, and he is a constant reminder that hard work and determination pay off. He is such a passionate person and doctor, and I have valued our time together the past two years.

I would also like to thank those that have always been dear friends of mine, Ms. Stephanie Morris, Ms. Lauren Cody and Mr. Brock Balouch. Their understanding and support have always meant so much to me. They have never taken our friendship for granted and I am truly blessed to have each one of them in my life.

Finally, I would like to extend my utmost appreciation to my family. My family has been my greatest support throughout my life, and especially in graduate school. They have never let me down. My mother has always shown her continuous love and I admire her in every way. My father has always wanted the best for me and has always given me more than I deserve. He is an excellent teacher and knows more about the world than anybody I know. My brother is so special to me. He has the biggest heart and would do anything for me. Without each of them, I would not have made it this far. They bring the most joy to my life and I cannot thank them enough for all they have done for me.

NOMENCLATURE

CMOS	Complementary Metal Oxide Semiconductor
STM	Scanning Tunneling Microscopy
STS	Scanning Tunneling Spectroscopy
AFM	Atomic Force Microscopy
CP-AFM	Conducting Probe Atomic Force Microscopy
FT-IR	Fourier Transform Infrared
RAIRS	Reflection Absorption Infrared Spectroscopy
IRAS	Infrared Reflection Absorption Spectroscopy
UV-Vis	Ultraviolet-Visible
XPS	X-ray Photoelectron Spectroscopy
DFT	Density Functional Theory
IETS	Inelastic Electron Tunneling Spectroscopy
SAMs	Self-Assembled Monolayers
DDT	Dodecanethiol
HOMO	Highest Occupied Molecular Orbital
LUMO	Lowest Unoccupied Molecular Orbital
I-V	Current-Voltage
HOPG	Highly Ordered Pyrolytic Graphite
CRLS	Contact Radius to Line Step
FWHM	Full Width at Half Maximum

3P1P	3-phenyl-1-propanol
16-MHA	16-mercaptohexadecanoic acid

TABLE OF CONTENTS

CHAPTER Page

LIST OF FIGURES

FIGURE Page

FIGURE Page

FIGURE Page

FIGURE Page

FIGURE Page

FIGURE Page

FIGURE Page

FIGURE Page

FIGURE Page

LIST OF TABLES

CHAPTER I

INTRODUCTION*

1.1 Overview

In light of reaching the limit of Moore's Law (which states the number of transistors on a chip will double approximately every two years), new and different strategies must be developed to modify conventional semiconductor technology (a.k.a. complementary metal oxide semiconductor, CMOS) which relies on top-down fabrication techniques. Top-down fabrication techniques such as photolithography which uses masks to create features are essential to the current chip manufacturing process. However, top-down types of fabrication are facing new and challenging limitations as the technology, or feature-size, is reaching into the nanoscale size regime. In the past fifty years, the idea has been to use "more Moore" strategies which involve the continuation of Moore's Law. Industries have relied on CMOS technology for the progression of smaller and faster devices being able to replicate the invaluable techniques to scale down the feature size with little or no modification to their methods.

This dissertation follows the style of the *Journal of the American Chemical Society*.

However, these methods can no longer be simply scaled much further beyond the current 32 nm technology, and new materials and manufacturing techniques are being explored to circumvent the issues at hand. Nowadays, the trend is moving toward "more than Moore" applications where a simple continuation of the technology no longer works. Instead, these "more than Moore" ideas focus on the diversification of new strategies to enhance the current technology.

One method to investigate enhancing the current technology involves a bottom-up approach where molecules self-assemble onto surfaces. Molecules innately assemble on metal and other surfaces by molecular interaction and the tether can be tailored to target a specific surface with a compatible functional group. The self assembly of the molecules requires no additional modification of their arrangement once adsorbed onto the surface. The only modification that could be foreseen would be altering the molecule for desired properties, type of adsorption, i.e. chemi- or physi-sorption to the surface, or desired patterning of molecules in a confined arrangement. Molecules have been targeted for research in this area due to their size and properties which make them excellent candidates for use in "more than Moore" applications. If the "nano" scale is the target goal for the future of electronic components on chips, molecules are ideal for designing these types of structures because they are inherently in this size regime. The innate properties of molecules can be tuned and manipulated to provide the desired properties of the type of device component, whether it is a switch or transistor or its application to function as a memory or sensor component as well.

After the molecules have been investigated for their potential, the next step is to spatially confine them. Spatially confining molecules is important to make smaller electronic devices which may rely on the behavior of only a few to thousands of molecules in a confined structure. Confining molecules allows for the local ensemble structure and electronic properties to be controlled and selectively modified. In recent years, thiol derivatized molecules have been significantly studied due to the fact that they are relatively stable and form nicely ordered two-dimensional structures on gold surfaces. Taking advantage of these molecules, the idea of using self-assembled monolayers is increasingly growing due to the ease of formation and preparation of a wide variety of organic molecules. Organic molecules specifically with pi conjugation have been of interest for use in molecularly-enhanced electronic applications since the pi electron delocalization inside such molecules typically results in more efficient conduction and the possibility for charge transport modulation in electronic devices.

1.2 Background

Many current electronic technologies are rapidly approaching the limit of performance and miniaturization in a growing number of applications across science and technology because traditional inorganic materials and component architectures are optimized to the edges of the theoretical limits of performance. Most currently employed techniques for mass production of silicon based electronic devices involve multiple chemically and energetically wasteful procedures such as purification and crystallization of the wafer, high energy radiation to make patterns, toxic etchants, and vapor deposition of nanolayers. As a consequence of manufacturing large arrays of chips, each with

millions of devices, fabrication facilities are stunningly expensive to build and operate. Additionally, most of the energy used to power these devices is lost as heat rather than used to perform intended functions, so there are additional production and energy costs needed to dissipate this heat. A great motivation towards the development of molecular electronics is part of efforts to increase performance while at the same time diminishing component size, reduce production costs, and minimizing the environmental impacts of production and operation.[1,2] Reimers Flexible display and electronics technologies, and ink-jet printing of circuitry will also benefit from molecule based electronics.

Molecules or collections of molecules functioning as electronic components have ample precedent in nature. Voltage, ligand, antibiotic, and other ion conducting channels are digital electronics self-assembled into biological membranes in that they have only 'on' or 'off' positions with unit conductance that are unique to a given channel.[3] Photosynthetic reaction centers transport electrons over about eight nanometers with remarkable efficiency. Ion pumps can also be gated. The photo-driven purple membrane pumps containing bacteriorhodopsin have been studied for many decades in terms of their potential as molecular electronic and photonic materials because they are very robust, can cycle many thousands of times, and the distinctive color changes impart a second functionality to these materials.[4,5] However, the rate of conducting ions in channels and bacteriorhodopsin proteins, and the stability of the former, limit the usefulness of these constructs as components of complex electronic devices. The various photosynthetic systems can provide much inspiration, but are too fragile for real-world applications.

The field of molecular electronics focuses on the molecule, but melds concepts from diverse fields such as: physics, chemistry, biophysics, and electrical engineering. Molecular electronics is a field that was first brought about in 1974 with Aviram and Ratner and their theoretical vision of a single organic molecule acting as a rectifier.[6] Since then, molecules have shown their potential for applications such as information storage, charge separation, single electron transistors, current routers and gates and continue to be designed for use in solar cells, organic light-emitting diodes, sensors, photocatalysts and more. Single molecules, clusters of molecules, monolayers and multilayers of molecules have all been explored for use as the active, electronic components for devices. In order for molecules to be used in any type of device structure, the charge transport characteristics of a molecule or ensemble of molecules must first be investigated since the electronic properties will govern the use of a specific molecule in its application. A variety of methods have been developed and utilized for charge transport measurements of molecular configurations on metal and semiconductor surfaces using Scanning Tunneling Microscopy (STM) or Conducting Probe Atomic Force Microscopy (CP-AFM) as well as in junctions such as nanogap electrodes, break junctions and cross-wire measurements. Ideally, STM and CP-AFM offer the advantage of being able to offer high resolution information of the molecular structure whilst obtaining electronic information of the tunneling probability and conductance of the molecule. Both STM and CP-AFM can deduce the configuration of the molecules in those types of electrical junctions without additional instrumentation, whereas the junction-type measurements of molecules inside electrodes in the nanogap or break

junction measurements do not allow for any high resolution characterization. However, the junction-type measurements can easily be configured to attain additional information by characterization using Raman spectroscopy or inelastic electron tunneling spectroscopy (IETS) in combination with the transport measurements which also aid in the evaluation of the configuration of the molecules inside the metal-molecule-metal arrangement. For example, IETS has shown to be compatible with cross-wire measurements[7] and tip-enhanced Raman (TERS) can be performed with a conducting AFM tip on patterned islands of molecules as well as monolayers to deduce information of the orientation of the molecules based on the modes of the molecules which are excited by the tunneling electron using these techniques.

Highly π-conjugated molecules are of particular interest since the π-electron delocalization inside such molecules typically results in lower injection barriers and more efficient tunneling or electron transfer.[8] However, in the beginning, considerable work focused on alkanethiol and dithiol molecules which are considered insulators.[9-13] Since then, π-conjugated molecules such as oligo(phenylene ethynylene)s (OPEs), oligo(phenylene vinylene)s (OPVs), oligothiopenes, oligoarylenes, DNA bases, as well as porphyrins and phthalocyanines have attracted considerable attention more recently.[14-19] There have been several recent reviews that focus on different aspects of molecular electronics ranging from surface chemistry to molecular design, to theory, including a beautiful discussion of mechanical bonds with molecular electronics applications by Stoddart.[20-24] Electronics fabricated from organic materials are potentially much less toxic, easier to recycle, and scalable. In addition, molecular electronics have the

potential to contribute to the continuation of Moore's law in the miniaturization of electronic components; pending the further development of bottom up nanofabrication techniques suitable for mass production.

In general, classic Coulombic charging, the relative spacing of the highest occupied molecular orbital (HOMO) and lowest unoccupied molecular orbital (LUMO), the spin, and the vibrational modes will determine single electron currents through molecules connected to electrodes with tunneling barriers.[25] Thus, the reversibility of accessible redox states of a molecules are important, e.g. in single molecule transistors.[25] In the case of conducting polymers, the conductance is dependent on the structure and conjugation of the molecular system and the length, but a recent study shows that the mechanical characteristics and topology of a polyfluorene are also important. Pulling this polymer from a gold surface with an STM tip allows about a 20 nm change in length whereupon the conductance curves show a exponential decay with increasing length and oscillations that correspond to a each monomer unit detaching from the surface.[26] The molecular electronic properties are also dependent on the matrix surrounding the molecule and the domain size (number of copies of a molecule in a discrete domain). Many of the same physical properties of ceramic semiconductor devices have analogies in hybrid molecular electronics. For example, image charges generated in the source and the drain can result in the localization of charges in molecules such as conjugated phenyls,[25] or in ensembled domains, until a critical charge density is reached whereupon the transistor switches (see below).

There are several reviews of the potential applications of porphyrins and phthalocyanines in molecular electronics,[27-31] and as sensitizers for solar cells.[32] This background will focus specifically on applications of porphyrin and porphyrinoid molecules as components of working molecular electronic devices on electronically active substrates from *ca.* the past decade. Particular emphasis will be placed on how the detailed molecular architecture dictates the electronic properties and how the performance of these molecules is affected by surface chemistry, attachment, orientation, and matrix around the electroactive species. Though there is excellent work on materials composed of porphyrin and phthalocyanine films and aggregates, for example as components of solar energy harvesting, electroluminescent and electronic devices,[33] these are not included in this background *per se*, except as a comparison to single molecule measurements or in terms of attachment chemistry.

1.2.1 Porphyrinoids

Porphyrins are stable, highly conjugated compounds, and as a ligand have been shown to bind nearly every metal in the periodic table. The choice of metal ion and substituents bound to the porphyrin macrocycle as well as other effects such as chemical surrounding and cluster size modulate the electronic and photonic properties of the molecule. Porphyrins and their derivatives are relatively non-toxic and due to their very rich photo- and electro-chemistry, and the fact that they have small gaps between the highest occupied molecular orbital and the lowest occupied molecular orbital (HOMO-LUMO) make them outstanding candidates for use in a number of molecularly-enhanced devices, including sensors, organic light emitting diodes, photovoltaics, memory cells

and light harvesting structures. From a synthetic standpoint, the porphyrin is a suitable candidate due to its tunability such as incorporating different metal centers into the macrocycle as well as attaching ligands to the macrocycle at the meso and/or beta positions. Drain and co-workers have optimized the conditions[34] for creating and modifying the compounds investigated in this work, and the generic form of the porphyrin thiol used in these experiments is shown in Figure 1.1.

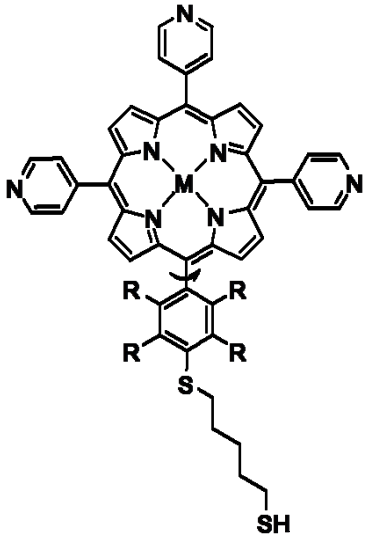

Figure 1.1. Porphyrin thiol derivatives. M- $2H^+$ or Zn^{2+}; R- H or F.

In general, porphyrins have been exploited for the use of functional components for device applications for the past two decades. Porphyrins have been chosen as the molecule of interest due to their highly conjugated systems, their stability and their small

HOMO-LUMO gaps which make them excellent candidates for applications in molecular electronics. Porphyrins have been studied on a variety of substrates because of their diverse photoelectrochemical, catalytic, electronic, and biochemical properties that enable their use as active components of devices for applications including chemical sensors, information storage, and for electrocatalytic or photocatalytic oxidations or reductions. The porphyrins investigated in this work have thiol tether for specific attachment to gold surfaces. The relatively small HOMO-LUMO gap (< 2 eV), the proximity of the HOMO states to the Fermi level of surfaces such as Au, and the ability to readily tune these energy levels via simple chemical modification makes porphyrins useful in many of these applications. In addition to single molecules, hierarchical assemblies of porphyrins self-organized by various strategies have also been explored as a means of creating light harvesting structures for energy conversion. For example, porphyrin-C_{60} assemblies on surfaces have been investigated to explore how these donor-acceptor pairs may be used to control injection barriers in organic light emitting devices and for solar energy conversion applications.[35,36] Lindsey, Bocian and co-workers have explored a range of device level applications of porphyrins appended to various surfaces, including Si and Au, and have shown based on electrochemical studies of extended monolayers, that their redox states could be used as active elements for memory cells.[37]

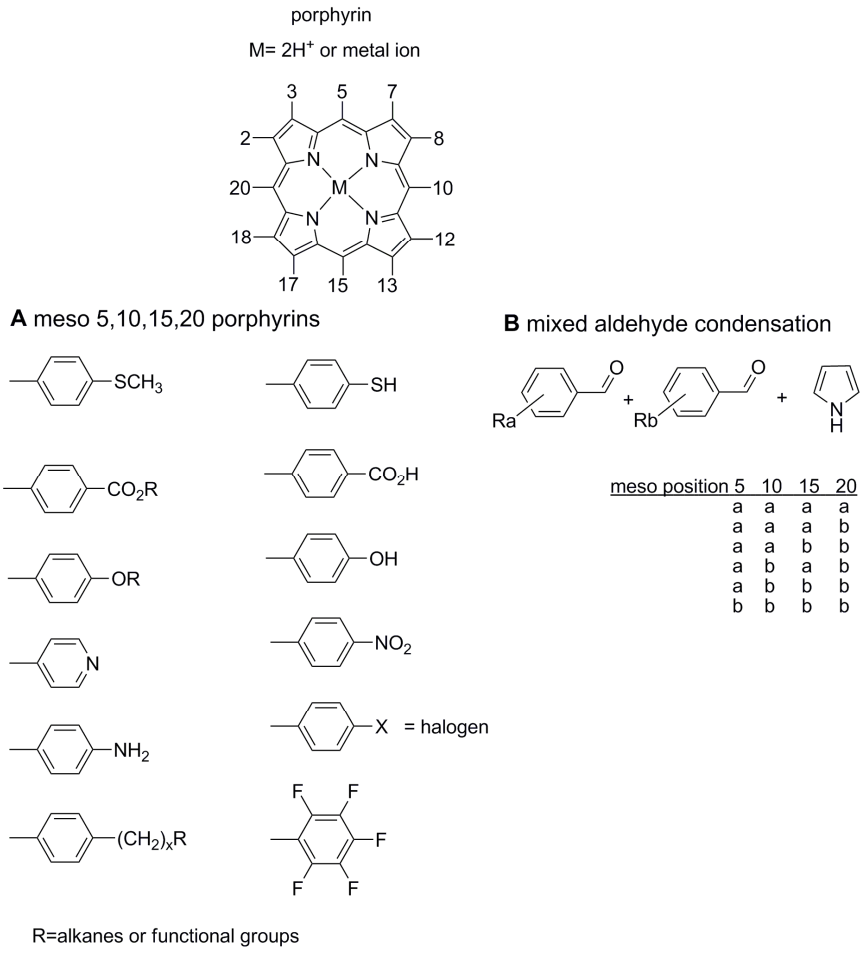

Figure 1.2. (A) Structure of the porphyrin macrocycles with a cadre of common *meso* (5,10,15,20) aryl derivatives. Note the *meso* alkane compounds are also readily accessible synthetically. (B) Much of the supramolecular chemistry of porphyrins uses less symmetric compounds, e.g. those used in the formation of SAMs on surfaces, rely on a mixed aldehyde synthesis wherein two aryl aldehydes are mixed with the pyrrole to form a 'combinatorial' library of six compounds. The chromatographic separation of the compounds and isomers yields compounds that can be used to study molecular topologies, surface binding geometries, and self-assembly into discrete arrays, or self-organization into films. Many of these compounds can also be made by more direct routes.

Single, small conjugated molecules have shown Kondo resonance.[38] Large, stable aromatic systems are particularly attractive as molecular electronics because the

HOMO-LUMO energy gaps are in a realistic operational range, they tend to be stable, and the oxidation and or reduction chemistry is reversible under appropriate conditions. Porphyrins and the related macrocycles such as phthalocyanines are large aromatic dyes that are about 1 and 1.5 nm across, respectively. The porphyrin cores have 11 pi bonds (Figure 1.2) and the phthalocyanines have an additional eight in the fused isoindole structure (Figure 1.3). This class of dyes has rich electrochemical and photophysical properties amenable to molecular electronics applications. These divalent ligands can bind almost every metal in the periodic table, which further modulates the electronic and photonic properties. There is an extensive literature on the chemistry, properties, and applications of porphyrin and phthalocyanines.[39-41] There are two notable early examples of supramolecular devices based on porphyrins. The self-assembly of photo generated porphyrin cations and lipophilic ions into ion chains inside membranes results in the formation of photo-gated ion conductors,[42-45] and the metal ion mediated self-assembly of porphyrin tetramers insides membranes results in photo-gated transistors.[46] Another early example of a porphyrin-based electronic device is the work of Bard, Fox and coworkers[47,48] on mesogenic porphyrins on ITO electrodes wherein thin films of porphyrins served as read-write devices that could be cycled about 1.5 billion times, and

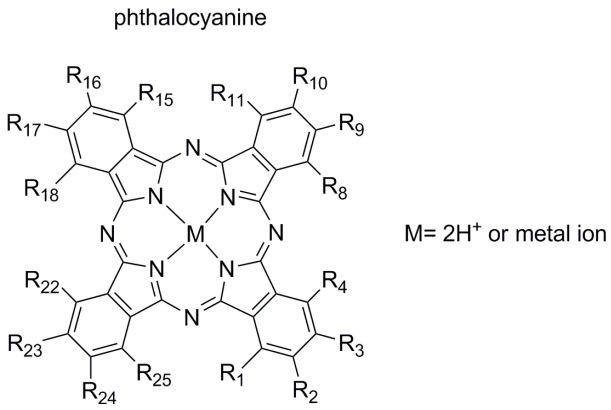

Figure 1.3. The phthalocyanine macrocycle with its numbering scheme. The isoindole positions near the ring are often referred to as α (i.e. 1,4,8,11,15,18,22,25) and those away from the ring β. Substitution at the β positions is more typical. For substituted phthalocyanines with an odd number of substituents on the isoindoles there are usually positional isomers, and these isomers are usually not specifically enumerated. PcF_{16} where all positions bear a fluorine and the Cu(II) complex, are commonly used in photovoltaic applications.

have an equivalent storage density of $8x10^{10}$ bits/cm^2. Some simple, symmetric porphyrins with potential for microelectronics are commercially viable,[49] and some phthalocyanines are used already in many applications ranging from compact disks to display technologies.[40] Currently, substantial strides have been made in the design and fabrication of porphyrinoid dye-based photovoltaics,[32,50-53] and relevant to this work: molecular wires,[54-58] transistors,[59] logic gates, junctions, memory storage, and other molecule-base systems.[28]

Porphyrins, metalloporphyrins, and their derivatives are relatively non-toxic and prime candidates for a host of molecular electronics applications. As a class of molecule, they possess distinctive, reversible oxidation and reduction chemistry that potentiates use as wires, switches, transistors, junctions, and photodiodes. The electronic and

photophysical properties are governed by the bound metal ion, which can be nearly every element in the periodic table, exocyclic moieties on the pyrrole and/or on the *meso* positions, and the matrix surrounding the chromophore. Synthetic porphyrin chemistry is well developed and the Gouterman[60] and Michl[61] molecular orbital models accurately predict the electronic consequences of appending organic substituents and binding metal ions.

Appending exocyclic moieties designed for specific intermolecular interactions, *e.g.* ligands and H-bonds, is now routinely used to construct supramolecular materials. As materials, there continues to be a substantial amount of work on the design of new porphyrin derivatives that self-assemble into discrete nanoarchitectures or self-organize into a diverse menu of nanostructures[62-66] such as films,[67,68] crystals,[55,69-71] tubes,[72-74] rods, wires,[75] nanoparticle spheres,[76,77] and complex fractal-like or chiral patterns.[78,79] A variety of nanofibers have also been reported.[80-83] Coordination chemistry is most often used because the metal ion binding geometry can be exploited as a design element and coordination bonds are robust,[84] but electrostatic[45,73] and hydrogen bond[71,85] interactions are also used in formation of porphyrinic materials. Reversible coordination of metal ions can alter the conformation of porphyrins linked by a bipyridyl bridge thereby altering the electronic communication between the chromophores.[86] Geometric complementaries between pyridyl substituted porphyrins and metal ion binding facilitates formation of many structures ranging from linear tapes to square boxes.[87] Coordination chemistry can also be used to stitch together different chromophores into 3 x 3 and other arrays,[88-92] and complementary coordination chemistry between covalently

linked porphyrins yields photonic and/or conducting wires.[57,93-97] In most cases, self-assembly and self-organization are accomplished under mild conditions. There is also a large amount of ongoing work on photo initiated electron transfer reactions in molecules and assemblies containing porphyrins.[98-100] In materials, the photonic properties of a given porphyrin are also highly dependent on the surrounding matrix of porphyrins, wherein the number, connectivity, relative orientation, and dynamics of both the molecules and the intermolecular interactions dictate the function of the chromophore and the material. Because of their adjustable photonic properties, robustness to decomposition, and ease of synthesis, porphyrins and porphyrinoid materials continue to be thoroughly investigated as components of organic light emitting devices, sensors, solar cells, and photocatalysts.

1.2.2 Chelated Metal Ions

In addition to serving as a design element in the formation of supramolecular materials *via* endocyclic and exocyclic metal ion coordination, it should be noted that metal ions bound by these macrocycles further potentiate molecular electronics applications. The degree of electron delocalization between the chelated metal ion and the porphyrins depends on the relative energies and mixing of the orbitals, and has been extensively studied by Electron Paramagnetic Resonance (EPR) and other spectroscopies for both paramagnetic metal centers and ligand centered radical ions. For example, diamagnetic closed shell Zn(II) complexes, diamagnetic open shell Ni(II), and paramagnetic Mn(III), Fe(II), Co (II) complexes have significantly different photophysical properties and redox chemistry. The availability and energies of the metal

orbitals can also be varied, e.g. closed shell Ti(IV), Zr(IV), and Hf(IV) complexes. The relative orbital energies, thus the electronic populations of the central metal ion, are also dictated by the coordination chemistry via ligand field effects. The forced square planar geometry of the macrocycles and the degree of axial ligation can have profound effects on the relative energies and population of the d orbitals of complexed open shell metalloporphyrins, such as for the Ni(II) porphyrins described below.[101,102] In non-luminescent Ni(II) porphyrins, the deactivation of the excited state proceeds through a metal centered d,d ($d_{x^2-y^2}$, d_{z^2}) excited state. Coordination of pyridine at both axial positions raises the d_{z2} orbital energy, thereby altering the photophysical properties, such that the population of the excited d,d state transiently forces the delegation of the pyridines.[103] It should also be noted that ground state[104] and excited state[101] molecular dynamics can have profound impacts on the function of these molecules in devices. The role of counter ions in complexes with trivalent and tetravalent metal ions can be equally important to the photonic properties, and thus their ability to serve as components of devices.[105] Similar orbital and metal ion binding considerations apply to phthalocyanines.[106] The role of metal ions in the conductance of porphyrin wires has been studied theoretically.[96]

1.2.3 Synthesis

Meso tetraarylporphyrin synthesis is generally accomplished by Rothemund-Adler-type reactions[107,108] and MacDonald-Lindsey-type reactions.[109-111] The former synthesis mixes an aldehyde with pyrrole and when two or more aldehydes are used a mixture is produced (Figure 1.2),[112] while the latter multistep strategy can yield specific

target macrocycles. A recent report on the synthesis of *meso*-tetraarylporphyrins under aerobic oxidation conditions produced tetraphenylporphyrin in over 60% yields.[113] The *meso* aryl substituents are orthogonal to the macrocycle because of steric interactions with the pyrrole βH, so the porphyrin faces are somewhat blocked. When the *meso* positions are unsubstituted and there are eight alkyl substituents on the pyrroles, most commonly octaethylporphyrin, the macrocycle can lay flat onto a substrate. There are likewise many routes to phthalocyanines. The most common methods are to heat phthalonitriles or phthalimides in high boiling solvents, sometimes in the presence of metal ion template. Non-symmetrically substituted starting materials result in isomers.[39,114]

1.3 Measurements of Charge Transport in Molecular Assemblies

Designing molecules for use in devices is one important aspect as well as studying the electronic properties. There are several ways to measure the transport characteristics of the molecule, but before the transport properties of the molecule can be investigated, first fundamental studies of the molecules adsorbed on surfaces must be done in order to develop higher order systems that can be incorporated into electronic components. Fundamental studies will be a significant portion of the research presented herein, due to the fact that the specific electronic properties of porphyrins govern their use as active electronic components and must therefore be fully characterized before the molecule can be implemented into a device. In order to characterize the electrical properties of molecules, a range of techniques have been developed. The electronic properties of single molecules or small ensembles of molecules have been measured

through a number of different electrical test beds. These include electrical and mechanical break junctions,[115-119] cross-wire junctions,[120] nanopores,[121] mercury drop contacts,[122] cyclic voltammetry (CV),[123,124] conducting-probe atomic force microscopy (CP-AFM),[125,126] and scanning tunneling microscopy (STM).[119,127,128] Among these, STM and CP-AFM can provide complementary surface analyses, as they enable investigation of individual molecules on surfaces on the atomic scale. In addition to structural details, the STM images themselves can further elucidate information regarding local tunneling probabilities as well as the local electronic density of molecular orbitals (*e.g.* HOMO and LUMO) participating in the tunneling process. Highly π-conjugated molecules, such as porphyrins are of particular interest since the π-electron delocalization inside such molecules typically results in lower injection barriers and more efficient tunneling or electron transfer. Specific electronic properties of porphyrins such as tunneling efficiency and the transport pathway are of significant interest in designing molecules for use as electrical components. These measurement techniques have been recently reviewed.[129,130]

1.4 Porphyrinoids on Surfaces

Porphyrinoids can be organized onto surfaces in two general ways: (1) self-assembled monolayers (SAMs) wherein the active molecules are covalently attached to the surface via well-established surface chemistries (Figure 1.4) and (2) self-organization into 2-dimensional arrays and/or layers by adsorption onto surfaces (Figure 1.5).[131-138] In both cases the surface chemistry, energetics, and structure play key roles in the final structure and organization of the photonic materials.[123,139,140] For SAMs, there are four

essential parts of the molecule: the electronically active dye, the linker, the tether, and the surface-reactive functional group. Each part plays a role in the molecular electronic properties.

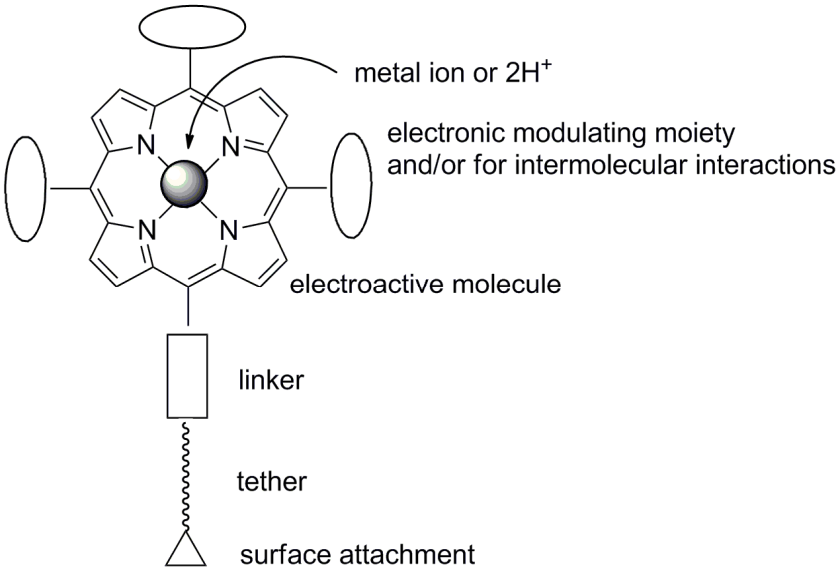

Figure 1.4. Parts of a porphyrin molecule for surface attachment include the reactive surface moiety, a tether, and the linking group to the porphyrin. Metal ions and exocyclic moieties modulate electronic properties.

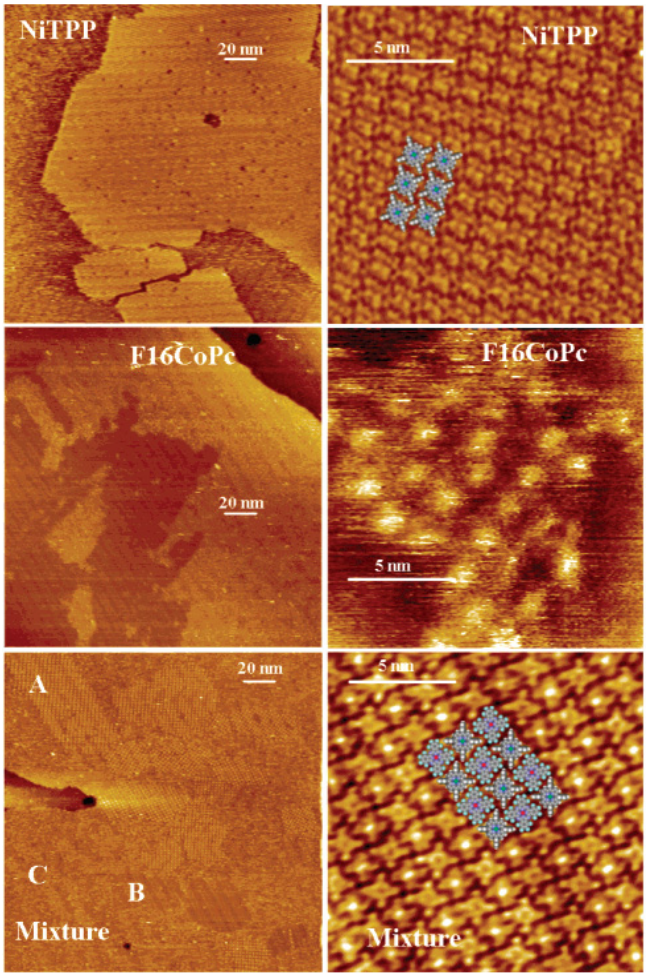

Figure 1.5. Large planar macrocycles such as porphyrins and phthalocyanines tend to adsorb cofacially on surfaces such as highly ordered pyrolytic graphite (HOPG), Au(III), NaCl, and other atomically smooth substrates. Here Ni(TPP) and PcF_{16} are deposited on HOPG as well as a 2:1 mixture. Reproduced from ref. [137] with permission of the copyright holders.

1.4.1 Adsorption

The self-organization of porphyrins on surfaces has been extensively studied by Hipps and co-workers, who have characterized the electronic properties of porphyrins and related compounds such as phthalocyanines adsorbed as monolayers on

surfaces.[133,135,136,138,141,142] These studies conclude that the orbital energies of the macrocycles including the metal ions, molecular states, and the surface states determine the coupling, thus tunneling probability (Figure 1.6). They have also conducted a variety of studies on the nanomanipulation and self-organization of porphyrins on HOPG as well as metal substrates such as Au. Studies which combine a range of surface analytical tools, such as X-ray photoelectron spectroscopy, inelastic tunneling spectroscopy, reflection absorption IR spectroscopy, ultra-violet photoelectron spectroscopy as well as orbital-mediated tunneling spectroscopy, along with STM have provided a significant amount of information regarding the physical and electronic properties of porphyrins on surfaces. This arena of research has shown that porphyrins can be valuable components of electronic devices since they possess desired properties such as the ability to be deposited on surfaces without a change in composition or oxidation state and their frontier orbital energies lie close to the Fermi level of the Au substrates.

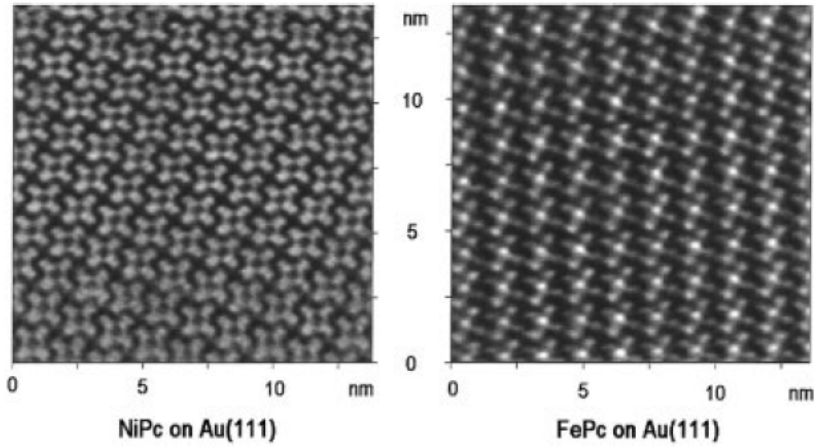

Figure 1.6. Assemblies of Ni(II) and Fe(II) phthalocyanine on Au(111). While both systems contain a central metal atom with the same valance, the Fe d^6 system has greater orbital density near the Fermi level leading to an observed increased tunneling probability than that of the Ni d^8 containing species. Reproduced from ref. [132] with permission of the copyright holders. These authors also examined d^7 and d^9 phthalocyanines [131].

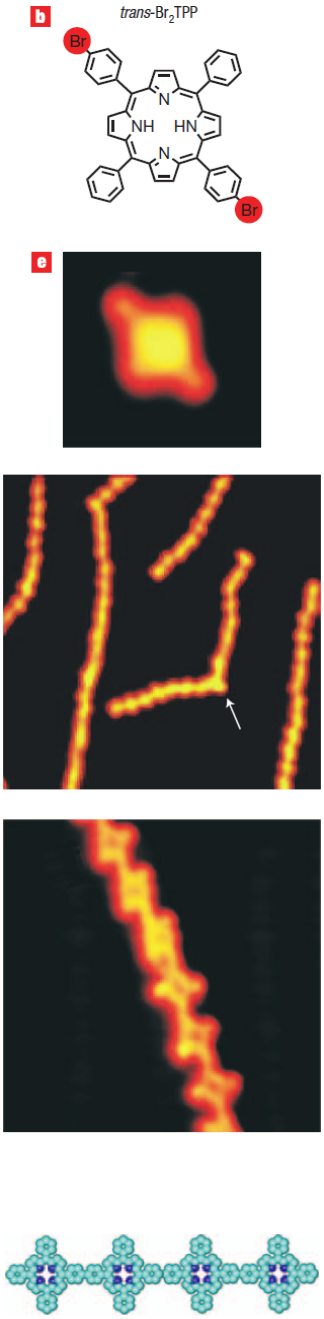

Figure 1.7. Formation of supramolecular arrays of halogenated aryl porphyrins allows covalent bond assembly of 1- and 2- dimensional structures on a gold surface upon heating. In this case the formation of the 1-dimensional tapes is shown. The arrow indicates overlapping of two linear chains rather than a covalent bond. Reproduced from ref. [[143]] with permission of the copyright holders.

Various strategies toward multiporphyrin arrays have been reported.[144-146] Recently, Hecht and coworkers reported the formation of 2-dimensional arrays of porphyrins on gold surfaces can be accomplished by evaporative deposition or casting of tetra(4-bromophenyl)porphyrin onto gold surfaces, which results in a reasonably well ordered supramolecular array of up to ca. 100 nm. These arrays are pre-positioned to form covalent 2-dimensional networks upon heating, or if deposited above a critical temperature.[143] Similar to the coordination arrays, the substitution pattern on the porphyrin can dictate the nanoarchitecture of the resulting covalent array, for example the 5,15-derivative leads to chains (Figure 1.7), but the formation of high fidelity 2-dimensional structures over large areas is yet to be achieved.[143] More than just thickness, research groups are able to control the orientation of the molecules comprising the SAM, and there are many reports on the effect of reaction conditions on the ordering of molecules in a monolayer. For example, Ha et al. demonstrated the effect of annealing the first adsorbed layer on the orientation of the second layer.[147] Hydrogen bonding interactions and halogen-halogen interactions alter the thermodynamic properties and therefore binding modes of the adsorbed molecules on surfaces.[148,149]

1.4.2 Surface Attachment

1.4.2.1 Thiols on Gold

The use of porphyrins in molecular electronics largely came about from the formation of liquid crystalline films and attachment of the molecules to surfaces in the form of the now ubiquitous self-assembled monolayer (SAM).[147,148,150] It was noted early on that alkanethiols create well ordered structures on gold substrates, and similarly

a variety of porphyrins have been bound to gold as SAMs.[34,151-156] SAMs are very common systems for the study of molecules on surfaces due to their ease of formation[157,158] and preparation by simply immersing a clean substrate into solutions for a period of time, typically ~ 24 hours. SAMs can be composed of pure monolayers of only one type of molecule, or can be mixed, where a host of matrix molecules are first formed on the surface followed by insertion of the molecule of interest. Self assembly has been studied in depth using alkanethiols on gold surfaces, specifically Au(111).[159-161] The general process for molecular self-assembly involves submersing a gold substrate, either gold on silicon or gold on mica, into a solution of the alkanethiol. Au(111) is typically used, which is a specific face of bulk Au, and the atoms are in a hexagonally close-packed arrangement. For the studies presented herein, a Au(111) substrate is immersed in a 1 mM solution of dodecanethiol in ethanol for 24 hours in which the molecules form a densely packed single layer of molecules on the surface, known as a monolayer. When alkanethiols assemble on gold, the molecules initially lie flat on the surface, and as the adsorption process progresses, gold vacancies, commonly known as etch pits, are formed along with gold adatoms. After proceeding to assemble through the lying down or striped phase, the molecules then stand up creating a densely packed monolayer with a tilt angle of ~ 30° from the normal of the surface. The sulfur atom of the dodecanethiol is adsorbed in a three-fold hollow site on the gold forming a ($\sqrt{3}$ x $\sqrt{3}$)R30 structure with respect to the underlying gold surface. The sulfur head groups are spaced ~ 5 Å apart in a hexagonal lattice shown in Figure 1.8. The dodecanethiol can also arrange in a more compact arrangement known as a c(4x2) superlattice.[162] After

formation of the dodecanethiol monolayer, the newly formed SAM is submersed into a solution of the porphyrin molecule to form a mixed monolayer. Alkanethiols are known to be insulating molecules and in this case act as a background matrix to prop up the porphyrins into an upright configuration to be analyzed for their electronic properties. Since alkanethiols are well-studied, their electronic properties are known and are used as a control for these experiments. Overall, much work has been done for designing molecular or molecularly-enhanced electronics with thiol-derivatized molecules on gold substrates.[163-166] Investigating SAMs of organic molecules are of interest to many for

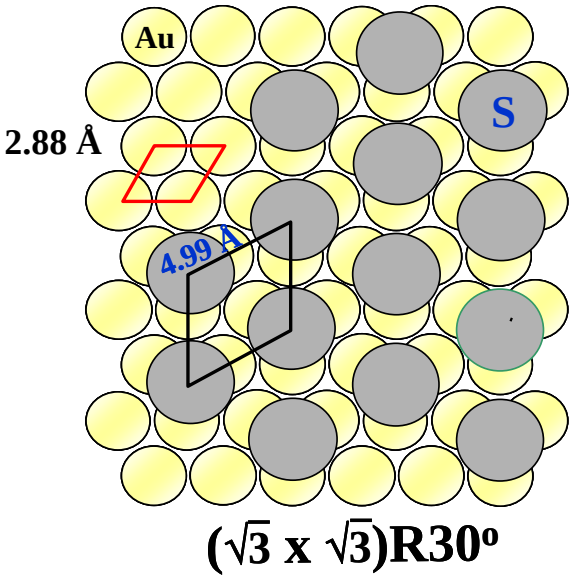

Figure 1.8. Schematic of DDT sulfur headgroup (gray) lattice on Au(111) surface (yellow).

applications involving molecularly-enhanced electronics. The robustness, stability and electronic properties as well as the cost-effective nature of organic molecules are of particular interest since inorganic materials have dominated the electronics industry up to now. Organic molecules are beginning to look more promising for use in device components such as switches, rectifiers, and transistors due to lower cost and proficiency and the inherent limitations of the inorganic counterparts. Looking towards molecules for use in sensors and devices, much work has been done in the area of charge transport[167] and measuring conductance of single-molecules,[130,168] SAMs,[169-174] and single molecules inserted into SAMs[175-179] with the overarching goal to study the charge transport characteristics of the molecule itself without significant contributions from intermolecular or junction effects.

Numerous patterns and arrangements of single molecules and supramolecular assemblies have been reported.[149] Many of the early SAMs were created as Langmuir Blodgett films, and later were fabricated by dipping the substrate into a solution containing the thiol for extended periods of time. Extensive techniques have been developed to fabricate and characterize these assemblies, especially ultrahigh vacuum techniques that allows layers to be patterned with precision approaching nanometer control.[180] Assembly approaches can be further extended by the use of nanopatterning, via techniques such as scanning probe lithography.[139,144,150] In this work, we have shown that porphyrin assemblies may be patterned on Au surfaces using nanografting. In nanografting, an AFM tip is used to displace surface bound matrix molecules (typically an alkanethiol) in a background solution of the molecule of interest. During this process,

the molecule of interest, a porphyrin appended with a thiol, then bonds within the open surface region created by the removal of the matrix molecules.[181] Using scanning probe lithography, thiol tethered porphyrin assemblies with features down to *ca.* 10 nm in dimension (Figure 1.9) can be fabricated to create well defined nanostructures on surfaces.

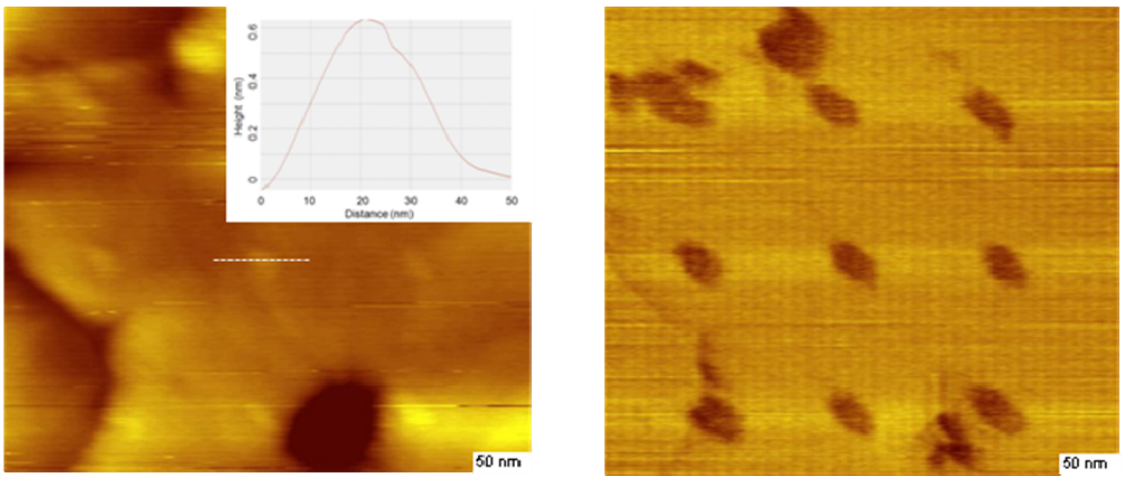

Figure 1.9. A 3 x 3 array of nanografted islands of a zinc porphyrin thiol patterned in a background matrix of dodecanethiol. The feature size illustrated here is *ca.* 20 nm (FWHM) as determined from the topographic image (left). The porphyrins are found to be protruding above the dodecanethiol matrix by *ca.* 0.6 nm. The friction image (right) more clearly shows the patterned array. (Batteas and coworkers, unpublished results).

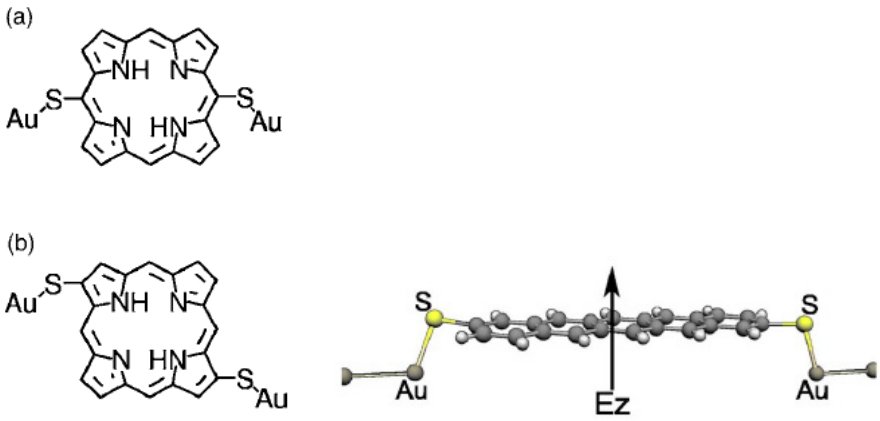

Figure 1.10. Perrine et al. demonstrated cofacial deposition of porphyrins on Au surfaces with thiols directly attached to the porphyrin. Reproduced from ref. [[182]] with permission of the copyright holders.

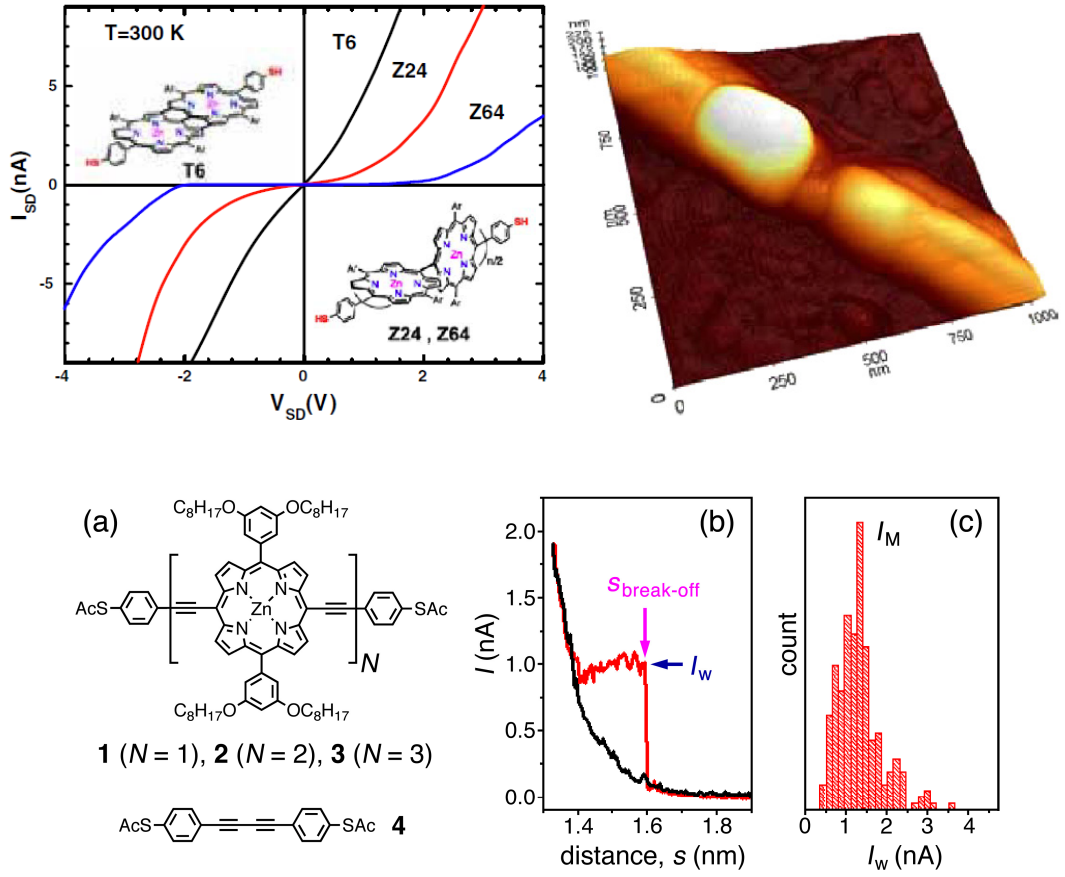

Figure 1.11. Top: Electrical properties of directly linked porphyrin wires across Au nanoelectrodes with spacing of less than 5 nm were prepared using an electromigration-induced break-junction technique Reproduced from ref. [[14]] with permission of the copyright holders. Bottom: an acetylene-linked porphyrin construct has been studied to look at distance dependence on the conductivity. Reproduced from ref. [[58]] with permission of the copyright holders.

There are several modes of porphyrin attachments to gold surfaces depending on the location and size of the linker moieties and attachment groups. For example, Perrine *et al.*, attached thiols directly to the porphyrin macrocycle on either opposing pyrrole β

positions or on opposing meso positions, therefore attached to different macrocycle molecular orbitals.[182] This geometry allows the cofacial deposition of the porphyrin with the π-system remarkably close to the Au surface with reasonable reliability (Figure 1.10). Porphyrin oligomers terminated on either end with thiols allow them to bridge between gold electrodes, and I-V plots show that the fused systems have markedly different electric properties than similar oligomers directly connected via *meso* positions (Figure 1.11).[14] Cycling of these electrodes however, indicated that the porphyrins may be aggregating due to mobility or lability of the Au-S bonds. Similar constructs with multimers of acetylene-bridged zinc porphyrins using phenylacetylene tethers on each end bridged between gold electrodes showed that the conductance is not linearly dependent on the distance (Figure 1.11).[58] A theoretical approach indicated that a porphyrin bearing eight thiols, two on each pyrrole, may bridge between four gold electrodes to serve as a photo gated current router, but construction of this type of device will be problematic.[183] The free base and the Co(II) tetra phenylporphyrins with thiols on the 4-positions on opposing meso positions (5,15 in Figure 1.2) can be attached to gold nanowires. In this case the metalloporphyrin served as a memory bit wherein the charge was located as the Co(II/III) couple, which then alters the conductance of the nanowire. The free base exhibited no memory effects.[59] In all of the constructs with thiols the facile formation of the disulfides, in the presence of oxygen or from electrode generated redox processes, can complicate the formation of the material and interpretation of the data. Also, the mobility and lability of the S-Au bond must be considered.

Table 1.1 Surface Attachment Chemistry

Structure/surface	Comments, and surface bond energies[21]	Recent examples
Por-tether-S-/gold	Migration and lability of S-Au bond can be used to form islands of electroactive molecules and can present issues for preparing useful devices. Surface bond energy ~1.9eV	[34,151-156]
Por-tether-CH=CH-/Si(100) Por-tether-CH_2-/Si(100)	This bond is less labile, surface bond energy ~3.7 eV.	[184]
Por-tether-O-/Si(100)	Surface bond energy ~3.7 eV	[185]
Adsorption	Surface bond energy <0.5 eV	[133,134,136,137,141,144]

1.4.2.2 Other Attachment Chemistry

The use of a single alkylthiol tether can also be used to implant these molecules into a background matrix, allowing for the investigation of single molecules as well as assemblies of these molecules to be investigated by techniques such as scanning tunneling microscopy (*e.g.* Figure 1.1). Beyond metal surfaces, attachment to semi-conducting and oxide surface can be accomplished via a range of addition reactions. These have different surface bond energies (Table 1.1). In each of these cases the first key issue surrounding this approach to device fabrication includes understanding the attachment chemistry required to organize the molecular components on surfaces and the

role of these bonds in electronic coupling. The implementation of strategies which link molecular components directly to semiconductors such as Si have a significant advantage in light of the extensive technologies and fabrication methods already built up around Si in the existing semiconductor industry. To this end, several groups are investigating the interactions of small organics with Si surfaces, and are remolding our views of traditional organic chemistry by establishing reaction mechanisms of small organics on semiconductor surfaces.[186-188] Recent work has also shown that porphyrin films can be attached to Si surfaces via Si-O linkages,[185] and that these molecular monolayers are very robust under elevated temperatures, maintaining their electroactivity, thus making them reasonable candidates for device fabrication.[124] Other linking chemistries, including use of chlorosilanes[189] and phosphates[190] can be used for the formation of self-assembled monolayers (SAMs) on oxide surfaces. Additionally, direct attachment to H-terminated Si can be accomplished through the use of alkyne and hydroxyl groups to form Si-C and Si-O bonds.[191,192] Absent from this body of work; however, are the details of how the film quality (i.e. defect density and local aggregate dimension) impact performance, as well as how the specifics of the electronic structure, packing geometry and coupling group exert influences on the charge transport behavior of the system.

1.4.3 Monolayers on Other Surfaces: Information Storage

Matching the appended attachment group to the surface chemistry allows formation of monolayers on a variety of surfaces. Alkynes add to Si(100) surfaces in hydrosilylation reactions. For example, an alkyne-terminated tether attached to silicon

can subsequently react with a porphyrin bearing an azido moiety on a pyrrole in a click-type 1,3-Huisgen cycloaddition.[184] Similarly, vinyl groups can be added to Si(100) surfaces.[193,194] Porphyrin and phthalocyanine based molecular memory devices are among the most promising in the arena of molecular electronics because these macrocycles are generally robust enough to withstand the elevated temperatures and reaction conditions needed to fabricate monolayers on silicon. Adsorbed or bound to a conducting or semiconducting surface, domains of porphyrins are excellent candidates for memory storage due to their distinct yet easily manipulated and often photoactive electronic states. By exploiting the reversible redox states of a porphyrin an "on off switch" is created to function as the unit by which information is stored. The porphyrin layer also stores charge in this manner thereby serving as a molecular capacitor and mimicking the inorganic transistor / capacitor system currently used for memory storage. Because applications for molecular memory demand a high charge density and a small footprint to minimize feature size, molecules with multiple reversible redox states may potentiate a new generation of devices.

Lindsey, Bocian and coworkers presented some of the best and most thorough approaches to designing and creating functional and potentially economically viable molecular memory devices that are stable to ~ 400 ^{o}C and can undergo ~10^{12} cycles.[124,195] These devices, and others like them, are well characterized by numerous electrochemical and microscopic techniques.[194] Molecules with as many as four discrete redox states maintain a small footprint because of their unique binding mode to the

surface (Figure 1.12).[196,197] Carcel et al. created a series of molecules to investigate: (a) electron transfer kinetics between the surface and the adsorbed molecule by varying the

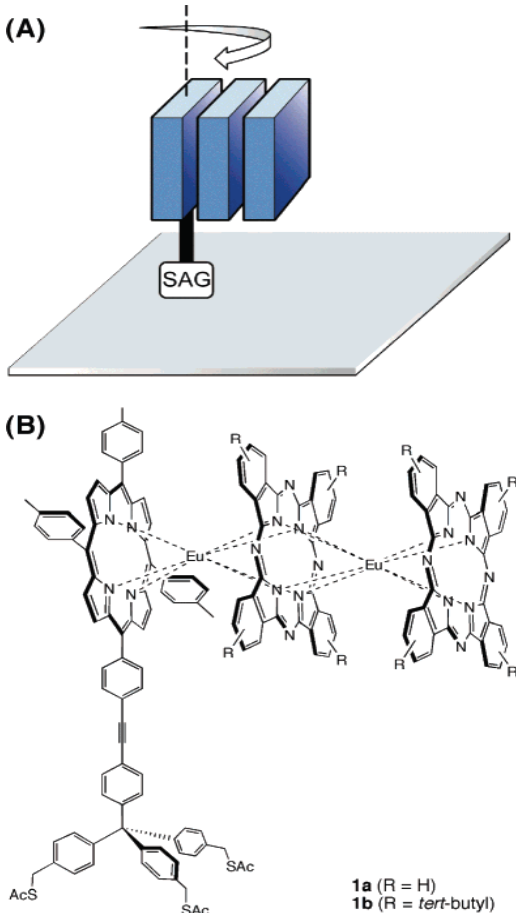

Figure 1.12. (A) The dynamics of a surface attached trimer is one of the factors that determine the surface density, where SAG is the surface attachment group. (B) The heteroleptic Por-Eu-Pc-Eu-Pc serves as a multi-bit information storage molecule. Reproduced from ref. [196] with permission of the copyright holders.

moiety used for attachment, (b) a series of porphyrins designed to investigate the effects of charge density, and (c) a set to investigate methods of chip patterning. Here it was found that electron transfer rates increase as packing density in the SAM decrease.[198]

Work by Lindsey and Bocian in the past decade has shown that the reversible redox activity of porphyrin complexes can be exploited for molecular information storage applications where the oxidation of the porphyrin is the write cycle and the reduction is the read cycle.[199,200] Several porphyrin complexes that can serve as molecular charge storage elements were designed to form robust monolayers and to be compatible with conventional semiconductor lithography. Careful investigations of the attachment chemistry and topology, tether, and linker moieties have yielded insights to the functional role of each part of the molecule. The electronic functional properties of monolayers of a diverse set of porphyrinoids were investigated to decipher the molecular architecture in terms of all four parts of the molecule (Figure 1.4). These studies included: monopodal, bipodal, and tripodal attachment geometries together with variations in the binding chemistry to silicon using oxygen, sulfur, and selenium.[152,154,193-198] These molecules and their derivatives have also found potential uses in the field of molecular memory devices. In terms of the electronically active porphyrinoid portion of the molecule, a single first row transition metal porphyrin complex usually has 1-2 reversible redox processes. Lanthanides and other metal ions with large ionic radii form sandwich complexes with porphyrins and phthalocyanines because they protrude significantly out of the mean plane of the macrocycle. Higher order, and mixed porphyrin-phthalocyanine sandwich complexes can also be formed in

reasonable yields, and these tend to have more reversible redox states than the monomers (Figure 1.12). Attachment of a tether to these large multiporphyrinoid systems allows construction of a monolayer wherein each molecule has a minimal footprint to maximize the surface density of the electronically active units, and the distinct oxidation states of each unit allows them to be used as multi-bit devices.[194]

1.4.4 Nano Islands

Particular interest has been in designing components for electronics using a porphyrin core system as shown in Figure 1.1. Specifically, a free-base porphyrin macrocycle bearing three 4-pyridyl moieties and one pentafluorophenyl substituent in the meso positions has been designed as a core platform for the rapid, high yield attachment of tethers that can be tailored to both the surface chemistry and other design criteria. In this case the pentafluorophenyl moiety serves as a "universal" linker to which a variety of nucleophiles can be appended via replacement of the 4-fluoro group.

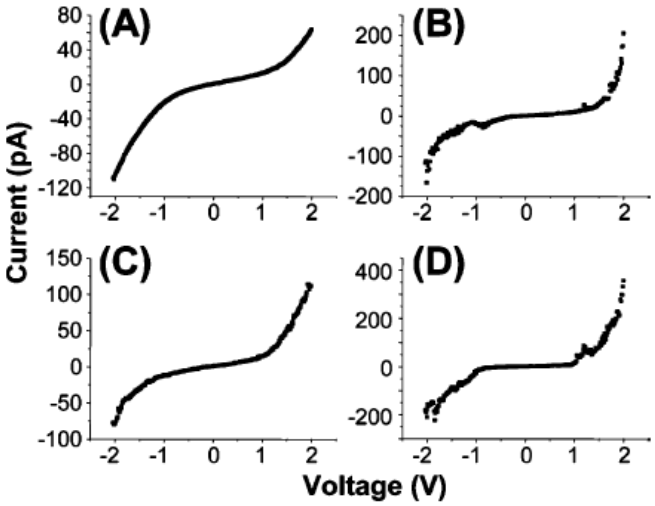

Figure 1.13. I-V spectra (averaged from 50 curves each) for the (A) dodecanethiol matrix, (B) small (~2 nm) porphyrin domains and (C, D) large (>6 nm) porphyrin domains. Reproduced from ref. [[34]] with permission of the copyright holders.

The pyridyl motifs allow design of intermolecular interactions to yield hierarchically organized monolayers or can provide a convenient attachment point for additional molecules via metal-ligand coordination chemistry. Initial studies used a terminal dithioalkane to yield a derivative for immobilization onto a gold surface via strong sulfur-gold chemisorption. Moreover, by controlling the extent of fluorination of this linker group, this phenyl ring, can be used as an internal barrier to control the tunneling between the macrocycle and the thiol tether. This barrier can be modulated by systematic variation of the number and position of the fluoro groups on the ring, thus affording some control of the relative orbital energies of this phenyl group and the degree of steric interactions between the 2,6-positions on this phenyl group with the

pyrrole β-hydrogens. Thus, control of these interactions provides a means to dictate the electronic coupling between the macrocycle and the tether.

To optimize the ability to investigate these molecules either individually or as small monolayer aggregates (about 6 – 10 nm in dimension), we have characterized SAMs of the free base and zinc porphyrin based molecules with thiol linkers mixed into a pre-assembled dodecanethiol matrix.[34] These insertion based experiments afford the means of orienting molecules at the surface by covering the surface with a protective capping group first (in this case a simple alkanethiol). Assemblies of such molecules on clean open metal surfaces show that they will frequently lay down on the surface as described above, driven by the strong interaction between the π system and the metal Au terraces. In characterizing both the free-base and zinc porphyrin derivatives, it was found that the molecule inserts on edges of the substrate and into defects in the pre-assembled dodecanethiol SAM. The free-base analogue tends to insert as single molecules and small monolayer domains dispersed within the background SAM. The small islands of the free-base porphyrin molecules undergo stochastic switching as observed during STM measurements in the mixed monolayer and this is likely associated with conformational changes within the monolayer. The I-V spectra are shown in Figure 1.13. The zinc metalated derivative has a much higher proclivity for aggregation mediated by both coordination chemistry and π-π interactions, thereby creating larger domains that are approximately 10 nm in width on average. These large domains of the metalloporphyrin afford interesting electronic properties, such as coulomb blockade, that is not seen in the small clusters or with the free-base analog (see below).

1.4.5 Other Devices

In many molecular electronic devices, efficient charge separation and charge stability is essential. Photo initiated charge transfer reactions of porphyrins have been extensively studied and many form long lived charge separate states; when combined with excellent charge carrier mobilities these systems are prime candidates for molecular electronic applications.[201-203] Photo initiated charge injection from porphyrins into semiconducting surfaces has been studied in the context of solar energy devices and the interfacial electron transfer rates are generally less than a picosecond.[32,98] Much work is being done in the design of new molecules capable of forming long lived charge separated states based on the distinct electronic states of porphyrinoids that enable functions such as current routers, gates and field effect transistors.[54,155,183,204-208] Linear gates and T gates have been fabricated and can be controlled by porphyrin redox chemistry as well as photochemistry.[209,210] Recent studies have also demonstrated that porphyrins on surfaces display stochastic switching.[34] Recently we have found that by forming nanoscale assemblies of zinc metalloporphyrins as those in Figure 1.9, stable Coulomb islands can be formed as evidenced by the appearance of a Coulomb staircase in the I-V measurements.

Derivatives of the generic molecule shown in Figure 1.4 have shown promise to serve as molecular capacitors and single electron tunneling devices in which small islands are assembled within electrode gaps and their charge state tuned using a gate voltage. In one example, we investigated the transport properties of zinc metalloporphyrin islands inserted into a dodecanethiol matrix on Au(111). Using

scanning tunneling microscopy (STM), it was shown that the zinc porphyrin islands exhibited bias dependent switching at high surface coverage, where the conductance of the molecules increased when sweeping above the threshold voltage and the islands returned to a lower conductance state when the tip was swept to the negative bias. This switching behavior at high coverage was found to result from the formation of Coulomb islands driven both by enhanced π-π aggregation of the macrocycles and by increased oxidation potential of the zinc metalloporphyrins. Low temperature measurements (~ 4 K) from crossed-wire junctions verified the appearance of a Coulomb staircase and blockade for only aggregates of the zinc porphyrins. In other examples, free base porphyrins in nanogap electrodes (formed as break junctions) have been reported to act as Coulomb islands.[211-213] Wakayama *et al.* observed Coulomb blockade staircases in the I-V measurements of these systems and also showed that the threshold voltages were sensitive to changes in the intermolecular interactions.[214-216] Overall, it has been shown that intermolecular interactions such as aggregation play a significant role in the electronic properties of porphyrin molecules. These aggregates readily show the ability to stabilize charge and this affords a means of creating bias switchable devices.

1.5 Space Charge

Materials composed of small molecular aggregates have been shown to exhibit the ability to store charge. In analogy to the semiconductor counterparts, the development of charge in the molecules of a SAM bound to a surface saturates before

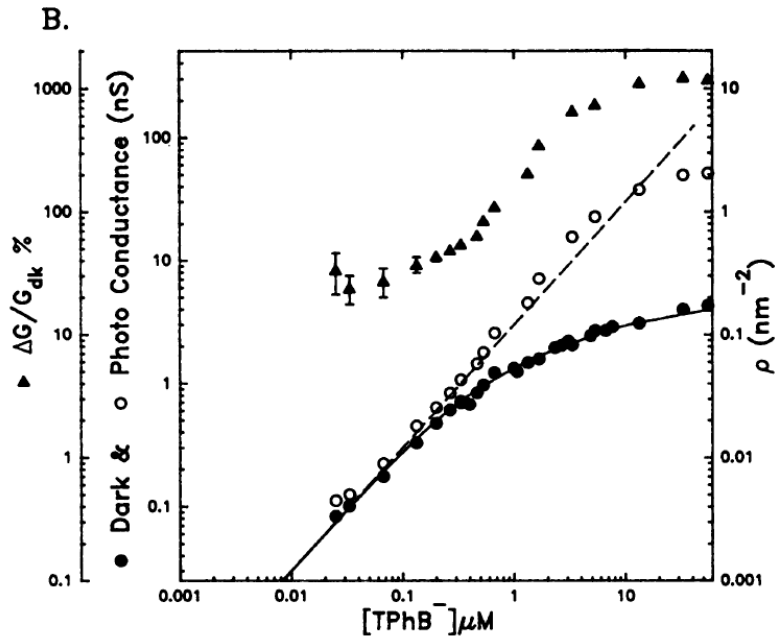

Figure 1.14. The conductance of tetraphenylboride ($TPhB^-$) through a lipid bilayer saturates with increasing concentration because of space charge limits (●). An implicit equation describes the space charge limited current, solid line: $\rho_{TPhB^-} = 0.602C\beta\exp(-qV_{TPhB})$ where 0.602 converts units of concentration mol $liter^{-1}$, to ions per nm^3, C is the concentration of the lipophilic ion, β is the partition coefficient, q is the molecular charge, and V is the potential of the ion inside the membrane based on electrostatic calculations. Cancelation of the space charge of the lipophilic anion by photo-formation of a porphyrin cation and self-assembly into an ion chain can increase the conductance by >20-fold (○), were the dashed line is the calculated non-space charge limited conductance. This photogated device is an early example of an all-organic molecular electronic. Reproduced from ref. [45] with permission of the copyright holders.

every molecule becomes ionized because of space charge limitations, and densely packed monolayers of porphyrinoids are an excellent example.[199,217,218] Space charge limited conductance of supramolecular porphyrin wires in lipid bilayers was previously noted (Figure 1.14).[42-45] Thus the optimum surface or device density of active molecules represents a balance between efficient use of molecules because of space charge limits and the need for redundancy to assure performance. Space charge scales with $q/4\pi\varepsilon_0\varepsilon_1$ where q is the charge, ε_0 is the vacuum permittivity (8.85×10^{-12} J^{-1} C^2m^{-1}), and ε_1 is the dielectric constant of the medium. Perhaps secondary SAM molecules in the matrix that can diminish the space charge effects by raising the dielectric constant (~3 for an alkane and 20-30 for a polyethyleneglycol) or serve as built-in counter ions which may allow greater surface densities of the active molecules.

Collectively, the conclusion is that organic molecules, especially porphyrins, show promise for future implementation into device architectures. The design of these molecules will continue to progress to the complete formation of functional devices. As a contribution to the allotment of current investigations, this thesis will provide evidence for the functionality of porphyrin and carboxylic acid terminated alkanethiols as components for working devices including fabrication strategies, measurement of properties, and theoretical modeling. STM has proven to be a powerful tool thus far for examining molecules for use in molecularly-enhanced devices, and as such, has been used to examine the properties of dodecanethiol/porphyrin mixed SAMs and patterned islands particularly for probing the electronic properties of the ensembles of porphyrin and 16-mercaptohexadecanoic acid molecules. The focus of the present research has

been on ensembles of molecules in confined spaces and to understand how the charge transport characteristics are altered in these confined settings.

1.6 Confined Geometries

Fundamental studies of the molecules, in this case, porphyrins, adsorbed on surfaces is the first step in developing higher order systems that can be incorporated into electronic components. The majority of studies mentioned previously focused on either single molecules or monolayers/thin films on surfaces. In almost any conceivable device to be made in the near future however, junctions containing ensembles of molecules on the order to tens to thousands are likely to be used. Moreover, even in self-assembled systems, domains and aggregates often predominate and their properties may depend significantly on domain size. As such, understanding how molecules assemble in confined geometries and how their local environment influences their conduction properties due to nearest neighbor interactions, via mechanisms such as pi stacking or vibronic coupling is required. To fully take advantage of the rich photochemistry of porphyrins and how they may be integrated with existing technologies such as CMOS, the details for controlling molecular assembly and charge transport in molecules on surfaces must be fully explored at the single molecule level as well as for small ensembles. As stated earlier, the electronic properties of single molecules or groups of molecules have been studied by others exploiting a range of different electrical testbeds, including mechanical and electrical break junctions,[117,219-222] cross-wire junctions,[223] nanopores,[224] and mercury drop contacts.[225] Other techniques such as conducting-probe atomic force microscopy (CP-AFM)[125,126] and scanning tunneling microscopy

(STM)[119,127,128] enable the observation of individual molecules on surfaces and can afford concomitant information on their local structural and electrical properties which will be used in the studies herein. It is critical to obtain direct topographic information, as well as transport properties such as the local tunneling probability as well as the electronic density of states including which molecular orbitals participate in the electron transport process.

Specific chemical or physical changes to molecules during charge transport however are difficult to assess *in situ*. A recent NSF report[1] specified that key to advancing our understanding of molecular conduction was the ability to probe chemical and/or structural changes simultaneously during charge transport in confined junctions. Several approaches to achieve this have been reported in the literature in recent years including inelastic electron tunneling spectroscopy (IETS)[226,227] and tip or surface enhanced Raman spectroscopy (T/SERS)[153,245-247] of electrical junctions. These approaches provide a powerful combination with electrical measurements and open the door to evaluating chemical changes that may be occurring in the buried interfaces formed by the molecules "sandwiched" between electrodes. IETS measurements provide a means to actually follow the conduction pathways in molecules by examining which modes become vibronically coupled to the conducting electrons[227] and how the local environment may perturb or alter these processes. It is important to examine the electronic pathway of the porphyrin thiol molecules to confirm that the transport is occurring through the molecule itself and that the electron is not just hopping from one junction to the next without current flowing through the molecule.

Lastly, understanding and controlling molecular assembly in the confined dimensions of electrical junctions is paramount to the development and implementation of molecule based nanoelectronics, whose function is dictated or enhanced (i.e. “more than Moore” applications) by the use of molecular assemblies to modulate charge transport. However little work has been done in examining how spatial confinement influences self-assembly in confined geometries. Various approaches using AFM, such as nanoshaving and nanografting, have been used to spatially organize molecules in confined assemblies. STM conducted in solution also provides a means to position new molecules in desired locations on surfaces.[228,229] From these studies it was found that the kinetics of the assembly process as well as the structures formed (i.e. differences in packing densities) can be distinctly different from molecular assembly on open surfaces. While for single molecules, the influence of surrounding molecules[175,230] on molecular conduction has been investigated, the way in which altering the chemistry in spatially confined structures impacts self-assembly and molecular conduction in confined molecular assemblies has not been thoroughly investigated. Porphyrin molecules assembled in confined matrices of dodecanethiol have been examined to ascertain the influence of the surrounding matrix on how the assembly and conduction of the molecule.

1.7 Past, Present, and Future

Previously in the pre-scanning probe era, there was excellent work on the conductivity of crystalline and polycrystalline materials that were in many ways the forerunners of today's efforts in molecular electronics. The pioneering works of Marks and coworkers on crystalline and polycrystalline halogen-doped $[M(Pc)O]I_x$, materials in the late 1970s (Figure 1.15)[231-233] is noteworthy. Electrical conductivities of the best performing wires, where M = Si, Ge, and Sn with x = 1 – 2, were ~0.1 Ω cm^{-1}. In view of the new analytical tools and new approaches to forming nanowires, it would be interesting to revisit these systems to assess the transport mechanism(s) and their photonic properties on the nano scale.

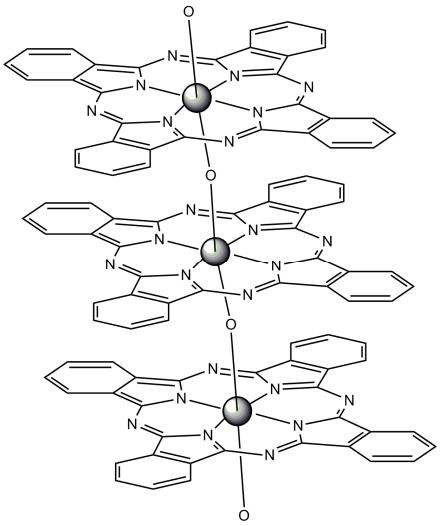

Figure 1.15. Conductive polycrystalline wires of Marks and coworkers reported in the early 1980s. Redrawn from refs. [218,233].

Currently, molecular electronics based on porphyrinoid systems show great promise for the future. The molecular design and formation of functional devices has been aided by new fabrication strategies, measurement tools, and theoretical models. Several key results should be noted. All parts of the molecule play critical roles in the molecular electronic properties: redox active moiety, linker, tether, and attachment group. The matrix surrounding the probed molecule has a profound effect on the activity of the molecule whether the matrix consists of passive alkanes, active molecules of the same kind, or active molecules of other types. The detailed electronic properties of a single molecule can be quite different than nanoscale domains or islands of these molecules. Space charge and redox potentials can limit the charge density on a given surface and number of charges on given molecules, respectively. The hierarchical organization of molecules, wherein the supramolecular structure varies with scale, has the potential to modulate function. For example, the intermolecular interactions between free-base porphyrins are different than the corresponding zinc metalloporphyrin in nanodomains of these molecules in SAMs. The precise architecture mediated by supramolecular interactions ranging from π-π to coordination bonds dictates the electronic communication between these nanodomains, thus having profound effects on the observed molecular electronic properties.

In the future, developing better theoretical and experimental probes of how both the ensemble and matrix affects molecular electronic properties will facilitate design of enabling technologies. For example, predictably designing specific switching properties and thresholds are a keystone issues to be developed. The matrix surrounding the active

molecules is an essential design element that has heretofore not been specifically studied. The role of molecular dynamics on multiple time scales (vibrational and conformational) on the molecular electronic properties is beginning to be appreciated both in terms of the initial charge transport efficiency and rate, and in terms of while the molecule is in the 'on' or 'off' redox state. Yet, there is a paucity of studies that systematically vary temperature with observed transport properties of porphyrinoid SAMs or those using matrix molecules with varying stiffness. The commercial viability of the dyes was not specifically discussed, but if the molecule is to be deployed on a large scale, easily scalable and economical synthetic strategies will be needed eventually.

Much of the work described above is on large areas of SAMs of porphyrinoids wherein little molecular level or nanoscale level measurements have been made. Though the surface may appear to be uniformly covered with the active molecules by electrochemical and spectroscopic methods, often it is yet to be determined how uniform is the molecular electronic properties are on the nanoscale. Are cadres of supramolecularly organized substructures present in the SAM? If so, do they have different transport properties as observed in the case of the porphyrins in the SAM matrix? Many of these systems are demonstrated to be remarkably robust, but can defective molecules be replaced to restore the functional parameters the device? What is the right balance between molecular economy and needed redundancy for a given function?

Indeed, as Feynman noted there has been a lot of public relations concerning the potential of molecular electronics, but as we develop a better understanding of Nature (e.g. the physics of molecular conduction), the long-held promise of molecular electronics may be moving from bench to successful technology.

1.8 Introduction to Subsequent Chapters

Organic molecules, specifically porphyrins and 16-mercaptohexadecanoic acid (16-MHA), were investigated for potential use as electronic components. Detailed 16-MHA studies were performed to investigate environmental effects of the molecules patterned in different solvents and different matrices. Environmental effects revealed that the type of solvent and background matrix can provide a robust, stable environment of nanoscale testbed arrays for investigation of organic molecules for future device components as well as metal-molecule-metal junction platforms. Self assembly versus directed assembly (or nanopatterning) of 16-MHA revealed interesting properties of the kinetic affects of monolayer versus bilayer formation with the carboxylic acid head group of the molecules as well as stochastic switching of the bilayer formation. 16-MHA was also used to explore how pattern density affects molecular assemblies while fabricating with SPL in confined geometries. The nature of the porphyrin studies was much more rigorous with a systematic investigation of derivatives of a thiol tethered porphyrin. Derivatives of the porphyrin were subject to modification of the coordination chemistry of the porphyrin macrocycle, fluorine attachment to the phenyl ring to control the barrier between the coupling of the pi conjugation with the tether, and surface attachment via a mono- or bipodal methylene spacer with a thiol tether. The porphyrin

thiol has been investigated as a pure monolayer, without any background surrounding matrix or a mixed monolayer, which provided a supportive, reference surrounding matrix on the Au surface before insertion of the porphyrin thiol. Whether pure or mixed monolayer, first a complete characterization of the porphyrin adsorbed on the surface was obtained which supplied information about the configuration of the molecules on the Au surface. Next charge transport analysis led to further modification of the structure of the porphyrin to obtain more desirable electronic properties, and this was carried out by specifically adding a zinc metal center or by adding a second surface linker to increase the stability and control the configuration of the molecular assemblies. Charge transport through these porphyrin derivatives in spatially confined versus unconfined geometries was the focus after physical and electronic characterization of each of the molecules. Low temperature I-V measurements showed Coulomb blockade and UHV-STM revealed the bias-induced switching behavior of zinc porphyrin islands on Au surfaces. These unique electronic properties provide evidence that these molecules could be used in single electron tunneling devices due to the capacitive behavior of the nanoscopic islands.

In Chapter II of this dissertation, an explanation of the experimental methods used throughout this research will be discussed. In Chapter III, the details of the complete characterization of thiol tethered porphyrin derivatized self assembled pure and mixed monolayers on Au surfaces will be provided. The characterization procedure provides information including: attachment orientation based on the angle and physical height of the molecule, conductivity which is determined based on the apparent height

and current-voltage (I-V) behavior of the molecule, conductance switching behavior due to conformational or other effects and stability of the molecules. A variety of characterization and analysis methods were employed including: Reflection Adsorption Infrared Spectroscopy (RAIRS), Atomic Force Microscopy (AFM), X-ray Photoelectron Spectroscopy (XPS), Scanning Tunneling Microscopy and Spectroscopy (STM/S) and low temperature STM, Density Functional Theory (DFT) calculations, and Inelastic Electron Tunneling Spectroscopy (IETS) which aid in the surface characterization and charge transport characteristics of each of the different assemblies. In Chapter IV, a metalloporphyrin with interesting electronic characteristics is examined in detail, while Chapter V provides insight into controlling molecular assemblies by using bipodal surface-attached porphyrin thiol derivatives. Chapters VI and VII will focus on nanopatterning techniques and optimization. Specifically in Chapter VI, scanning probe lithography was used to create well-defined patterns of organic carboxylic acid terminated molecules and investigating environmental effects when fabricating nanoscale assemblies. Chapter VII covers the fabrication and charge transport behavior of directly assembled zinc porphyrin thiol nano-islands for future investigation of electrical junctions for implementation into nanoelectronics. In Chapter VIII, a summary will be given along with future directions of this project. Overall, porphyrins are known to have π-electron delocalization and small HOMO-LUMO gaps resulting in lower charge injection barriers, more efficient charge transfer, and accessible states near the Fermi level of the metal. These well-known properties as well as the investigated electronic properties in this dissertation have provided us with the knowledge of

molecules that show great potential as electronic components, and spatially organizing organic molecules on surfaces using nanolithography methods moves us one step closer for future implementation of molecules into devices.

CHAPTER II

EXPERIMENTAL METHODS

2.1 Preparation of SAMs

Molecular electronics is an ever-growing field,[165,234,235] but before molecules can be implemented into electronics, the molecule or assembly of interest must undergo full characterization and structure-function relationship analysis. All of the porphyrins studied are first adsorbed onto a Au surface using a method known as self-assembly. When the porphyrin self assembles through solution based methods onto a surface, in this case, it forms a monolayer, or one layer of molecules on the Au. The molecules attach to the Au surface through chemisorption where the thiol tether bonds to the Au surface. Once the porphyrins form a self-assembled monolayer (SAM) on the Au, the molecule can undergo rigorous characterization.

2.2 STM and STS

To better realize the potential of the molecules studied in this dissertation, many tools are required including one of the most valuable tools for surface scientists, the Scanning Tunneling Microscope (STM). Developed in 1981 by Binnig and Rohrer,[236] the STM has become a powerful tool in examining the electronic nature of atoms and molecules on conducting surfaces. The STM provides high resolution images of a surface using a quantum mechanical phenomenon known as tunneling. Tunneling is a phenomenon when an electron passes through a classically forbidden region. In STM, when the tip is very close to the sample, the wavefunction of the tip and sample overlap

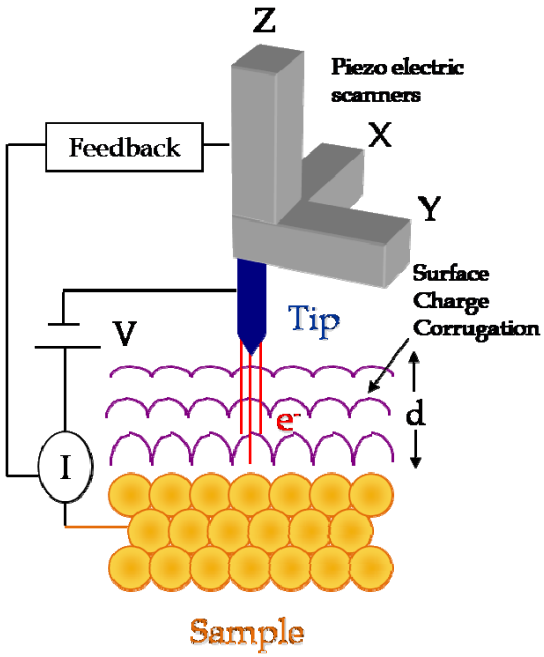

Figure 2.1. Schematic of Scanning Tunneling Microscopy (STM).

and the electron can tunnel from the tip to the sample or vice versa depending on the direction of the applied bias. The STM is comprised of major components including the electronics, the probe (typically a Pt/Ir tip), a positioner (piezoelectric components to convert voltage into a physical motion), and a feedback loop as shown in Figure 2.1. When an ultra-sharp Pt/Ir tip is near the sample surface the electrons will tunnel from the tip to the surface due to the overlap of wavefunctions. A voltage bias is applied which shifts the alignment of the energy levels of the tip and surface causing the electrons to tunnel through a classically forbidden barrier. The potential difference is maintained and

the distance of the tip from the surface is controlled using a feedback mechanism to signal if the current is too high or too low and the tip distance will adjust in order to maintain a constant current. The STM will produce a topographic image of the surface based on the apparent height of the sample which is a convolution of the actual physical height and electronic structure. Therefore, a molecule that is conductive will appear brighter and higher in height in the STM image compared to an insulator. Scanning tunneling spectroscopy (STS) uses an STM tip to obtain current-voltage (I-V) and current-distance (I-z) measurements to gather information about the sample such as the barrier height (φ), tunneling constant (β), and conductance of a sample which are necessary to determine the type of application of the molecules.

2.3 AFM

Another tool to examine the detail of surfaces is Atomic Force Microscopy (AFM) which was invented by Binnig, Quate, and Gerber in 1986.[237] The AFM has a major advantage since it has the ability to image all types of surfaces, whereas the STM is limited to conducting and semi-conducting surfaces only. Similarly to an STM, the AFM is comprised of a probe (typically Si or Si_3N_4 tip on a cantilever), piezoelectric elements, and a feedback loop which relies on molecular forces to modulate the tip-sample interaction (see Figure 2.2). In contact-mode imaging, the AFM tip follows the physical profile of the surface maintaining a constant lever deflection, δx, translating into a topographic image of the sample surface. The force, F, applied during imaging is determined by knowing the deflection of the lever and the stiffness or spring constant, k,

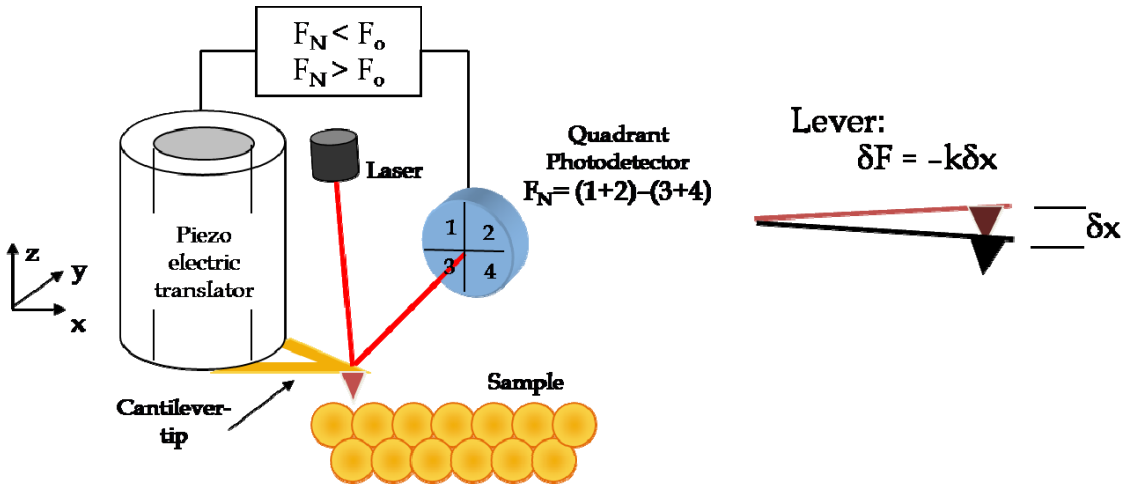

Figure 2.2. Schematic of Atomic Force Microscopy (AFM).

of the cantilever. Other than visualizing molecules on a surface, the AFM can also be used to manipulate molecules using lithographic techniques such as nanoshaving and nanografting[229] as well as Nanopen Reader and Writer (NPRW).[238] More specifically, nanoshaving uses the AFM tip to shave away a host of matrix molecules and leaves behind a hole, or nanowell, of exposed underlying substrate. Nanografting is similar to nanoshaving, however as the matrix molecules are shaved away, new molecules from solution are bound to the surface where the shaving took place, forming a pattern on the surface. NPRW combines nanografting with Dip Pen Nanolithography (DPN)[239] and uses a precoated tip to displace background molecules which are replaced with the molecules on the tip. Typical AFM measurements use a Si_3N_4 tip in order to resolve surface details, but if the tip is coated with a metal such as gold or platinum, e.g. a

conducting tip, it is known as Conducting Probe AFM (CP-AFM) which can be used to evaluate the electronic properties of the surface. CP-AFM differs from STM in that the force of the tip is maintained as the feedback loop unlike the current which is used for STM.

2.4 IR Spectroscopy

Other techniques which are not necessarily surface sensitive techniques can also be applied to explore molecules adsorbed on surfaces. Conventional Fourier Transform Infrared spectroscopy (FT-IR) has been transformed to acquire the vibrational modes of molecules on surfaces known as Reflection Adsorption Infrared Spectroscopy (RAIRS).[240,241] RAIRS is similar to conventional IR spectroscopy, but in this case the molecules are deposited on a surface which have characteristic vibrational modes that can be detected as long as the dipole change is perpendicular to the metal surface. RAIRS can also used to characterize the molecules on the surface, specifically it is used to calculate the orientation of the molecule by studying the in-plane and out-of-plane vibrational modes.[242]

2.5 XPS

X-ray Photoelectron Spectroscopy (XPS) is a technique developed in the 1960s which is based on the photoelectric effect. XPS uses a photoelectron source illuminated onto a sample surface and the beam from the source ejects electrons from the sample which have characteristic binding energies. These characteristic binding energies are described as the amount of attraction the electron has with the nucleus and are dependent on the type of atom and environment they are in. Due to these binding energies, XPS is

a tool used to distinguish which elements are present on the surface. XPS is considered a surface sensitive technique even though the bulk material is still excited with the source as the ejected photoelectrons have mean free paths of only ca. 1 nm. XPS aids in the characterization process by determining which elements are present and the chemical environment of the elements after the molecule is adsorbed onto the surface.

2.6 IETS

Inelastic Electron Tunneling Spectroscopy (IETS) is a method also developed in the 1960s and is used to measure the tunneling pathway of a molecule in a metal-molecule-metal sandwich array. The inelastic pathways of the molecule are observed in which the electron loses some energy to another pathway such as a vibrational or electronic mode. IETS is a powerful tool for studying molecular conduction in a confined junction.[243-245] IETS measurements provide a means to actually follow the conduction pathways in molecules by examining which modes become vibronically coupled to the conducting electrons, and how the local environment may perturb or alter these processes.

2.7 Computational Methods

A theoretical approach will also be used in this dissertation which is pertinent to model and verify the experimental results. Density Functional Theory (DFT) is used as the main method to calculate the molecular structure as well as the analytic vibrational modes, electronic structure, and rotational energy barriers. Time-dependent density functional theory (TDDFT) and other computational methods such as ADF will also be

used to investigate the charge transport, molecular stacking arrangement and other surface characteristics of the porphyrins on Au.

CHAPTER III

SYNTHESIS AND CHARACTERIZATION OF A THIOL-TETHERED TRIPYRIDYL PORPHYRIN ON AU(111)*

3.1 Introduction

In recent years, thiol-derivatized molecules on gold substrates have been widely implemented for elaborate designs of molecular electronics.[163-166] The use of self-assembled monolayers (SAMs)[158] has been extensively employed for this development because of the relatively stable, two-dimensional, and densely packed structures that can be formed on metal or semiconductor surfaces through robust chemical bonds (e.g. Au-S, Si-O and Si-C bonds) as compared to Langmuir-Blodgett (LB) films[246] and lipid bilayers.[4] The electronic properties of single molecules or small groups of molecules have been studied by constructing different electrical testbeds, including electrical and mechanical break junctions,[119,168,247-249] cross-wire junctions,[223] nanopores,[224] mercury drop contacts,[225] conducting-probe atomic force microscopy (CP-AFM),[12,125] and scanning tunneling microscopy (STM).[119,127,128] STM is a powerful surface analysis technique, as it enables the observation of individual molecules with atomic resolution on surfaces. In addition to topographic details, STM images can elucidate details of the local tunneling probability as well as the electronic density of molecular orbitals (e.g.

---

*Reproduced with permission from *Journal of Physical Chemistry C*; Yang-Hsiang Chan, Amanda E. Schuckman, Lisa M. Pérez, Mikki Vinodu, Charles M. Drain and James D. Batteas, "Characterization of a Thiol-Tethered Tripyridyl Porphyrin on Au(111)," *J. Phys. Chem. C*; **2008**; 112(15); 6110-6118. Copyright 2008 American Chemical Society.

highest occupied molecular orbital, HOMO and lowest unoccupied molecular orbital, LUMO) participating in the tunneling process and thus can influence the local transport behavior.

Although organic molecules with[250-252] and without[12,230,253] π-electron conjugated system have attracted considerable attention for the potential manufacturing of electronic devices down to the molecular level, highly π-conjugated molecules are of particular interest since the π-electron delocalization inside such molecules typically results in lower injection barriers and more efficient tunneling or electron transfer. Recent work in this aspect has been explored on polythiophenes,[254-256] oligo(phenylene ethynylene)s (OPEs),[257-259] oligo(phenylene vinylene)s (OPVs)[260] as well as phthalocyanines,[261] porphyrins,[262,263] Re/Ru-bipyridyl molecules,[264] and metal string complexes.[265,266] There have been a number of previous studies on porphyrins anchored to various substrates[156,267-270] because of their remarkably diverse photoelectrochemical, catalytic, electronic, and biochemical properties[271] that enable their use as active components of devices for applications including chemical sensors,[272,273] information storage,[124,274] and electrocatalytic or photocatalytic oxidations or reductions.[275,276] The relatively small HOMO-LUMO gap (ca. 2 eV) and the proximity of the HOMO states to the Fermi level of Au can be an advantage in many of these applications. In addition to single molecules, hierarchical assemblies of porphyrins self-organized by various strategies have also been explored as a means of creating light harvesting structures for energy conversion.[76,87,277,278]

Key in the implantation of hierarchical assembly of porphyrins for the construction of molecular based devices is the ability to readily create assemblies that can be reliably organized and attached to surfaces in high yields. In the work presented here, a free-base porphyrin macrocycle bearing three 4-pyridyl moieties and one pentafluorophenyl substituent in the *meso* positions was synthesized as a core platform for the rapid, high yield attachment of tethers that can be tailored to both the surface chemistry and other properties. In the present case a terminal dithiolalkane replaces the 4-fluoro group to yield a derivative for immobilization onto a gold surface via strong sulfur-gold chemisorption (Figure 1.1). The work described herein is the first in a series of molecular systems being investigated by our groups for the creation of light harvesting and molecular/organic electronic devices. The pyridyl moieties provide a convenient attachment point for additional molecules via metal-ligand coordination chemistry, while the use of the fluorinated phenyl ring provides an easy surface attachment group. Moreover, by controlling the extent of fluorination of this linker group, this phenyl ring, can be used as an internal barrier to control the tunneling between the pyrrole macrocycle and the thiol tether. This barrier can be modulated by systematic variation of the number and position of the fluoro groups on the ring, thus affording some control of the relative orbital energies of this phenyl group and the degree of steric interactions between the 2,6-positions on this phenyl group with the pyrrole β-hydrogens. Thus, control of these interactions provides a means to dictate the electronic coupling between the macrocycle and the tether.

In this chapter, the tri-pyridyl porphyrin with the fully fluorinated ring has been explored. In addition to the synthesis, we describe the preparation and characterization of mixed monolayers of the thiol tethered porphyrin inserted into a pre-assembled *n*-dodecanethiol monolayer on gold surfaces. The surface assembly has been characterized utilizing STM, AFM, X-ray photoelectron spectroscopy (XPS), and reflection absorption infrared spectroscopy (RAIRS). Density Functional Theory (DFT) calculations have also been employed to aid in detailing the molecular and electronic structures, as well as the analytic vibrational modes of this molecule for comparison to experiment.

3.2 Experimental

3.2.1 Materials

Self-assembled monolayers were prepared on Au films, including Au(111) on mica (Molecular Imaging-Agilent, Phoenix, AZ) and on evaporated Au films on Si. Au films on Si substrates were prepared by thermal evaporation onto single-side polished Si(100) wafers (Virginia Semiconductor Inc.) in a bell-jar evaporator (BOC Edwards, Auto 306). The chromium (5 nm) and gold (200 nm) films were deposited under vacuum ($p < 2.0 \times 10^{-6}$ Torr) at the rate of 0.5 and 3 Å/s, respectively. Dodecanethiol (DDT) was purchased from Aldrich (98% purity) and used as received.

3.2.2 Synthesis of Porphyrin Thiol Compound

5,10,15-tri(4-pyridyl)-20-(4-(1',5'-dithiopentyl)-2,3,5,6-tetrafluorophenyl) porphyrin (TPy_3PF_4-SC_5SH) was synthesized in two steps. First, a mixed aldehyde condensation in propionic acid using one equivalent of pentafluorobenzaldehyde, three equivalents isonicotinaldehyde and four equivalents pyrrole yields a statistical mixture

of compounds that are readily separated by flash chromatography.[87] The 4-fluoro group of the target 5,10,15-tri(4-pyridyl)-20-perfluorophenylporphyrin (15 mg, 21.2 mmol), was reacted with 1,5-dithiopentane (25 mL, 180.5 mmol) and diethyl amine (60 mL, 580 mmol) in a solvent mixture of DMF, chloroform and methanol (4:4:1 v/v, 3 mL) in the dark under nitrogen at room temperature for 24 h. After evaporation of the solvent at reduced pressure, the crude product was purified by flash silica gel column chromatography with a 97% CH_2Cl_2 / 3% CH_3OH (v/v) eluent. The major fraction was collected and subjected to one more column purification with the same solvent system (yield 13.8 mg, 79% based on compound 1). UV-visible in CH_2Cl_2 (λ_{max} nm (rel. intensity): 416 (100), 511 (9.28), 544 (3.85), 585 (4.25) and 640 (2.39). NMR (500MHz, $CDCl_3$):δ = 9.10 (d, J = 5.3 Hz, 6H), 8.91 (m, 8H), 8.20 (m, 6H), 3.31 (t, 2H), 2.67 (m, 2H), 1.91 (m, 2H), 1.79 (m, 4H), 1.45 (t, 1H) and –2.81 (s, 2H). UV-Vis ($CHCl_3$): 416, 511, 544, 585 and 640. ESI-MS: 824 (MH^+).

3.2.3 Preparation of Pure and Mixed Monolayers

Au(111) substrates (purchased from Molecular Imaging Inc.) were ~150 nm flame-annealed gold films on mica. Before each experiment, all substrates were treated with UV/ozone for 20 min, followed by rinsing the gold film in sequence with high purity (18.2 MΩ•cm) water (NANOpure Diamond, Barnstead), ethanol, and dried with streaming nitrogen. Pure SAMs were formed by immersion of the Au films in 0.5 mM free base porphyrin thiol dissolved in dichloromethane for one to eight days to allow the assembly of the porphyrin molecules. After assembly, the substrates were removed from the solution and were rinsed with dichloromethane and blown dry with streaming

nitrogen. Mixed SAMs were formed by first making SAMs of *n*-dodecanethiol which were formed by immersion of the Au films in 1 mM *n*-dodecanethiol in ethanol for 24 h. After rinsing liberally with ethanol, the substrates were soaked in 0.5 mM porphyrin thiol dissolved in dichloromethane for five days to allow the insertion of the porphyrin molecules into *n*-dodecanethiol matrix. After insertion, the substrates were removed from the solution and were rinsed with dichloromethane and blown dry with streaming nitrogen.

3.2.4 Scanning Tunneling Microscopy

STM measurements were taken both in air and under ultrahigh vacuum (UHV) conditions. STM measurements in air were carried out with a NanoScope IIIa (Veeco Metrology Group, Santa Barbara, CA) using a low-current scanning head under ambient conditions. High resolution images were collected under UHV conditions using an Omicron UHV-XA STM system. The system was operated with a typical base pressure of $< 3 \times 10^{-10}$ Torr. Images were collected using Pt/Ir (70/30) tips which were mechanically cut. The typical imaging conditions of tunneling current and tip bias voltage ranged from 10 pA to 200 pA and from +500 mV to +1.5 V, respectively. Current-voltage (I-V) spectra were collected under UHV conditions over a voltage range of -2 V to + 2 V.

3.2.5 Atomic Force Microscopy

AFM images were acquired with a Molecular Imaging 4500 Pico SPM (Agilent, Phoenix, AZ) with a deflection-type detection scanning head interfaced with an SPM1000 control electronics Revision 8 (RHK Technology Inc., Troy, MI). All AFM

images were acquired in contact mode under ethanol using commercially available Si_3N_4 AFM tips (Veeco/TM Microscopes, Sunnyvale, CA) with nominal tip radii of ~ 10 nm and nominal spring constants ranging from 0.03-0.1 N/m.

3.2.6 X-ray Photoelectron Spectroscopy

XPS data were acquired with a Kratos Axis ULTRA X-ray photoelectron spectrometer equipped with a 165 mm hemispherical electron energy analyzer. The incident radiation was the MgKα X-ray line (1253.6 eV) with a source power of 180 W (15 kV, 12 mA). The analysis chamber was maintained at a steady base pressure of $<6 \times 10^{-9}$ Torr during sample analysis. Survey scans of up to 1100 eV were carried out at a analyzer pass energy of 160 eV with 1.0 eV steps and a dwell time of 300 ms. Multiplexed high resolution scans (Au 4f, C 1s, S 2p, N 1s, and F 1s) were taken at a pass energy of 40 eV with 0.1 eV steps and a dwell time of 60 ms. The survey and high resolution spectra were obtained with averages of 5 and 50 scans, respectively. The Au 4f peak at 84.0 eV was set as a reference for all XPS peak positions to compensate for energy shifts due to the spectrometer work function. The fitting of high-resolution sulfur peak was executed by utilizing XPSPEAK 4.1 in which a Shirley-type background[279] (from ~159 eV to ~168 eV) with an 80% Lorentzian-Gaussian curve-fitting program were used. The spin-split doublets of the S(2p) were fitted by fixing the area ratio at $2p_{3/2}$:$2p_{1/2}$ = 2:1 and setting their energy difference to 1.2 eV. The full width half-maximum of each peak was also maintained at a constant value.

3.2.7 FT-IR Spectroscopy

Transmission IR spectra of the solid porphyrin compounds were obtained in KBr pellets. FT-IR spectra of the mixed monolayers were collected on evaporated Au films on Si. Reflection-absorption spectroscopy was collected using an FT-IR spectrometer (Nicolet 6700, Thermo Electron Corporation, Madison, WI) equipped with a liquid nitrogen-cooled HgCdTe (MCT) detector. FT-IR data were acquired in single reflection mode with polarized light generated by a ZnSe polarizer adaptor (FT-80, Thermo Electron Corporation). The light path, MCT detector, and sample chamber were purged with dry nitrogen during the measurements. An UV/ozone cleaned gold substrate was used as the reference. The IR spectra were collected with a total of 1024 scans of both the sample and the reference at 4 cm^{-1} resolution.

3.2.8 Theoretical Calculations

Calculations of the molecular structure, electronic structure, and analytic vibrational modes were carried out using Density Functional Theory (DFT).[280] All calculations were carried out with the Gaussian 03[281] suite of programs. The TPy_3PF_4-SC_5SH molecule was fully optimized and analytical frequencies were calculated at the DFT level with the TPSS[282] functional with a density-fitting basis set.[283] A Pople style[284,285] double-ζ quality basis set with a diffuse[286] and optimized polarization function on heavy atoms[287] (6-31G+(d')) was used for all atoms. Polarization (d) functions used spherical harmonic representations.

We chose the TPSS functional and basis set, 6-31G+(d'), by calibrating against the unsubstituted free base porphine. The TPSS/6-31G+(d') frequencies fit the

experimental data for the unsubstituted free base porphine very well and with reasonable computational cost. Larger basis sets as well as the B3LYP [Becke three-parameter exchange functional (B3)[288] and the Lee-Yang-Parr correlation functional (LYP)[289]] DFT was also used for the optimization and analytical vibrational frequency calculations for the unsubstituted free base porphine and compared to the TPSS and experimental results.

3.3 Results and Discussion

3.3.1 Theoretical Calculations

Density functional theory calculations were used to optimize the gas phase structure of the porphyrin thiol compound and the results were compared with the experimental studies. The optimized structure of the porphyrin thiol is shown in Figure 3.1B shows that the pyridyl groups are canted at ~ 65^{o} relative to the macrocycle, which is constant with the numerous crystal structures of *meso* aryl porphyrins.[290] The tetrafluorophenyl group is found to be nearly perpendicular to the macrocycle. The length of the porphyrin from the attaching sulfur atom to the nitrogen in the top pyridyl group is 2.42 nm. The calculations indicate the porphyrin macrocycle is distorted slightly with C5 to C15 length of 0.70 nm and the C10 to C20 length of 0.69 nm. This differs from the optimized structure of the unsubstituted free base porphine molecule (Figure 3.1A) with a symmetric macrocycle with a length of 0.69 nm across both the C5 to C15 and the C10 to C20 directions. The HOMO - LUMO gap for the porphyrin thiol was calculated to be 1.83 eV which is a smaller gap than the unsubstituted free base porphine with a calculated HOMO - LUMO gap of 1.98 eV. The small HOMO - LUMO

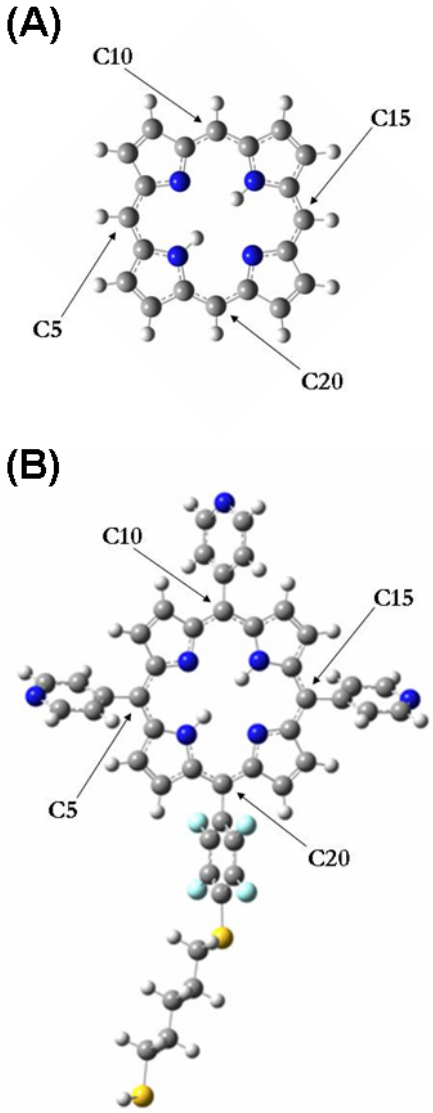

Figure 3.1. TPSS optimized structures for the (A) unsubstituted free base porphine and (B) free base porphyrin thiol.

gaps for these materials make them good candidates for molecular electronics, in comparison to many other molecules that have been studied, which exhibit gaps in excess of 2.5 eV.[8] Moreover, the location of the HOMO state (-5.27 eV) relative to the Fermi level of the Au substrate (-5.1 eV)[291] based on these calculations (with all of their associated caveats), suggests a small injection barrier of ca. 0.2 eV. The frontier orbitals that should participate in the electron transport process as shown in Figure 3.2 reveal no overlap between the orbitals of the porphyrin macrocycle and the tetrafluorophenyl ring that links the macrocycle to the thiol tether. Thus, there is an inherent barrier to charge transport located directly within the molecule, which may contribute to the observed low current values observed by STM current-voltage measurements of the molecules on Au as described below. Future experiments will aim to alter the porphyrin – phenyl coupling group by systematically removing fluorine groups from the phenyl ring. This would enable us to control the ring rotation dynamics and predictably alter the orbital overlap between the macrocycle and the alkyl chain, thereby affording a means to control the charge transport characteristics.

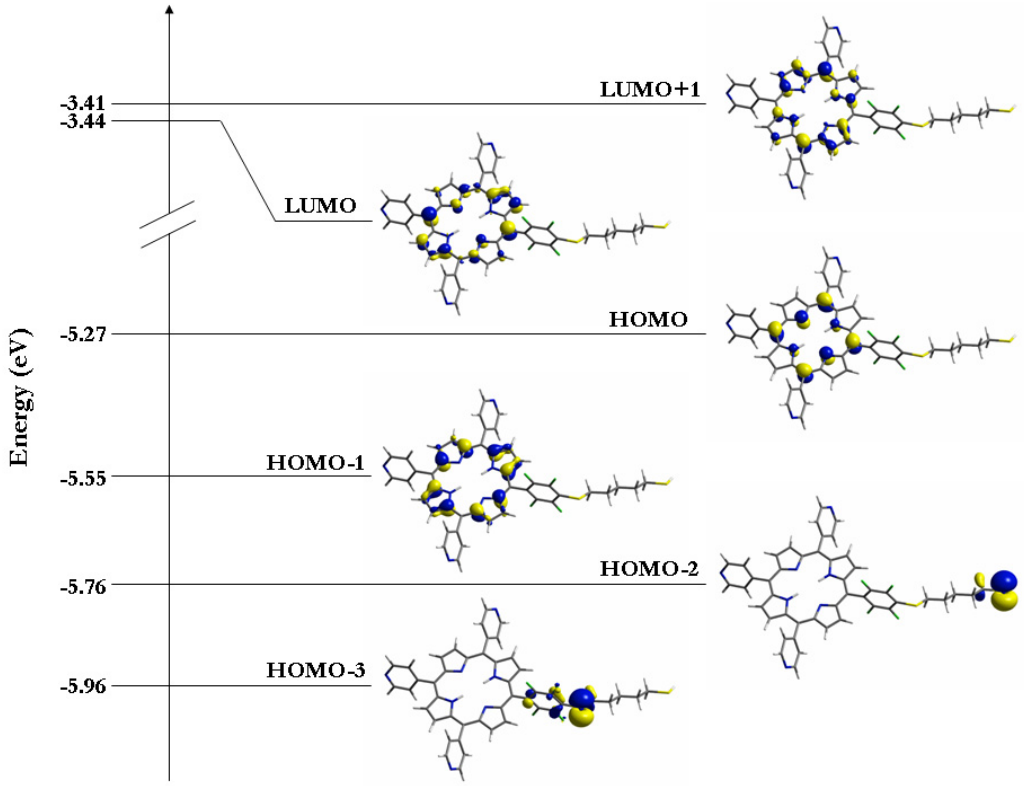

Figure 3.2. Frontier molecular orbitals (HOMO-3 to LUMO+1) for the porphyrin thiol.

3.3.2 Spectroscopy- Pure Monolayers

The free base porphyrin thiol molecule has been analyzed using UV-Vis spectroscopy, FT-IR measurements as well as AFM and STM. UV-vis spectroscopy of porphyrin molecules typically results in very characteristic spectra. The spectra have two Q-bands which are present in the visible region around 500 – 600 nm for metalloporphyrin complexes. The lower energy band is the electronic origin of the lowest-energy excited singlet states. The higher energy band includes one mode of

vibrational excitation. For free base porphyrins, there are four Q-bands since the spectrum goes from a D_{4h}-type to a D_{2h}-type. Breaking of the D_{4h} symmetry splits each Q band owing to a vibronic overtone. Each porphyrin absorption spectrum also has a characteristic Soret band (or B band) which is very intense around 380 – 420 nm. It is

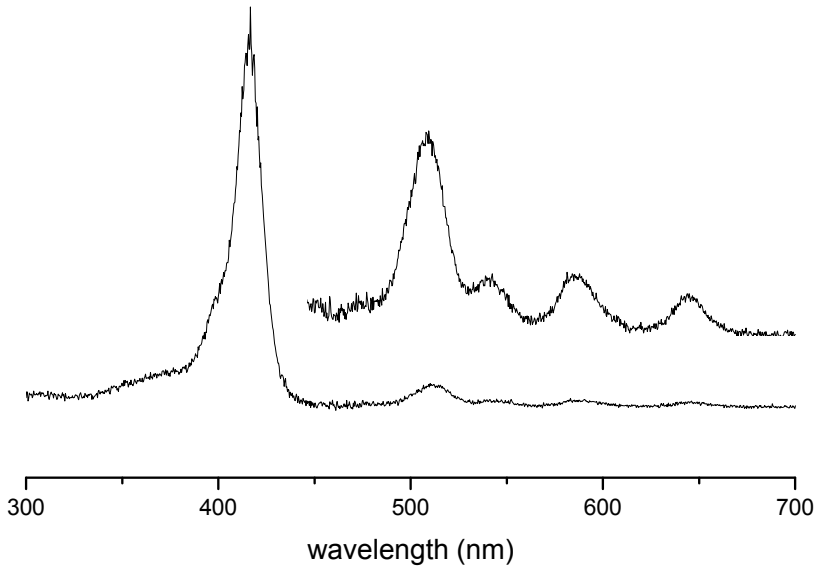

Figure 3.3. UV-Vis spectrum of porphyrin thiol in CH_2Cl_2.

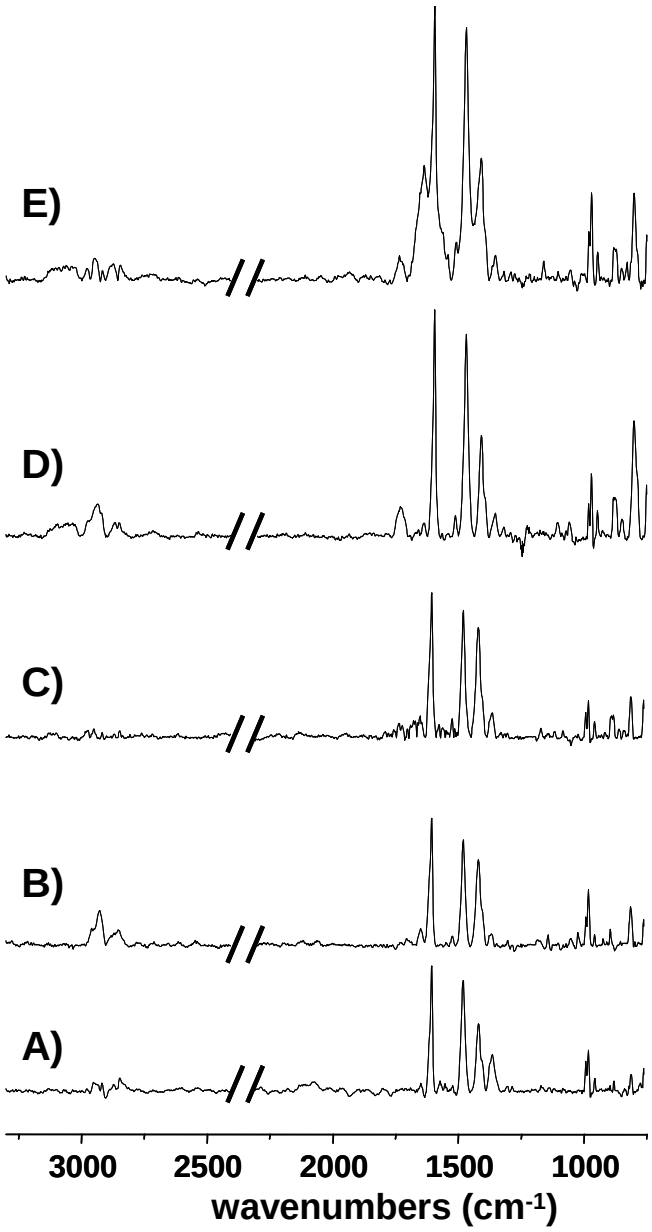

Figure 3.4. IR spectra of pure porphyrin monolayers on Au/Cr/Si after (A) 1 day, (B) 2 days, (C) 4 days, (D) 8 days and (E) 12 days soaking time.

the origin of the second excited singlet state. The UV-Vis spectrum of the porphyrin thiol is shown in Figure 3.3, which has a Soret band prevalent at ~ 417 nm and four Q-bands which have been magnified for visualization.

SAMs can be composed of pure monolayers of only one type of molecule, or can be mixed, where a host of matrix molecules are first formed on the surface followed by insertion of the molecule of interest. Pure monolayers of the free-base porphyrin thiol molecule assembled onto a bare Au substrate have been analyzed. The Au substrates were soaked in the pure porphyrin solution over a number of days. The IR spectra were taken at 1, 2, 4, 8 and 12 days and the porphyrin peaks (from ~ 650 – 1600 cm^{-1}) increased in intensity over that time period as shown in Figure 3.4. By comparing the IR spectra of the monolayers with the KBr and calculated IR spectra (shown in Figure 3.5), it has been found that the porphyrin molecules tend to lie close to the surface with a tilt angle of ~ 48° with respect to the normal of the Au surface. It is expected that without a surrounding matrix, the porphyrin molecules will not favor a stable upright position on the surface.

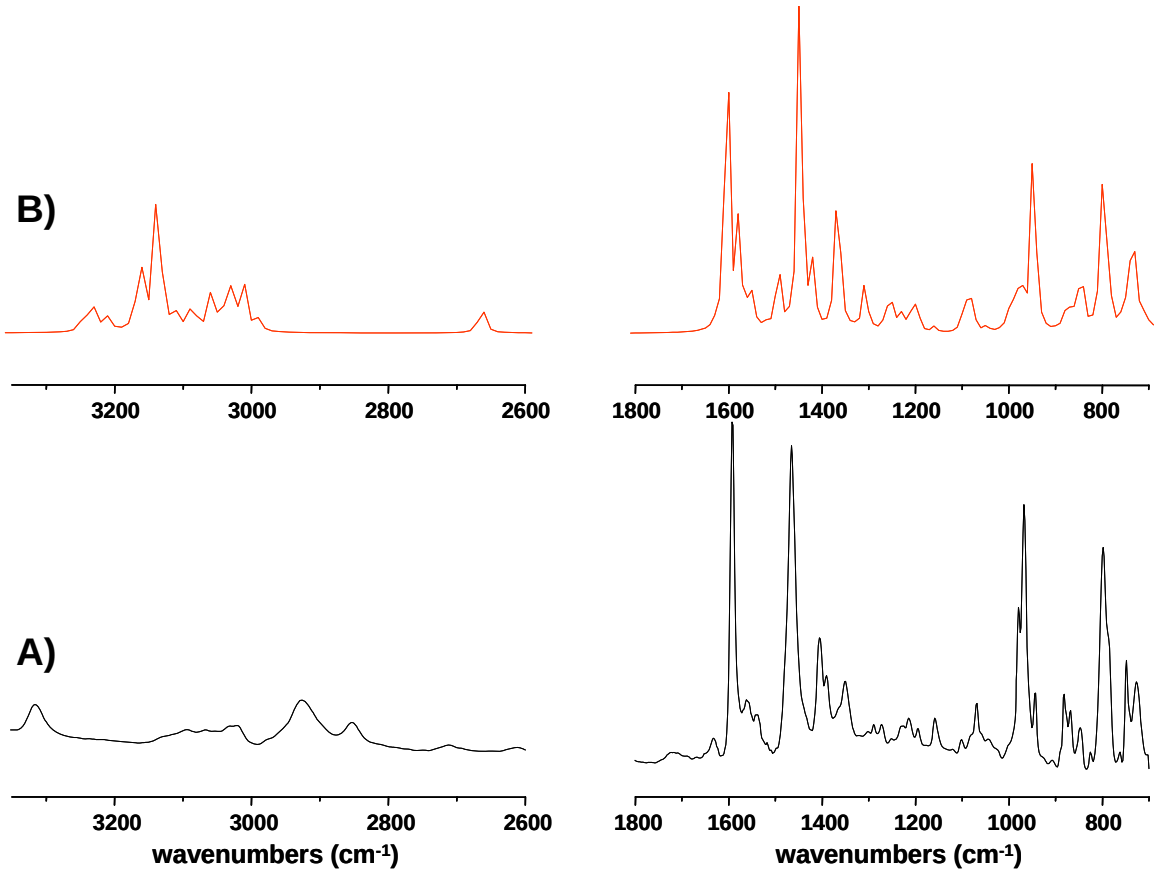

Figure 3.5. IR spectra of porphyrin thiol in (A) KBr pellets and (B) DFT calculated.

3.3.3 Surface Imaging- Pure Monolayers

Utilizing surface imaging such as AFM and STM has allowed for the visualization of the molecules on the surface after immersion into solution after 1, 4 or 8 days. AFM images of the sample indicate that after longer soaking times of the Au substrate in the porphyrin thiol solution, the porphyrin molecules begin to form clusters and aggregate together (Figure 3.6). These clusters have a physical height of ~ 2 nm above the Au surface which is approximately the actual height of the molecules. As the

molecules begin to pi-stack and aggregate together, they have the ability to stand more upright and not lie completely flat on the open Au surface. Since there is not a matrix monolayer, the pure porphyrin thiol monolayers are not inhibited and have the freedom to move around on the Au surface. The STM images reveal that the porphyrin thiol does not appear as segmented clusters but rather a uniform film on the Au surface.

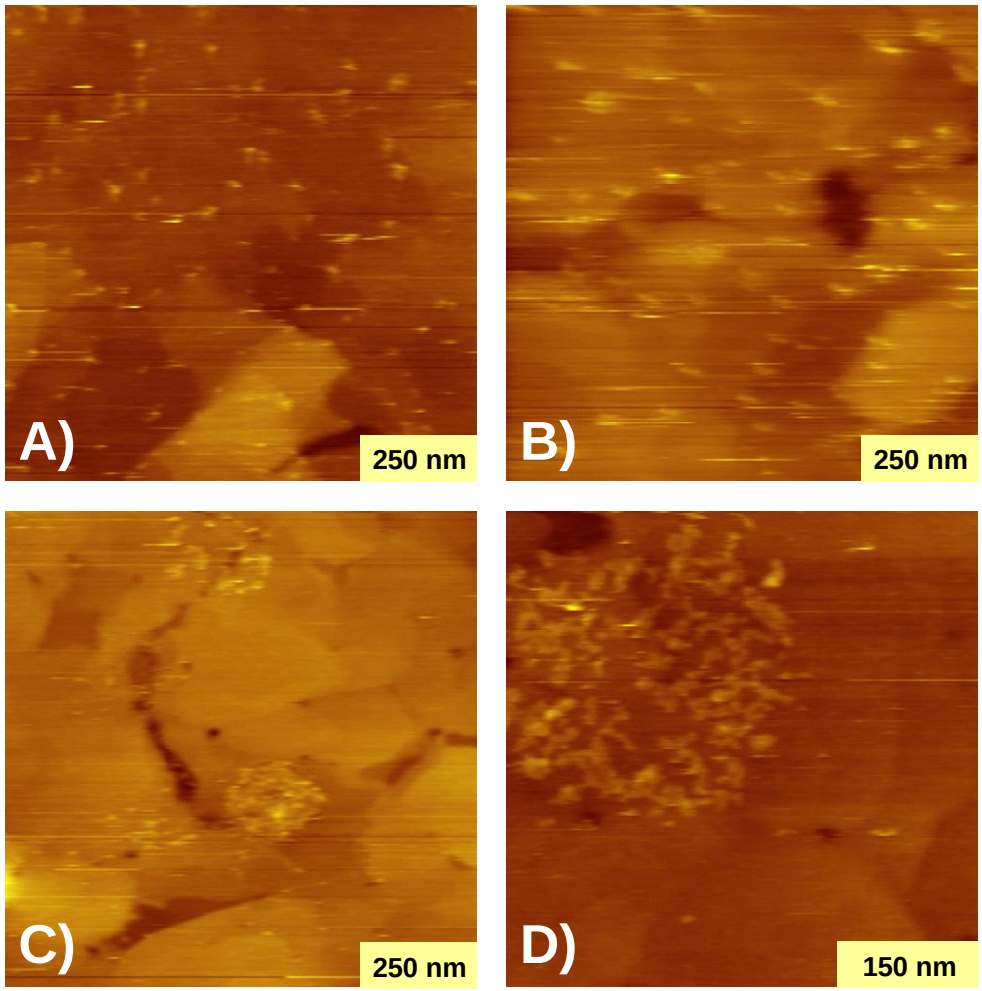

Figure 3.6. AFM topography images of pure porphyrin thiol monolayer on Au(111) after (A & B) 1 day and (C & D) 4 days.

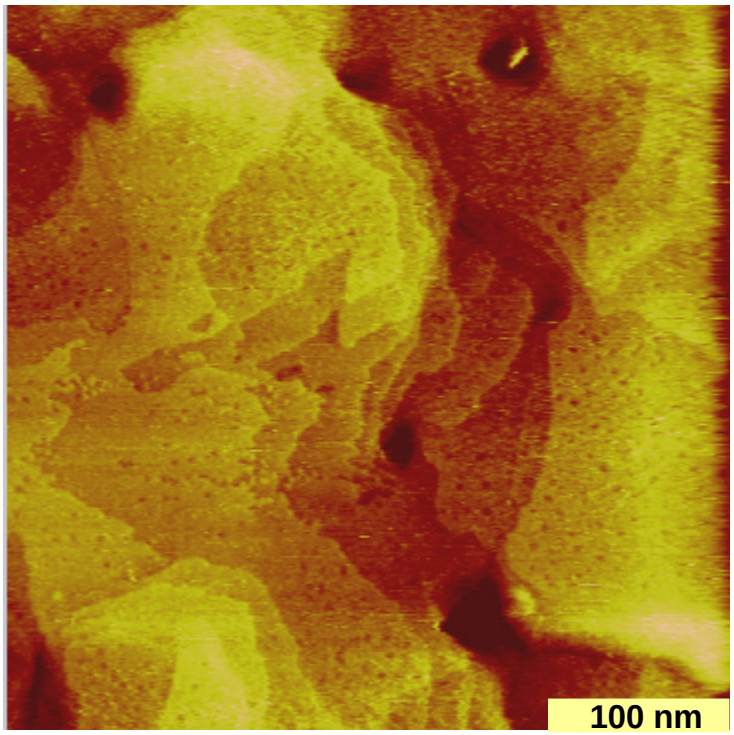

Figure 3.7. STM image of pure porphyrin monolayer on Au/mica after 8 days.

In Figure 3.7, after 8 days of soaking the porphyrin thiol, there are no bright spots on the surface which would indicate single molecules standing upright on the surface. However, we do see etch pits from the thiol terminated porphyrin adsorbing onto the Au which is seen for all types of thiol terminated molecules assembling on Au surfaces.[292,293] The mobility and the freedom of the molecules on the surface can be seen in Figure 3.8 where approximately a 50 nm region is continuously scanned with the STM tip. Upon zooming out of the scanned area, it can be seen that the etch pits have

diffused together (Figure 3.8D). This freedom poses problems for studying charge transport and prevents them from being implemented into electronics applications.

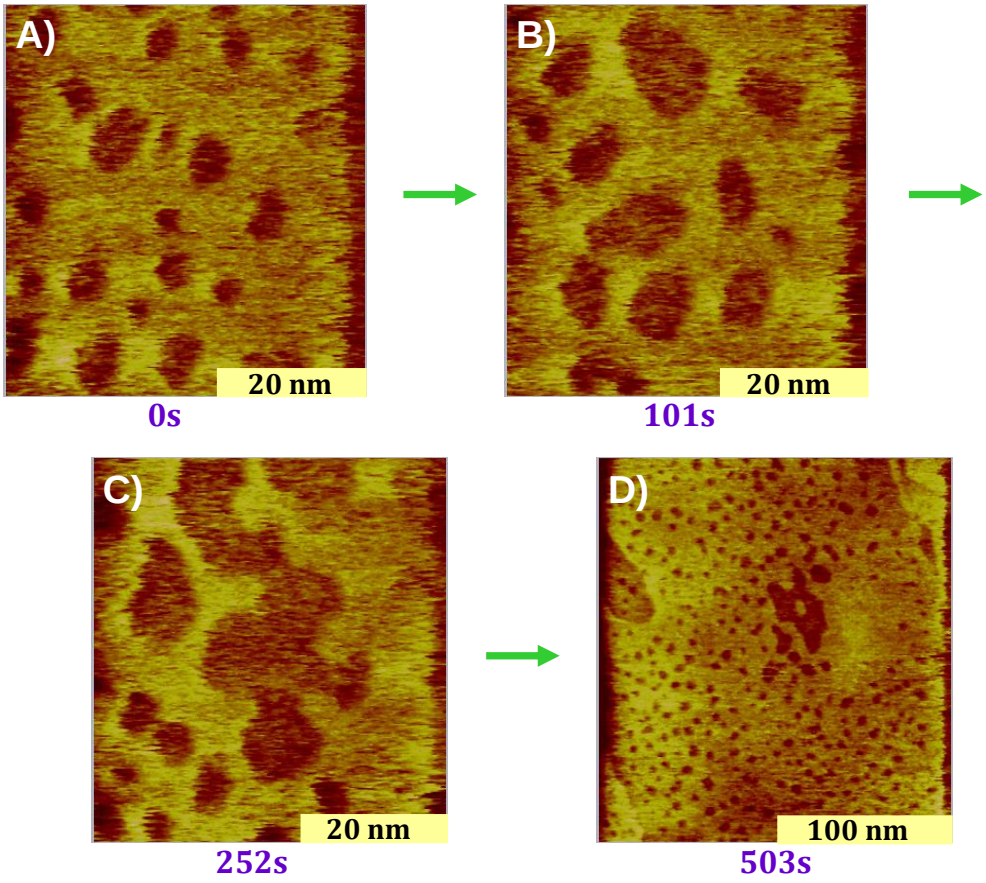

Figure 3.8. Diffusion of porphyrins while scanning pure porphyrin thiol monolayer with the STM tip after initial time (A) 0 s, (B) 101 s, (C) 252 s and (D) 503 s.

In order to overcome these obstacles, mixed SAMs have been implemented to force the molecules in an upright, less mobile configuration. Mixed SAMs are made of the free-base or zinc porphyrin thiol inserted into a host alkanethiol matrix, more

specifically a dodecanethiol (C12SH) matrix on Au(111). The alkanethiol chains prevent the porphyrin molecules from lying down on the surface and limit the movement of the porphyrin molecules across the surface.

3.3.4 FT-IR Measurements- Mixed SAMs

The calculated vibrational spectrum for the porphyrin thiol molecule is shown in Figure 3.9A. Using the calculated porphyrin thiol vibrational spectrum, the peaks in the mixed monolayer IR spectrum can be assigned and used to calculate the orientation of the porphyrin thiol molecule in the mixed monolayer. The optimized porphyrin thiol

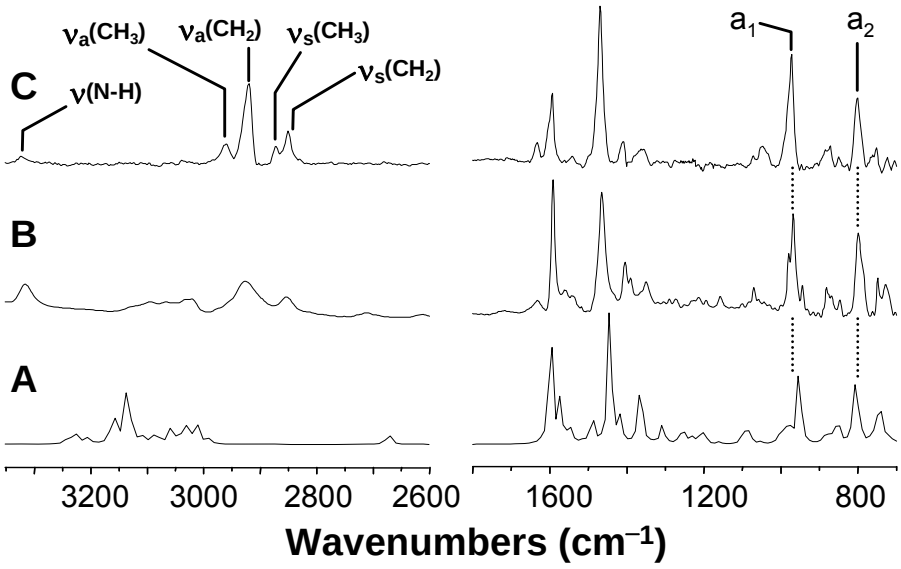

Figure 3.9. IR spectra of TPy_3PF_4-SC_5SH (A) calculated by TPSS and (B) prepared in KBr pellets; and (C) RAIRS spectrum of TPy_3PF_4-SC_5SH/dodecanethiol mixed monolayers.

structure was used in the proposed model for the orientation of the porphyrin thiol inserted in the mixed monolayer as shown in Figure 3.10 with the rotational axis through the alkyl chain. The peak at 970 cm^{-1} in the mixed monolayer spectrum is assigned to the porphyrin in plane pyrrole breathing mode and the one at 798 cm^{-1} is the ν_{11}(CH) out of plane bending mode of the pyrrole moieties. These two peaks were used to calculate the average molecular orientation on the surface using a previously published method.[242] The calculated free porphyrin thiol spectrum agrees well with the experimental KBr spectrum in the lower wavenumbers region from 700-1800 cm^{-1} and is shifted slightly at higher wavenumbers.

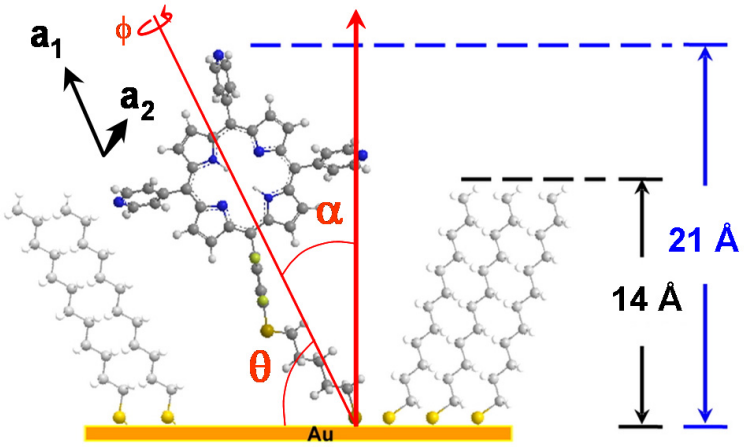

Figure 3.10. Proposed binding scheme of TPy_3PF_4-SC_5SH inserted into *n*-dodecanethiol SAMs and corresponding in-plane (a_1) and out-of-plane (a_2) dipole vectors of porphyrin macrocycle.

The IR spectra of TPy_3PF_4-SC_5SH calculated by DFT and prepared in KBr pellets are presented Figure 3.9A and 3.9B, respectively. The molecules in KBr pellets are ground thoroughly and thus presumably exhibit isotropic orientation. Figure 3.9C displays the infrared reflection absorption spectroscopy spectrum of porphyrin thiol/dodecanethiol mixed monolayers on Au. The observed peak frequencies and vibrational modes were assigned based on the calculations and previously reported literature[267,268,294,295] and are summarized in Table 3.1.

Table 3.1. Peak assignments for the porphyrin thiol in KBr Pellets, in monolayers mixed with dodecanethiol and TPSS calculations. [a]The peak intensity is negligible. [b]Calculated with density functional theory TPSS/6-31G+(d').

peak position (cm^{-1})			
in KBr	**in mixed SAMs**	**DFT[b] calc.**	**vibrational mode**
3316	3318	3470	ν(N-H), stretching
-----[a]	2964	-----[a]	$\nu_a(CH_3$, ip), asym stretching
-----[a]	2936	-----[a]	$\nu_s(CH_3$, FR), sym stretching
2926	2919	3058	$\nu_a(CH_2)$, asym stretching
-----[a]	2877	-----[a]	$\nu_s(CH_3)$, sym stretching
2853	2850	3010	$\nu_s(CH_2)$, sym stretching
2533	-----[a]	2663	ν(SH)
1592	1593	1603	ν_{8b}(C=C), in-plane stretching
1465	1468	1447	ν_{19a}(C=C), in-plane stretching
1069	1045	1077	ν_{18b}(CH), in-plane bending
968	969	970	pyrrole breathing
798	~791	800	ν_{11}(CH), out-of-plane bending
~726	723	729	pyrrole deformation

A proposed model of the porphyrin thiol derivative embedded in *n*-dodecanethiol SAMs tilting away from the surface normal by ~ 30^{o} is illustrated in Figure 3.10, where the in-plane pyrrole ring breathing mode, a_1, and out-of-plane pyrrole C-H bending mode, a_2, are sketched. The tilt angle of the porphyrin macrocycle (α) with respect to the surface normal can be derived from the intensity ratio of these two transition dipoles. The observed disappearance of the ν(SH) mode at 2534 cm^{-1} confirms the formation of S-Au covalent bonds. The absorptions between 2800 and 2965 cm^{-1} are *n*-alkyl stretch modes ($\nu(CH_2)$ and $\nu(CH_3)$ originating from dodecanethiol matrix and the porphyrin thiol alkyl tether). The corresponding vibrational peaks for the in-plane and out-of-plane contributions from the porphyrin thiol pyrrole moieties (a_1 and a_2, respectively) are denoted in Figure 3.10 for deducing the molecular tilt angle of the thiol-derivatized porphyrin SAMs.

The increase of intensity ratio of I_{a1}/I_{a2} in the mixed monolayers (Figure 3.9C) as compared with the KBr pellets (Figure 3.9B) suggests that the porphyrin macrocycle orients at a certain angle relative to the surface normal rather than lying flat on the Au surface according to the surface dipole selection rule[296] in which the dipole moments perpendicular to the metallic substrates can be enhanced, while those parallel to the substrates will be canceled out. Based on the intensity ratios of the orthogonal vectors of I_{a1}/I_{a2} in mixed monolayers versus the isotropic KBr sample, the average tilt angle (α) was determined to be ~ 39.0^{o} relative to the surface normal.[242] The value of the average azimuthal tilt angle was obtained by assuming that the rotation angle (ϕ) around the main molecule axis was 0^{o} and the porphyrin ring was planar which is in accordance with the

results of theoretical calculation (*vide infra*). Although the rotation angle might vary from 0^o, the value of the calculated tilt angle is not affected much by the variation of rotation angle. If the relative isotropic intensity, I_{a1}/I_{a2}, from the calculated spectrum is used in place of the experimentally measured KBr sample, the tilt angle of the macrocycle in the mixed monolayers would be similar at ~ 41.0^o.

3.3.5 X-ray Photoelectron Spectroscopy

A representative survey spectrum of the porphyrin thiol/dodecanethiol mixed monolayer is shown in Figure 3.11. High-resolution spectra of the C(1s), N(1s), and F(1s) regions show peak binding energies of 284.8 ± 0.1, 399.0 ± 0.1 and 687.0 ± 0.1 eV, respectively, while the high-resolution S(2p) signal can be fitted into two sets of doublets from the S($2p_{3/2}$) and S($2p_{1/2}$) components split by 1.2 eV. The two S($2p_{3/2}$) peaks are centered at 162.1 ± 0.1 and 163.7 ± 0.1 eV, respectively (Figure 3.12). The first type of sulfur corresponds to the thiol chemisorbed onto the gold substrate,[297] while the second at higher binding energy can be attributed to the presence of the S coordinated to the tetrafluorophenyl ring.[275] The experimentally determined value of F:N atomic ratio is consistent with the expected 4:7 stoichiometry within a deviation of 10-15% which demonstrates that the integrity of the porphyrin thiol molecules is retained after insertion into the *n*-dodecanethiol matrix.

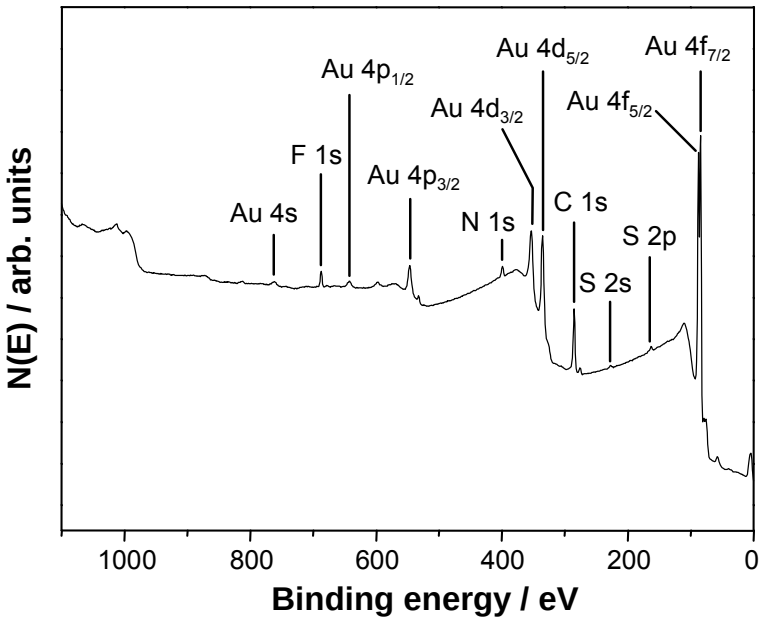

Figure 3.11. X-ray photoelectron survey spectrum for TPy_3PF_4-SC_5SH/dodecanethiol mixed monolayers on Au (111).

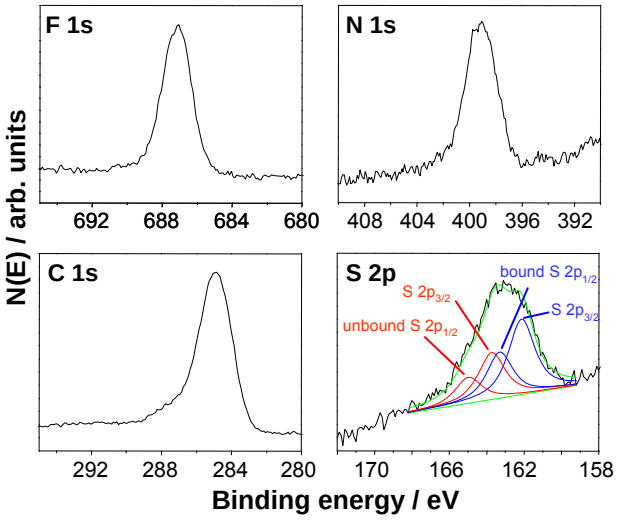

Figure 3.12. High-resolution XPS for TPy_3PF_4-SC_5SH/dodecanethiol mixed SAMs, showing the F 1s, N 1s, C 1s, and S 2p spectral regions.

3.3.6 Surface Imaging- Mixed SAMs

In order to examine the surface structure of the inserted porphyrin molecules, both atomic force and scanning tunneling microscopies were employed. AFM images of the mixed monolayer show clusters inserted into the dodecanethiol matrix, suggesting that the porphyrin molecules are sticking up out of the dodecanethiol background. Based on the physical heights determined from contact mode images in ethanol, the porphyrins were observed to extend above the dodecanethiol SAM anywhere from 0.5 nm to 2 nm (Figure 3.13A). The variation in heights is likely due to differences in bonding location, such as near defects or step edges in the film. The average measured height difference was found to be ~ 0.9 nm, which is consistent with the average structure illustrated in Figure 3.10 as deduced from the FT-IR data, in which the porphyrin macrocycle is tilted ~ 39^{o} away from the surface normal. Due to the large size of the AFM tips used (ca. 10 nm) sufficiently high resolution images however were not possible by AFM to detail the molecular organization of the dodecanethiol matrix. As such, scanning tunneling microscopy was employed to obtain molecular resolution images of the mixed monolayer films.

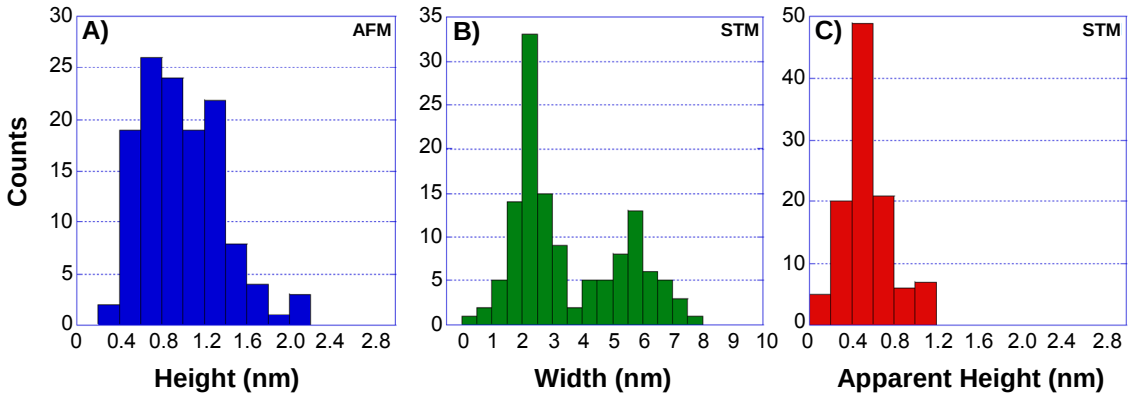

Figure 3.13. Height and domain size distributions from AFM and STM measurements. (A) Physical height difference between the dodecanethiol and porphyrins deduced from AFM images in ethanol. (B) Domain size histogram and (C) apparent height distribution for the ON conductance state of TPy_3PF_4-SC_5SH embedded in *n*-dodecanethiol SAMs from UHV-STM (V_{bias} = 1.4 V, I_{tunnel} = 20 pA).

STM images of the dodecanethiol matrix on the Au(111) surface shows the close-packed structures typically observed for alkanethiols that have been previously reported[160,298,299] (Figure 3.14). When the porphyrins are inserted into the SAM, they are found to organize next to and into defects in the film and appear as bright unresolved clusters. From the examination of a number of self assembled mixed monolayers, the clusters are found to form two predominate average domain sizes of ~ 2 nm and ~ 6 nm

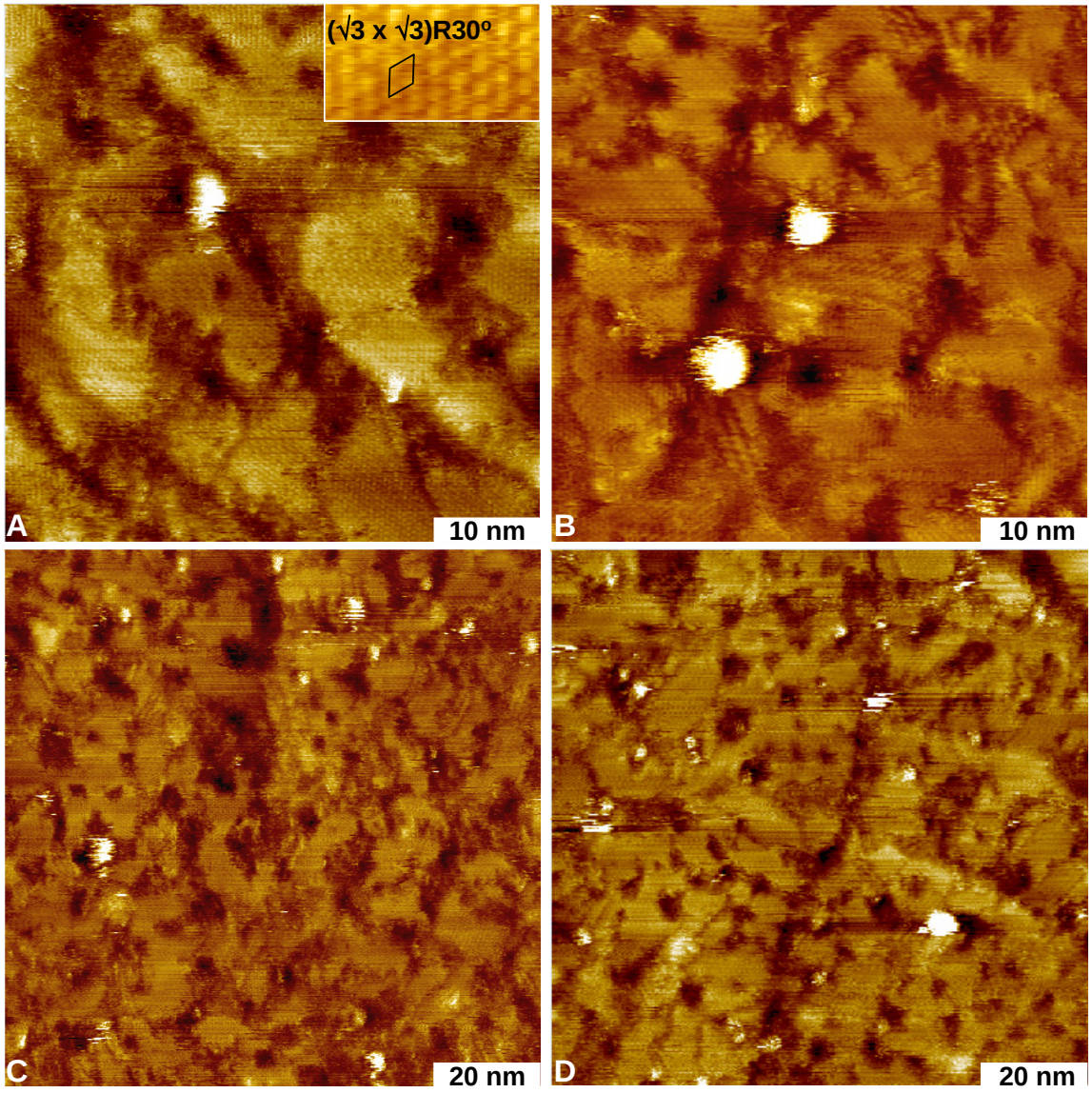

Figure 3.14. UHV-STM images of TPy_3PF_4-SC_5SH molecule(s) isolated within *n*-dodecanethiol matrix on Au(111) under UHV conditions. Imaging size: (A) 50 x 50 nm, (B) 50 x 50 nm, (C) 100 x 100 nm, and (D) 100 x 100 nm; imaging conditions: V_{bias} = 1.4 V, I_{tunnel} = 20 pA. The inset in (A) magnifies the (√3 x √3)R30° lattices for *n*-dodecanethiol SAMs.

in width (Figure 3.13B). The ~ 2 nm domains are likely single inserted porphyrins whose physical width from pyridyl-pyridyl group is ~ 1.5 nm, convoluted with the STM tip shape,[300,301] or broadened by thermal motion, while the ~ 6 nm domains are porphyrin aggregates (likely 3-5 molecules) which tend to have strong π–π coupling between macrocycles. This distribution is observed when imaging either in air or under UHV conditions. Interestingly, all of these domains show similar apparent heights of 0.5 nm on average relative to the dodecanethiol matrix. The apparent height distribution for these porphyrin thiol domains is displayed in Figure 3.13C. This apparent height is nearly half that of the observed physical height deduced from AFM images of the same samples and suggests that the barrier to tunneling within the molecules is significant.

Comparing the physical height as deduced from AFM measurements to the observed height in the STM, the electron tunneling decay constant, β, for the porphyrin thiol can be estimated using a two layer tunnel junction model[179,250,302] assuming that the contact conductance between the two molecules is essentially equivalent. Based on this assumption, the decay constant for the porphyrin thiol can be estimated from the apparent height difference as follows:

$$\beta = [\beta_{DDT} h_{DDT} - \alpha(\delta h_{STM} - \delta h)] / h_{por},$$

where β_{DDT} is the tunneling decay constant for dodecanethiol (1.2 $Å^{-1}$), h_{DDT} is the physical thickness of the dodecanethiol layer (~ 14 Å, based on a molecular tilt angle of 30°), α is the decay constant between the tip and molecule in vacuum, (~ 2.3 $Å^{-1}$), δh_{STM}

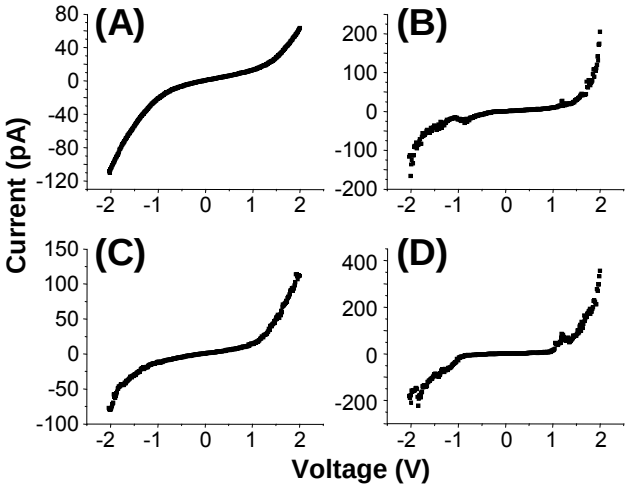

Figure 3.15. I-V spectra (averaged from 50 curves each) for the (A) dodecanethiol matrix, (B) small (~ 2 nm) porphyrin domains and (C, D) large (> 6 nm) porphyrin domains.

is the apparent height difference determined by STM, and δh is the height difference deduced by the AFM topographic data, h_{por} is the physical height of the porphyrin thiol as deduced by AFM and FT-IR measurements. Utilizing this formalism, the tunneling constant β for the porphyrin thiol was estimated to be ~ 1.4 $Å^{-1}$. This β value is consistent with current-voltage (I-V) spectroscopy measurements (Figure 3.15) of the dodecanethiol SAM compared to the inserted porphyrins, which show similar current values over the range of bias probed from (-2 V to +2 V) despite the conjugated nature of the porphyrin moiety and the potentially low injection barrier as suggested from DFT calculations, which places the HOMO ~ 0.2 eV below the Fermi level for Au (~ 5.1 eV).

This high β value suggests that the tunneling in this molecule is ultimately dominated by the alkyl tether which binds the molecule to the surface, which has been seen previously for other systems,[179] and is consistent with the alkyl tether decoupling the macrocycle from the surface, as has been seen for napthyl compounds by 2-photon photoemission.[303] There is also likely a contribution from the lack of orbital overlap between the porphyrin macrocycle and the alkyl tether due to the orientation of the tetrafluorophenyl ring coupling the two and we are in the process of systematically investigating how changing the chemistry and orientation of the phenyl ring influences the conduction properties.

Current-voltage (I-V) curves from the small (ca. 2 nm) and large (~ 6 nm) domains show some distinct differences (Figure 3.15). The single molecules show a roughly symmetric I-V curve, as compared to that of dodecanethiol, with an upturn in current flow around -1 V and + 1.5 V. When examining the I-V curves for the larger aggregates (Figure 3.15C and D), the upturn in current appears nearly symmetrically at ± 1 V. Moreover, two families of I-V curves appear, one with a distinct current blockade and one without. This may be due to local intermolecular interactions shifting the HOMO-LUMO levels as is typically observed during the formation of H and J aggregates for porphyrins.

In addition to their relatively low conductance, the inserted porphyrins show the phenomenon of stochastic switching[128,175,177,304] whereby the molecules in the "ON" state exhibit several Å's of apparent height protrusion relative to the surrounding alkanethiol matrix, while the "OFF" state shows little to no contrast from the host matrix (Figure 3.16). Such "ON/OFF" conductivity switch-like behavior has been explored

both theoretically and experimentally to be associated with orientation changes of the molecules,[305,306] interactions among neighboring molecules,[307] reduction of functional groups,[308] bond-fluctuation,[177,309] and changes in molecule-substrate bond hybridization.[128,310] Weiss et al. has demonstrated how controlling the rigidity of the local matrix in which the molecules are implanted may be used to influence switching behavior arising from molecular orientation dynamics.[175]

Unlike many previous examples, the switching behavior that we observe generally occurs only a few times for each molecule or cluster of molecules. In fact, after extended periods of imaging a region, virtually no porphyrins are further observed within the scan area. Upon expanding the scan area, clusters are again observed, but only outside the region that had been previously imaged. This suggests that the molecules are either removed from the surface, chemically altered by oxidation or reduction, or that an irreversible conformational change has occurred that renders them

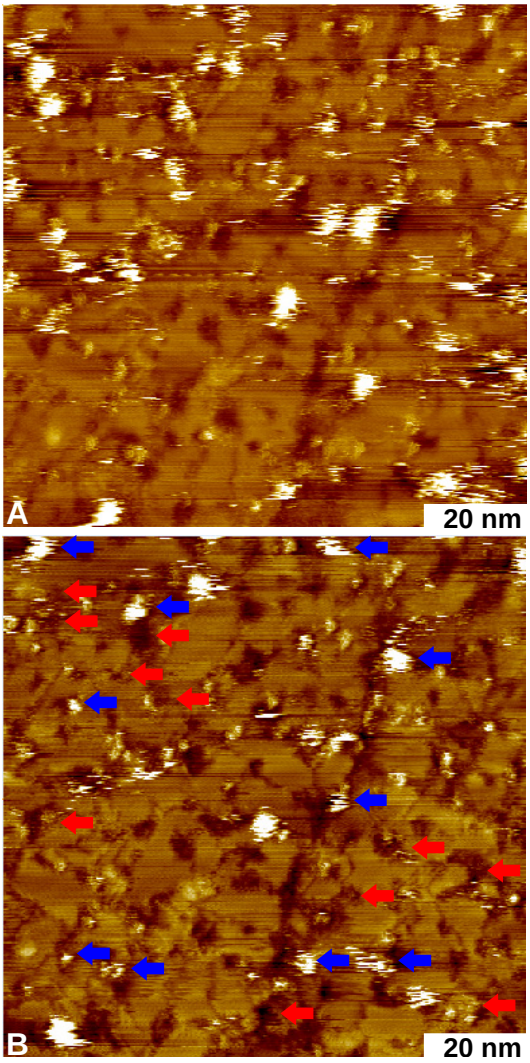

Figure 3.16. Representative STM images for ON and OFF switching behavior of TPy_3PF_4-SC_5SH. The red arrows in (B) indicate the OFF conductance state switching from the ON conductance state in (A), while the blue arrows exhibit the ON state turning from the OFF state in (A). Total measurement time = 8.2 minutes, 100 x 100 nm, V_{bias} = 1.4 V, I_{tunnel} = 20 pA.

undetectable by STM in their new conformation. The redox pathway is unlikely because the first two oxidations and reductions of the porphyrin macrocycle are reversible under

UHV conditions. While the majority of the inserted molecules appear near defects in the SAM layer, even those that have been found in the center of well ordered domains show "switching" behavior. As such, the dodecanethiol near the porphyrins may be more disordered than can be deduced simply from the STM images, due to the bulkiness of the macrocycle impeding imaging directly near the inserted molecules, and still enables local conformational changes in the inserted molecule.

3.4 Conclusions

Tri-pyridyl porphyrin compounds have been attached to Au surfaces by a thiol tether, through a tetrafluorophenyl linker. The use of the fluorinated linker provides a facile means of attachment to any dithiol tether. When inserted into a background matrix of dodecanethiol, the porphyrins are observed to tend to bind near the edges of defects within the alkanethiol layer as either single molecules or small ensembles (ca. 3-5 molecules). Based on the apparent height of the molecules relative to the dodecanethiol matrix, the tunneling efficiency was found to be low, similar to that of a simple alkanethiol which is considered a molecular insulator. From DFT calculations, the low tunneling efficiency can be attributed to the lack of effective orbital overlap between the frontier orbitals of the porphyrin macrocycle and the thiol tether due to the orthogonal dihedral angle between the porphyrin ring and the perfluorophenyl linking group. In addition to the electronic effects on the phenyl ring, the 2,6 fluoro moieties increase the rotation barrier and diminish the dynamics of the aryl – porphyrin bond. Thus, this group introduces an effective tunneling barrier directly within the molecule reducing the tunneling efficiency, despite of the close proximity of the HOMO of the

molecule to the Au Fermi level. Future studies will examine how selective removal of the fluorine groups from the tether can be used to tune the tunneling properties by both electronic and steric interactions. Also, once attached to the surface, additional porphyrin rings will also be coordinated to this compound via metal-ligand coordination to create energy harvesting structures.

CHAPTER IV

COULOMB BLOCKADE AND BIAS-INDUCED SWITCHING OF ZINC COORDINATED THIOL-TETHERED TRIPYRIDYL PORPHYRINS ON AU(111)

4.1 Introduction

Exploring the use of single molecules[311,312] and molecular assemblies[313] for molecular/organic electronic applications has been of significant interest in recent years to control charge injection at interfaces[314-317] and for light harvesting applications.[318-321] The transport properties of such assemblies have been characterized using a range of methods including nanogap electrodes, scanning tunneling microscopy (STM), mechanically controlled break junctions as well as cross-wire junctions among others.[322] Most of these techniques, with the exception of STM however, cannot provide molecular detail inside the junction. Nonetheless, from such measurements it has been shown that molecules and their assemblies can exhibit unique transport properties such as negative differential resistance (NDR), switching, hysteresis and other non-linear current-voltage behavior. These properties can vary for single molecules as compared to when the molecules aggregate to form an ensemble. As such, comparing the transport properties of single molecules to that of their aggregated structures is of interest.[323]

Recent studies on molecular systems have focused on their use in single electron tunneling devices[324,325] in which small islands are assembled within nanoscale electrode gaps and their charge state can be tuned using a gate voltage. For example, assemblies involving free base porphyrins in nanogap electrodes have been purported to act as

Coulomb islands. However, from these studies no detailed understanding of the assembled structures within the electrode gaps could be discerned.[215,326-328] Other molecular systems have been shown to portray similar Coulomb blockade-like behavior for single molecules[117,329,330] as well as multilayer assemblies.[331] A ruthenium(II) bis(σ-arylacetylide) complex[329] was found to exhibit Coulomb blockade behavior at liquid helium temperatures with a purported hopping-type electron transport mechanism. Utilizing the coordination of a cobalt ion bound between two terpyridinyl linker molecules[117,330] was also found that electron transport could be readily controlled through well-defined charge states. Studies of multilayer assemblies of nickel-octanedithiol, created through the incorporation of the Ni atoms between the dithiol layers have also been shown to exhibit Coulomb blockade.[331] From these studies it was suggested that the metal centers could provide charge traps and show Coulomb blockade-like behavior at low temperatures with stochastic charge-defect gating.

In the work presented here, we have found that the transport properties of singly inserted molecules of zinc porphyrin thiol are different than when they assembled into island via aggregation. Here, zinc coordinated tri-pyridyl porphyrin thiols have been assembled in a dodecanethiol matrix on Au(111). Through self-assembly, the molecules are found to insert into the dodecanethiol matrix as isolated single molecules or as aggregates (islands) depending on deposition time. Through a combination of STM and crossed-wire inelastic electron tunneling spectroscopy (IETS) measurements, the conductance properties and charge transport pathway in these molecular assemblies have been investigated. From these studies we have found that when molecular aggregates

are formed, the assembled islands (of *ca.* 10 nm in dimension) show a clear and reversible bias-induced switching behavior. From our earlier studies of free base porphyrin thiols, we found that these islands are fairly small (*ca*. 3 - 6 nm in diameter).[34] By inserting Zn(II) into the porphyrin macrocycle, the aggregation of the molecules increases, and these molecular assemblies were found to exhibit clear bias dependent switching. We believe that the switching mechanism is unlike other mechanistic effects previously described such as dipole, conformation changes, bond hybridization, or interactions from neighboring molecules, since the free base analog of the this porphyrin thiol did not exhibit bias-induced switching. Here, we purport that switching results from charge stabilization by the zinc metal center as well as an electronic effect from the clustering of these molecules, since switching was only observed with the aggregates of the zinc-coordinated porphyrin thiol and not singly inserted molecules. Moreover, depending on the aggregate island size, Coulomb blockade was observed at low temperatures indicating that these ensembles can act as molecular capacitors. Again, it is interesting to note that this is not observed for single molecules or for islands of the free base analog of the zinc porphyrin thiol molecule.

4.2 Experimental

4.2.1 Materials

Self-assembled monolayers were prepared on Au films, including Au(111) on mica (Molecular Imaging-Agilent, Phoenix, AZ), and dodecanethiol was purchased from Aldrich (98% purity) and used as received.

4.2.2 Synthesis of Zinc Porphyrin Thiol Compound

5,10,15-tri(4-pyridyl)-20-(4-(1',5'-dithiopentyl)-2,3,5,6-tetrafluorophenyl) porphyrin (TPy_3PF_4-SC_5SH) was synthesized in two steps and the complete details and associated spectral characterizations are provided in a previous paper.[34] The previously published synthetic method was followed by coordination of the compound with zinc and the details and associated complete characterization of the synthesized and metallated molecules can be found in the Supporting Information of the published manuscript.

4.2.3 Preparation of Mixed Monolayers

Au(111) substrates (purchased from Molecular Imaging Inc.) were ~150 nm flame-annealed gold films on mica. Before each experiment, all substrates were treated with UV/ozone for 20 min, followed by rinsing the gold film in sequence with high purity (18.2 MΩ•cm) water (NANOpure Diamond, Barnstead), ethanol, and then dried with streaming nitrogen. SAMs of n-dodecanethiol were formed by immersion of the Au films in 1 mM n-dodecanethiol in ethanol for 24 h. After rinsing liberally with ethanol, the substrates were soaked in 0.5 mM zinc porphyrin thiol dissolved in dichloromethane for a period of one to five days to allow the insertion of the zinc porphyrin molecules into n-dodecanethiol matrix. After insertion, the substrates were removed from the solution and were rinsed with dichloromethane and blown dry with streaming nitrogen. The surface characterization of mixed SAMs of the zinc porphyrin inserted into the dodecanethiol matrix were carried out using Atomic Force Microscopy (AFM), Fourier Transform Infrared Reflection Absorption Spectroscopy (FT-IRAS), X-

ray Photoelectron Spectroscopy (XPS), Scanning Tunneling Microscopy (STM), and Inelastic Electron Tunneling Spectroscopy (IETS).

4.2.4 Atomic Force Microscopy

AFM images were acquired with a Molecular Imaging 4500 Pico SPM (Agilent, Phoenix, AZ) with a deflection-type detection scanning head interfaced with an SPM1000 control electronics Revision 8 (RHK Technology Inc., Troy, MI). All AFM images were acquired in contact mode under ethanol using commercially available Si_3N_4 AFM tips (Veeco/TM Microscopes, Sunnyvale, CA) with nominal tip radii of ~ 10 nm and nominal spring constants ranging from 0.03 - 0.1 N/m.

4.2.5 Scanning Tunneling Microscopy

STM measurements were taken under ultrahigh vacuum (UHV) conditions using an Omicron UHV-XA STM system. The system was operated with a typical base pressure of $< 2.3 \times 10^{-10}$ Torr. Images were collected using Pt/Ir (70/30) tips which were mechanically cut. The typical imaging conditions of tunneling current and tip bias voltage ranged from 5 pA to 100 pA and from -2.0 V to +2.0 V, respectively. Current-voltage (I-V) spectra were collected under UHV conditions over a voltage range of -2 V to +2 V. The STM images were analyzed with commercially available Scanning Probe Image Processor (SPIP) software (version 4.8.1, Image Metrology, Lyngby, Denmark), and the Grain Analysis module with Threshold algorithm was used to estimate the surface coverage of the zinc porphyrin thiol for the 5 day mixed SAMs.

4.2.6 X-ray Photoelectron Spectroscopy

XPS data were acquired with a Kratos Axis ULTRA X-ray photoelectron spectrometer equipped with a 165 mm hemispherical electron energy analyzer. The incident radiation was the monochromatic Al Kα X-ray line (1486.6 eV) with a source power of 120 W (12 kV, 10 mA). The analysis chamber was maintained at a steady base pressure of $< 6.0 \times 10^{-9}$ Torr during sample analysis. Survey scans up to binding energies of 1200 eV were carried out with an analyzer pass energy of 160 eV with 1.0 eV steps and a dwell time of 300 ms. Multiplexed high resolution scans of the Au(4f), C(1s), S(2p), Zn(2p), N(1s), and F(1s) regions were taken with a pass energy of 40 eV with 0.1 eV steps (with the exception of Zn(2p) which was acquired at 0.05 eV steps) and a dwell time of 60 ms. The survey and high resolution spectra were obtained with averages of 5 and 30 scans, respectively (with the exception of C(1s) which was obtained with an average of 10 scans). The Au($4f_{7/2}$) peak at 84.0 eV was set as a reference for all XPS peak positions to compensate for energy shifts due to the spectrometer work function. The fitting of high-resolution sulfur peak was executed by utilizing XPSPEAK 4.1 in which a Shirley-type background[279] (from ~159 eV to ~168 eV) with an 80% Lorentzian-Gaussian curve-fitting program were used. The spin-split doublets of the S(2p) were fitted by fixing the area ratio at $2p_{3/2}$:$2p_{1/2}$ = 2:1 and setting their energy difference to 1.2 eV. The full width half-maximum of each peak was also maintained at a constant value.

4.2.7 FT-IR Spectroscopy

Transmission IR spectra of the solid porphyrin compounds were obtained in KBr pellets. FT-IR spectra of the mixed monolayers were collected on evaporated Au films on Si. Au films on Si substrates were prepared by thermal evaporation onto single-side polished Si(100) wafers (Virginia Semiconductor Inc.) in a bell-jar evaporator (BOC Edwards, Auto 306). The chromium (5 nm) and gold (200 nm) films were deposited under vacuum ($P < 2.0 \times 10^{-6}$ Torr) at the rate of 0.5 and 3 Å/s, respectively. Reflection-absorption spectroscopy was collected using an FT-IR spectrometer (Nicolet 6700, Thermo Electron Corporation, Madison, WI) equipped with a liquid nitrogen-cooled HgCdTe (MCT) detector. FT-IR data were acquired in single reflection mode with polarized light generated by a ZnSe polarizer adaptor (FT-80, Thermo Electron Corporation). The light path, MCT detector, and sample chamber were purged with dry nitrogen during the measurements. A UV/ozone cleaned gold substrate was used as the reference. The IR spectra were collected with a total of 1024 scans for both the sample and the reference at 4 cm^{-1} resolution.

4.2.8 Theoretical Calculations

We chose the TPSS functional and basis set, 6-31G+(d'), by calibrating against the unsubstituted free base porphine. The TPSS/6-31G+(d') frequencies fit the experimental data for the unsubstituted free base porphine very well and with reasonable computational cost. Larger basis sets as well as the B3LYP [Becke three-parameter exchange functional (B3)[288] and the Lee-Yang-Parr correlation functional (LYP)[289]] DFT was also used for the optimization and analytical vibrational frequency calculations

for the unsubstituted free base porphine and compared to the TPSS and experimental results. Calculations of the electronic structure, molecular structure, and electrostatic potential (ESP) maps were performed using Density Functional Theory (DFT).[280] Calculations were carried out with the Gaussian 03[281] suite of programs and the Amsterdam Density Functional (ADF) suite version 2008.01.[332] The zinc porphyrin thiol molecule was fully optimized using Gaussian 03 at the DFT level with the TPSS[282] functional with a density-fitting basis set.[283] Two basis sets were used in this study. BSI consists of the triple-ζ SDD basis set and effective core potential (ECP) on zinc and a Pople style[284,285] double-ζ quality basis set with a diffuse[286] and optimized polarization function on the heavy atoms[287] (6-31G+(d')) for all other atoms. Polarization (d) functions used spherical harmonic representations for the free base porphyrin thiol and Cartesian coordinates for the zinc porphyrin thiol molecule. BSII was used for single point energy (SPE) calculations and consists of a 6-311+g(d) basis set for zinc and 6-31g+(d') basis set for all other atoms. The ESP and density were calculated at the (TPSS/BSII//TPSS/BSI) level. The ESP maps were generated using GaussView 3.0 at a 0.0005 isodensity value and a color scale of -0.050 (red) to +0.043 (blue) a.u.'s. Calculations of the electronic structure of the stacked zinc metalloporphyrins were carried out with the ADF program. The stacked zinc porphyrin thiol molecules were fully optimized at the DFT level with the PW91[333] functional with the all-electron basis set from the DZP database for all atoms except zinc which used the TZP database of the ADF suite.

4.2.9 Inelastic Tunneling Spectroscopy

SAMs of n-dodecanethiol (C12) were formed by immersion of the Au wires in 1 mM dodecanethiol in ethanol for 24 h. After sonicating in ethanol for 5 minutes, the wires are soaked in 0.5 mM zinc porphyrin thiol dissolved in dichloromethane for one to five days to mirror the STM experiments. After assembly the wires are sonicated in dichloromethane for five minutes before being soldered to the crossed wire setup.

Crossed wire junctions of the mixed dodecanethiol/zinc porphyrin thiol molecular monolayer are formed at liquid helium temperature. The transport measurements were preformed with standard ac modulation technique where the dI/dV and d^2I/dV^2 signals are recorded simultaneously with the I-V characteristics. To remove any junction area dependency from the data, the IET spectra are presented as the amplitude $(d^2I/dV^2)/(dI/dV)$.

4.3 Results and Discussion

The drive to integrate molecules as active components of optoelectronic devices requires a detailed understanding of how they assemble on surfaces and how this assembly influences their transport properties. The surface assembly of the mixed monolayers of the thiol tethered zinc porphyrin molecules inserted into a pre-assembled *n*-dodecanethiol monolayer on Au(111) surfaces has been characterized utilizing Scanning Tunneling Microscopy (STM), Atomic Force Microscopy (AFM), Fourier Transform Infrared Reflection Absorption Spectroscopy (FT-IRAS), X-ray Photoelectron Spectroscopy (XPS), and Inelastic Electron Tunneling Spectroscopy (IETS). Density Functional Theory (DFT) calculations have also been employed to aid

in detailing the electronic and molecular structures, as well as mapping the electrostatic potential for the zinc porphyrin thiol molecule.

4.3.1 Theoretical Calculations

DFT calculations were used to optimize both the gas phase structure of the zinc porphyrin thiol compound and the results were compared with experimental studies. The model and the calculated gas phase optimized structure of the zinc porphyrin thiol molecule are shown in Figure 4.1 a & b, respectively. The optimized structure of the zinc porphyrin thiol is similar to the findings of the free base analog in which the tetrafluorophenyl ring is canted nearly perpendicular at ~ 83 degrees with respect to the macrocycle, and the three pyridyl rings are found to tilt out of the plane of the macrocycle ranging between ~ 65 – 67 degrees. The HOMO-LUMO gap for the zinc porphyrin thiol was calculated to be 1.99 eV which is slightly larger than the free base analog with a calculated HOMO-LUMO gap of 1.89 eV. Moreover, the location of the

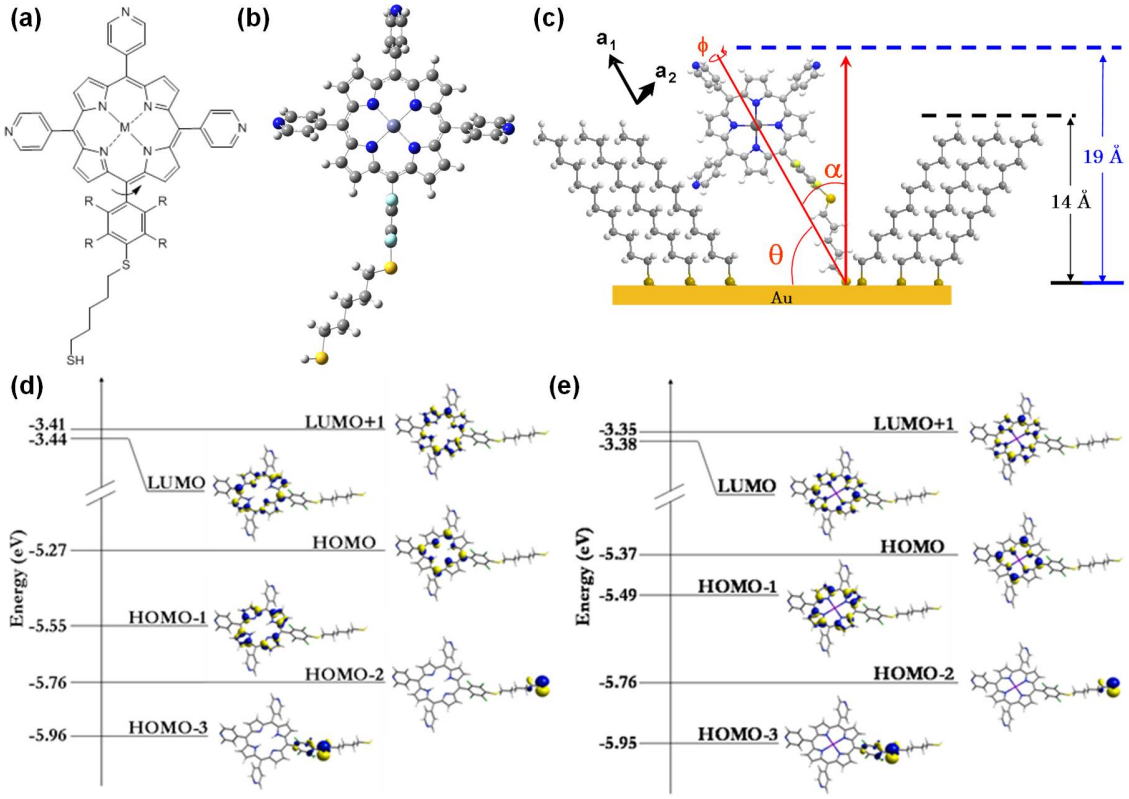

Figure 4.1. (a) Zinc porphyrin thiol model where M = Zn, R = F, (b) TPSS optimized structure and (c) proposed binding scheme of zinc porphyrin thiol inserted into *n*-dodecanethiol SAMs including the corresponding in-plane (a_1) and out-of-plane (a_2) dipole vectors of porphyrin macrocycle. Frontier molecular orbitals (HOMO-3 to LUMO+1) for the (d) free base and (e) zinc porphyrin thiol.

HOMO state (-5.37 eV) relative to the Fermi level of the Au substrate (-5.1 eV) based on these calculations (with all of their associated caveats), suggests a small injection barrier of *ca.* 0.3 eV. Also, the frontier orbitals that should participate in the electron transport process as shown in Figure 4.1 d & e of the free base and zinc porphyrin thiol derivatives reveal no overlap between the orbitals of the porphyrin macrocycle and the

tetrafluorophenyl ring that links the macrocycle to the thiol tether. As such, there is an inherent barrier to charge transport located directly within the molecule even after incorporation of the zinc metal center.

A proposed model of the zinc porphyrin thiol molecule embedded in *n*-dodecanethiol SAMs tilting away from the surface normal by ~ 30^{o} is illustrated in Figure 4.1c as deduced from IR spectroscopy measurements described below.

4.3.2 FT-IR Measurements

In Figure 4.1c, the proposed model of the zinc porphyrin thiol derivative embedded in *n*-dodecanethiol SAMs tilting away from the surface normal by ~ 30^{o} is illustrated where the in-plane pyrrole ring breathing mode, a_1, and out-of-plane pyrrole C-H bending mode, a_2, are sketched. The tilt angle of the porphyrin macrocycle (α) with respect to the surface normal can be derived from the intensity ratio of these two transition dipoles. The absorptions between 2800 cm^{-1} and 2965 cm^{-1} arise from the$\nu(CH_2)$ and $\nu(CH_3)$ stretching modes originating from the dodecanethiol matrix and the zinc porphyrin thiol alkyl tether. The IR spectra of zinc porphyrin thiol calculated by DFT (blue spectrum) and prepared in KBr pellets (black spectrum) are presented in Figures 4.2a and 4.2b, respectively. The molecules in the KBr pellets are ground thoroughly and thus presumably exhibit isotropic orientation. Figure 4.2c (red spectrum)

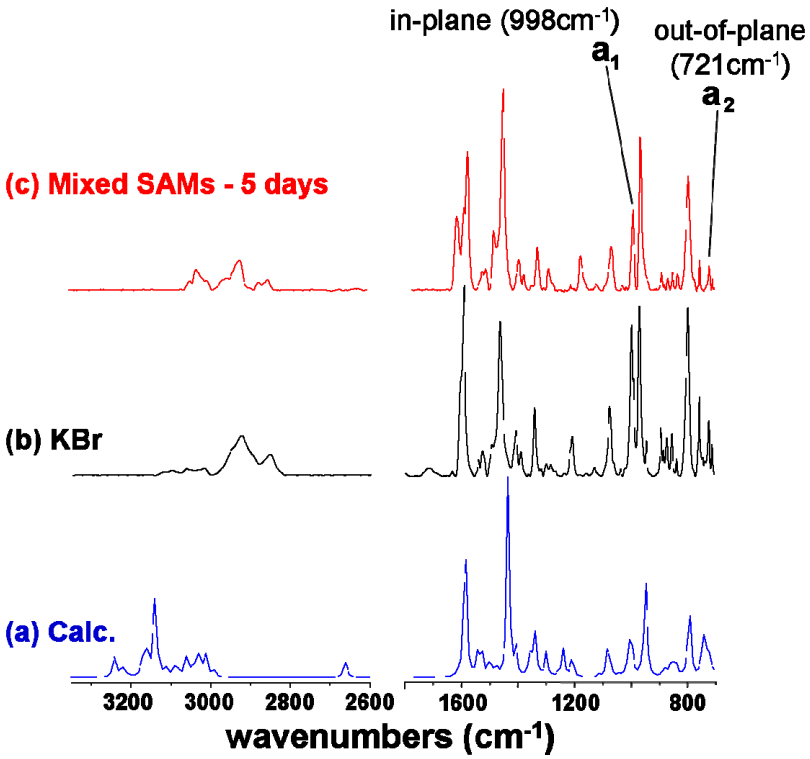

Figure 4.2. IR spectra of zinc porphyrin thiol (a) calculated by TPSS and (b) prepared in KBr pellets; and (c) IRAS spectrum of zinc porphyrin thiol/dodecanethiol mixed monolayers.

displays the infrared reflection absorption spectrum of zinc porphyrin thiol/dodecanethiol mixed monolayers on Au with exposure to the zinc porphyrin thiol solution for 5 days. The observed peak frequencies and vibrational modes were assigned based on the DFT calculated IR frequencies and previously reported literature.[294,295,334,335] From IR spectroscopy,[336] the average tilt angle (α) of the porphyrin molecules in the mixed SAMs was determined to be ~ 42.0° relative to the

Table 4.1. Vibrational mode assignments for the zinc porphyrin thiol in KBr Pellets, in monolayers mixed with dodecanethiol and TPSS calculations. (Note: s- strong intensity, sh- shoulder).

Type of IR Spectrum					
KBr	Experimental- Mixed SAMs			Calculated	Mode
	1 day	3 days	5 days		
				654	pyridyl elongating stretch
665	668			664	pyridyl elongating stretch
	678		677		
		697	697		
709	707	711	708		
722	721	721	723	719	pyrolle out of plane bending
756	757	754	757	743	CH_2 wagging
				790	pyrolle out of place bending
795	795 (s)	795	795	795	pyridyl CH out of plane bending
835	830	830	833		
854	856	855	852	844	pyridyl, CH oop
870	870	873	870	857	SH wagging, phenyl stretch
882	880	882	882		
891	893	891	891	883	pyrolle wagging in plane
943					
968	972 (s)	971	968	949	C-F asym stretch
997	999	997	999	1006	pyrolle asym breathing
1017	1019	1021	1021		
1036	1035	1035	1036	1048	CH_2 rocking IP
1073	1074	1076	1076	1088	pyrolle CH scissor (bend IP)
1129		1123	1130		
1157				1215	CH_2 rocking in sync oop
1179		1179	1186	1216	pyrolle deformation
1206			1205		
1235					
1266					
1284					
1299	1296	1301	1300	1251	CH_2 rocking sep and phenyl
1318					
1340	1340	1340	1340	1309	CH_2 rocking in sync asym oop
1362					
1389	1389	1389	1392		
1408	1410	1408	1408	1353, 1370(sh)	pyrolle and pyridyl CH wagging IP
1464 (s), 1490 (sh)	1466 (s), 1481(sh)	1466, 1492(sh)	1466, 1500(sh)	1421(sh), 1449	pyridyl and CH bend IP, phenyl C=C asym stretch
1526	1528	1528	1527	1514	macrocycle C-C asym stretch
1540	1549	1541	1540	1557	pyridyl rock IP
1592	1593 (s), 1603(sh)	1595, 1603(sh)	1595, 1606(sh)	1604	pyridyl C=C sym stretch
1634	1633	1630	1635	1627	phenyl C=C sym stretch
2548	-	-	-	2661	SH stretch
2853	2852	2850	2853	2990, 3011, 3028, 3042	CH_2 symm stretch
2926	2922	2920	2922	3058, 3086, 3109	CH_2 asym stretch
2949	2956	2956	2956	3130 (sym), 3164 (asym)	pyridyl CH stretch
3020	3024	3026	3030	3217	CH asym stretch-pyrolle
3064	3059	3063	3043	3239	CH symm stretch-pyrolle
3100			3091		
			3396		
			3444		

surface normal. Figure 4.2 and Table 4.1 show the IR spectra and the assignments of the peaks, respectively, of the KBr sample, the mixed monolayers and the calculated zinc porphyrin thiol spectrum. If the relative isotropic intensity, I_{a1}/I_{a2}, from the calculated spectrum is used in place of the experimentally measured KBr sample, the tilt angle of the macrocycle in the mixed monolayers would be similar at ~ 43.0°. In comparison, the tilt angle (α) of the free base porphyrin thiol was similar at ~ 39.0° and ~ 41° relative to the surface normal for the experimental and calculated IR spectra, respectively.

4.3.3 X-ray Photoelectron Spectroscopy

A representative survey spectrum of the porphyrin thiol/dodecanethiol mixed monolayer is shown in Figure 4.3. High-resolution spectra (Figure 4.4) of the C(1s), N(1s), F(1s) and Zn(2p) regions show peak binding energies of 284.8 ± 0.1, 398.0 ± 0.1, 687.3 ± 0.1 eV and 1020.5 ± 0.1 eV, respectively, while the high-resolution S(2p) signal is able to resolve the S($2p_{3/2}$) and S($2p_{1/2}$) peaks from the thiol chemisorbed on the gold substrate which are centered at 162.2 ± 0.1 and 163.4 ± 0.1 eV, respectively. Since there are two types of sulfur atoms present in the porphyrin molecule which can be distinguished by their chemical shifts, the S(2p) signal can be fitted into two sets of doublets from the S($2p_{3/2}$) and S($2p_{1/2}$) components split by 1.2 eV. The two S($2p_{3/2}$) peaks are centered at 162.2 ± 0.1 and 163.6 ± 0.1 eV, respectively (Figure 4.4). The first

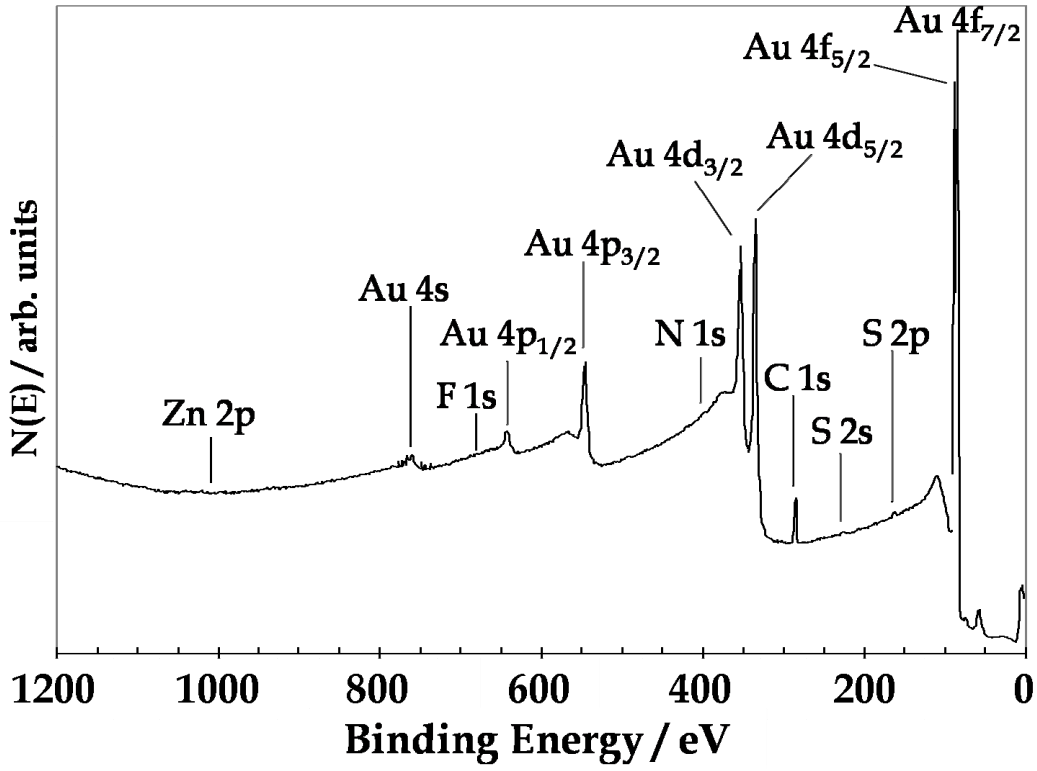

Figure 4.3. (mono Al source) X-ray photoelectron survey spectrum for zinc porphyrin thiol/dodecanethiol mixed monolayers on Au (111).

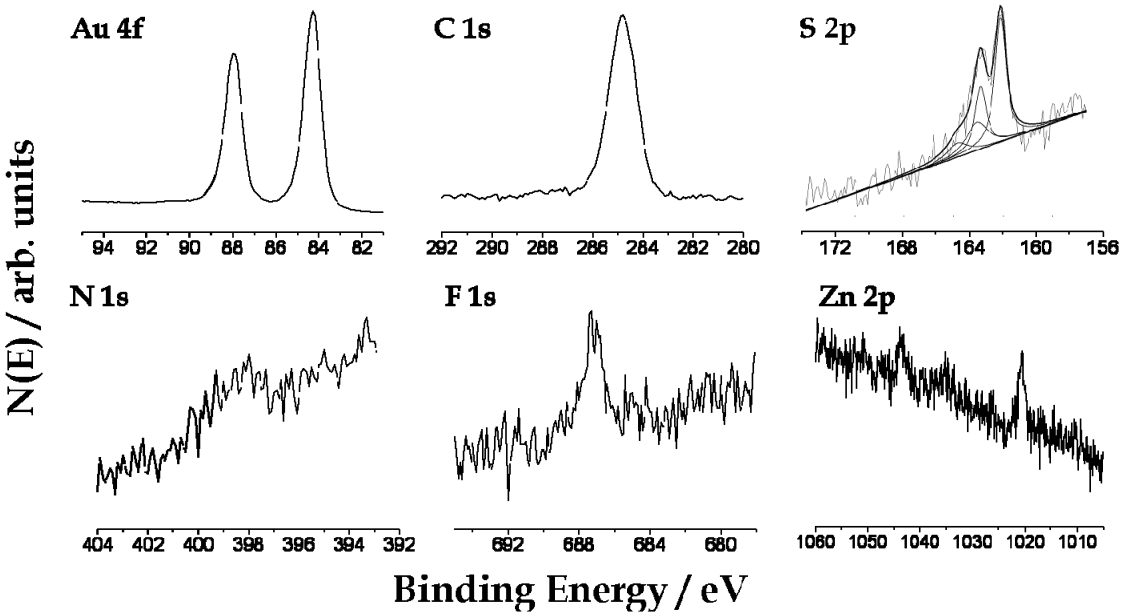

Figure 4.4. (mono Al source) High-resolution XPS for zinc porphyrin thiol/dodecanethiol mixed SAMs, showing the Au 4f, C 1s, S 2p, N 1s, F 1s and Zn 2p spectral regions.

type of sulfur corresponds to the thiol chemisorbed onto the gold substrate,[297] which is present due to the dodecanethiol and the zinc porphyrin thiol while the second at higher binding energy can be attributed to the presence of the S coordinated to the tetrafluorophenyl ring.[337] The intensity of these two S($2p_{3/2}$) peaks can be used to determine the percentage of the total number of zinc porphyrin thiol molecules on the surface. The attenuation of the thiol chemisorbed on the gold has to be considered for the total peak intensity. The percent attenuation of the sulfur peak of the thiol-Au bond due to the inelastically scattered photoelectrons by the interaction with the alkyl chains in the mixed SAM has been determined using a previous method.[338] The method

accounts for the thickness of the SAM, the attenuation length or escape depth of the photoelectrons,[339,340] as well as the angle between the plane of the sample and the detector. We have found that the sulfur peak of the thiol-Au bond was attenuated by ~ 43%. Using the integrated peak intensity of the S in the zinc porphyrin thiol and the S from the thiol-Au bond with the attenuation factor, the zinc porphyrin coverage as a function of the thiol adsorption sites was ~ 24 % for the 5 day soaked mixed SAM. Taking the ($\sqrt{3}$ x $\sqrt{3}$)R30° lattice constant of 5 Å for *n*-dodecanethiol SAMs on Au, an approximate estimate of ~ 4 molecules/nm^2 has been determined. With this approximate value, the full surface coverage of all thiol adsorbed molecules on the Au surface yields a total coverage of 6.6 x 10^{-10} mol/cm^2. The coverage of zinc porphyrin thiol is then 1.6 x 10^{-10} mol/cm^2 as determined from the percentage by XPS. The coverage reported here is reasonably consistent with previous findings of alkanethiol/porphyrin mixed SAMs on gold considering our calculation was determined based on XPS instead of using electrochemical or absorption spectroscopy methods.[341] Also, we expect that the coverage of the zinc porphyrin thiol molecule presented here should be slightly higher due to the fact that the meso substituents are not as bulky as the three di-tert-butylbenzene substituents in comparison, and therefore the zinc porphyrin thiol can insert more freely into the alkanethiol matrix.

4.3.4 Surface Imaging

In order to examine the surface structure of the inserted zinc porphyrin thiol molecules, both atomic force and scanning tunneling microscopies were employed. AFM images of the mixed monolayer show clusters inserted into the dodecanethiol matrix, suggesting that the zinc porphyrin thiol molecules are sticking up out of the dodecanethiol background. Based on the physical heights determined from contact mode images in ethanol, the zinc porphyrins were observed to extend above the dodecanethiol SAM by ~ 0.3 nm (Figure 4.5a) which is much lower than the free base porphyrin thiol with an average physical height of ~ 0.9 nm above the dodecanethiol background SAM. This is consistent however with the FT-IR measurements of the molecular orientation, which would estimate that the molecule extends from the dodecanethiol monolayer by ~ 0.5 nm. Due to the large size of the AFM tips used (*ca.* 10 nm) sufficiently high resolution images were not possible by AFM to detail the molecular organization of the dodecanethiol matrix. As such, scanning tunneling microscopy was utilized to obtain molecular resolution images of the mixed monolayer films.

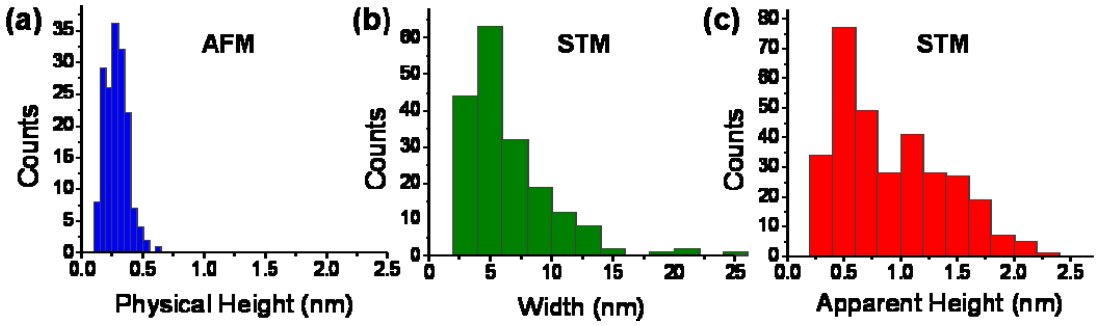

Figure 4.5. Height and domain size distributions from AFM and STM measurements (5 days soaking time for zinc porphyrin thiol into dodecanethiol matrix). (a) Physical height difference between the dodecanethiol and zinc porphyrins deduced from AFM images in ethanol. (b) Domain size histogram and (c) Apparent height distribution of zinc porphyrin thiol embedded in *n*-dodecanethiol SAMs from UHV-STM (V_{bias} = 1.4 V, I_{tunnel} = 20 pA).

STM images of the dodecanethiol matrix (see inset in Figure 4.6) on the Au(111) surface show the close-packed structures typically observed for alkanethiols[160,298,299] which shows that the matrix order is maintained after insertion of the porphyrin. When the zinc porphyrins were inserted into the SAM, they were found to organize next to and into defects in the film and appeared as bright unresolved clusters as shown in the representative STM images in Figure 4.6 of zinc porphyrin thiol inserted into the dodecanethiol matrix after 5 days. For the 5 day samples, the coverage as determined by STM on average was ~ 17 % which is lower than the estimated coverage by XPS of ~ 24 %. The lower estimated coverage by STM is most likely due to the fact that the average

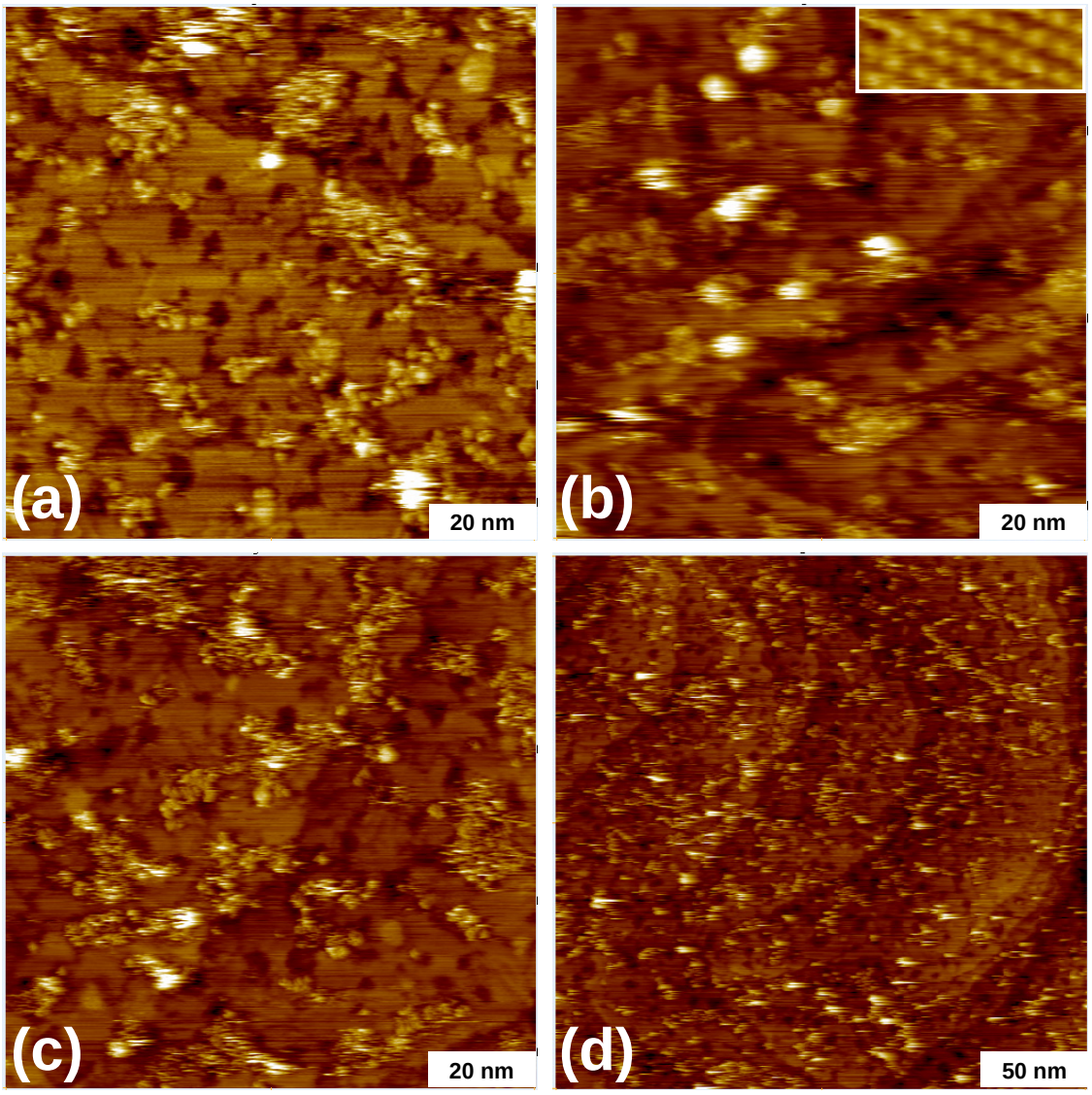

Figure 4.6. UHV-STM images of zinc porphyrin thiol molecules isolated within *n*-dodecanethiol matrix on Au(111) under UHV conditions. Imaging size and conditions: (a) 100 x 100 nm; V_{bias} = 1.2 V, I_{tunnel} = 5 pA (b) 100 x 100 nm; V_{bias} = 1.4 V, I_{tunnel} = 20 pA (c) 100 x 100 nm; V_{bias} = 1.4 V, I_{tunnel} = 30 pA and (d) 250 x 250 nm; V_{bias} = 1.4 V, I_{tunnel} = 30 pA. The inset in (b) magnifies the ($\sqrt{3}$ x $\sqrt{3}$)R30° lattices for *n*-dodecanethiol SAMs.

is based on the area of only the detected zinc porphyrin thiols by the SPIP software. The SPIP grain analysis only works properly on smooth, flat surface areas which is why the total coverage is underestimated since Au(111) has many terraces and uneven regions which are negated or even removed during the calculated grain analysis surface coverage. From examination of a number of mixed monolayers, the zinc porphyrin thiol molecules were found to form much larger aggregates (Figure 4.5b) than the free base porphyrin thiol which formed two dominate average domain sizes, small clusters of ~ 2 nm and larger clusters ranging from ~ 6 nm in width. The domain size of the zinc porphyrin aggregates increases from ~ 3 nm in width for the 1 and 3 day samples to an average width of 6 nm for the 5 day samples. As shown in the histogram in Figure 4.5b, the domain size for the 5 day has a large number of 6 nm aggregates and tails off up to ~ 20 nm in width. The large domains of the free base and zinc porphyrin thiol molecules are aggregates of molecules since porphyrins tend to have strong π–π coupling between macrocycles, and the increase in the aggregate size with the zinc porphyrin thiol molecules is most likely due to the added interactions of the zinc centers.[342] For the different soaking times, the average apparent height of the clusters increased from 0.3 nm for the 1 day to 0.8 nm for the 3 and 5 day samples. Since the clusters are measured by their longest dimension, a single porphyrin would measure the same width as a small cluster that is in a pi-stacked arrangement, but the apparent height would increase for the clusters. This explains why the average width of 3 nm is the same for the 1 and 3 day mixed SAMs, however, the apparent height increased from 0.3 nm to 0.8 nm consistent with aggregation of the molecules. Further soaking of the zinc porphyrin thiol with the 5

day mixed SAMs did not increase the average apparent height which is consistent with the 3 day samples at 0.8 nm, but the zinc aggregation increases drastically to form much larger clusters from ~ 6 to 20 nm in width. We also noted that in the STM images for the 5 day samples there appeared to be a predominant apparent height of ~ 0.5 nm and higher apparent heights greater than ~ 1 nm relative to the dodecanethiol matrix as shown in Figure 4.5c. Although the average apparent height was ~ 0.8 nm, there is a distinct lower apparent height of zinc porphyrin thiol molecules around 0.5 nm which is an aggregate in a different configuration than the clusters that appear above 1 nm in apparent height. The lower and higher apparent heights are shown in Figure 4.6 where the brighter features correspond to the higher apparent height. On average, the observed apparent height was more than double the observed physical height deduced from AFM images of the same samples. Since the apparent height is a convolution of the physical topography of the zinc porphyrin thiol and its electronic structure, the larger values of the apparent height suggest that the Zn analog of this porphyrin thiol is much more conductive than the free base. The electron tunneling decay constant, β, was previously determined for the free base porphyrin thiol using a two layer tunnel junction model,[302,343,344] and was found to be ~ 1.25 $Å^{-1}$. Using this same type of model, the decay constant for the zinc porphyrin thiol could not be quantified for the higher apparent height molecules as the calculated tunneling decay constant for the zinc porphyrin thiol would yield a negative value which corresponds to an unphysical situation.[343] Due to this discrepancy, we suspect that tunneling is not the dominant transport mechanism for the zinc porphyrin thiol molecule that appear above ~ 1 nm in

apparent height in the STM. However, for the lower apparent height molecules, taking an approximate average height of 0.5 nm, the tunneling decay constant is a reasonable value at ~ 0.59 $Å^{-1}$ which suggests an efficient tunneling electron transport mechanism.

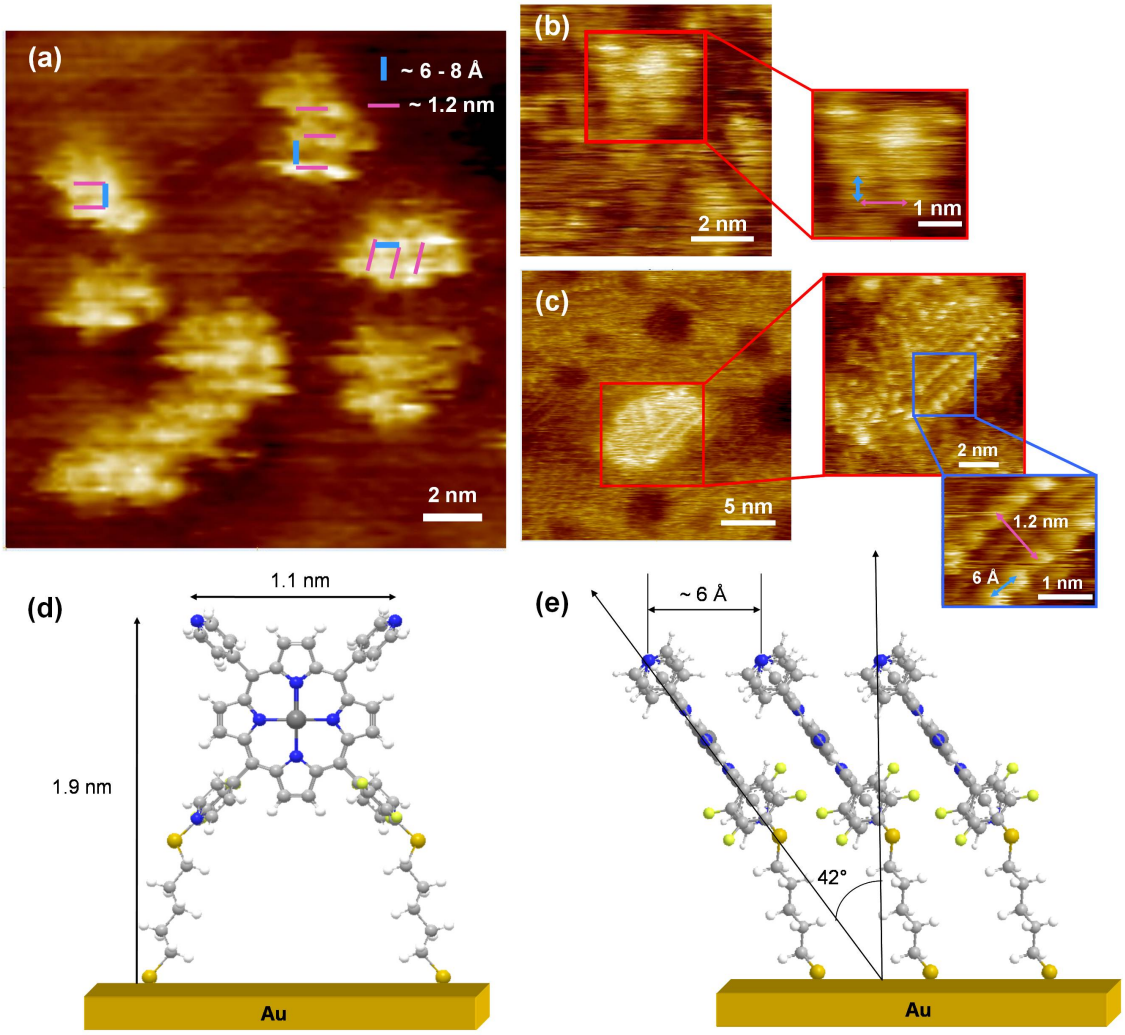

Figure 4.7. UHV-STM image of (a) low apparent height zinc porphyrin thiol clusters, (b) high resolution image of a cluster and (c) another high resolution image of a cluster. A model of the (d) front-on view and (e) the side view of clusters of zinc porphyrin thiol molecules.

Imaging of the lower and higher apparent height zinc porphyrin clusters at high resolution images were attempted in the UHV-STM to identify the configuration of these aggregates. However, the higher apparent height clusters were unable to be resolved due to inherent limitations of the STM at room temperature. The high resolution images of the lower apparent height clusters, i.e. less than 0.5 nm, can be seen in Figure 4.7. We have computationally investigated the conformation of the stacked zinc porphyrin molecules in the lower apparent height configuration and have verified that there are two stable structures for the aggregated zinc porphyrin thiol molecules in a face to face configuration which are shown in Figure 4.8 a & b. The DFT optimized face to face stacking orientation as shown in Figure 4.8a matches the experimental high resolution images obtained from UHV-STM in Figure 4.7 a, b, and c. The calculated distance of the two pyridyl N atoms of 1.1 nm with a separation distance of ~ 6 Å between the pi-stacked porphyrin macrocycles supports the images obtained from the STM of the low apparent height zinc porphyrin island clusters. In panels a, b, and c of Figure 4.7, the experimentally obtained pyridyl N atom distance of ~ 1.2 nm is shown in blue and the pi-stacked macrocycle distance of 6 - 8 Å is shown in pink. In panels d and e of Figure 4.7, the model of these lower apparent height clusters are shown based on the DFT calculated distances and the tilt of the molecules as determined by FT-IR.

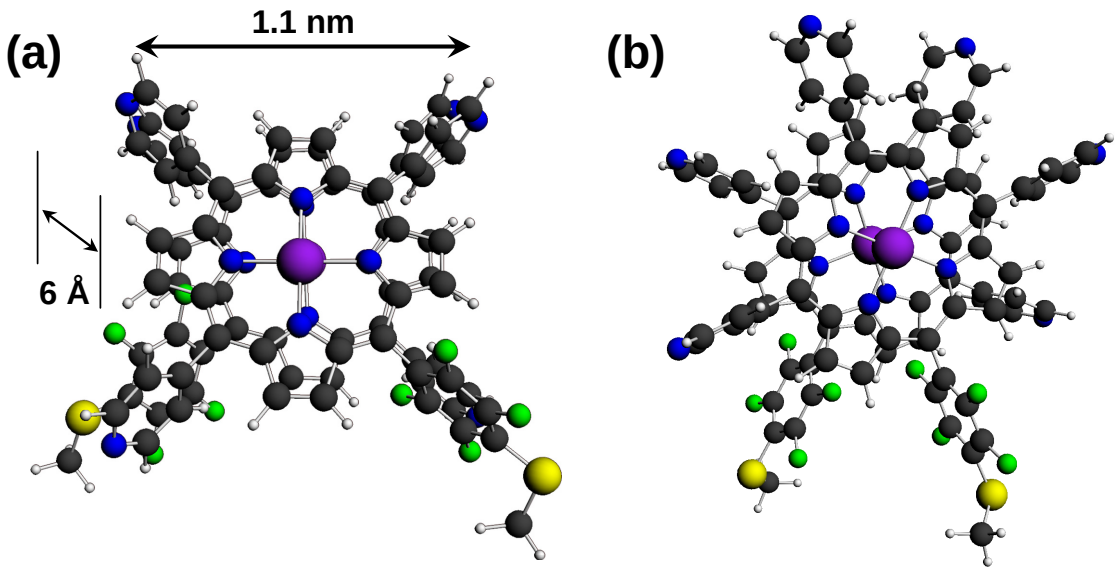

Figure 4.8. DFT calculated stacked orientations of the macrocycles of zinc porphyrin thiol molecules (a) overlaid and (b) tilted ~ 90° with respect to the other. Atom Colors- Purple: Zn, Black: C, White: H, Green: F, Blue: N, Yellow: S.

4.3.5 Electrical/Switching Behavior

Investigations of the electronic properties of these compounds have shown that the incorporation of the zinc metal center affords unique properties compared to its free base analog. First, from the DFT calculations, the HOMO-LUMO gap for the zinc porphyrin thiol was calculated to be 0.1 eV larger than the free base analog with a calculated HOMO-LUMO gap.[34] Moreover, the location of the HOMO state (-5.37 eV) suggests a small injection barrier of *ca.* 0.3 eV relative to the Fermi level of the Au substrate (-5.1 eV). The frontier orbitals that should participate in the electron transport process as shown in Figure 4.1e for the zinc porphyrin thiol reveal no overlap between the orbitals of the zinc porphyrin macrocycle and the tetrafluorophenyl ring that links the

macrocycle to the thiol tether. As such, there is an inherent barrier to charge transport located directly within the molecule even after incorporation of the zinc metal center.

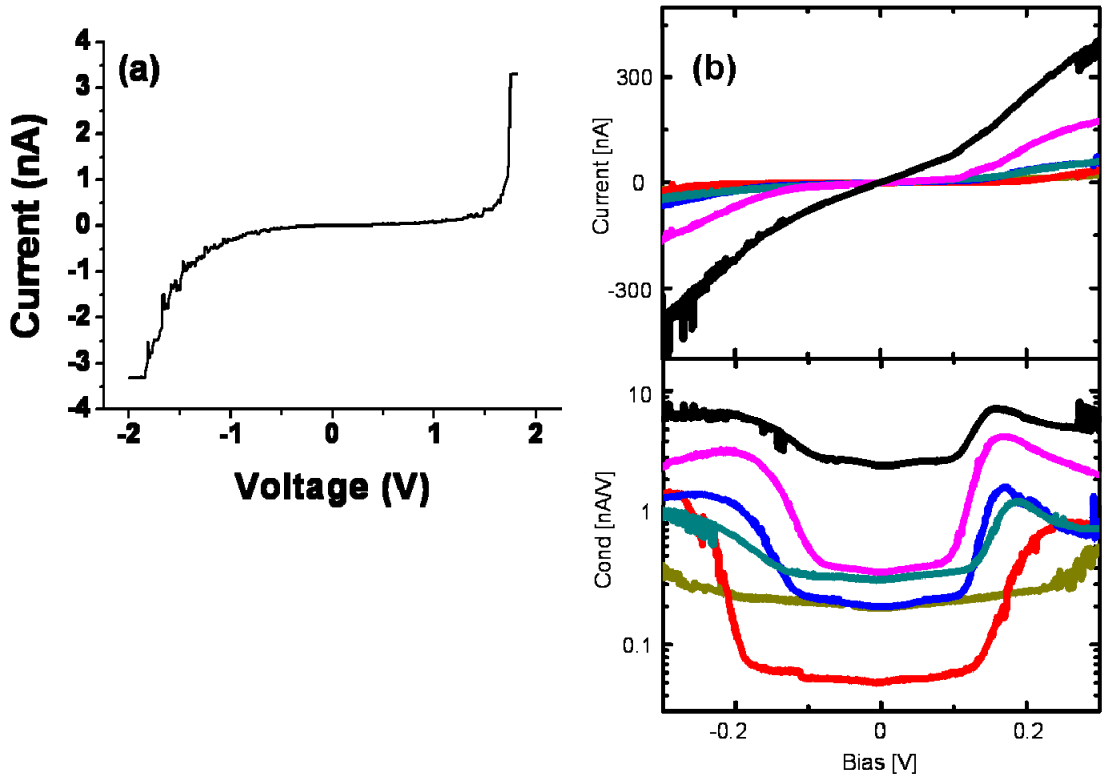

Figure 4.9. I-V spectrum zinc porphyrin thiol at (a) room temperature and (b) low temperature exhibiting Coulomb blockade of the 5 day mixed SAMs sample.

To study the charge transport through the zinc porphyrin molecules, current-voltage (I-V) measurements using STM have been obtained at room temperature. Figure 4.9a shows that the zinc porphyrin molecules have larger conductance ranges in the

nanoampere range compared to the free base porphyrin thiol which only produced currents into the hundreds of picoampere range.[34] In the free base analog, some current blocking effect was observed[34] for the small aggregates and in order to increase the current blocking effect of the porphyrin thiol molecule, the incorporation of the zinc metal center was employed for these studies. As mentioned previously, the zinc increases the affinity for aggregation and formation of islands which are useful for creating single electron tunneling devices.

At room temperature, the I-V curves for the zinc porphyrin islands can be unstable and irregular, so further electrical characterization was carried out at low temperatures using a cross-wire technique on the mixed monolayers with different deposition times to match those studied by STM. At low temperature (~ 4 K), it was found that approximately 20 % of the junctions formed from gold wires that were soaked in zinc porphyrin thiol for three to five days exhibited consistent nonlinear I-V characteristics (Figure 4.9b). In junctions formed from wires that were soaked in zinc porphyrin thiol for only one day and in control dodecanethiol/free base porphyrin thiol junctions, nonlinear I-V characteristics were not observed. In some of the junctions that displayed nonlinear I-V characteristics, stochastic gating behavior reminiscent of electronic devices that exhibit Coulomb blockade are observed. In these junctions discontinuous changes in the I-V characteristic were observed as a function of time, and each shift results in modification of the low bias behavior of the junction (see Figure 4.9b). Based on these measurements, the π-π stacking of the macrocycles as well as the zinc metal interactions are playing a significant role in the amount of current passing

through the molecule as well as the turn-on voltage in the I-V curve. Since the zinc metal center increases aggregation, the zinc porphyrin clusters form large enough islands with the 5 day sample which are able to stabilize charge through the extended pi system, and when a high enough bias is applied, *i.e.* the voltage threshold is reached, the charge is released which in turn results in an increase in the current flow. This result is not completely unexpected, as porphyrins have previously shown to act as Coulomb islands in break junctions,[327] metal-molecule-metal junctions,[326] as well as embedded in metal-oxide-semiconductor junctions.[215,328] At low temperatures (~ 5 K), typical Coulomb blockade staircases were observed in the I-V measurements, and the threshold voltages were sensitive to changes in the intermolecular interactions such as clusters of the porphyrin molecules.[215,328] As described earlier, molecules other than porphyrins such as a ruthenium(II) bis(σ-arylacetylide) complex,[329] a cobalt ion bonded to two terpyridinyl linker molecules,[117,330] and a nickel-octanedithiol multilayers[331] have also been found to exhibit Coulomb blockade or Coulomb blockade-like behavior at low temperatures. The ruthenium compound was found to exhibit a hopping-type electron transport mechanism which could also be the case for our zinc coordinated porphyrin thiol molecule. However, future temperature dependent current-voltage measurements will be needed to confirm the mechanism of charge transport. It is not well-understood at this time in our system how the intermolecular interactions of the zinc porphyrin molecules are affecting the I-V measurements, but we have initially verified that the Coulomb blockade gap range does appear to change as a function of the island size suggesting the zinc porphyrin molecules can act as a molecular capacitor.

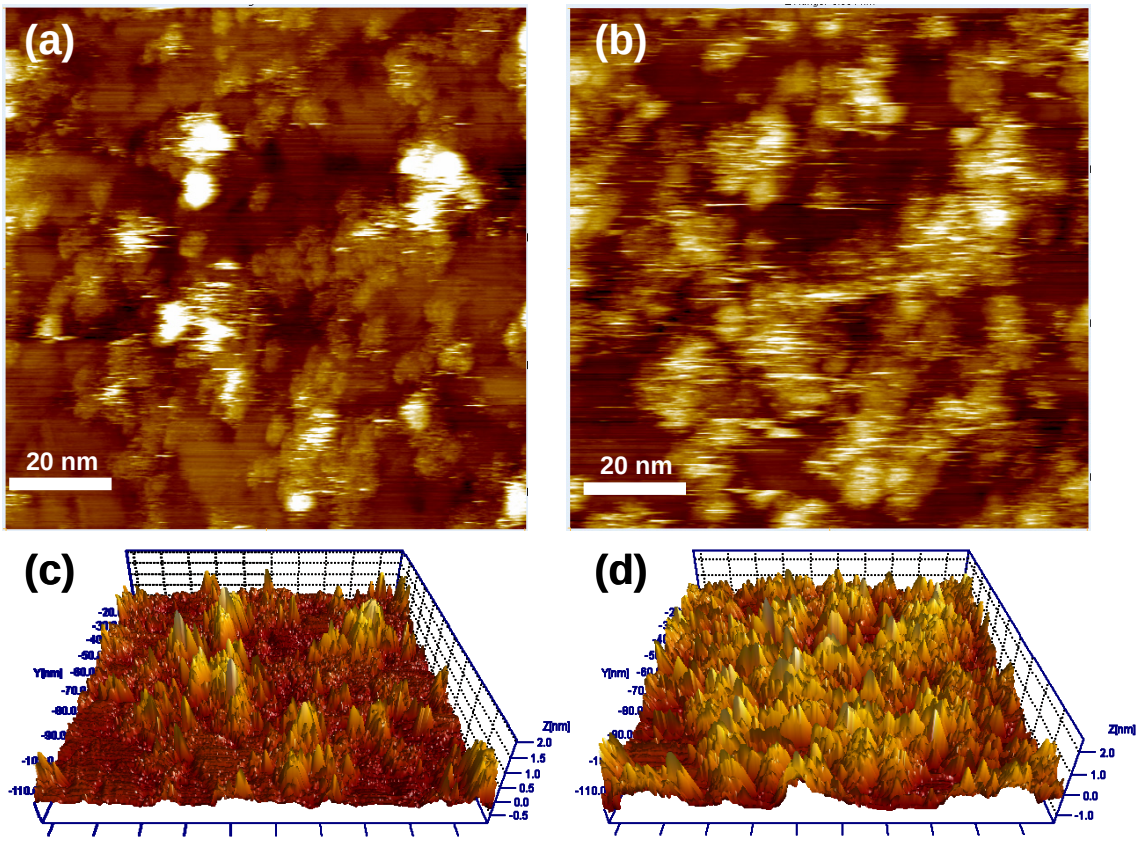

Figure 4.10. Bias-induced switching of 5 day soaked zinc porphyrin thiol in dodecanethiol matrix. UHV-STM images of the (a) OFF state at 1.4 V and 20 pA and (c) the corresponding 3-D version. (b) The ON state of zinc porphyrin thiol molecules imaged at 2.0 V and 20 pA and (d) the corresponding 3-D version. Note: Color scale on right side of STM images is in nanometers.

We have, however, ascertained that the addition of the zinc metal center into the porphyrin thiol must be playing a role in the bias-induced switching behavior because this was not previously seen for the free base porphyrin thiol. Specifically, as the bias was increased from 1.4 V to 2.0 V, a larger number of higher apparent height zinc porphyrin islands appeared in the STM image as shown in Figure 4.10 a and b and in the 3-D depiction in panels c and d of Figure 4.10, it is obvious that the lower apparent height porphyrins are the ones that are turned ON by the increase in bias of the STM tip. Considering the higher apparent height islands to be in the ON state, we have found that the zinc porphyrin molecules can be continuously cycled and switched back to an OFF state (lower apparent height) if the bias is swept back to -1.4 V (as shown in Figure 4.11). Switching behavior in molecules has been attributed to a number of reasons including dipole induced switching,[345] conformational[128] and/or orientational changes of the molecules,[305,306] interactions among neighboring molecules,[307] fluctuations of the molecular bundle,[309] and changes in molecule-substrate bond hybridization.[310] Dipole -

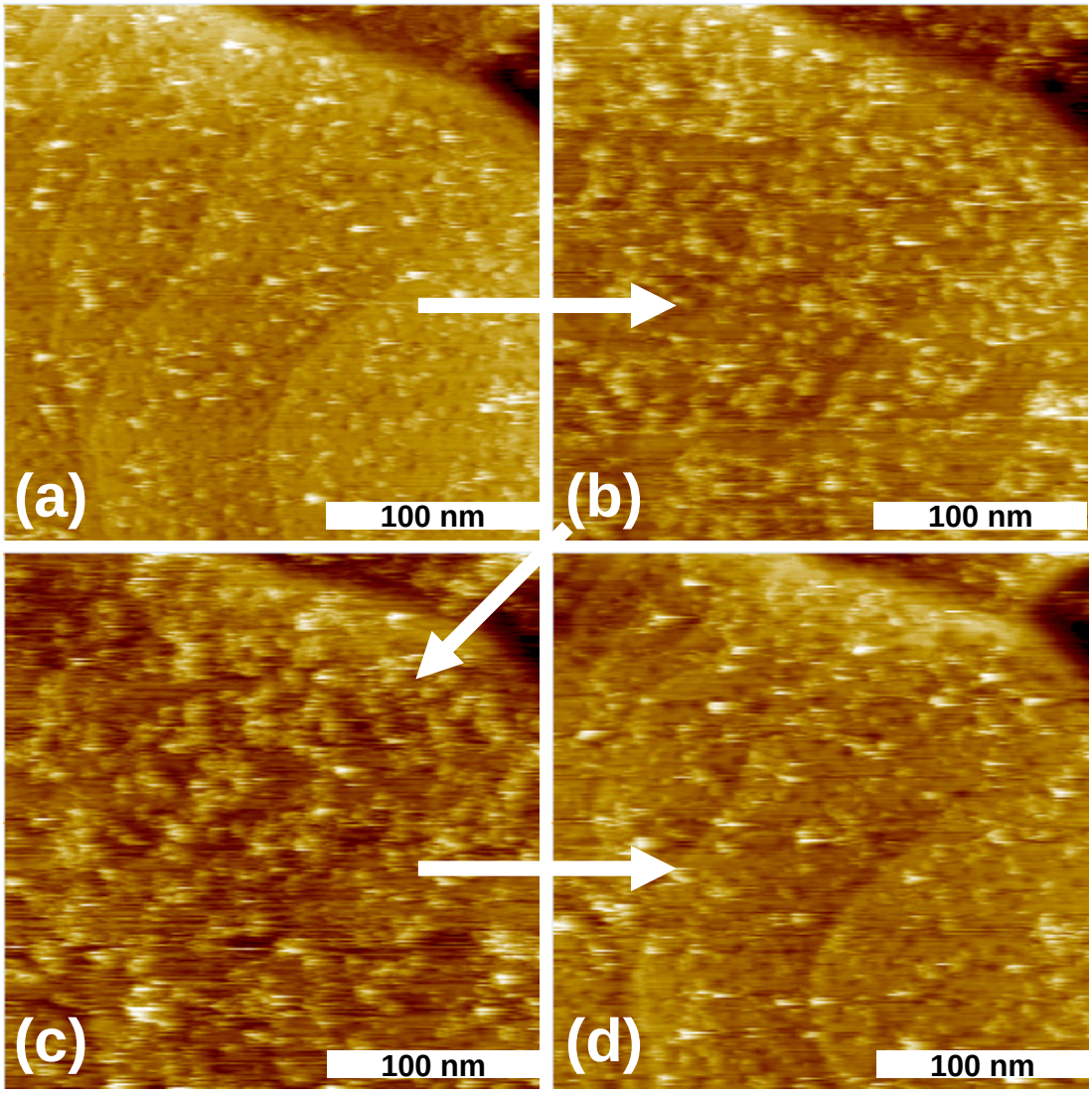

Figure 4.11. UHV-STM images of zinc porphyrin thiol molecule(s) isolated within *n*-dodecanethiol matrix on Au(111) under UHV conditions. Imaging size: (a - d) 250 x 250 nm; imaging conditions: (a) V_{bias} = 1.4 V, I_{tunnel} = 20 pA, (b) V_{bias} = 2.0 V, I_{tunnel} = 20 pA, (c) V_{bias} = 1.4 V, I_{tunnel} = 10 pA, (d) V_{bias} = -1.4 V, I_{tunnel} = 10 pA.

induced switching is most likely not the reason for the switching behavior of the zinc porphyrins since coordination of the porphyrin with zinc does not have a significant effect on the overall dipole moment of the molecule, which was determined to be 2.38

Debye and 2.42 Debye with and without the zinc coordination of the porphyrin thiol molecule, respectively. Moreover, the calculated electrostatic potential maps for the free base and zinc coordinated porphyrin thiol molecules do not show a significant difference as shown in Figure 4.12, so we do not expect that the switching is due to electrostatic effects from the applied tip bias. One possibility is that the switching is most likely an ensemble size effect, such that with increasing island size a more extended pi coupled system could be formed, allowing for greater charge stabilization. If the zinc porphyrin thiol was inserted in the dodecanethiol SAM at lower surface coverage (*i.e.* the dodecanethiol SAM is only exposed to zinc for only 1 day instead of 5), the switching behavior was not apparent in the UHV-STM measurements, and Coulomb blockade was not observed at low temperatures. Here we should recall that for the 1 day soaked mixed SAM, smaller domain sizes and single molecules, similar to what was seen for the free -

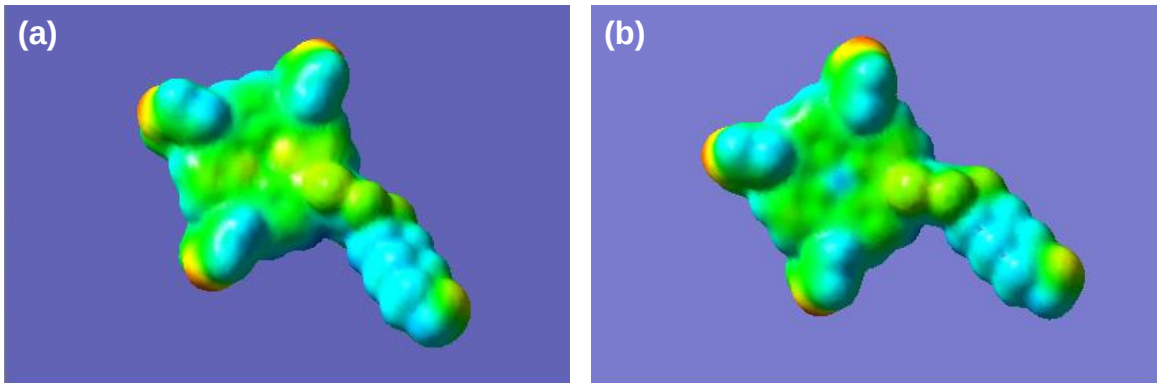

Figure 4.12. Electrostatic potential maps of (a) the free base and (b) zinc coordinated porphyrin thiol molecules. The maps were generated with GaussView 3.0 at a 0.0005 isodensity value and a color scale of -0.050 (red) to +0.043 (blue) a.u.'s.

base porphyrin thiol, dominate the inserted structures, and exhibited no switching when the bias was increased from 1.4 V to 2.0 V. However, for the 5 day soaked mixed SAMs sample, *i.e.* the surface with the most zinc porphyrin thiol coverage, both Coulomb blockade as well as the bias-induced switching behavior was observed. From the images following the switching of the 5 day sample, it is evident in Figure 4.10 that the lower apparent height molecules are the ones that turn ON in the image at 2.0 V and this can also be seen in their I-V curves since the turn-on for the current is ~ 1.7 V. The difference in the two observed apparent heights in the STM images was not due to a topographical effect since there is not a broad distribution of physical heights from the AFM images and therefore the difference in apparent height must be due to electronic effects. As stated previously, the molecules that appear in the STM with a lower apparent height are most likely in a different configuration compared with those of the higher apparent height. The lower apparent height clusters are oriented in a pi-stacked face to face arrangement as shown in Figure 4.7e while the higher apparent height molecules are most likely stacked so that the pyridyl nitrogen interacts with the zinc metal center of a neighboring molecule. Figure 4.7 a - c show STM high resolution images of lower apparent height clusters while Figure 4.7 d & e depict the model of the pi-stacked face to face structure of clusters of zinc porphyrins. Further evidence of our conclusion that the low apparent height zinc porphyrin clusters have this pi-stacked arrangement comes from our former study of the free base analog.[34] With the free base porphyrin thiol, there were an abundance of molecules with an apparent height of ~ 5 Å, and there were very few molecules observed with an apparent height higher than this

average. There were also two predominate widths of ~ 2 and 6 nm, or single molecules and small clusters, respectively. Since the free base analog does not have a zinc metal center, there is no possibility for the zinc-pyridyl interaction and therefore the arrangement of the small clusters with a low apparent height can only favor a pi-stacked arrangement. The previous assessment of the free base analog agrees well with our current presumption that the low apparent height zinc porphyrin clusters arrange with a pi-stacked configuration as well. On the other hand, we could not resolve the structure of the high apparent height clusters with STM due to streaking of the images and interaction of the tip disturbing these clusters even at low currents less than 5 pA. We conjecture that the "ON" state of the zinc porphyrins are in the same pyridyl N-Zn coordinated configuration as the zinc porphyrin clusters that already appear with an apparent height > 1 nm which are abundant on the surface after 5 days of immersion time. The free base porphyrin thiol analog did not exhibit any switching behavior which makes sense since there is not a higher apparent height configuration for the molecule to switch "ON" to, nor were there any large aggregates for the charge to be stabilized in the extension of the pi system. When the zinc porphyrins begin to aggregate as islands of ~ 10 nm, it is unclear at this time specifically how the stacking influences their electronic structure as a unity and therefore their switching behavior. Calculations are in progress to gain more insight into the stacking effect of larger clusters which could ultimately explain why the lower apparent height zinc porphyrins are the ones that switch ON with a higher applied bias.

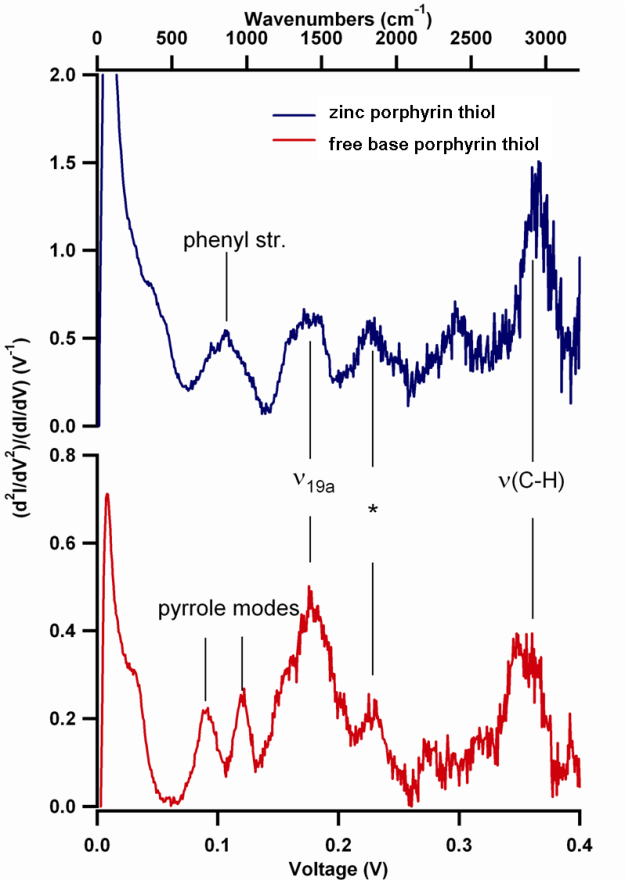

Figure 4.13. IET spectra of gold coated wires of mixed SAMs of dodecanethiol/free base porphyrin thiol and dodecanethiol/zinc porphyrin thiol.

We have enabled the use of inelastic electron tunneling spectroscopy (IETS) to study the conduction pathway of the free base and zinc porphyrins in mixed SAMs in a gold-molecule-gold junction to observe any differences in the charge transport pathway of the two derivatives. IETS of metal-molecule-metal junctions can provide insight into the conduction pathway of a molecule because IETS enables chemical differentiation since the vibrational spectrum of a molecule provides its chemical signature[7] and the

spectrum displays the vibrational modes that are excited by the electron during transport.[227] The IET spectra of the dodecanethiol/free base porphyrin thiol junction in Figure 4.13a and the dodecanethiol/zinc porphyrin thiol junction in Figure 4.13b exhibit excellent agreement with IR spectra of the molecular compounds in KBr, in mixed SAMs and from DFT calculations. Changes of the electronic pathway are evident in the IET spectra of the free base and zinc coordinated porphyrin thiol. Figure 4.13 a and b shows one peak at 970 cm^{-1} for the free base and a different peak at 870 cm^{-1} for the zinc porphyrin thiol due to pyrolle breathing and phenyl stretching IR active modes, respectively. A summary of the peak frequencies for the two porphyrin thiol molecules has been outlined with their assigned vibrational modes and are shown in Table 4.2. The assignment at 1840 cm^{-1} in both the free base and zinc porphyrin thiol IET spectra are still unclear at this time. IETS has verified that the transport pathway is distinct to its molecular components.

Table 4.2. IR active modes for the free base porphyrin thiol in KBr Pellets, in monolayers mixed with dodecanethiol and TPSS calculations. Yellow highlighted modes are present in both free base and zinc porphyrin IET spectra. Red and blue highlighted modes are only present in the free base or zinc porphyrin mixed SAMs, respectively. [a]The peak intensity is negligible or the peak is not applicable. [b]Calculated with density functional theory TPSS/6-31G+(d') [c]Data taken from zinc porphyrin thiol.

peak position (cm^{-1})			
in KBr	**in mixed SAMs**	**DFT[b] calc.**	**Vibrational mode**
3316	3318	3470	ν(N-H), stretching
-----[a]	2964	-----[a]	$\nu_a(CH_3$, ip), asym stretching
-----[a]	2936	-----[a]	$\nu_s(CH_3$, FR), sym stretching
2926	2919	3058	$\nu_a(CH_2)$, asym stretching
-----[a]	2877	-----[a]	$\nu_s(CH_3)$, sym stretching
2853	2850	3010	$\nu_s(CH_2)$, sym stretching
2533	-----[a]	2663	ν(SH)
1592	1593	1603	ν_{8b}(C=C), in-plane stretching
1465	1468	1447	ν_{19a}(C=C), in-plane stretching
1069	1045	1077	ν_{18b}(CH), in-plane bending
968	969	970	pyrrole breathing
870	870	857	phenyl stretching[c]
798	~791	800	ν_{11}(CH), out-of-plane bending
756	757	743	CH_2 wagging[c]
~726	723	729	pyrrole deformation

4.4 Conclusions

In summary, when inserted into a background matrix of dodecanethiol, the zinc coordinated porphyrins tend to bind near the edges of defects within the alkanethiol layer as large ensembles due to π–π and zinc interactions. From DFT calculations, there is

still a lack of effective orbital overlap after incorporation of the zinc metal center between the frontier orbitals of the porphyrin macrocycle and the thiol tether due to the orthogonal dihedral angle between the porphyrin ring and the perfluorophenyl linker group. Coordination of the porphyrin macrocycle with zinc lowers the proximity of the HOMO of the molecule by only a tenth of an electronvolt with respect to the Au Fermi level and does not induce a significant change in the electrostatic potential map of the molecule when compared with the free base analog. Although, the only change to the molecule has been the incorporation of the zinc metal, there is a major difference in the behavior of the zinc coordinated molecule compared to the free base porphyrin thiol under an applied STM bias that leads to bias-induced switching and Coulomb blockade. We attribute the switching to an ensemble size effect since the switching behavior was more evident in the 5 day mixed SAMs which contain larger clusters of porphyrins than the 1 day mixed SAMs. Further temperature dependent charge transport studies will be necessary to elucidate the electron transport mechanism for the zinc coordinated porphyrin thiol and more in depth analysis of the electronic states of the aggregated porphyrins will be required to accurately determine the mechanism for switching. Non-linear I-V characteristics are exhibited at low temperatures with the incorporation of the zinc metal center suggesting that the molecule can be used in single electron tunneling devices where the Coulomb island is isolated and until a high enough potential is applied the current through the molecule will remain blocked. Studies relating the island size to its threshold voltage and Coulomb blockade range are currently being done to investigate the molecular capacitance of the zinc porphyrin islands.

CHAPTER V

CONTROLLING MOLECULAR INTERACTIONS USING BIPODAL PORPHYRIN DERIVATIVES FOR ORGANIC ELECTRONICS

5.1 Introduction

Derivatives of the monopodal porphyrin thiol studied in Chapters III and IV are of interest to continue to develop active components for devices. The free base monopodal porphyrin thiol showed a slight current blocking effect when aggregates on the order of ~ 6 nm were formed by self assembly after 5 days of soaking. For the zinc monopodal derivative, more interesting electronic properties were observed. Bias-induced switching and Coulomb blockade were observed with larger, ~ 10 nm aggregates of the zinc porphyrin thiol. For these clusters, the zinc porphyrin thiol molecules were arranged in a pi-stacked configuration with alternating orientations of the monopodal tethers. In order increase the number of porphyrin thiol molecules on the surface and ultimately the number of porphyrin aggregates, a cis-bipodal porphyrin thiol was synthesized and pure and mixed monolayers were investigated. With a bipodal porphyrin thiol, there are two tethers for adsorption to the Au surface which increases the number of electronically active molecules on the surface. In this chapter, the adsorption of the free base and zinc cis-bipodal porphyrin thiol was examined with pure and mixed monolayers in a dodecanethiol matrix using AFM and STM. In order to further investigate the different monolayers, XPS and FT-IR were also used, and the

electronic structures and frontier molecular orbitals were calculated to detail the electronic overlap of the macrocycle with the two fluoro-phenyl coupling groups.

5.2 Experimental

5.2.1 Materials

Self-assembled monolayers were prepared on Au films, including Au(111) on mica (Molecular Imaging-Agilent, Phoenix, AZ) and on evaporated Au films on Si. Au films on Si substrates were prepared by thermal evaporation onto single-side polished Si(100) wafers (Virginia Semiconductor Inc.) in a bell-jar evaporator (BOC Edwards, Auto 306). The chromium (5 nm) and gold (200 nm) films were deposited under vacuum ($p < 2.0 \times 10^{-6}$ Torr) at rates of 0.5 and 3 Å/s, respectively. Dodecanethiol (DDT) was purchased from Aldrich (98% purity) and used as received.

5.2.2 Preparation of Monolayers

Au(111) substrates (purchased from Molecular Imaging-Agilent) were ~150 nm flame-annealed gold films on mica. Before each experiment, all substrates were treated with UV/ozone for 20 min, followed by rinsing the gold film in sequence with high purity (18.2 MΩ•cm) water (NANOpure Diamond, Barnstead), ethanol, and dried with streaming nitrogen. SAMs of *n*-dodecanethiol were formed by immersion of the Au films in 1 mM *n*-dodecanethiol in ethanol for 24 h. After rinsing liberally with ethanol, the substrates were soaked in 0.1 mM free base or zinc metallated cis-bipodal porphyrin thiol dissolved in dichloromethane for one to three days to allow the insertion of the porphyrin molecules into *n*-dodecanethiol matrix. After insertion, the substrates were removed from the solution and were rinsed with dichloromethane and blown dry with

streaming nitrogen. Pure SAMs were formed by immersion of Au substrates in 0.1 mM solution of the free base cis-bipodal porphyrin thiol dissolved in dichloromethane for one day. After insertion, the samples were removed from solution and rinsed with dichloromethane and blown dry with streaming nitrogen.

5.2.3 Scanning Tunneling Microscopy

STM measurements were taken under ultrahigh vacuum (UHV) conditions using an Omicron UHV-XA STM system. The system was operated with a typical base pressure of $< 3 \times 10^{-10}$ Torr. Images were collected using Pt/Ir (70/30) tips which were mechanically cut. The typical imaging conditions of tunneling current and tip bias voltage ranged from 5 pA to 30 pA and from -2.0 V to +2.0 V, respectively.

5.2.4 Atomic Force Microscopy

AFM images were acquired with a Molecular Imaging 4500 Pico SPM (Agilent, Phoenix, AZ) with a deflection-type detection scanning head interfaced with an SPM1000 control electronics Revision 8 (RHK Technology Inc., Troy, MI). All AFM images were acquired in contact mode under ethanol using commercially available Si_3N_4 AFM tips (Veeco/TM Microscopes, Sunnyvale, CA) with nominal tip radii of ~ 10 nm and nominal spring constants ranging from 0.03 - 0.5 N/m.

5.2.5 X-ray Photoelectron Spectroscopy

XPS data were acquired with a Kratos Axis ULTRA X-ray photoelectron spectrometer equipped with a 165 mm hemispherical electron energy analyzer. The incident radiation was the monochromatic Al Kα X-ray line (1486.6 eV) with a source power of 120 W (12 kV, 10 mA). The analysis chamber was maintained at a steady base

pressure of $< 6 \times 10^{-9}$ Torr during sample analysis. Survey scans of up to 1100 eV were carried out at an analyzer pass energy of 160 eV with 0.5 eV steps and a dwell time of 300 ms. Multiplexed high resolution scans (Au 4f, C 1s, S 2p, N 1s, and F 1s) were taken at a pass energy of 40 eV with 0.1 eV steps and a dwell time of 60 ms. The survey and high resolution spectra were obtained with averages of 5 and 30 scans, respectively with the exception of Au 4f with an average of 10 scans. The Au 4f peak at 84.0 eV was set as a reference for all XPS peak positions to compensate for energy shifts due to the spectrometer work function.

5.2.6 FT-IR Spectroscopy

Transmission IR spectra of the solid porphyrin compounds were obtained in KBr pellets collected with a total of 256 scans of both the sample and the reference at 1 cm^{-1} resolution.. FT-IR spectra of the mixed monolayers were collected on evaporated Au films on Si. Reflection-absorption spectroscopy was collected using an FT-IR spectrometer (Nicolet 6700, Thermo Electron Corporation, Madison, WI) equipped with a liquid nitrogen-cooled HgCdTe (MCT) detector. FT-IR data were acquired in single reflection mode with polarized light generated by a ZnSe polarizer adaptor (FT-80, Thermo Electron Corporation). The light path, MCT detector, and sample chamber were purged with dry nitrogen during the measurements. A UV/ozone cleaned gold substrate was used as the reference. The IR spectra were collected with a total of 1024 scans of both the sample and the reference at 4 cm^{-1} resolution.

5.2.7 Theoretical Calculations

Calculations of the molecular structure, electronic structure, and analytic vibrational modes were carried out using Density Functional Theory as detailed in earlier chapters.

5.3 Results and Discussion

5.3.1 Theoretical Calculations

Density functional theory calculations were used to optimize the gas phase structure of the both the free base and zinc cis-bipodal porphyrin thiol compounds. The optimized structure of the free base and zinc cis-bipodal porphyrin thiol molecules are shown in Figure 5.1A and B, respectively. For the free base analog the pyridyl groups are canted at 66.4° and 65.7° relative to the macrocycle compared to the zinc analog both pyridyl groups are canted at ~ 66.5°. The tetrafluorophenyl groups of the free base are canted at 75.3° and 74.7° relative to the macrocycle compared to the zinc analog which are canted at 77.3° and 76.7°. The sulfur-sulfur bipodal tether distance was calculated to be 17.2 Å for the free base and 16.9 Å for the zinc analog. The HOMO -

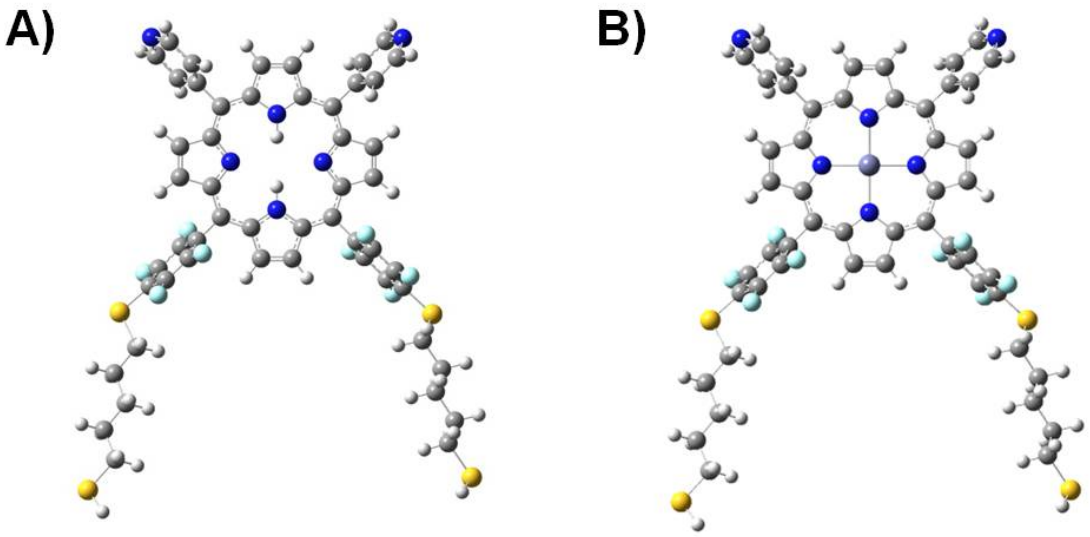

Figure 5.1. TPSS optimized structures for the (A) free base cis-bipodal porphyrin thiol and (B) zinc cis-bipodal porphyrin thiol.

LUMO gap for the free base cis-bipodal porphyrin thiol was calculated to be 1.84 eV which is almost identical to the free base monopodal porphyrin thiol. The zinc cis-bipodal porphyrin thiol calculated HOMO-LUMO gap was 1.98 eV. The location of the HOMO states of both molecules (-5.31 eV and -5.38 eV) relative to the Fermi level of the Au substrate (-5.1 eV) based on these calculations (with all of their associated caveats), suggests a small injection barrier of ca. 0.2 eV. The frontier orbitals that should participate in the electron transport process as shown in Figure 5.2 reveal no overlap between the orbitals of the porphyrin macrocycle and the tetrafluorophenyl rings that link the macrocycle to the thiol tether. Thus, there is an inherent barrier to charge

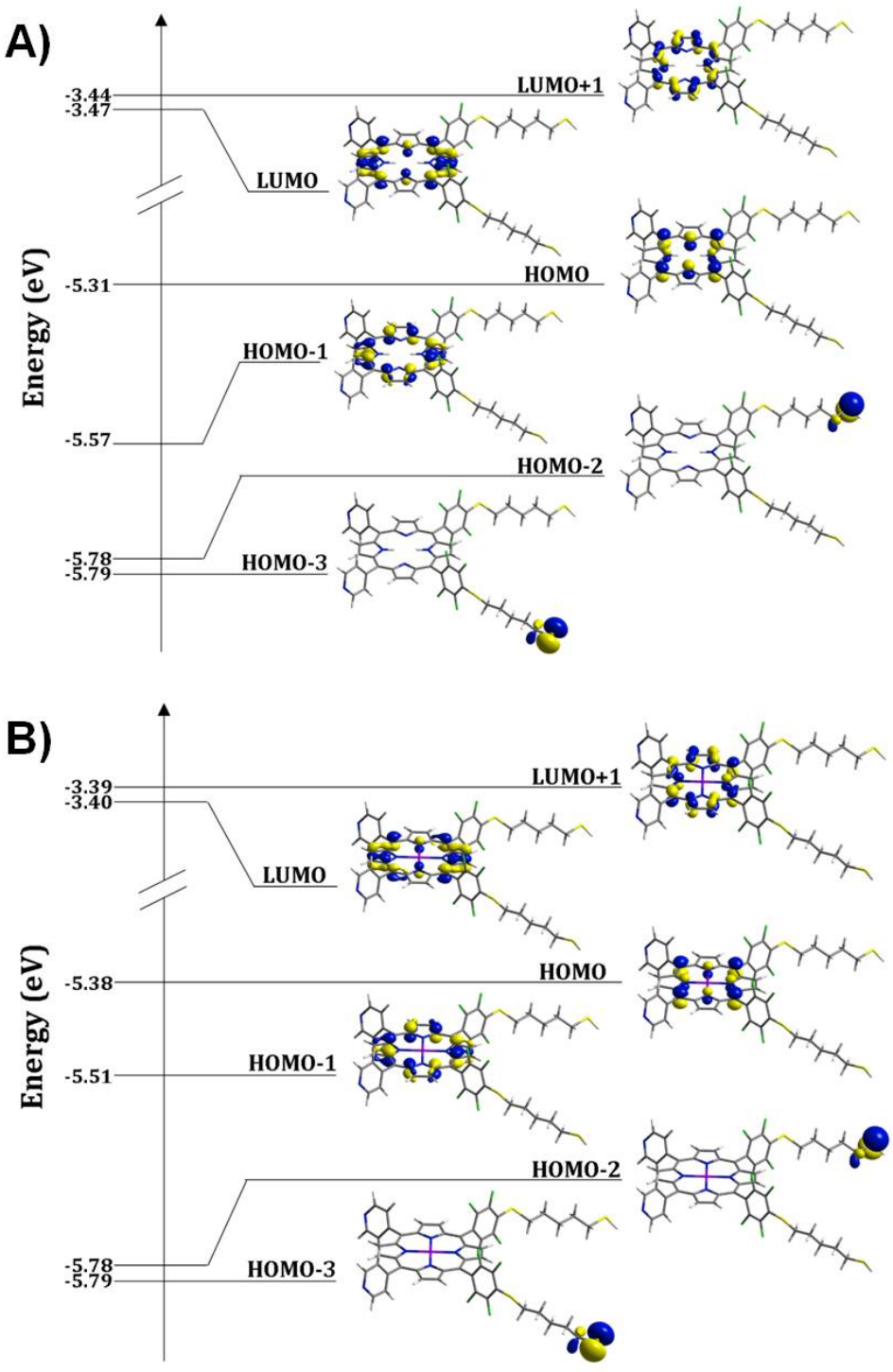

Figure 5.2. Frontier molecular orbitals (HOMO-3 to LUMO+1) for the (A) free base cis-bipodal porphyrin thiol and (B) zinc cis-bipodal porphyrin thiol.

transport located directly within the cis-bipodal derivative of the porphyrin thiol which was seen for the free base and zinc monopodal derivatives as well.

5.3.2 FT-IR Measurements

The IR spectra of the free base cis-bipodal porphyrin thiol as calculated by DFT and prepared in KBr pellets are presented Figure 5.3A and 3B, respectively. The molecules in KBr pellets were ground thoroughly and thus presumably exhibit isotropic orientation. Figure 5.3C displays the infrared reflection absorption spectroscopy spectrum of porphyrin thiol/dodecanethiol mixed monolayers on Au after 1 day of sample immersion while Figure 5.3D shows the pure monolayer formation after 1 day. The observed peak frequencies and vibrational modes were assigned based on the calculations. Typically, a model of the free base cis-bipodal porphyrin thiol derivative embedded in *n*-dodecanethiol SAMs would be proposed using FT-IR methods. Previously, for the free base and zinc monopodal derivatives of the porphyrin, the tilt angle of the porphyrin macrocycle with respect to the surface normal has been determined using the intensity ratio of the two transition dipoles of the in-plane pyrrole ring breathing mode, a_1, and out-of-plane pyrrole C-H bending mode, a_2. In Figure 5.3, the corresponding vibrational peaks for the in-plane and out-of-plane contributions from the porphyrin thiol pyrrole moieties (a_1 and a_2, respectively) for deducing the molecular

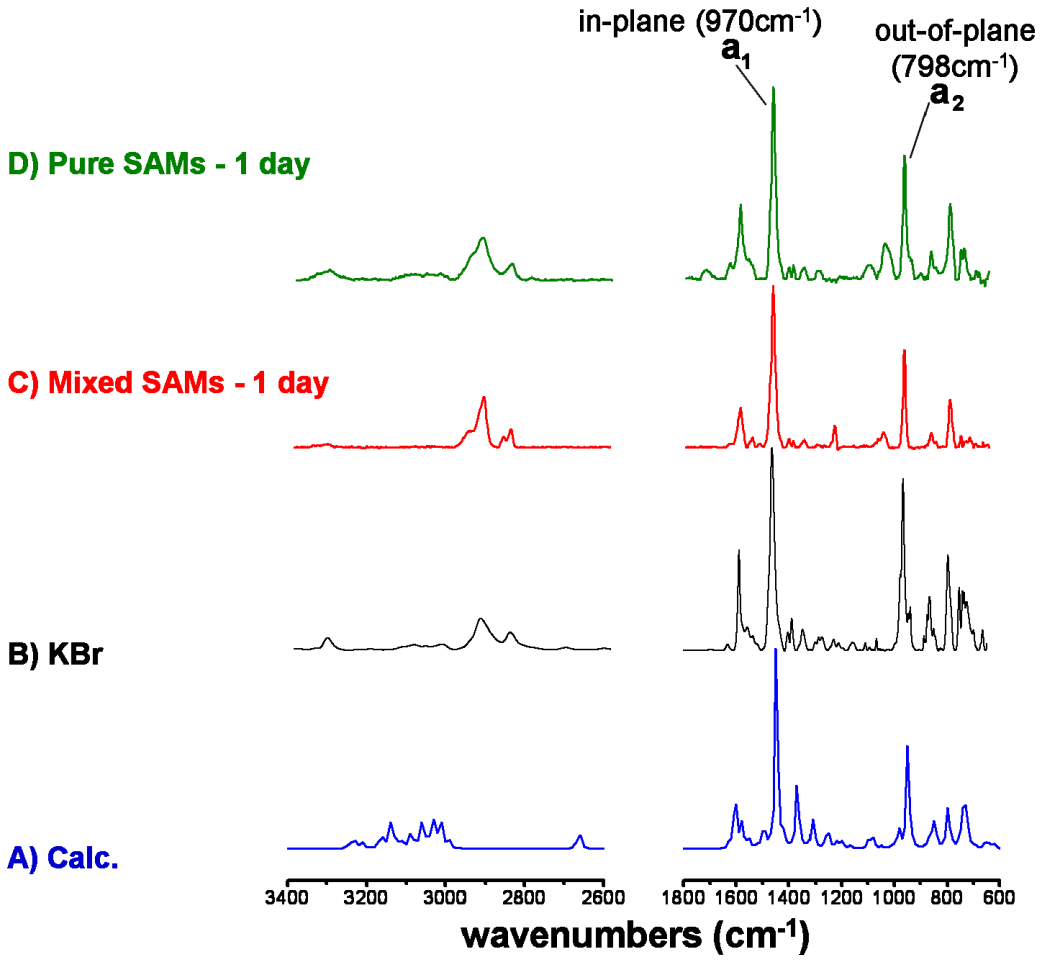

Figure 5.3. IR spectra of free base cis-bipodal porphyrin thiol (A) calculated by TPSS and (B) prepared in KBr pellets; and FT-IR spectrum of (C) free base cis-bipodal porphyrin thiol/dodecanethiol mixed monolayers and (D) pure monolayer.

tilt angle of the porphyrin SAMs are denoted. However, for the current bipodal derivative, there is not a single orientation axis since there are two tethers on the Au surface. If a similar approach is used as compared to previous studies of the monopodal derivatives, by using the increase of intensity ratio of I_{a1}/I_{a2} in the mixed monolayers

(Figure 5.3C) or pure monolayers (Figure 5.3D) as compared with the KBr pellets (Figure 5.3B), the results would indicate that the porphyrin macrocycle orients at an angle relative to the surface normal of 54° for the mixed and 45° for the pure monolayer with the physical height of the porphyrin standing at 13 Å or 16 Å, respectively. If the relative isotropic intensity, I_{a1}/I_{a2}, from the calculated spectrum is used in place of the experimentally measured KBr sample, the tilt angle of the macrocycle in the mixed monolayers would be similar at ~ 48° and 39° for the pure monolayers. The situation for the mixed monolayers suggests that the porphyrin physical height would be less than the height of the background dodecanethiol SAM which has a physical height of ~ 14 Å. This model does not agree with the surface imaging experiments presented later in this chapter since it has been proven with AFM imaging that the porphyrin does indeed protrude above the background SAM. Due to this discrepancy, there is an inherent problem using the previous method[242] suggesting that this approach is just too simplistic for a molecule with two tethers to the surface.

5.3.3 X-ray Photoelectron Spectroscopy

A representative survey spectrum of the porphyrin thiol/dodecanethiol mixed monolayer is shown in Figure 5.4. High-resolution spectra of the C(1s), N(1s), and F(1s) regions show peak binding energies of 284.8 ± 0.1, 399.0 ± 0.1 and 687.0 ± 0.1 eV, respectively, while the high-resolution S(2p) signal can be fitted into two sets of doublets from the S($2p_{3/2}$) and S($2p_{1/2}$) components split by 1.2 eV. The two S($2p_{3/2}$) peaks are centered at 162.1 ± 0.1 and 163.7 ± 0.1 eV, respectively (Figure 5.5). The first

type of sulfur corresponds to the thiol chemisorbed onto the gold substrate while the second at higher binding energy can be attributed to the presence of the S coordinated to

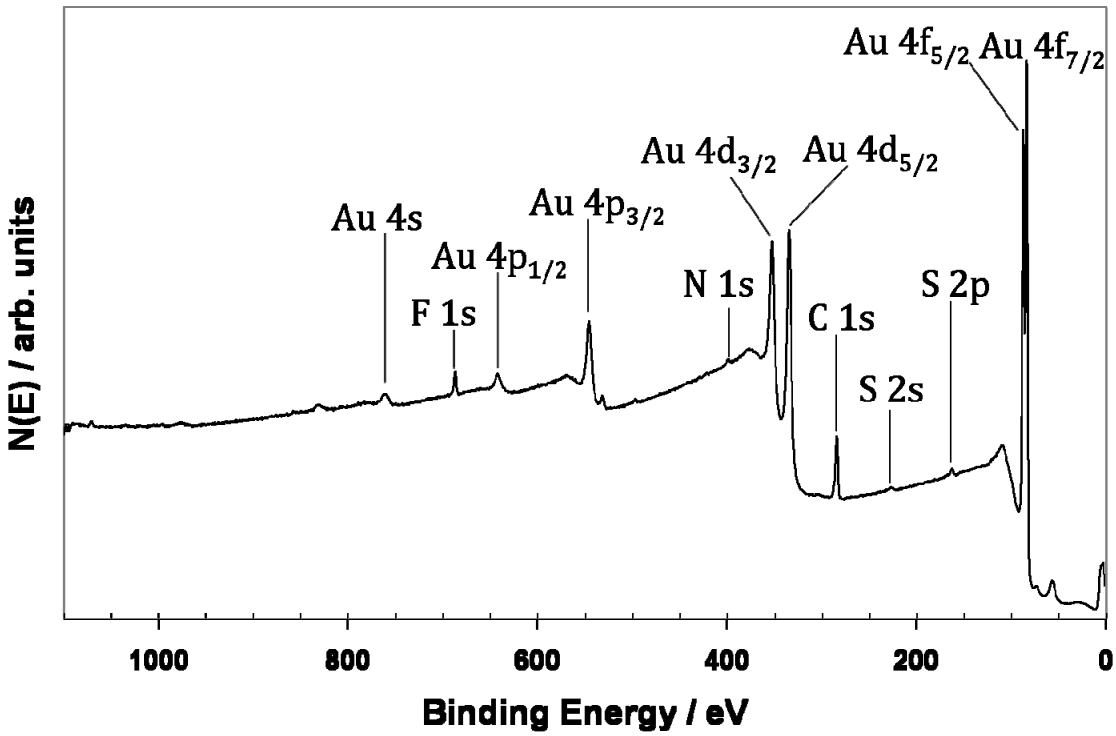

Figure 5.4. (mono Al source) X-ray photoelectron survey spectrum for 3 day free base cis-bipodal porphyrin thiol/dodecanethiol mixed monolayers on Au (111).

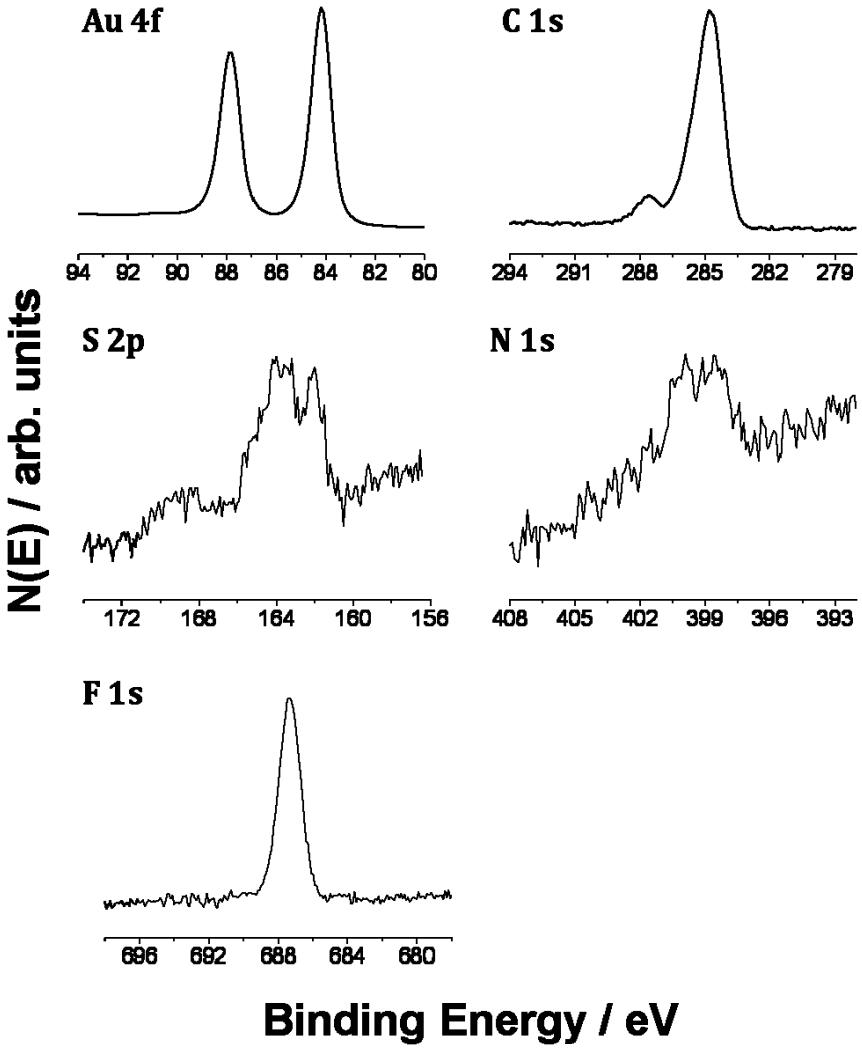

Figure 5.5. (mono Al source) High-resolution XPS for 3 day free base cis-bipodal porphyrin thiol/dodecanethiol mixed SAMs, showing the Au 4f, C 1s, S 2p, N 1s and F 1s spectral regions.

the tetrafluorophenyl ring. Both the C(1s) and S(2p) regions have smaller peaks at higher binding energies indicative of the presence of an oxide species present on the surface. The oxide species can either be from the cis-bipodal porphyrin thiol being

oxidized either in solution before deposition on the surface or after SAM formation being oxidized after exposure to ambient conditions while handling.

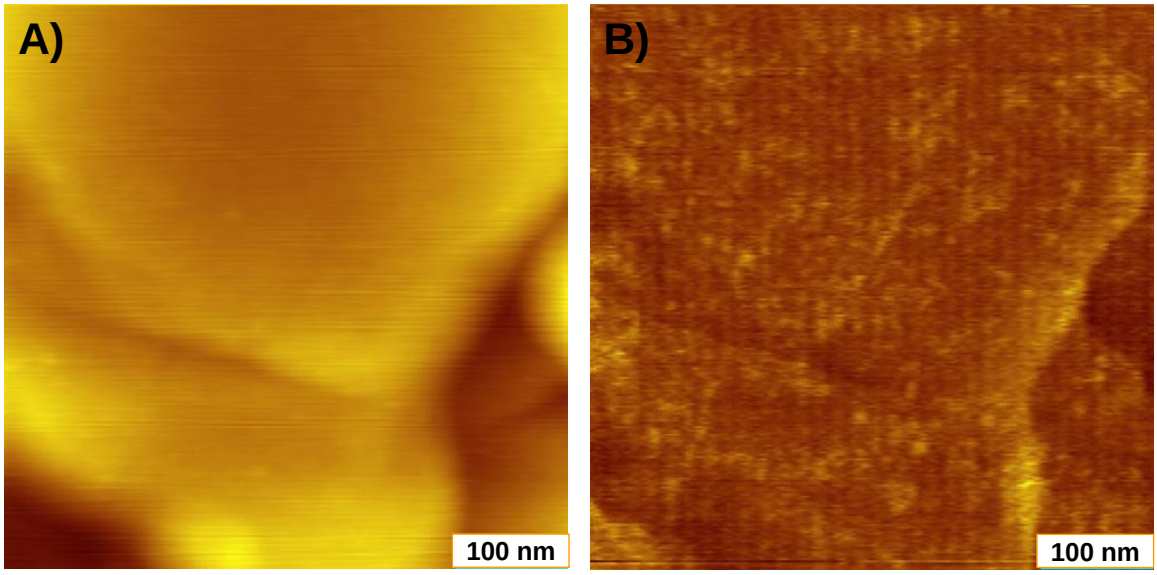

Figure 5.6. AFM images of 1 day free-base cis-bipodal porphyrin thiol/C12 mixed SAM, (A) topography and (B) friction.

5.3.4 Surface Imaging

In order to examine the surface structure of the inserted bipodal porphyrin assemblies, both atomic force and scanning tunneling microscopies were employed. AFM topography and friction images of the 1 day free base cis-bipodal mixed monolayer show clusters inserted into the dodecanethiol matrix (Figure 5.6), with the porphyrin molecules protruding from the dodecanethiol background by ~ 2 – 4 Å. The small clusters of the free base cis-bipodal porphyrin thiol molecules are clearly visible in

the UHV-STM images shown in Figure 5.7 where the apparent height ranges from ~ 1 – 1.5 nm and widths of approximately 8 nm. Single porphyrin molecules are also visible

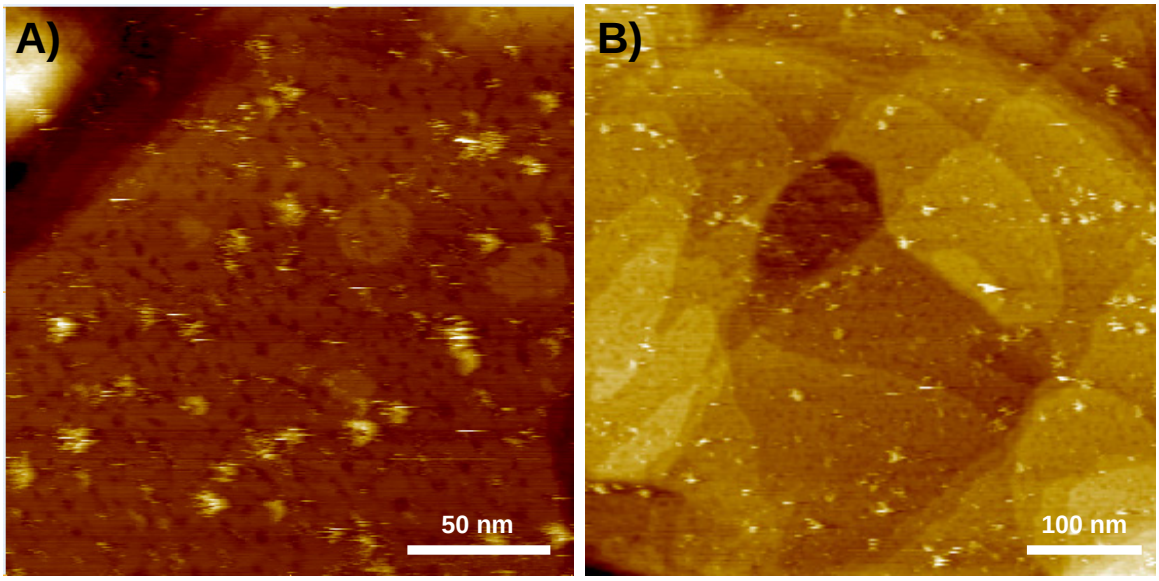

Figure 5.7. (A,B) Representative UHV-STM images of 1 day free-base cis-bipodal porphyrin thiol/DDT mixed SAM; imaging conditions: 1.4 V and 20 pA.

in the images which are only 3 nm wide with an apparent height of 6 Å. When the free base cis-bipodal porphyrin thiol molecules assemble on an open Au(111) surface, the entire surface was covered in the porphyrin assemblies after only 1 day of immersion as shown in Figure 5.8. There did not seem to be any long-range ordering, only large unresolved clusters as determined by STM. Since the aggregate size was on the order of ~ 5 – 10 nm after 1 day of immersion of the bipodal porphyrin thiol in the mixed SAMs, in order to increase the aggregate size, the immersion time was increased to 3 days. The

mixed monolayer of the 3 day cis-bipodal free base porphyrin thiol and DDT sample shows a marked increase in the physical height ranging from ~ 15 – 25 Å which could indicate a bilayer formation on the surface as evident in the AFM topography images shown in Figure 5.9. Instead of the aggregate size increasing in width, the bipodal

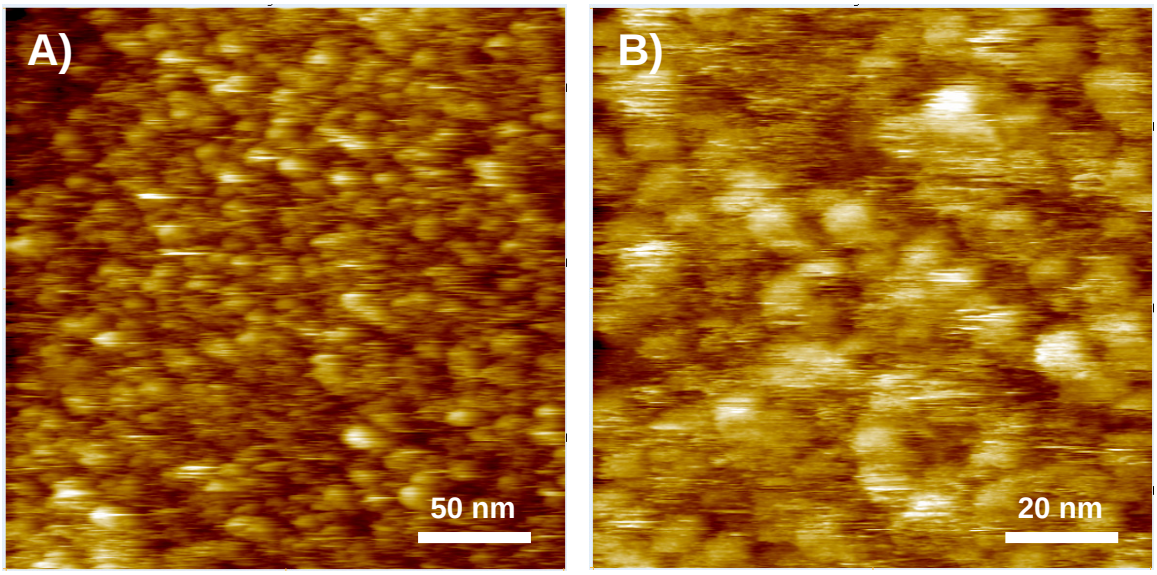

Figure 5.8. (A,B) Representative UHV-STM images of 1 day pure free-base cis-bipodal porphyrin thiol SAM; imaging conditions: 1.4 V and 20 pA.

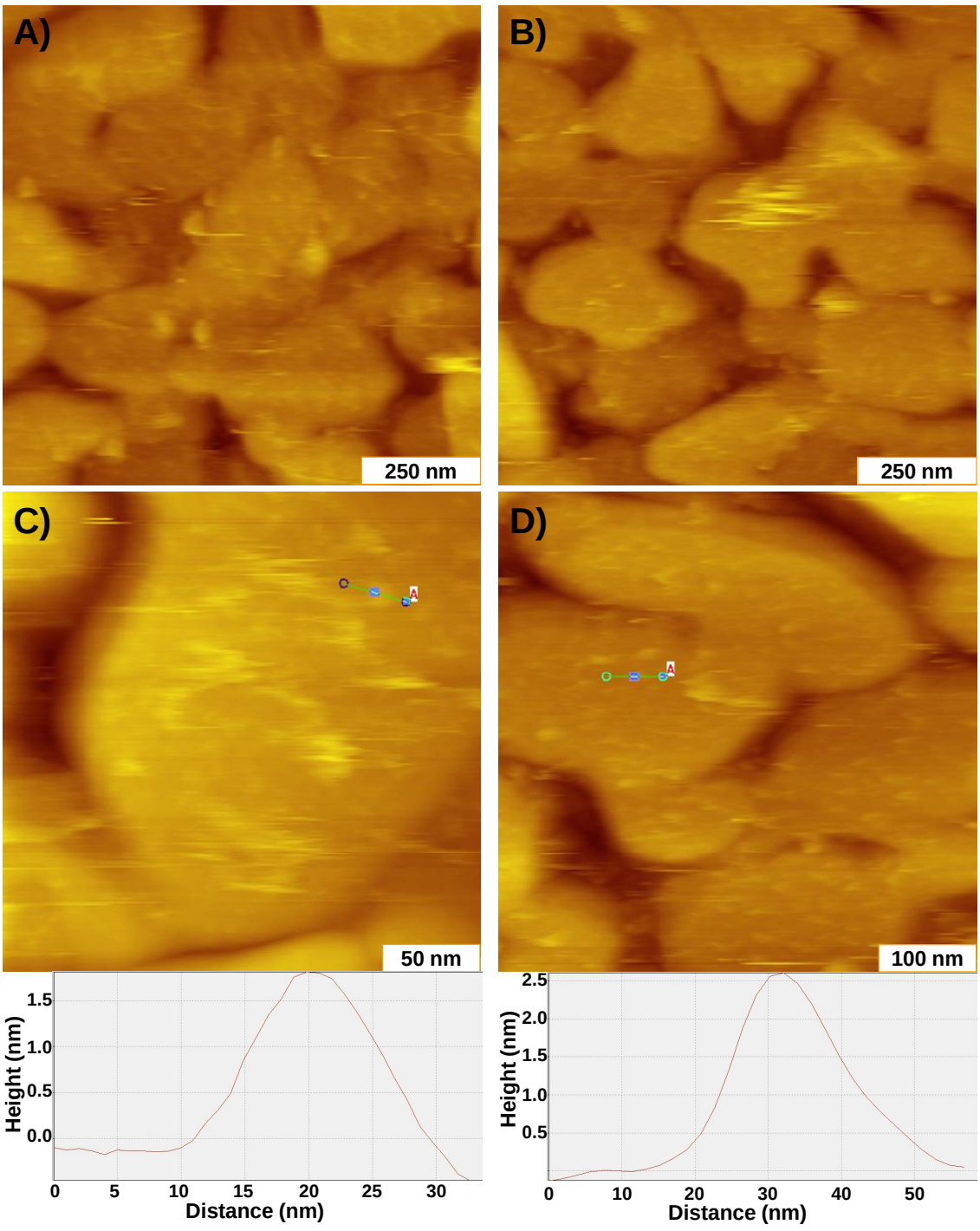

Figure 5.9. (A – D) AFM topography images of 3 day free-base cis-bipodal porphyrin thiol/C12 mixed SAM.

assemblies increased in height after longer soaking times. In the STM images (Figure 5.10A), it is easy to see that the 3 day assemblies are not larger aggregates, but rather similar in width to those after only soaking for 1 day. Instead of an increase in the size of each cluster, the number of clusters present after 3 days increased dramatically as shown in Figure 5.10A. The free base cis-bipodal clusters also increased in apparent height ranging from 1.5 – 2.0 nm which could also indicate a bilayer formation where the macrocycles interact face to face, but the bipodal tethers are pointing in opposite directions. Since the bipodal tethers make the molecule more sterically hindered from inserting into the pre-assembled dodecanethiol, but still have an affinity for each other, this could likely be a favored configuration. However, the bipodal bilayer assemblies in this configuration would not be very stable and after scanning with an STM tip for 1 hour, the number of aggregates on the surface has significantly diminished (Figure 5.10B). The STM tip can interact with the bipodal assemblies and alter their configuration essentially knocking them over which would explain the decrease in the number of molecules present in the STM image.

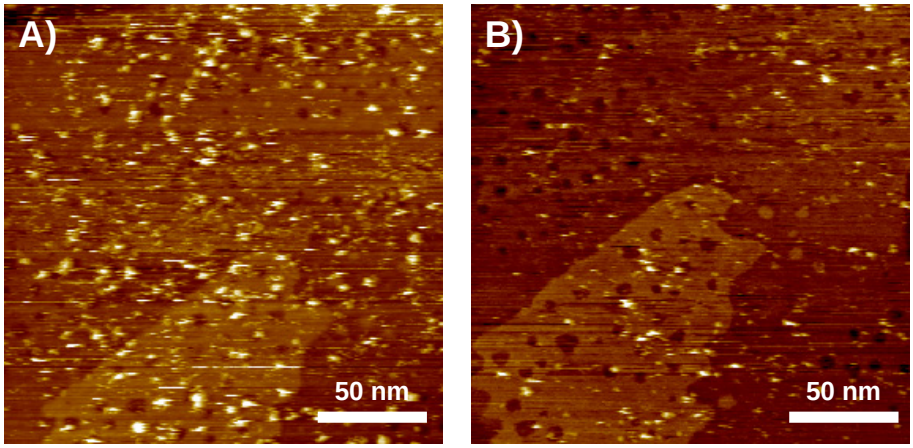

Figure 5.10. (A) Representative UHV-STM image of 3 day free-base cis-bipodal porphyrin thiol/C12 mixed SAM and (B) after 1 hour of scanning the same area; imaging conditions: 1.4 V and 20 pA.

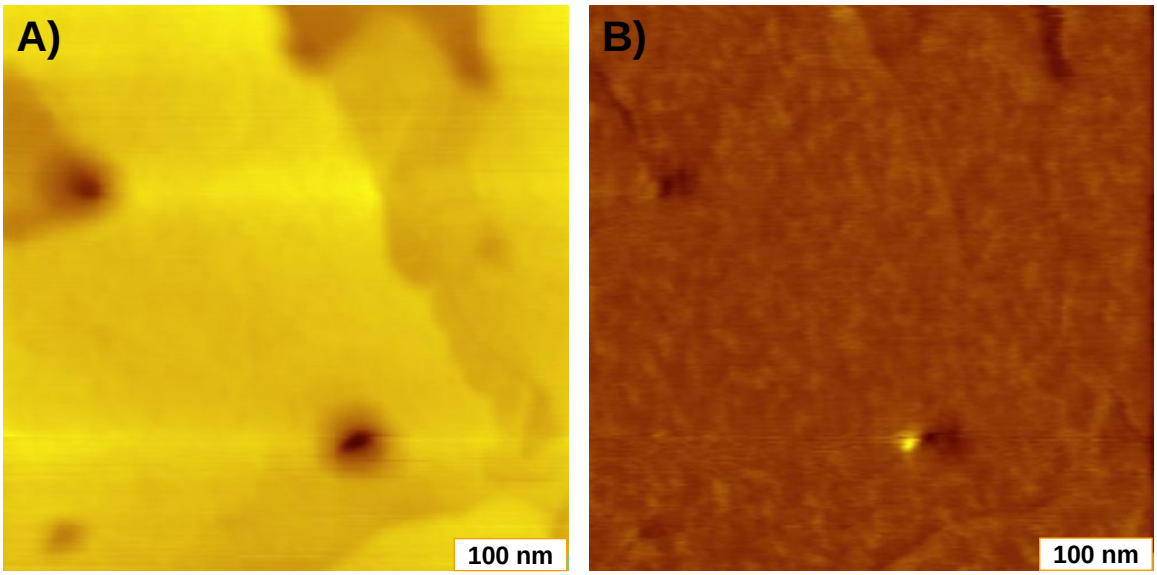

Figure 5.11. AFM images of 1 day zinc bipodal porphyrin thiol/DDT mixed SAM, (A) topography and (B) friction.

Since large clusters on the order of ~ 10 nm of the zinc monopodal porphyrin thiol exhibited interesting electronic properties such as bias-induced switching and Coulomb blockade at low temperatures, it was expected that by using a cis-bipodal zinc porphyrin thiol affording two tether attachment to the Au surface aggregation would increase and therefore the island size would form more consistently. However, this was not the case. In the topography and friction images in Figure 5.11, the assembly of the zinc bipodal derivative in the mixed SAM after 1 day does not show an obvious protrusion above the matrix SAM (Figure 5.12A) with a film thickness of approximately 1 nm as determined by nanoshaving a 100 nm^2 well (Figure 5.12B). The free base however did show a slight protrusion above the dodecanethiol which was similar to the monopodal porphyrin where the zinc and free base analog protrude above the dodecanethiol matrix by ~ 3 and 9 Å, respectively. The zinc molecules have a higher affinity to aggregate due to the added interaction of the zinc metal centers adding to the pi-pi stacking interactions and tend to have a lower physical height compared to the free base. The zinc bipodal derivative did show an increase in apparent height compared to the free base analog in the STM images shown in Figure 5.13. The apparent height, which is a convolution of the physical height and conductivity, of the small clusters in the 1 day mixed monolayers ranged from ~ 1.0 – 1.4 nm which is higher than the physical height determined from AFM. The increase in apparent height is likely due to the zinc metal center increasing the conductivity of the assemblies.

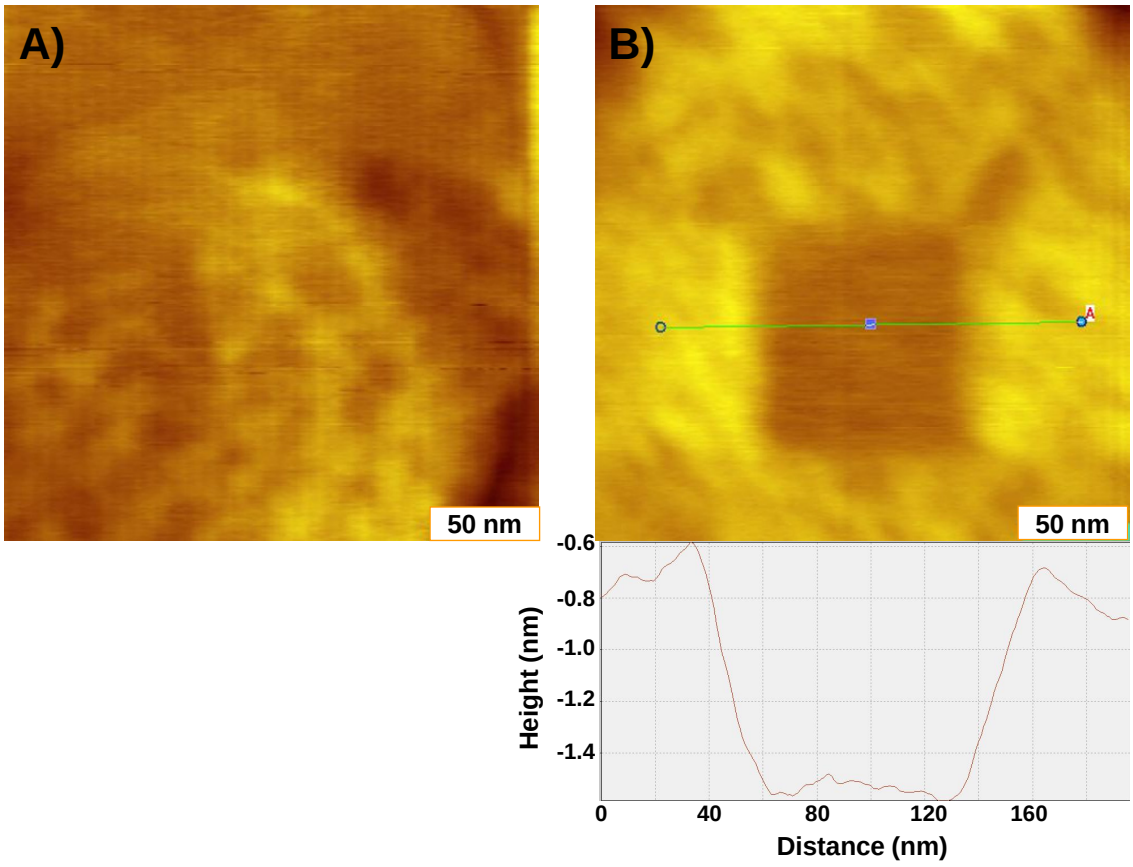

Figure 5.12. AFM images of 1 day zinc bipodal porphyrin thiol/DDT mixed SAM, (A) before nanoshaving and (B) after nanoshaving a 100 nm well.

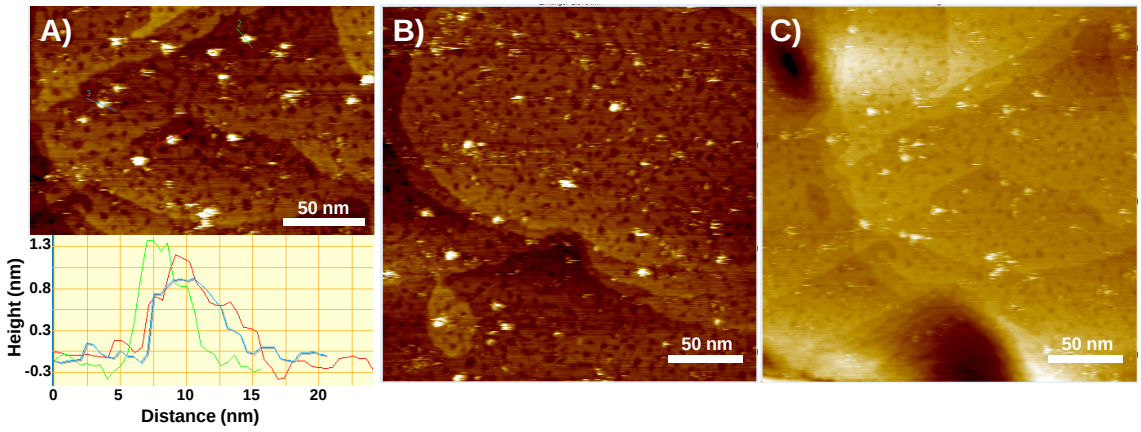

Figure 5.13. (A – C) Representative UHV-STM images of 1 day zinc bipodal porphyrin thiol/DDT mixed SAM; A, B and C imaging conditions: 1.4 V and 20 pA.

It is likely that the cis-bipodal assemblies did not create large clusters due to the steric interactions of the fluorophenyl groups which hindered the molecules from forming large aggregates. Since large aggregates were not observed, the effect of bias-induced switching was not observed either. In Figure 5.14, a cycling of the applied bias is shown from 1.4 V to 2.0 V, which is what was used to turn "ON" the clusters for the zinc monopodal porphyrin thiol. In their "ON" state, the clusters of the zinc monopodal derivative exhibited a higher apparent height due to an increase in their conductance. For the zinc cis-bipodal assemblies, the switching effect was not observed as seen in Figure 5.14 where there is no difference in the apparent height after increasing the bias

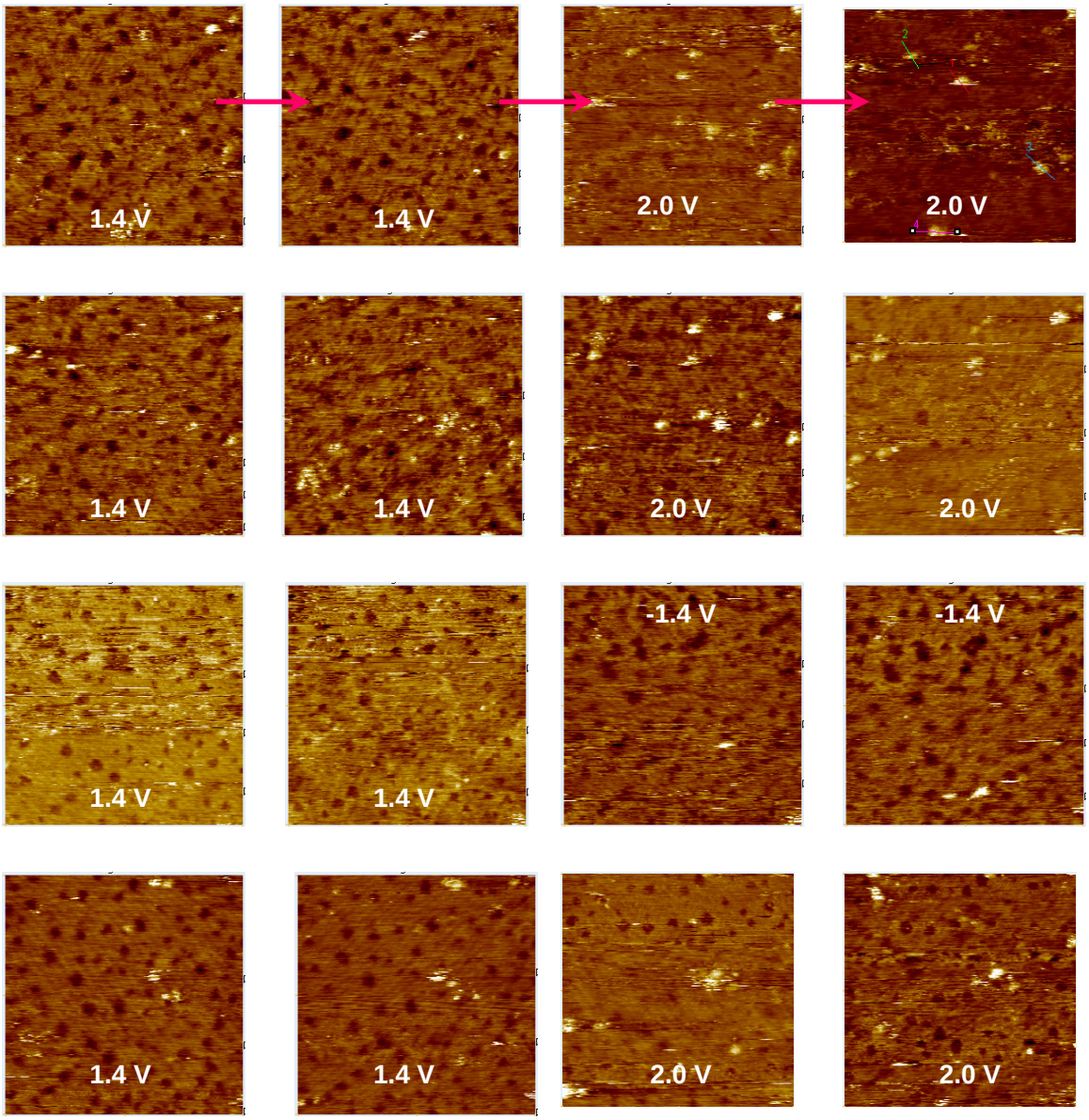

Figure 5.14. UHV-STM images of 1 day zinc bipodal porphyrin thiol/DDT mixed SAM: Switching cycle: 1.4 V to 2.0 V to 1.4 V to -1.4 V; I_{tunnel} = 20 pA.

from 1.4 to 2.0 V. This can be attributed to the fact that for the zinc monopodal assemblies, there are two apparent heights and therefore two molecular aggregate configurations of the molecules. One molecular aggregate, the lower conductance state, is an all face to face pi-stacking arrangement, and when the threshold bias is exceeded, the molecules can re-orient into a configuration where the pyridyl N interacts with the zinc metal center, also known as the higher conductance state. The latter and higher conductance state would be unlikely with the bipodal assemblies due to hindrance of the pyridyl N unable to interact with the metal center since there are two tethers anchoring the molecule to the surface. Since the zinc bipodal porphyrin thiol molecules are hindered from orienting in a way that allows them to switch on and off, increasing the aggregation or immersion time of these molecules would not be beneficial. The immersion time also did not affect the aggregate size which was observed for the free base analog as well. In Figure 5.15A and B, the immersion time of the zinc cis-bipodal porphyrin thiol in the dodecanethiol SAM was increased to 5 days and there was no significant increase in the width or apparent height of the molecules. The width was still ~ 8 nm with an apparent height of the clusters of ~ 1.2 nm (Figure 5.15B).

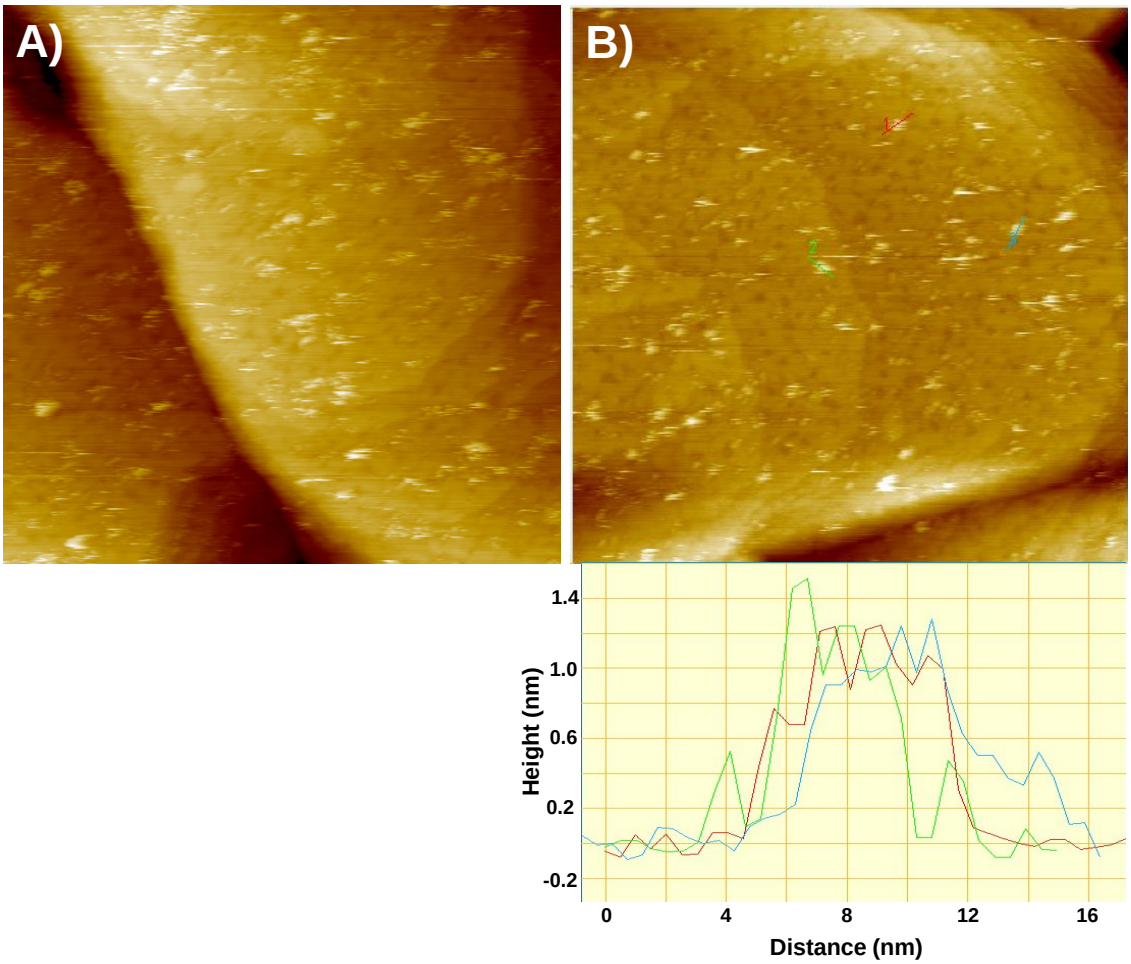

Figure 5.15. (A,B) Representative UHV-STM images of 5 day zinc bipodal porphyrin thiol/DDT mixed SAM; imaging conditions: 1.4 V and 20 pA.

5.4 Conclusions

It was anticipated that the cis-bipodal porphyrin thiol derivatives would form large clusters reminiscent of the zinc monopodal porphyrin thiol islands since there were two tethers for adsorption to the Au surface. It was predicted that the clusters formed with the bipodal porphyrin thiol would be consistent with those with the monopodal zinc

porphyrins with a pi-stacked arrangement. However, this was not the case and both the free base and zinc bipodal derivatives did not form aggregates larger than ~ 8 nm and the zinc bipodal derivative did not exhibit any interesting electronic properties such as bias-induced switching. Since there are two tethers to anchor the porphyrin to the Au surface, increased coverage of the molecules was also expected and was clearly evident in the pure monolayers on the surface, where complete coverage of the substrate was observed after 1 day of soaking the Au substrate in the free base bipodal porphyrin thiol. The free base bipodal derivatives were not stable in the mixed SAM since the molecules would disappear after imaging with the STM tip after 1 hour. Overall, the increase in the number of porphyrin thiol molecules on the surface was observed in the pure monolayers but not in the mixed monolayers since no large clusters were formed. The lack of aggregation of the cis-bipodal porphyrin thiol could be due to the bulkiness of the molecule, with two tethers in a cis orientation, preventing insertion of the molecules into the defects of the pre-assembled DDT matrix to form the Coulomb islands as was observed with the zinc monopodal derivative. Other derivatives will be investigated in the future, including the porphyrin thiol without an alkanethiol tether, in order to continue examining possible molecules with interesting electronic properties for molecularly-enhanced electronics.

CHAPTER VI

EMPLOYING SOLVENT EFFECTS IN NANOGRAFTING TO CONTROL PATTERNING OF NANOSCALE ASSEMBLIES

6.1 Introduction

In general, research focusing on the formation of nanostructures in the past decade has relied on various techniques with materials ranging from self-organizing polymer and molecular assemblies,[346-349] to proteins and other biomolecules[350-353] and even metallic nanostructures.[177,354,355] The ability to create ordered, reproducible molecular structures of nanoscale dimension is key to advancing the area of molecule-based nanoelectronics.[356] To actively integrate molecules into CMOS technologies, molecules must be able to be controllably organized onto surfaces with nanoscale precision, with feature sizes on the order of 10 nm.[357,358]

Scanning probe lithographies are becoming more frequently employed for the design and assembly of nanoscale structures on surfaces.[359-365] A range of scanning probe based patterning techniques have been used to create nanoscale molecular structures and patterns on surfaces including nanoshaving, nanografting,[366-368] Nanopen Reader and Writer (NPRW)[238] and Dip Pen Nanolithography (DPN).[239] While there are many other derivative scanning probe based patterning methods,[369-371] here we will focus on force-induced types of nanofabrication using Atomic Force Microscopy (AFM). Among these fabrication approaches, DPN is perhaps the mostly broadly employed. In DPN, an AFM tip coated with the molecule of interest is brought into contact with the

substrate and through capillary forces the molecules are then "inked" onto the surface where the AFM tip contacts the support. Structures fabricated by DPN are generally formed in ambient environments and factors such as the writing speed and ambient humidity can dramatically impact the resolution of the structures formed. As such, for patterns of self-assembled monolayers such as alkanethiols on Au, feature sizes are typically limited to *ca.* 20 – 50 nm due to molecular diffusion.[9,372,373] One way to mitigate the effects of diffusion at the interface and decrease feature size is to pattern directly into a surface bound host matrix such as a molecular monolayer. Here, approaches such as nanoshaving and nanografting have been shown to be capable of resolutions below 10 nm. In nanoshaving, a structure is formed when a force is applied by the AFM tip to a surface covered with a host matrix (such a molecular monolayer), which is displaced under the load into a solvent capable of solubilizing the matrix molecules once they are displaced. Following shaving a hole, or nanowell, of exposed underlying substrate remains which can then bind new molecules into the fashioned feature. Nanografting is similar to nanoshaving, however, in lieu of just a solvent as the background, nanoshaving is carried out in the presence of a new molecule, such that as the matrix molecules are removed; new molecules from solution are bound to the surface where the shaving took place forming a pattern on the surface. Depending on the size of the newly inserted molecules from solution, negative or positive patterns with respect to the background molecules can be formed depending if the grafted molecules are shorter or longer, respectively.[366,374] In both nanoshaving and nanografting methods, the AFM tip displaces the matrix molecules when the contact load between the tip and substrate is

sufficiently high to break the molecule-substrate bonds of the matrix molecules. While nanografting is most commonly performed in contact mode, it can also be performed in tapping mode which allows for reduced shear by the AFM tip to aid in mitigating damage of the newly grafted molecules.[375] NPRW combines nanografting with DPN and uses a precoated tip to displace background molecules, which are replaced with the molecules from the tip.

In this chapter, molecular assemblies will be created using controlled patterning techniques in two different solvents, ethanol and one with a lower vapor pressure, 3-phenyl-1-propanol. Undesirable surface displacement of molecules, which can be an issue when creating patterned arrays with an AFM tip, is avoided by controlling the type of solvent, concentration of the grafted molecules, and the loading force during the patterning process. Since nanografting is a lithographic technique that can achieve precise and reproducible patterns,[376] we have employed nanografting in this chapter to manipulate molecules into ordered arrays on a Au surface to create a nanoscale test array. Specifically, nanografting of 16-mercaptohexadecanoic acid (16-MHA) in a dodecanethiol (DDT) self-assembled monolayer (SAM) on Au surfaces is performed in two different liquid media, ethanol and 3-phenyl-1-propanol (3P1P), to compare displacement of the matrix molecules as well as the resulting patterned nanoscopic structures.

6.2 Experimental

6.2.1 Preparation of Self Assembled Monolayers (SAMs)

All patterning experiments were carried out on Au(111)/mica substrates (Agilent Technologies, Inc., Santa Clara, CA) which consisted of ~150 nm flame-annealed gold films on mica. *n*-dodecanethiol (DDT, 98% purity), 16-mercaptohexadecanoic acid (16-MHA, 90% purity), and 3-phenyl-1-propanol (3P1P, 98% purity) were purchased from Aldrich; glycerol (ACS grade) was purchased from EMD chemicals and ethanol (200 proof) was purchased from Pharmco-AAPER, and all chemicals were used as received. Before each experiment, all Au(111) substrates were treated with UV/ozone for 20 min, followed by rinsing the gold film in sequence with high purity (18.2 MΩ•cm) water (NANOpure Diamond, Barnstead), ethanol, and then dried with streaming nitrogen. SAMs of *n*-dodecanethiol were formed by immersion of the Au films in 1 mM *n*-dodecanethiol/ethanol solution for 24 h followed by rinsing liberally with ethanol and blown dry with streaming nitrogen.

6.2.2 Atomic Force Microscopy (AFM)

AFM images were acquired with a Molecular Imaging 4500 Pico SPM (Agilent, Santa Clara, CA) with a deflection-type detection scanning head interfaced with an SPM1000 Revision 8 control electronics (RHK Technology Inc., Troy, MI). All AFM imaging and nanografting experiments were carried out in contact mode under liquid environment using commercially available Si_3N_4 AFM tips (Veeco/TM Microscopes, Sunnyvale, CA) with nominal tip radii of ~ 10 nm and nominal spring constants of ~ 0.5 N/m. For quantitative measurements, calibration of the tip dimensions were carried out

using Au(111) substrate step edges and blind tip reconstruction provided with Scanning Probe Imaging Processor, SPIP, software. Both methods were consistent yielding a tip radius of ~ 25 nm. The spring constants were estimated using the Sader method which uses the resonance frequency of the tip and quality factor of the cantilever.[377]

6.2.2.1 Nanografting

Before a nanografted pattern was created with the AFM tip, first the optimized force was determined by nanoshaving. Here, the optimized force was defined as the minimum applied force required to reproducibly create a uniform shaved well by removing the DDT molecules without disrupting the gold surface layer. Imaging forces ranged from 16 to 25 nN in ethanol and 7 to 20 nN in 3P1P while fabrication nanografting forces ranged from 57 to 90 nN in ethanol and 35 to 58 nN in 3P1P. The forces in ethanol were much higher for fabrication due to a spring constant of 1.07 N/m compared to 0.51 N/m in 3P1P. Both tips were nominally 0.5 N/m, however as indicated by the manufacturer there is always a range that the tip spring constant can fall in between. Each of the nanografted assemblies was patterned with the AFM tip by manually determining the position and size of the feature to be fabricated with a resolution of 256. For the contact radius to line step (CRLS) ratio analysis, the tip radius of curvature was determined to be 23 nm and the cantilever spring constant (k) determined from the Sader method was 0.47 N/m. The loads for imaging and nanografting were determined using the spring constant of the tip, the force-distance measurements on the matrix SAM, and any additional loading imparted on the tip. The average load for imaging in 3P1P was ~ 7 nN while for nanografting the average load

was determined to be ~ 36 nN. The values of the Poisson ratio (ν_i) and Young's modulus (E_i) for the Si_3N_4 cantilevers[378] are 0.24 and 220 GPa and for the Au substrate[379] are 0.3625 and 62.5 GPa, respectively. Using these values, the CRLS ratio can be determined using the calculated contact radius (a) divided by the line step (LS).[380] The line step is described as the length of the nanografted structure in the slow scan direction divided by the resolution (256 for our experiments). Using the values listed above, the contact radius is calculated to be 1.29 nm during imaging and 2.26 nm during nanografting. If the CRLS value is less than or equal to 0.5 then there is no overlap of the AFM tip within the nanografted region. For a typical 100 nm nanografted square, the LS is 0.39 nm and the CRLS value is well above the threshold for the nonoverlapping limit. If there is no control over the line spacing, the AFM tip will overlap several times in the nanografted region. In order to circumvent this issue, the overlap can easily be controlled using lithography software or manual scripting techniques to design specific line spacing parameters during nanografting. We have controlled the line spacing in nanografting experiments in 3P1P where the density of the assembled structure is controlled through a script to designate the value of the spacing between each line sweep by the AFM tip. The line spacings have been designated from 1 to 5 nm in 1 nm increments. This has successfully allowed for CRLS values above the nonoverlapping limit, i.e. above 0.5, at 1, 2, and 3 nm line spacings; a CRLS value of ~ 0.5 at 4 nm line spacing and a CRLS value of less than 0.5 at 5 nm line spacing which prevents the AFM tip from overlapping inside the nanografted region. From this

variation in line spacing, the densities of the 16-MHA molecules in the assembled nanografted structures can be varied.

6.3 Results and Discussion

Some challenges that are typically faced when creating nanostructures are reproducibility, consistency in formation and shape, as well as insertion of foreign molecules or non-specific binding. Reproducibility and consistency can be controlled using a directed assembly approach such as nanografting as compared to self-assembly where the molecules naturally form structures of different size and shape depending on their interaction at the surface. Using nanografting, the shape and size of the nanostructures can be easily controlled using AFM lithography software, but the size of the patterned regions are typically on small scales on the order of microns, whereas patterning using particle lithography or template-based lithography can produce more macroscale size patterns. Nanografting allows for more precise control at the molecular level, and we have been able to fabricate precise patterned structures of monolayers or bilayers from ~ 10 to 100 nm. By choice of solvent, we can either produce an assembled bilayer of 16-MHA or insertion of single 16-MHA molecules into the DDT matrix.

To explore the impact of solvents on the assembly of molecular nanostructures, self assembly versus nanografting experiments were performed of 16-MHA into DDT in ethanol and 3P1P. Here we examined the ability to control the position of the molecules and the quality of assembled 16-MHA structures that could be formed in a DDT matrix. We also compared the self and directed assembly of 16-MHA by first nanoshaving a

well into the DDT SAM and then allowing the 16-MHA to assemble in that well to the fabrication of a 16-MHA structure by directed nanografting for both solvent systems.

Nanografting experiments were performed to investigate the construction of 16-MHA bilayer structures in a controlled fashion using ethanol and 3P1P at four different concentrations of 16-MHA: 0.5, 1, 2, and 5 mM. Imaging loads for both solvents ranged from ~ 6 – 20 nN due to the stiffness of the lever and jump to contact forces high enough to maintain engaged contact with the surface. These loads are higher than the typical AFM imaging forces which tend to be less than 1 nN to maintain SAM quality. Often fabrication forces for force-induced nanofabrication experiments range between 2 – 20 nN,[369,374,376] however, much higher loads ranging between 35 – 90 nN for nanografting 16-MHA in both solvents have been implemented. Again, these forces were determined based on the experimental nanofabrication force needed to completely remove the matrix DDT SAM during nanoshaving prior to nanografting for each concentration. An increase in load is also required to account for blunter AFM tips. The applied loads used for nanografting in ethanol produced bilayer structures for all concentrations of 16-MHA, but when the 16-MHA molecules were flown into the AFM liquid cell, the 16-MHA molecules naturally self-assembled as monolayer structures into the prefabricated shaved wells. Nanografted assemblies have been known to produce different structures than compared to the natural self assembly of the same molecules on open surfaces or in confined spaces.[367,381-383] Consistent with Liu and coworkers,[381,383] the kinetics were altered when the 16-MHA molecules were grafted into a confined region. With the concentrations and fabrication forces used during the nanografting process of these

experiments, the 16-MHA was driven to form assemblies of bilayers. The directed assembly, i.e. nanografted, patterns of 16-MHA squares in ethanol had a diverse range of physical heights between the center of the square compared to the outer lying edges, which is typical since the tip spends more time scanning the edges during the nanografting process. The non-uniform patterned squares are shown in Figure 6.1 A - D where it is evident that the 16-MHA molecules are inserted into the background DDT monolayer.

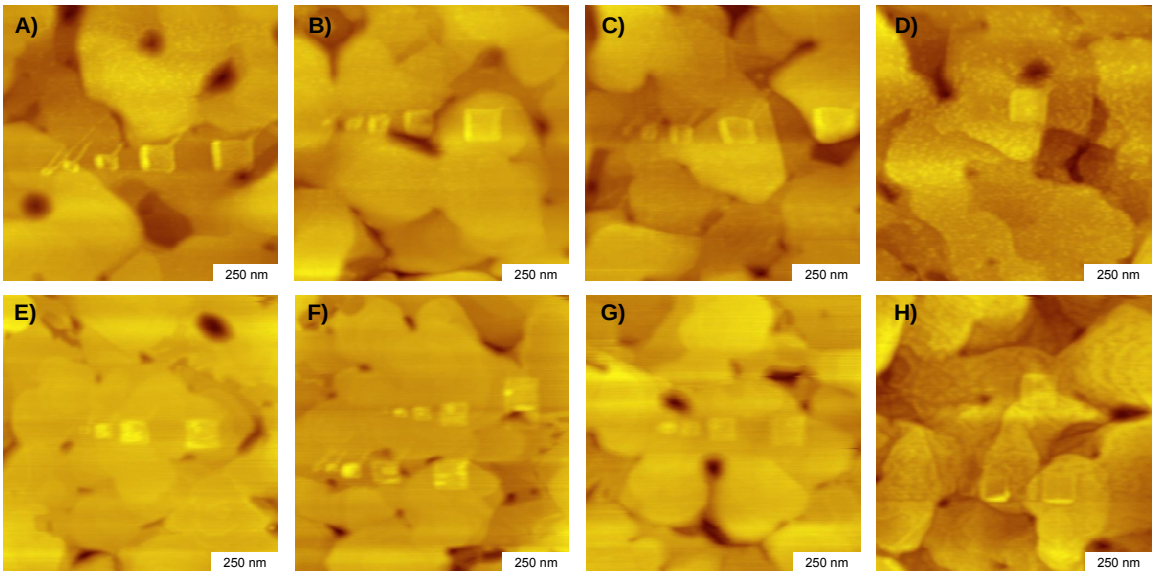

Figure 6.1. (A – H) Nanografted 16-MHA squares in DDT matrix (A – D) in ethanol and (E – H) in 3P1P. (A, E)- 0.5 mM 16-MHA; (B, F)- 1 mM 16-MHA; (C, G)- 2 mM 16-MHA; (D, H)- 5 mM 16-MHA.

For all four concentrations of 16-MHA in ethanol, the 16-MHA molecules insert into the background DDT SAM, and the insertion was observed in the AFM image immediately after the nanografting process. Two plausible explanations for insertion of the 16-MHA molecules are either the DDT matrix molecules are being displaced from their original position on the Au surface but remain bound to the Au or the DDT molecules are being replaced by the newly inserted 16-MHA. It has been shown in previous studies that 1-adamantanethiol molecules are displaced by alkanethiols on Au(111) surfaces due to lack of intermolecular stabilization and weakened Au-molecule bonds as compared with the alkanethiols.[384] It is believed in our case that the 16-MHA inserts into the defects of the DDT matrix and forms a more stable SAM from the increased van der Waals interactions of the longer alkyl chain of the 16-MHA molecules compared to DDT.[385,386] We have seen evidence of 16-MHA displacing DDT molecules of a pre-assembled SAM when the DDT SAM was immersed into a 5 mM solution of 16-MHA. After approximately 1.5 hours, the DDT SAM was imaged in situ with AFM and then removed and imaged in an ultra-high vacuum scanning tunneling microscope. The insertion took approximately 1.5 hours compared to instantaneous insertion with disruption of the DDT with the AFM tip. The 16-MHA inserted as small clusters and even bilayers which has been determined by AFM physical height measurements. The difference in the insertion assembly is most likely due to the AFM tip which causes a weakening (defects in the packing) of the DDT SAM allowing for the 16-MHA molecules to immediately penetrate into very small regions of the SAM and slightly displace the location of the DDT molecules. The STM images in Figure 6.2 show areas

of 16-MHA which appear bright compared to the DDT as well as a reorganization of the background DDT molecules into the more densely packed c(4 x 2) phase instead of the more common (√3 x √3)R30° structure. A more densely packed lattice suggests that the 16-MHA molecules are inserting into the DDT SAM and not replacing them.

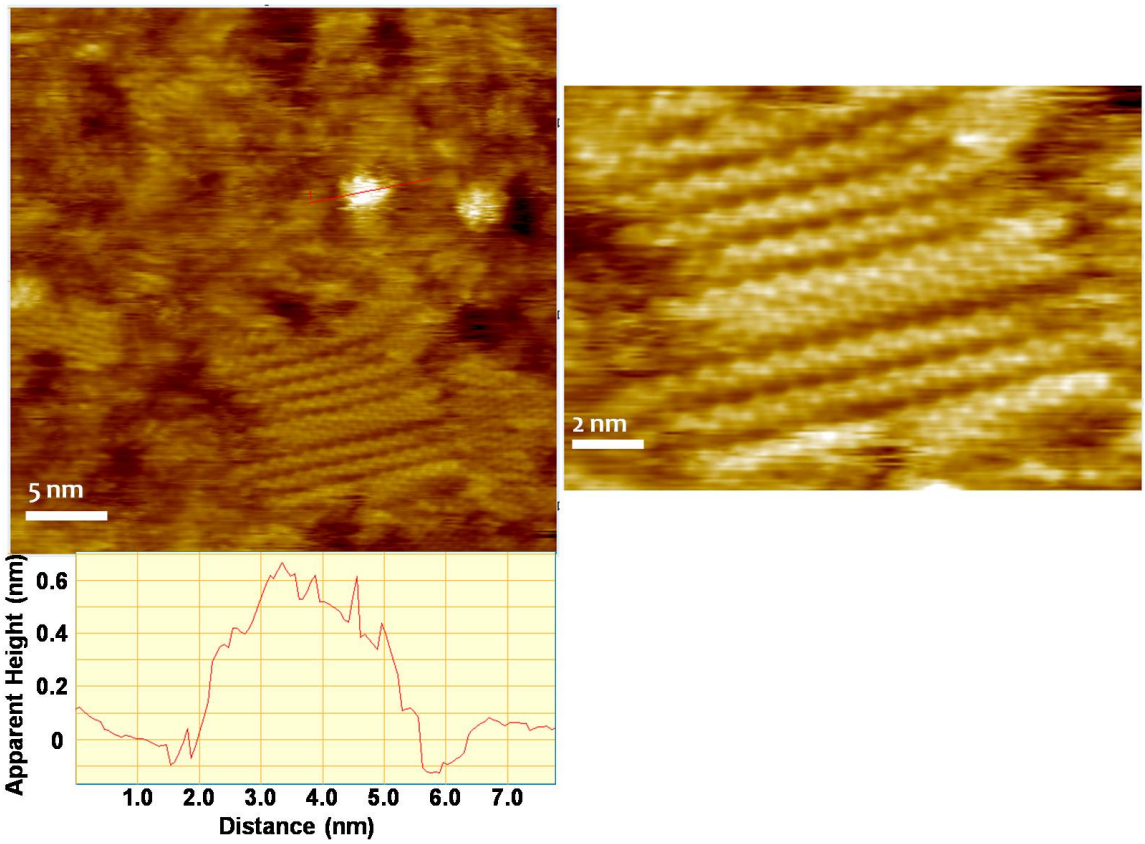

Figure 6.2. UHV-STM image of bright clusters of 16-MHA bilayers inserted into a DDT SAM and magnification of the compressed c(4 x 2) DDT lattice on the right.

In 3P1P, the 16-MHA molecules also formed bilayer structures from nanografting and monolayers during self-assembly into the preshaved nanowells, and this is shown in Figure 6.3 A & B. To explore self-assembly of 16-MHA into an open well versus nanografting in a confined region, a nanowell of 100 nm in dimension was formed by shaving away DDT matrix molecules with the AFM tip. At that point, 16-MHA was introduced into the AFM liquid cell and the nanowell was filled with a monolayer of 16-MHA (Figure 6.3A). The same size nanowell was grafted next to the open well where a structure formed that was physically higher than a monolayer (Figure 6.3B). This is the bilayer structure which is stabilized through hydrogen bonding of carboxylic acids of two 16-MHA molecules (schematic shown in Figure 6.3C). The exact molecular tilt angle is unclear at this time due to the height variations of the double

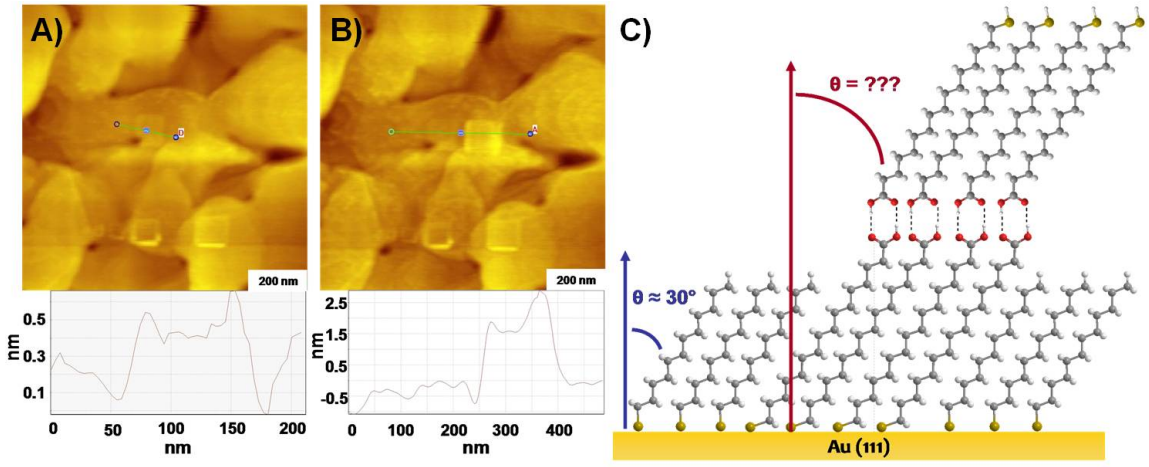

Figure 6.3. (A) Nanowell filled with monolayer of 16-MHA. (B) Nanografted bilayer of 16-MHA next to preshaved nanowell. (C) Schematic of 16-MHA bilayer structure formed inserted into DDT background (Grey- carbon, White- hydrogen, Yellow- sulfur, Red- oxygen).

layered structures when patterning in the two solvents. However, as the assembly of the 16-MHA becomes more densely packed, the tilt angle of the molecules will shift to a more upright configuration which is consistent with the model of alkanethiol self-assembled monolayers on Au which begin predominately lying down and stand up as the packing density increases.[161] Evidence from the literature shows that multilayer structures have also been formed for dithiol molecules grafted into an inert SAM.[387] Another group has observed nanografted bilayer carboxylic acid structures in ethanol and aqueous media that can be manipulated to form acid terminated monolayer grafted assemblies by controlling the concentration of the solution.[388] In our case, to prove a bilayer was actually formed during the nanografting process, the same experiment was repeated, but after the square was grafted into the DDT matrix, a basic solution of 18.27 % (v/v) of glycerol/water (pH ~ 10) was introduced into the liquid cell where the bilayer structure was destroyed as shown in the sequence of images shown in Figure 6.4. If an acidic glycerol/water solution (pH ~ 3) was introduced, the bilayer structure remained intact through H-bonding of the terminal acid groups.

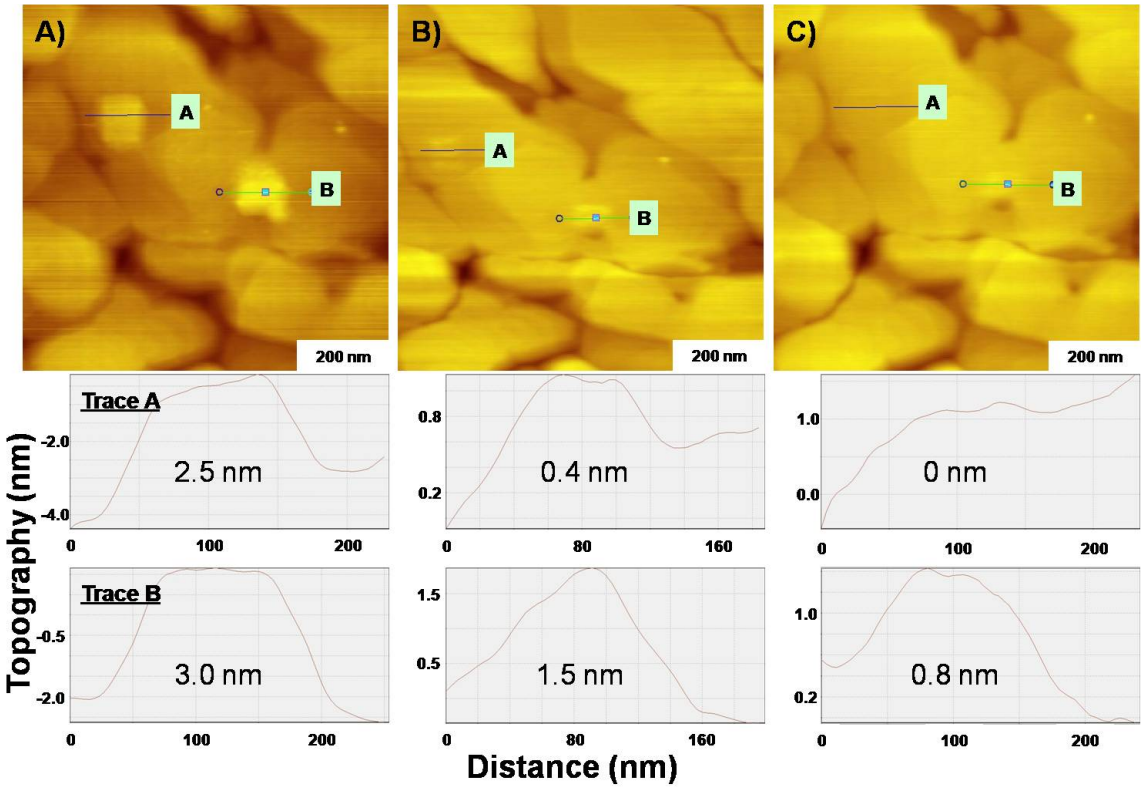

Figure 6.4. Nanografted squares in DDT matrix in ethanol solvent (A) before adding basic solution, (B) first image immediately after adding base and (C) second image after adding base. *Note: The values listed inside the line trace boxes are the approximate physical heights of the squares.*

Experiments were performed in 3P1P to change the density of 16-MHA molecules inside the nanografted squares using line spacings from 1 to 5 nm. Previously, similar studies have been done with nanografting 16-MHA in ethanol at different line spacings which showed that more densely packed nanografted squares at smaller line spacings showed higher friction contrast compared to the background SAM.[389] It was confirmed from our experiments that the physical height of the square

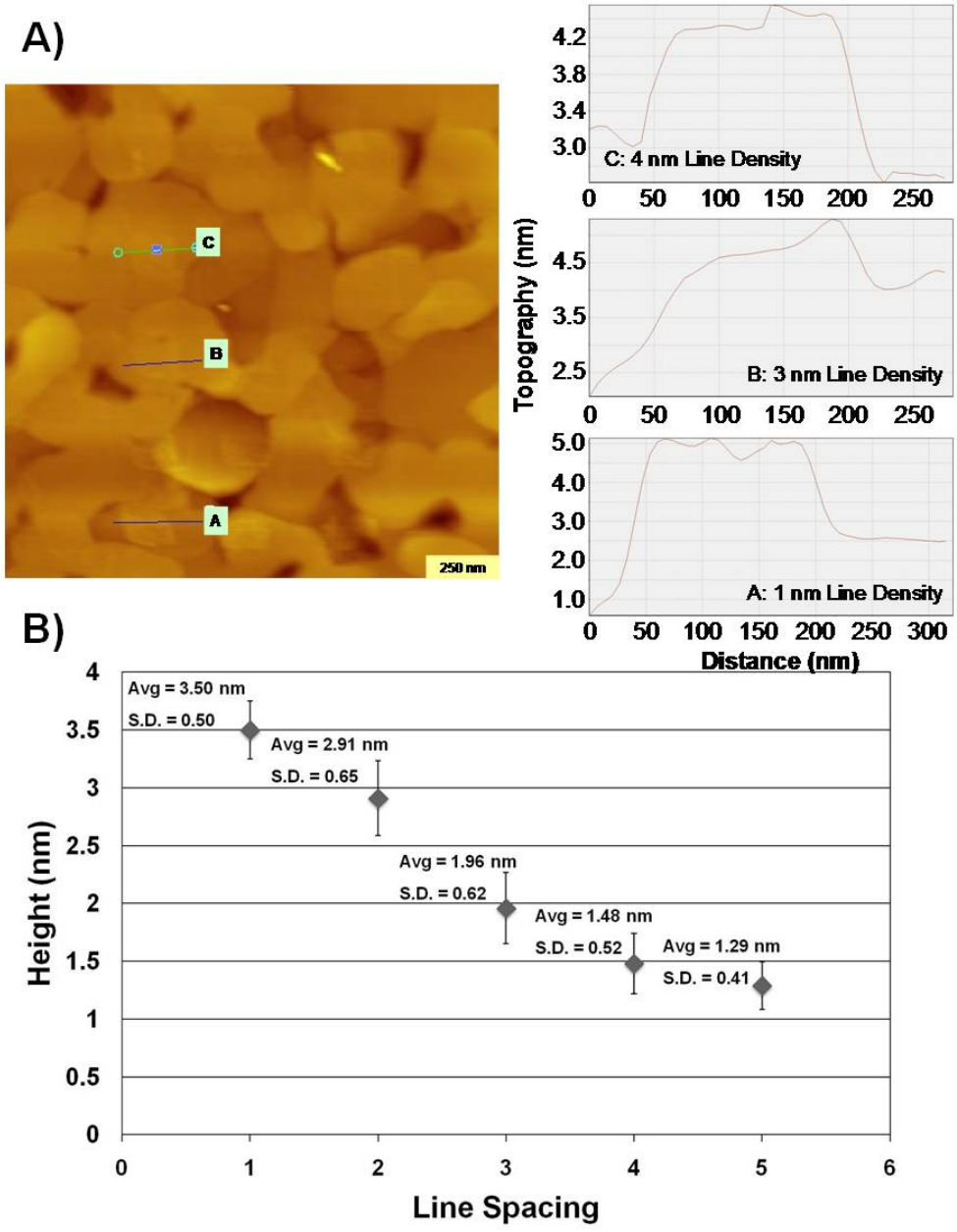

Figure 6.5. (A) Representative AFM topography image of nanografted squares with decreasing line density A → C and corresponding line traces. (B) Average height and standard deviation plot of nanografted squares with line density from 1 to 5 nm. Averages are from at least 18 different nanografted squares.

increases with smaller line spacings. Bilayers of 16-MHA are more prominent for squares grafted with a smaller line spacing, i.e. 1 nm (see Figure 6.5). A plot of the average physical height of the nanografted squares is shown in Figure 6.5 for line spacings of 1, 2, 3, 4 and 5 nm inside a 100 nm square. The average height increases with the increasing number of scanned lines (i.e. the lowest line spacing of 1 nm) inside the nanografted assembly. The increasing height of assemblies from 5 nm to 1 nm line spacing was due to the formation of more densely packed bilayers, and patterns of 16-MHA with similar heights have been formed using NPRW as well.[388] Therefore, monolayers are not formed inside the nanografted squares of 16-MHA as compared with self-assembly of the molecules due to the high density of lines scanned by the AFM tip creating densely packed bilayers during the nanografting process. Applying a CRLS analysis[380] confirms these findings. Since the contact area of the tip is 2.26 nm during nanografting with an applied load of ~ 36 nN, we can determine that the AFM tip will overlap inside the nanografted region with the 1, 2 and 3 nm line spacings. At these line spacings, we get a CRLS value of 2.26, 1.13, and 0.75 which are all above the threshold value of 0.5. With the AFM tip overlapping while scanning inside the nanografted square, the matrix DDT should be completely removed from the surface with the most amount of matrix molecules removed at the smallest line spacing. With these three line spacings, the 16-MHA molecules have free range to assemble into the entire open area behind the scanning AFM tip which accounts for the more densely packed structures. With a 4 nm line spacing, the CRLS value was determined to be 0.57 which indicates the AFM tip is only slightly overlapping, so most of the DDT should be removed, although

some molecules may remain causing the nanografted 16-MHA square to not be as densely packed. At 5 nm line spacing, the CRLS value was 0.45 which is consistent with the AFM tip not overlapping inside the nanografted region. In this case, there are still DDT molecules present inside the patterned assembly making the 16-MHA more sparse and produces a lower physical height structure.

A benefit of nanografting in 3P1P was that the patterned squares at lower concentrations, i.e. 0.5, 1, and 2 mM, were slightly more uniform when compared to the molecular structures in ethanol. The nanografted squares for all four concentrations of

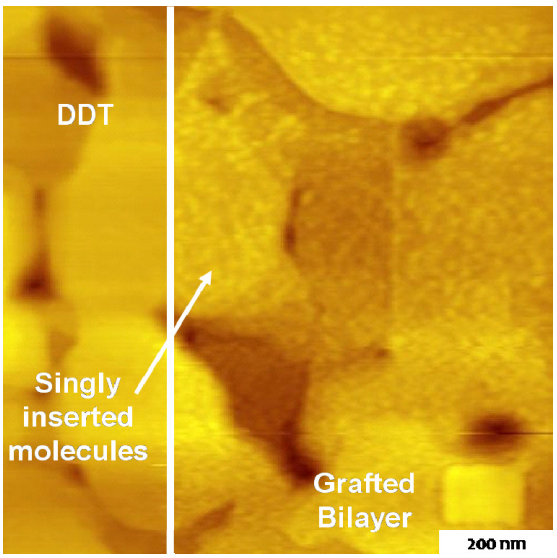

Figure 6.6. Testbed for singly inserted 16-MHA molecules (arrow), grafted ensembles, and DDT matrix.

16-MHA fabricated in the more viscous solvent resemble more densely packed structures in the area inside the squares which is evident in Figure 6.1 E - G where the edges are the same height as the rest of the square. Another noticeable difference for nanografting experiments performed in 3P1P was that the 16-MHA molecules inserted into the background DDT matrix with only the highest concentration of 16-MHA at 5 mM. At lower concentrations of 16-MHA in 3P1P, i.e. 0.5, 1, and 2 mM, the 3P1P solvent acts as a barrier and prevents the 16-MHA from insertion into the matrix SAM. Prior to our present studies, it was believed that 16-MHA inserted into the DDT matrix over the entire gold substrate; however we have noticed that with the exception of long immersion times, insertion only occurs where the tip has been previously scanning for both the ethanol and 3P1P experiments. In Figure 6.6, the matrix DDT SAM is still intact and there is no evidence of insertion where the tip was not previously scanning the image even with the 5 mM concentration of 16-MHA in ethanol. Therefore, since the insertion into the matrix DDT seems to be largely affected by the AFM tip disturbing the pre-assembled SAM matrix as was discussed earlier, the 3P1P must be providing a barrier for insertion of foreign molecules. Since 3P1P has an alkyl chain, the methylene groups can interact with the DDT SAM and we have determined that approximately 7% of 3P1P intercalates into the DDT matrix. It was determined with the ethanol experiments that insertion of the self-assembled 16-MHA will occur but over a longer period of time if undisturbed by the AFM tip. However, large clusters of 16-MHA molecules were observed after self-assembly into the DDT whereas with the AFM tip disturbing the SAM, single molecules can penetrate and displace the DDT. The average

height of each of the inserted 16-MHA molecules was approximately 0.7 nm and the average width of the structures was ~ 40 nm as determined by AFM topographical images. By reconstructing the tip shape using the step edges of the gold substrate,[390,391] the full width at half maximum (FWHM) radius of the tip was ~ 25 nm. Looking at the model shown in Figure 6.7A, the inserted 16-MHA features are most likely singly inserted molecules or clusters of a few molecules. The blue dotted line in Figure 6.7 represents the line trace of the AFM tip, which shows that a single inserted 16-MHA molecule would appear to be approximately 40 - 50 nm in width which is what is observed in the images and is the limit of our resolution with the AFM tip. If the replacement molecules were clusters of a large number of molecules, as shown in Figure 6.7B, the features would appear in the image to have a more flattened region which would be distinguishable with the AFM tip.

The average physical height of the singly inserted molecules was much lower than the directed assembly nanografted 16-MHA structures suggesting that the molecules replacing the background DDT were only monolayers of 16-MHA. Due to

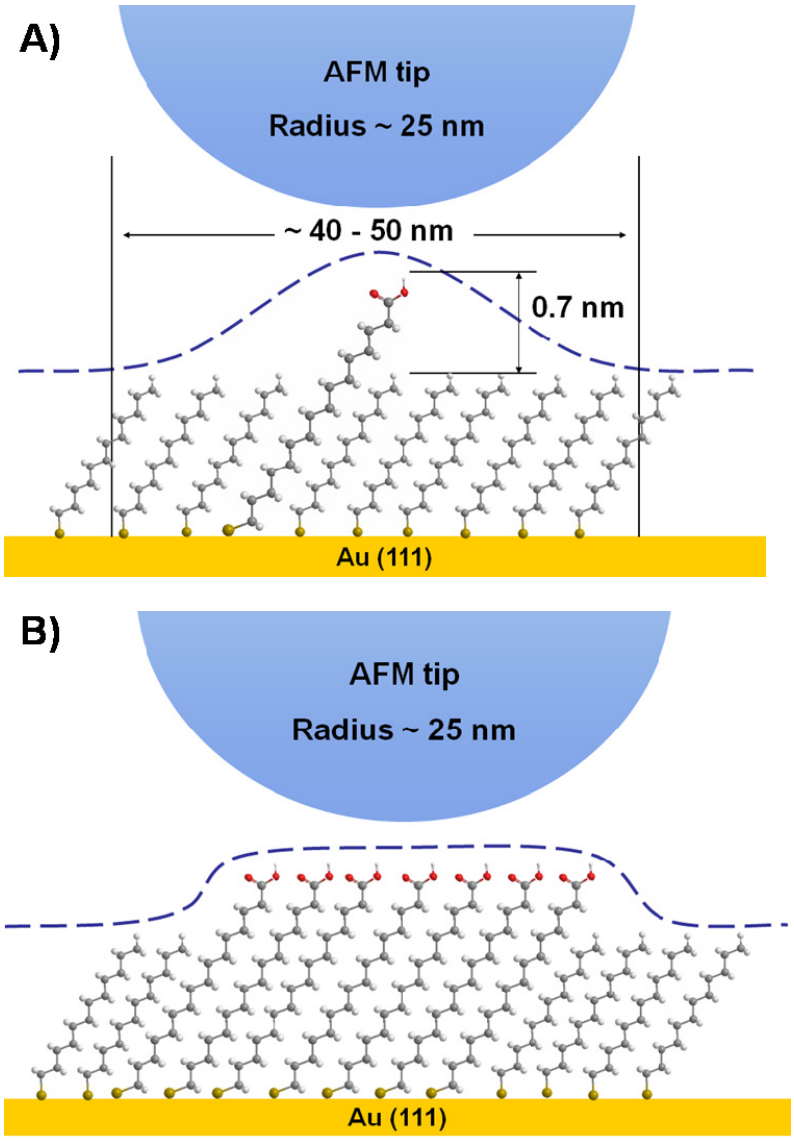

Figure 6.7. Model of (A) a single inserted 16-MHA molecule and (B) cluster of 16-MHA molecules imaged by an AFM tip.

this new discovery, a nanoscale test bed including nanografted molecular assemblies, singly inserted molecules (due to the tip disturbing the matrix), and a reference SAM can be fabricated all in one experiment. The inserted molecules and the nanografted

structures allow for a range of measurements to be made from single molecules to organized ensembles all in one test bed. The reference SAM provides an internal reference which allows for systematic comparisons from sample to sample, a key element in reproducing, standardizing and understanding any variations between sample test beds. This opens up possibilities for a variety of measurements for molecular electronic applications with the ability to fabricate and test the same structure with the AFM. When creating well-defined nanostructures, factors such as concentration, line spacing, and solvent should all be considered in order to fabricate reproducible patterned assemblies. The ability to control all of these factors has proven to yield molecular assemblies of different packing densities and uniformity. Spatial confinement is proving to applicable not only for molecular electronic applications but others as well such as sensing and monitoring enzyme reactions.[392]

6.4 Conclusions

We have compared nanografting of 16-MHA in ethanol and 3-phenyl-1-propanol. The results indicate that formation of well-defined nanostructures can be achieved in both solvents with differences regarding the integrity and packing of the nanografted assemblies. The 16-MHA molecules were found to assemble as bilayers when grafted into a DDT matrix, however, monolayer nanostructures can also be fabricated if the molecules naturally self-assemble into the preshaved wells in the DDT matrix. With the use of a more viscous solvent, 3P1P, 16-MHA assembled into more uniform structures with little to no undesirable insertion of the 16-MHA molecules into the background matrix SAM. It is a possibility that the 3P1P molecules stabilize the

matrix and the nanografted structures by inserting into the DDT matrix SAM forming van der Waals interactions between the 3P1P and the DDT molecules. Since ethanol and 3P1P both have alcohol functional groups, the phenyl ring and the longer alkane chain on the 3P1P could be the reason for the higher degree of chemical interaction with the background DDT providing a lubricative protection layer. If the 3P1P molecules are inserted at the terminal end of the matrix, this could create a barrier hindering the 16-MHA molecules from inserting into the background DDT. The higher quality of patterned assemblies in 3P1P and the little to no insertion of the 16-MHA into the DDT matrix could also be due to the physical property of the 3P1P solvent having a higher viscosity than compared to ethanol. The higher viscosity of 3P1P not only creates a resistance for the 16-MHA molecules to penetrate into the DDT matrix but also forms a protective layer around the 16-MHA assemblies. Additional factors other than solvent choice must also be considered in order to reproduce the nanoscale assemblies on Au surfaces. The packing of the nanografted 16-MHA molecules was affected by the line spacing of the AFM tip inside the patterned region and therefore the physical heights of the bilayer formation. A more densely packed structure will lead to a nanografted ensemble that was physically higher, and using a CRLS analysis can provide a more precise control over the molecular assemblies. In order to create well-defined nanostructures for use in molecularly-enhanced electronic applications, the pattern consistency must be controlled using these methods.

CHAPTER VII

FABRICATION OF ZINC PORPHYRIN NANO-ISLAND ARRAYS ON AU(111) USING SCANNING PROBE LITHOGRAPHY

7.1 Introduction

Molecularly-enhanced electronic devices are currently being explored using a diverse range of molecules from nanotubes to porphyrins to DNA with applications such as switches, molecular memory, organic field effect transistors as well as single electron transistors.[393-395] Porphyrinoids, with known roles in biological electron transport and photosynthetic systems, are obvious candidates for such devices, having a low band-gap electronic structure that is relatively unaffected by the choice of substrate or the molecular environment. Studies which combine a range of surface analytical tools, such as X-ray photoelectron spectroscopy, inelastic electron tunneling spectroscopy, reflection absorption IR spectroscopy, ultra-violet photoelectron spectroscopy as well as orbital-mediated tunneling spectroscopy via break-junction techniques and scanning tunneling microscopy (STM) have provided a significant amount of information regarding the physical and electronic properties of porphyrins on surfaces.[396] Work by Armstrong et al. has employed phthalocyanines in conjunction with C_{60}[397,398] and perylene derivatives[399] to develop structures that could be used in photovoltaic and OLED devices.[400] Porphyrinoids adsorbed as monolayers on surfaces have also been extensively studied by Hipps and co-workers who are investigating the self-assembly[401,402] and tunneling properties[403] of these molecules. Their work includes

studies on HOPG as well as metal substrates, suggesting a certain indifference of the porphyrin electronic structure to the substrate involved, potentially simplifying the challenge of technology transfer from experimentally convenient substrates like gold to more applicable substrates like silicon. Lindsey, Bocian and coworkers have been investigating in the past decade the direct correlation of the read/write speed to the electron transfer rates of porphyrins, and they have demonstrated a potential role that these molecules may play in future devices.[124,217,404] Their work has also shown that the reversible redox activity of stacked lanthanide porphyrinoid complexes, having several stable oxidation states, can be exploited for molecular information storage applications whereby oxidation and reduction of the clusters correspond to read and write cycles, with the ability to achieve substantially higher charge densities then existing silicon technology.[196] All of these studies conclude that the orbital energies of the macrocycles including the metal ions, molecular states, and the surface states determine the electronic properties, and ultimately the roles such molecules might play. Their extensive characterization and design of various porphyrin derivatives has shown that the attachment chemistry and topology, tether, and linker moieties have yielded insights to the functional role of each part of the molecule[105,152,153,209,274,405,406] which provides directions for further development of the field of molecularly-enhanced devices.

Substantial research contributing to the field of organic electronics has involved the study of single molecules. Tao et al. has examined the specific properties of single organic molecules such as alkanedithiols,[407] oligothiophenes[408] and perylene derivatives[409] using electrochemical and break junction techniques where quantized

conductance measurements have been possible. This work on single molecules is certainly highly applicable to molecularly enhanced devices, however the development of molecular ensembles has seen increasing consideration, perhaps owing to the many challenges involved in fabrication of reliable single molecule devices as well as the fact that single molecules, while potentially quite capable as diodes and rectifiers, cannot achieve the necessary charge stabilization at room temperature necessary for effective Coulomb blockade and thereby operation as single electron transistors. Weiss et al. has also been a major contributor towards enhancing or replacing conventional electronics using molecules, and much of his work has involved the development of single molecule devices[322] and optimizing their properties using synthetic methods.[410] Creating ordered, reproducible structures is important in order to advance the knowledge of the molecule-based nanoelectronics field, whose function is dictated or enhanced (i.e. "more than Moore" applications) by the use of molecular assemblies to modulate charge transport. Molecules must not only be characterized and analyzed for their ability to be integrated with existing technologies such as CMOS but must also be controllably organized onto a surface at the nanoscale. It would be ideal to reproducibly and controllably create molecular architectures on surfaces in dimensions from 10 – 100 nm to carry out specific applications for memory cell and sensing devices.

To develop a better understanding of electron transport through molecules, we have studied thiol tethered porphyrin molecules, as detailed in earlier chapters and illustrated here (Figure 7.1). Careful investigations of the attachment chemistry and

topology, tether, and linker moieties can yield substantial information on electron transport through molecular systems. Our group has found through a crosswire junction

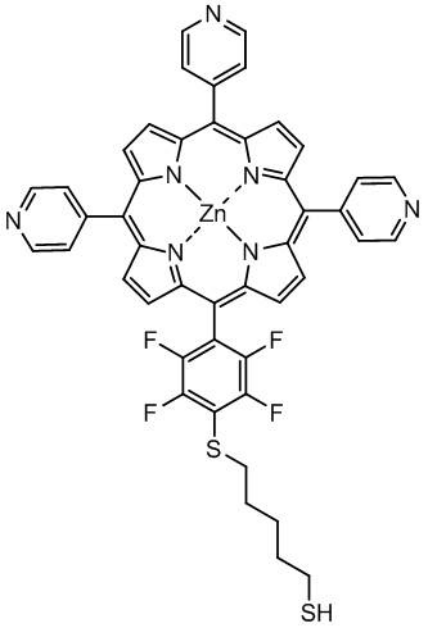

Figure 7.1. Zinc porphyrin thiol model.

technique, that the porphyrin shown is capable of Coulomb blockade at liquid helium temperatures, making it a potential candidate for roles in single electron transistors. At room temperature, bias-induced switching of the molecules is observed via Scanning Tunneling Microscopy (STM), a behavior most prominent for aggregates of the molecule. In this previous work, such aggregates were formed randomly as the molecules were allowed to insert into a preexisting self-assembled monolayer (SAM) at

defects in the film, with no direct control over the insertion process. In this work our goal was to direct the insertion of these molecules to reliably produce molecular ensembles.

In order to fabricate any of these types of devices, the inherent electronic properties of molecules must first be investigated. Once a molecule shows promise for any one of these applications, the single molecule or ensembles of molecules must be reproducibly patterned on a surface. Various patterning techniques have been used to create nanoscale structures and patterns on surfaces, in particular, a variety of scanning probe methods exist including Dip Pen Nanolithography (DPN),[239] Nanopen Reader and Writer (NPRW),[411] as well as nanoshaving[412] and nanografting.[366,367] Other than DPN, these techniques are limited from a fabrication standpoint as they are not easily parallelizable and mass-producible, however developments in this regard have been made.[413] In this work, nanografting, whereby a pre-existing SAM is displaced by an Atomic Force Microscope tip allowing for insertion of the molecule of interest, has been employed to fabricate ensembles of a zinc porphyrin molecule on a Au surface. This type of directed assembly patterning technique has the ability to create nanoscopic structures which are necessary in the fabrication of smaller electronic devices which may rely on the behavior of only 10's to 1000's of molecules in a confined structure. Furthermore, spatial confinement in the grafted regions assists in the assembly of self-organized porphyrin structures.[414] The most common solvent for nanografting is ethanol or mixtures with ethanol,[387,415-417] however, the results presented herein are the first example to our knowledge of nanografting in pure dichloromethane. Nanografting in

such a volatile solvent can create issues during patterning, such as the limited amount of time before the solvent completely evaporates, which reduces the size scale of the entire patterned region as well as the instability of the AFM tip which is unable to equilibrate, not to mention the tendency of dichloromethane to dissolve a variety of plastics and adhesives. Others have imaged in a mixture of solvents such as ethanol/dichloromethane (85/15) to overcome these inherent issues, but we were unable to use a solvent mixture due to the highly favorable aggregation of this molecule resulting in particularly poor solubility.

In order to overcome these inherent issues associated with dichloromethane, we have utilized a custom made glass nose cone and sample holder to facilitate the patterning of the zinc porphyrin thiol. Since the original nose cone for the Agilent 5500 AFM is made of PEEK polymer which swells in the presence of dichloromethane and has an epoxy that holds the viewing window which dissolves in dichloromethane, a glass nose cone was manufactured by Mindrum Precision Inc. (Rancho Cucamonga, CA) so the entire piece would be compatible with the solvent. The o-rings around the nose cone which seal the electronics from solvent were also exchanged for a material which had a better chemical resistance to dichloromethane. A custom sample holder was also designed and fabricated out of Teflon to contain the Au sample and zinc porphyrin thiol solution. Compatibility with the AFM set up was not the only issue to overcome for these experiments, finding the patterned area in the STM after nanografting the zinc porphyrin thiol in the AFM was another major dilemma. First, a large scratch in an "X" shape was made on the Au surface using Pt wire in order to delineate where the general

patterned area would be located. The apex of the "X" was then used to localize a 100 μm^2 area. Using the AFM software, an AFM probe was then approached into silver epoxy (Epotek) until the tip made contact and was immediately retracted from the surface. Once the AFM probe was coated with the silver epoxy, the tip was approached four times in a diamond shape to the surface and held for a few seconds. The epoxy dots were cured in the oven at 150°C for 1 hour and were resistant to dichloromethane. The Au sample was then placed into the AFM liquid environment and the nanografting experiments were carried out inside the 100 μm^2 area of the epoxy dots. This procedure allowed for repetitive nanografting of the zinc porphyrin thiol molecules and afterwards, the sample was removed from the AFM and immediately placed into the UHV-STM chamber. Once inside the STM chamber, the STM tip was approached inside the epoxy dots which easily allowed for investigation of the patterned area.

Since nanografting is capable of achieving precise and reproducible patterns,[376] we have employed this scanning probe lithographic technique in this chapter to manipulate porphyrin molecules into well-defined structures on a Au surface for the ultimate goal of creating a nanopatterned array of Coulomb islands to be electrically characterized using Scanning Tunneling Microscopy (STM) or Conducting-Probe Atomic Force Microscopy (CP-AFM). We have also employed the nanografting technique to pattern larger arrays of assemblies of zinc porphyrin thiols in a dodecanethiol (DDT) matrix on Au surfaces to investigate the assembly, stability, and electronic properties of the nanostructured arrays. Our goal of consistently fabricating

nanostructures is ultimately expected to yield consistent electronic characteristics which is a necessity for implementation of such devices to enhance existing silicon technology.

7.2 Experimental

7.2.1 Materials

Au(111) substrates (purchased from Agilent Technologies, Inc., Santa Clara, CA) were ~150 nm flame-annealed gold films on mica or (purchased from PHASIS, Geneva, Switzerland) were ~200 nm freshly grown gold films on mica. Dodecanethiol (DDT, 98% purity) was purchased from Aldrich and used as received.

7.2.2 Preparation of Self Assembled Monolayers (SAMs)

Before each experiment, all Au(111) substrates were treated with UV/ozone for 20 min, followed by rinsing the gold film in sequence with high purity (18.2 MΩ•cm) water (NANOpure Diamond, Barnstead), ethanol, and then dried with streaming nitrogen. SAMs of *n*-dodecanethiol were formed by immersion of the Au films in 1 mM *n*-dodecanethiol/ethanol solution for 24 h followed by rinsing liberally with ethanol and blown dry with streaming nitrogen.

7.2.3 Atomic Force Microscopy (AFM)

AFM images were acquired with either a Molecular Imaging 4500 Pico SPM (Agilent, Santa Clara, CA) with a deflection-type detection scanning head interfaced with an SPM1000 control electronics Revision 8 (RHK Technology Inc., Troy, MI) or an Agilent 5500 (Agilent, Santa Clara, CA). All AFM imaging and nanografting experiments were done in contact mode under liquid environment using commercially available Si_3N_4 AFM tips (Veeco/TM Microscopes, Sunnyvale, CA and MikroMasch,

San Jose, CA). The Veeco AFM tips have nominal tip radii of ~ 10 nm and nominal spring constants of ~ 0.5 N/m and were used for fabricating the arrays of zinc porphyrin of different sizes and shapes. The MikroMasch tips were characterized fully for the 5 and 20 nm islands studies. The tips used for the fabrication of the 5 nm and 20 nm islands had spring constants of 0.39 N/m and 0.77 N/m, respectively with tip radii of ~ 35 nm. The imaging force of the tip on the surface of the sample was calculated to be between 2 – 4 nN, whereas for nanografting, the forces were much higher at 214 nN and 363 nN for the 5 and 20 nm islands, respectively. Lithography scripts were programmed to regulate and vary tip speeds, line spacing, and applied force.

7.2.4 Scanning Tunneling Microscopy (STM)

STM measurements were taken under ultrahigh vacuum (UHV) conditions using an Omicron UHV-XA STM system. The system was operated with a typical base pressure of $< 2.3 \times 10^{-10}$ Torr. Images were collected using Pt/Ir (70/30) tips which were mechanically cut. The typical imaging conditions of tunneling current and tip bias voltage ranged from 5 pA to 30 pA and from -2.0 V to +2.0 V, respectively. Current-voltage (I-V) spectra were collected under UHV conditions over a voltage range of -2.0 V to +2.0 V. The STM images were analyzed with commercially available Scanning Probe Image Processor (SPIP) software (version 4.8.1, Image Metrology, Lyngby, Denmark).

As detailed in the Introduction, characterizing the nanografted patterned regions with the STM was enabled by developing a technique in order to mark the sample to find the nano-islands. Briefly, an “X” was scratched onto the Au(111) surface with a Pt wire.

At the intersection of the "X", an AFM tip was used to drop four, ~ 10 μm size beads of silver epoxy (Epotek) in a diamond shape. The Au was then heated to 150°C for 1 hour to cure the silver epoxy so that it would not dissolve in the nanografting dichloromethane solvent. The nanografting was then performed inside the diamond shape and immediately after, the sample was placed into the UHV-STM for further imaging and electronic characterization of the zinc porphyrin nano-islands.

7.3 Results and Discussion

7.3.1 Zinc Porphyrin Nanografting and Characterization

Nanografting has been employed to create a variety of different molecular assemblies of the zinc porphyrin thiol on Au(111) surfaces. To create the different patterns of molecules, lithography scripts were employed using the computer software to control the placement, force and speed of the AFM tip. Lithography scripts have been programmed to nanograft different shapes of the zinc porphyrin thiol molecules into a dodecanethiol matrix such as a 4 x 4 array of circles, an array of squares or frames and ultimately the optimal Coulombic 10 nm islands as shown in Figure 7.2. For the circles arranged in a four leaf clover shape, the AFM tip scanned each circle 5 times. The width of each individual circle was ~ 10 - 20 nm, which is the optimal size of the confined domain desired. From the topography images achieved, the zinc porphyrin thiol readily grafted into this pattern of circles. The physical height of the outer circles was ~ 5 Å, shown in Trace A in Figure 7.2 which is consistent with the calculated monolayer height

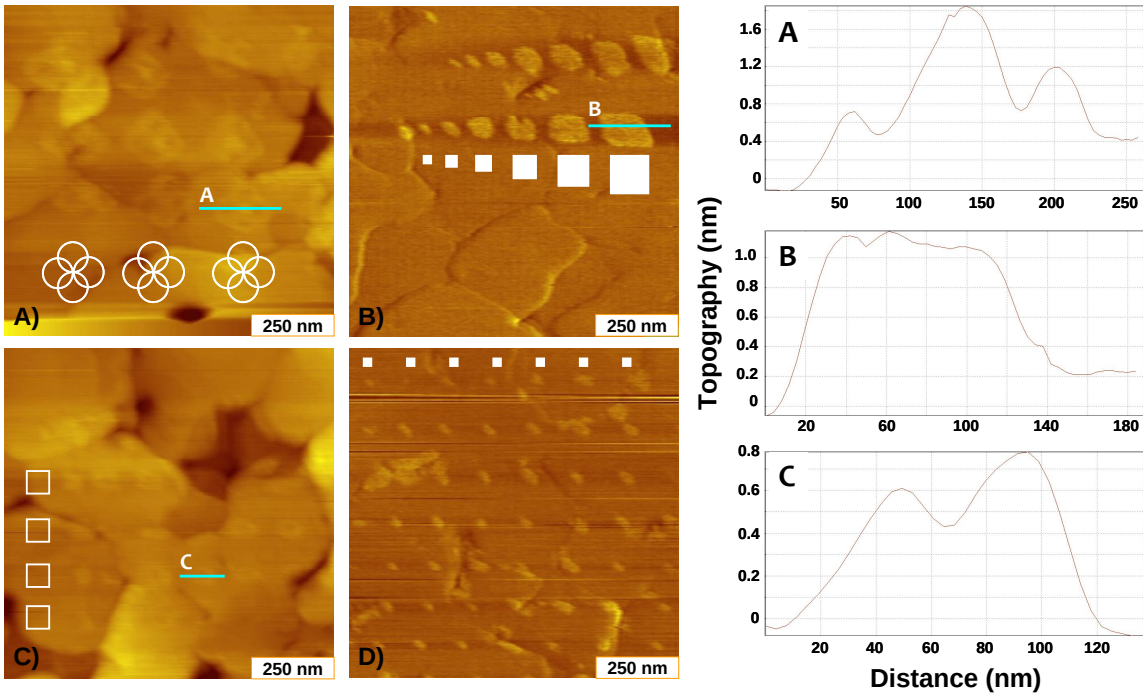

Figure 7.2. AFM images of nanografted patterns of zinc porphyrin thiol in dodecanethiol matrix. (A) 4 x 4 circular pattern array, (B) different size squares from 10 – 100 nm, (C) 8 x 8 array of 50 nm frames and (D) 8 x 8 array of 10 nm islands. The traces on the right hand side correspond to the blue line traces in panels A – C, respectively.

of the zinc porphyrin thiol and IR measurements as described in Chapter IV.[418] Since the AFM tip has scanned the middle of the array of circles more than the outer edges of the circles, the physical height in the middle of the circles (16 Å) was higher than the height observed on the cross section of a single circle. The successful nanografting of the zinc porphyrin molecules was reproducible using this lithography script. To show the versatility of the zinc porphyrin thiols to be nanografted, an array of different size squares from 10 – 100 nm was patterned. The largest, 100 nm, square had a physical

height of ~ 10 Å. The discrepancy of each of the patterns having different heights is likely due to the arrangement of the zinc porphyrin thiols inside the nanografted structures. Since the porphyrins can aggregate in a variety of ways such as pi stacking or arrange so that the pyridyl N from one molecule interacts with the Zn metal center of another or a mixture of the two, the physical height of the zinc porphyrins above the DDT matrix can vary. From past studies of the self-assembled zinc porphyrin, we know that the zinc porphyrin islands on average are only ~ 3 Å above the dodecanethiol matrix. The physical height above the background matrix SAM can range from essentially no difference if the zinc porphyrins are leaning over up to ~ 12 Å if the zinc porphyrins are standing completely upright. In Figure 7.2C, the zinc porphyrin thiol molecules were nanografted into an 8 x 8 array of 50 nm frames spaced 70 nm apart. The physical height of the zinc porphyrin thiol was observed to be between 6 - 8 Å shown in Trace C of Figure 7.2.

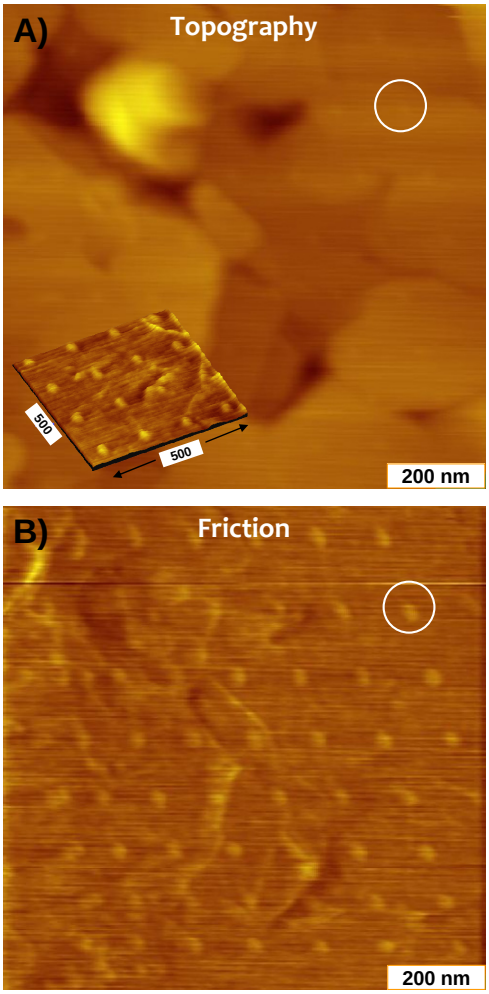

Figure 7.3. (A) Topography and (B) friction AFM images of the 8 x 8 array of 10 nm zinc porphyrin islands. Inset in (A) is a 3-D friction image for clarity.

The lithography script for the 50 nm patterned array of frames was modified to graft the zinc porphyrin thiol into patterned arrays with 10 nm feature sizes. Since the AFM tip is often much larger than 10 nm, the lithography script was modified so that only a square frame was drawn in order to minimize the buildup of excess porphyrins in the nanostructure. By not grafting inside the frame, this allowed for the creation of the

10 nm islands of zinc porphyrin. Patterning arrays of 10 nm frames was better than patterning arrays of squares due to the fact that the tip does not spend a significant amount of time in the center of the square which can cause the porphyrins that assemble on the edges to be swept away in some instances. Nanografting can also cause a buildup of the porphyrin molecules, thus, scanning the AFM tip in a frame pattern has grafted monolayers rather than bilayers or stacks of the zinc porphyrin thiol.

The patterning of these nano-islands was a very quick process, less than a few minutes, for the 8 x 8 array shown in Figure 7.2D, so there was not an issue with the volatility of the dichloromethane solvent, and the AFM topography could be imaged after the nanografting took place. However, in order to graft larger regions of zinc porphyrin islands, the solvent must be stable for much longer periods of time. The 8 x 8 pattern of the 10 nm islands was grafted successfully and is clearly visible in the friction images in Figure 7.3. It is difficult to discern the zinc porphyrin in the larger scale topography image due to the small physical height of the zinc porphyrins, however from higher magnification images, the islands become visible as bright dots (Figure 7.4). Due to the sharp radius of curvature of the tip and the 10 nm nominal radius, the observed porphyrin islands had a FWHM of ~ 15 nm in width and did not resemble a frame, but a filled in square. The physical height of the 10 nm frame was observed to be approx. 5 Å

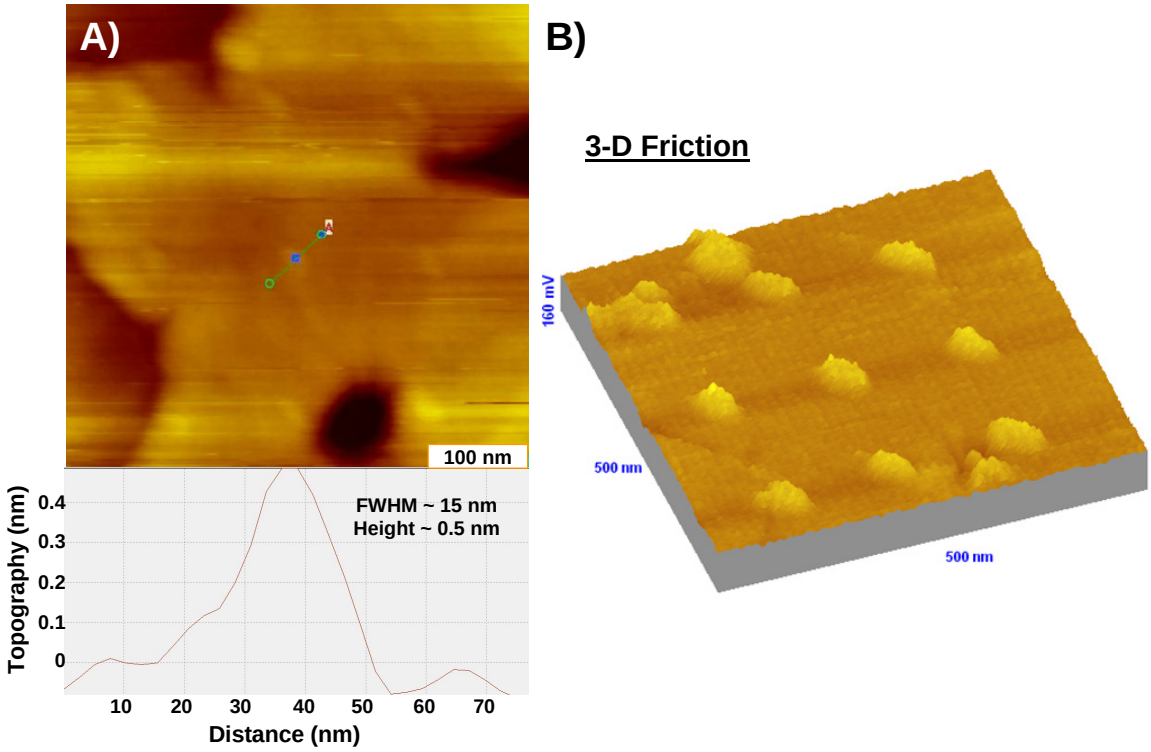

Figure 7.4. (A) Topography AFM image of a 3 x 3 array of 10 nm zinc porphyrin islands with corresponding line trace and (B) its respective 3-D friction image.

as shown in the line trace of Figure 7.4A, consistent with the calculated physical height of the zinc porphyrin monolayer.[418] The 10 nm islands created by nanografting with an AFM tip will allow us to further investigate the Coulomb blockade behavior of these ensembles as described in Chapter IV. The self-assembled islands are difficult to obtain conclusive information regarding the electronic properties of the ensembles because the molecular clusters are not isolated from one another and therefore their electronic communication is not localized to individual islands. During the self-assembly process, the zinc porphyrin clusters do not have precisely controlled geometric constraints. The molecular structures are driven to self-assemble by thermodynamic control into the

defects of the DDT matrix and the final ensembles of zinc porphyrins are various sizes and shapes. The self-assembly of the zinc porphyrins in the DDT matrix leads to molecular clusters that are not isolated from each other and therefore the I-V behavior of the aggregates was not consistent from island to island or even within the island. It is suspected that the charge transport behavior for the zinc porphyrin thiols in the mixed monolayers has been unreliable due to the uncontrolled size and shape of the islands. In order to reproducibly create molecular ensembles isolated from one another, nanografting was employed to control the precise placement and shape of the zinc porphyrin nanostructures. Also, by creating the islands directly with an AFM tip, we have the ability to control the shape of the nano-islands based on imposing defined geometric constraints inside the DDT matrix. The nanografting process also forms ensembles which are kinetically controlled by the speed it takes for the molecules to assemble inside the open well unlike the self-assembled molecular ensembles which have days to form on the Au surface. Liu and coworkers have shown that there is a spatial confinement effect due to the difference in kinetics for assembled structures formed instantly by nanografting.[381] Due to the differences in the assembled islands on the Au surface during nanografting versus self-assembly, the charge transport behavior was markedly different of the nanografted zinc porphyrin islands which will be discussed in more detail later in this chapter.

7.3.2 STM of Zinc Porphyrin Nanografted Arrays

Now that we have the ability to graft the zinc porphyrin thiol nano-islands, one of the most important aspects of creating the Coulomb islands is to investigate the

significance of controlling the island size. Coulomb islands are known to exhibit distinct electron transport behavior whereby the electron passes through the islands one at a time. The threshold voltage as well as the Coulomb blockade gap range should depend on the size of the Coulomb islands. Since the properties of the molecular islands should be dictated by the size and shape as well as the assembly of the molecules inside the different nano-islands, we have investigated two different size islands, 5 and 20 nm. Using STM, we have been able to investigate the assembly of the molecular islands using high resolution imaging of individual clusters as well as probe the charge transport behavior of different size nano-islands. Very few studies have been done exploring the charge transport behavior of fabricated nanostructures. SAMs with electroactive headgroups fabricated using STM replacement lithography have shown an interesting phenomenon known as Negative Differential Resistance (NDR), however these studies were fabricated and investigated within the same instrument.[419] In our current investigations, the Coulomb islands have been fabricated with an AFM and subsequently moved into a UHV-STM for charge transport studies. Beyond controlling island size and looking at the charge transport behavior as a function of island size, patterning large arrays for a functioning device is also of worth for our studies and has been demonstrated using lithography scripts with AFM. As molecules are being proposed as active electronic components, we would like to further investigate if the zinc porphyrin thiols can act as molecular capacitors since there has been preliminary evidence that the

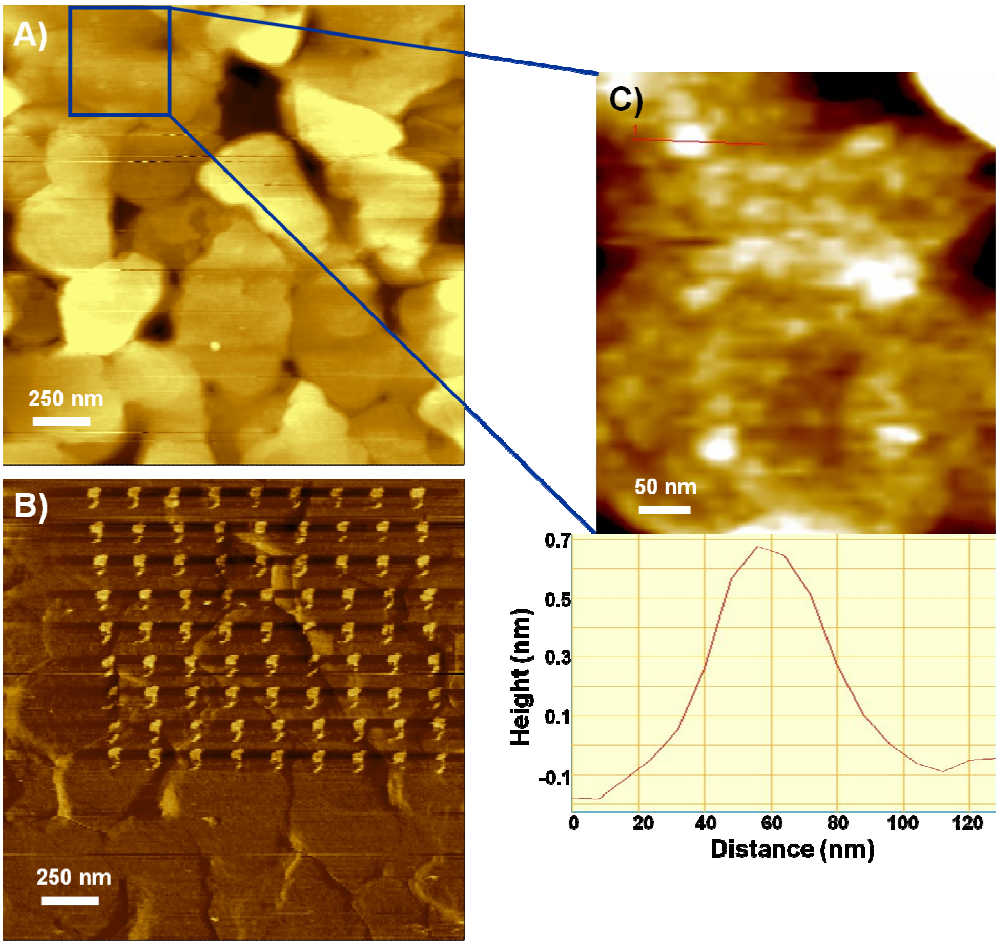

Figure 7.5. (A) Topography and (B) friction AFM images of a 9 x 9 array of ~ 5 nm zinc porphyrin islands in a dodecanethiol matrix. (C) Magnified region with corresponding line trace of nano-island.

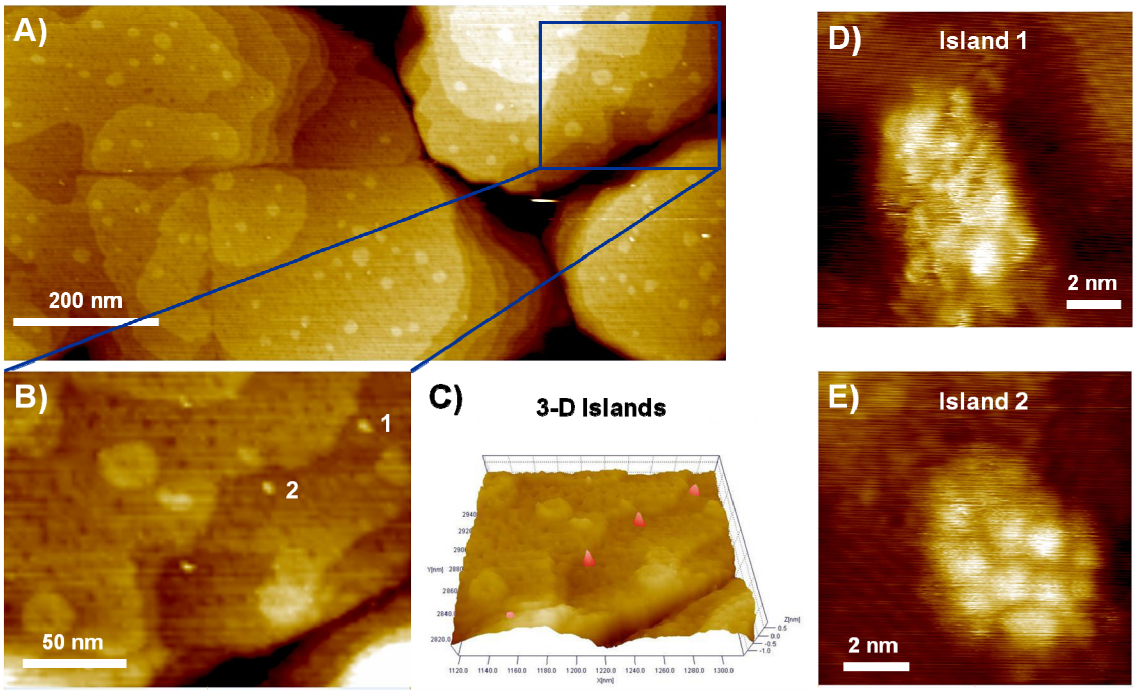

Figure 7.6. (A) UHV-STM image of large scale patterned area and (B) zoomed in 2-D and (C) 3-D images of 4 zinc porphyrin islands. High resolution STM images of ~ 5 nm zinc porphyrin (D) island 1 and (E) island 2 in a dodecanethiol matrix. Imaging conditions: 1.2 V and 5 pA.

Coulomb blockade gap range does appear to change as a function of the island size. Since capacitance depends on island size, we have focused on creating large arrays with total patterned areas on the order of microns of the ~ 5 and 20 nm islands of zinc porphyrin thiols. Using the AFM lithography scripting techniques, a 9 x 9 array of 5 nm zinc porphyrin islands has been patterned as shown in Figure 7.5A & B. The physical height of the islands was ~ 8 Å consistent with the height of a monolayer of zinc porphyrin thiol molecules and the FWHM was ~ 40 nm shown in the line trace of Figure

7.5C. The width determined from AFM was larger than the actual patterning size to the large radius of the AFM tip.

The patterned area was imaged in an UHV-STM to characterize the apparent height and orientation of the nanografted structures. In the STM, a line of 4 zinc porphyrin islands are observed as outlined in the blue box in Figure 7.6A. The apparent height of these islands was ~ 3 – 5 Å and ~ 6 nm wide which is much smaller compared to the 40 nm width in the AFM. Again, due to the size of the AFM tip, the width of the porphyrin ensembles appears much wider than their actual dimension. Due to the heating step to cure the epoxy on the Au surface, small terraces of Au adatoms appear in the STM images in Figure 7.6. Since these tiny Au terraces are only ~ 3.0 Å tall, they are not resolved in the AFM images. The magnified STM region, Figure 7.7B, and the 3-D respective area, Figure 7.6C, show the islands clearly organized in a straight line. In Figure 7.6D and E, high resolution images of the nanografted region show no clear order inside Island 1. However the pyridyl N's spaced ~ 1.1 nm apart are clearly evident in the STM image from Island 2 imaged with very low currents of 5 pA. Island arrays of 20 nm have also been fabricated as shown in the AFM topography images in Figure 7.7. A 2 x 2 array is shown in Figure 7.7A and B, and this technique was scaled up to create a 9 x 9 array as shown in panel C and an 18 x 18 array as shown in panel D. In Figure 7.8, the magnified region of the 18 x 18 array shows the physical height of the islands is ~ 8 Å with a FWHM of ~ 60 – 80 nm shown in the line trace of Figure 7.8B which again was expected due to the large radius of the AFM tip. When the 20 nm island patterned

arrays were imaged with the STM, the islands typically exhibited a FWHM ~ 10 – 20 nm.

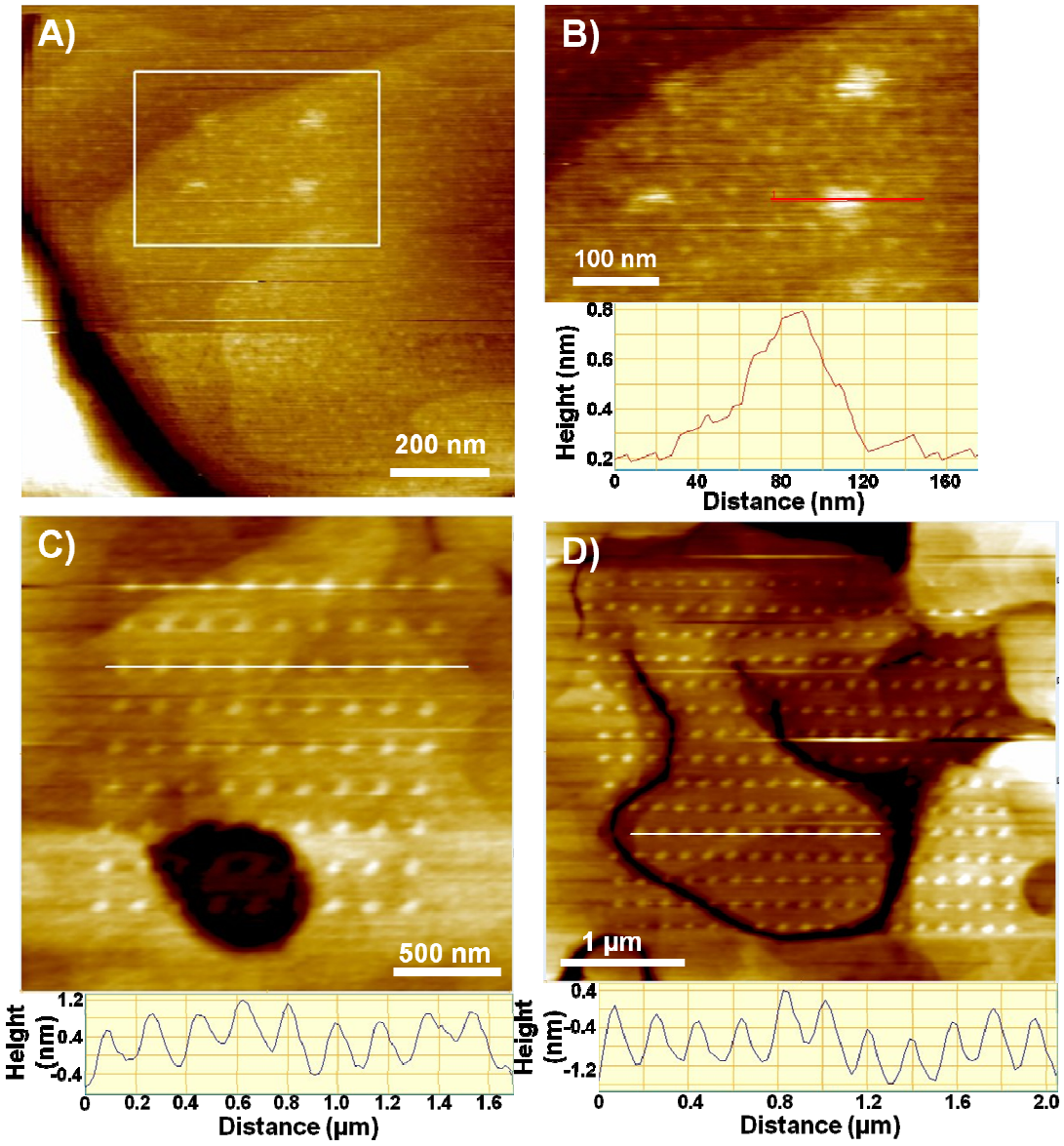

Figure 7.7. (A) Topography AFM images of a 2 x 2 array, (B) Magnified region of 2 x 2 array with corresponding line trace of island, (C) 9 x 9 array with line trace and (D) 18 x 18 array with line trace of ~ 20 nm zinc porphyrin islands in a dodecanethiol matrix.

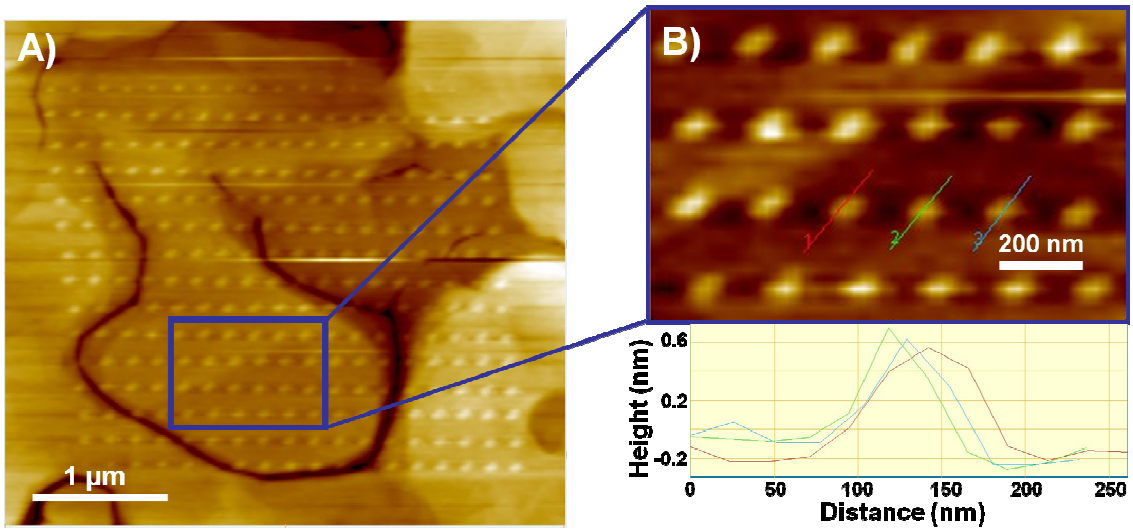

Figure 7.8. (A) Topography AFM images of an 18 x 18 array of ~ 20 nm zinc porphyrin islands in a dodecanethiol matrix. (B) Magnified region with corresponding line traces of islands.

The major difference with the larger islands was the apparent height of these nanostructures. The apparent height in the STM was ~ 2.0 nm which was more than double that of the smaller, 5 nm, zinc porphyrin islands and suggests an increase of the electronic communication inside the ensembled nanostructure. When the zinc porphyrin thiols self-assemble on Au surfaces, the clusters naturally appear in the STM with two different apparent heights, one typically around 5 Å which exhibit bias-induced switching in a face to face pi-stacked orientation and other clusters which appear greater than 1 nm. The self-assembled islands in the higher conductance state show a large range in apparent height from ~ 1 to 2.5 nm. These nanografted 20 nm islands appear to

match the higher conductance state of the self-assembled structures. Although it is unclear at this time how the molecules are organized inside the 20 nm islands since the clusters appear so bright in the STM images. It is always difficult to obtain high resolution images of clusters that have apparent heights greater than 1 nm due to the increased electronic communication in the aggregated structures. The 20 nm islands were also much less stable than the 5 nm islands in the lower conductance state. After

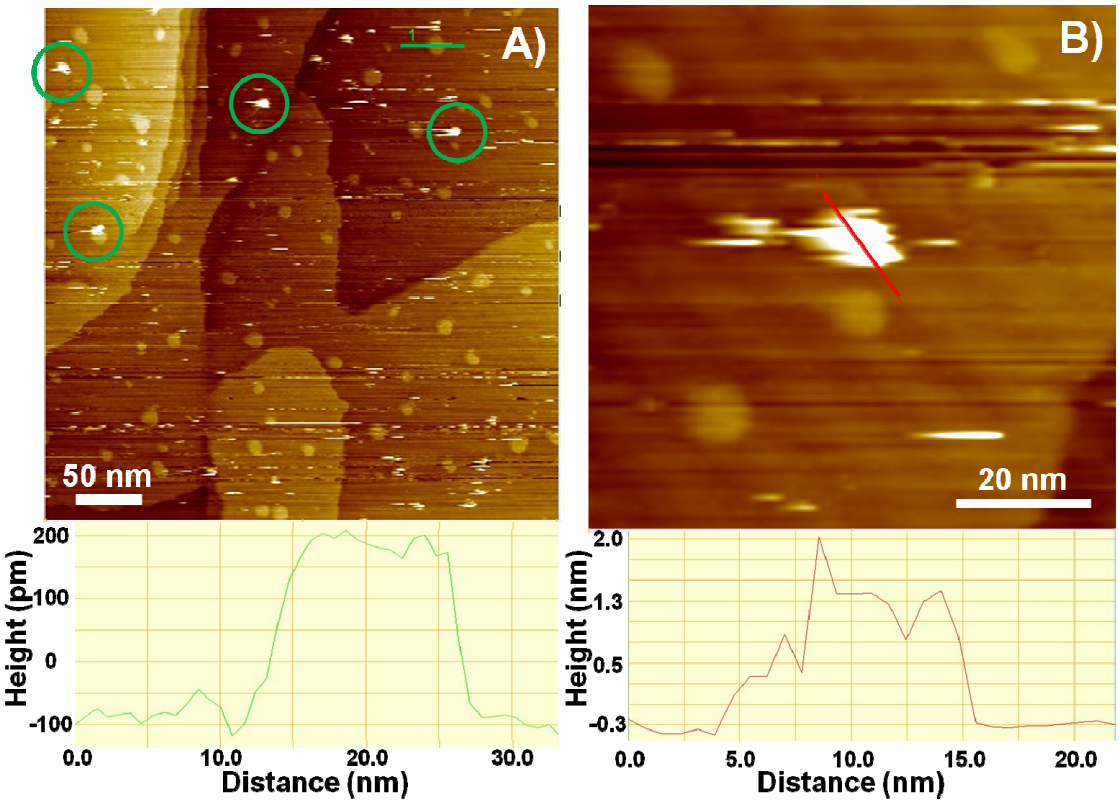

Figure 7.9. (A) UHV-STM image of large scale patterned area of 20 nm islands and line trace of gold terrace and (B) magnified image of a single 20 nm island with its corresponding line trace.

the STM tip path crosses over the 20 nm islands one or two times, the STM images no longer show the clearly defined islands, but rather a smear across the surface even at very low currents of 5 pA. In Figure 7.9, it is clear that there is a lot of smearing out of the porphyrins since only a partial pattern, circled in green, is observed of the 20 nm islands. The lower apparent height islands in the background of the STM image are the small Au terraces created during the heating step of the sample preparation. These islands are only 3 Å, the approximate diameter of a Au atom, as shown in the line trace of Figure 7.9A. Since the apparent height of these molecules inside the nano-islands are around 2 nm (shown in the line trace of Figure 7.9B) and the packing density is unclear inside the fabricated structure, each porphyrin could be oriented in an upright fashion without very many nearest neighbor molecules. If this is the case, the molecules can be easily manipulated with the STM tip and any slight interaction can cause the cluster to fall apart. After taking a set of current-voltage (I-V) measurements on the isolated islands, the cluster would also disappear in the STM image as shown in Figure 7.10 which also confirms that the higher apparent height, 20 nm islands are unstable. Due to the lack of high resolution images, no conclusions can be made with regards to the molecular orientation of the 20 nm islands.

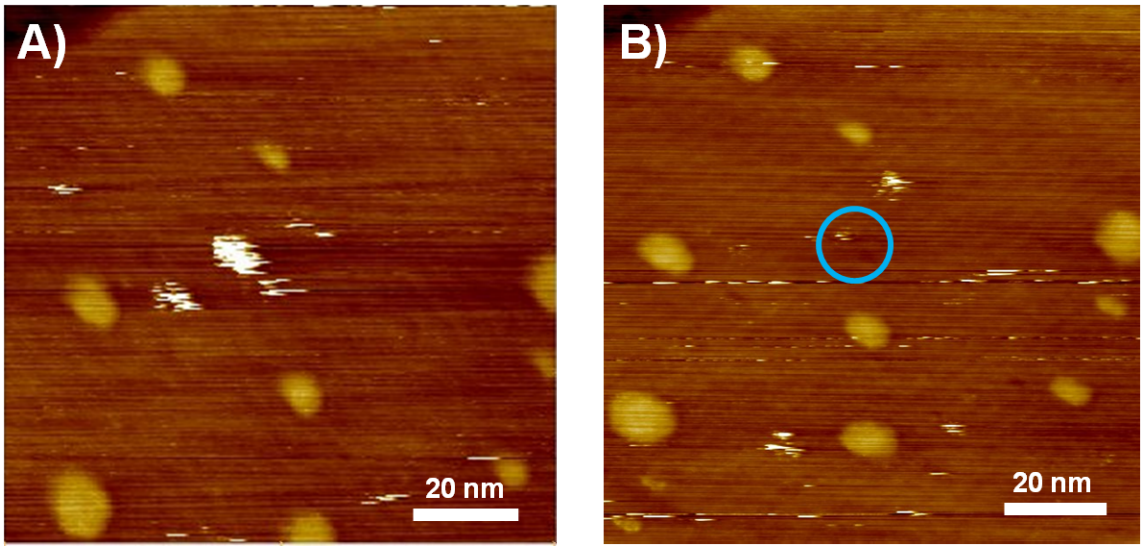

Figure 7.10. (A) UHV-STM image of 20 nm island before and (B) after taking I-V measurements. Blue circle indicates where the zinc porphyrin island disappeared.

7.3.3 Charge Transport Behavior of Zinc Porphyrin Nano-Islands

Now that we have investigated the reproducibility and stability of nanografted arrays of zinc porphyrin thiols, the next challenge is related to obtaining conclusive information regarding the charge transport behavior of the fabricated 5 and 20 nm Coulomb islands at room temperature. Based on prior junction measurements which investigated the porphyrins acting as Coulomb islands, we have seen that the π-π stacking of the porphyrin macrocycles as well as the zinc metal interactions played a significant role in the amount of current passing through the molecule as well as the turn-on voltage in the I-V curve. Since the zinc metal center increases aggregation, the zinc porphyrin clusters are capable of forming large enough islands during self-assembly after 5 days in the zinc porphyrin solution which are able to stabilize charge through the

extended pi system, and when a high enough bias is applied, *i.e.* the voltage threshold is reached, the charge is released which in turn results in an increase in the current flow. Now, by creating the Coulomb islands with a desired feature size, we can investigate the properties of these nano-islands of different sizes. The 20 nm islands, although clearly unstable in the STM, did afford reproducible I-V measurements. When investigating the self-assembled molecular ensembles of the zinc porphyrin in mixed monolayer, the I-V measurements were never consistent and each ensemble would display very random charge transport behavior. Now that the zinc porphyrins are precisely placed on the surface in the desired shape of a square and have been geometrically confined by the DDT matrix, the charge transport was much more uniform even among several different islands of the same size. The 20 nm islands clearly showed very low current in the hundreds of pA range with a symmetric I-V curve as shown in Figure 7.11A and have been compared to the background C12 SAM as a reference in Figure 7.11B. One of the issues when obtaining electronic measurements on the self-assembled islands was that they are not isolated from others because the molecules cannot be placed accordingly. In comparison to the self-assembled islands, the nanografted islands may not have molecules oriented in a similar direction but the shape and constrained size of the islands are consistent which most likely leads to the uniform I-V behavior.

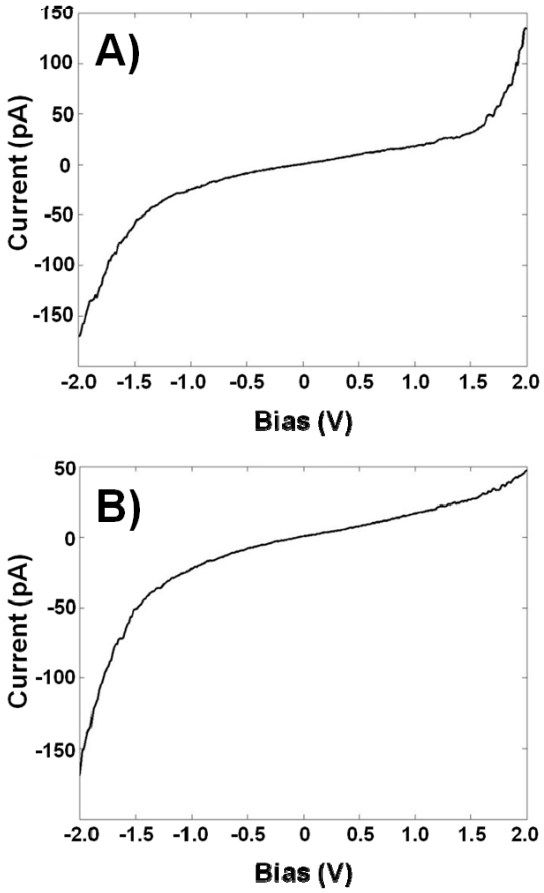

Figure 7.11. Average I-V curve for (A) 20 nm zinc porphyrin island and (B) reference C12 SAM.

Now that the porphyrins can be placed directly on the surface as desired and the spacing and size of the islands can be controlled, the I-V measurements were much more consistent. With self-assembly, each island can be in contact with surrounding molecules from a different island which can make the I-V curves very inconsistent. Since there is no control over the molecule placement during the self-assembly process, obtaining reliable information regarding the electronic properties of the islands was very

difficult. Using scanning probe lithography to pattern the zinc porphyrin thiol molecules, the I-V data acquired on each 20 nm island was shown to be consistent and reliable. With the 20 nm islands, it is expected that the I-V curves should not exhibit any sharp turn on voltage since the porphyrins are already in the higher conductance state, and the molecules are therefore unable to turn "ON". Previously, it was seen with the self-assembled islands that only the molecules in the lower conductance state, i.e. those with apparent heights of ~ 5 Å, were the ones that turned on when the bias was increased from 1.4 to 2.0 V. Since the fabricated 5 nm islands are indeed in the lower conductance state as determined by STM, further experimental studies examined the bias-induced switching behavior and charge transport of these zinc porphyrin islands. As shown in Figure 7.12A and B, the molecular islands do exhibit bias-induced switching when the tip bias was increased from 1.4 to 2.0 V. The switching results in a the apparent height of the zinc porphyrin island increasing from ~ 8 Å to 18 Å. The increase in apparent height by 1 nm confirms that the 5 nm molecular islands turn "ON" into a higher conductance state as was previously observed with the lower apparent height self-assembled zinc porphyrin islands. Now, the molecular island size can be controlled using scanning probe lithography and large patterned arrays can be fabricated of the molecular switches. The charge transport behavior of the 5 nm island was remarkably different when compared to the 20 nm zinc porphyrin islands. As shown in Figure 7.12C, the average I-V curve of one 5 nm zinc porphyrin island shows a sharp turn-on in

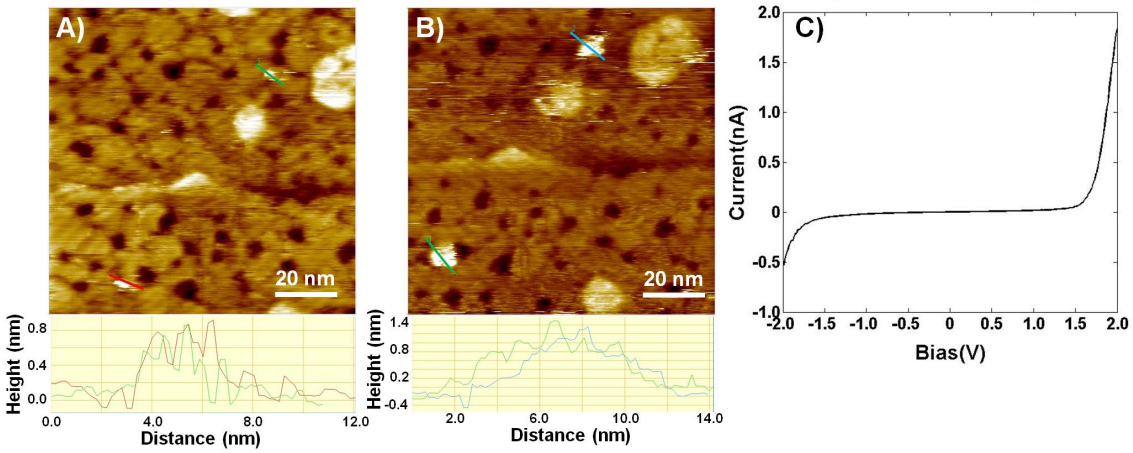

Figure 7.12. Bias-induced switching of 5 nm islands (A) in low conductance "OFF" state at 1.4 V and (B) high conductance "ON" state at 2.0 V with corresponding apparent height traces and (C) average I-V curve for 5 nm zinc porphyrin island.

current above ~ 1.6 V with total current in the nanoampere range. The I-V measurement for the 20 nm islands were symmetric in the picoampere range and did not display any sharp turn on in the current above a bias threshold. The difference in the charge transport behavior for the two different sized islands could be due to the ability of the charge to be stabilized on nano-islands of a distinct size. It is also unclear at this time the specific orientation of the porphyrin molecules inside the 20 nm islands since their apparent height is over 2 nm. Therefore, molecular configuration inside these molecular islands could also play a role.

The future of this project will focus on obtaining consistent conductance information of the 5 and 20 nm fabricated islands as well as 40 nm islands. Experiments are underway involving creating patterned arrays with 3 various size nano-islands. Once the arrays have been fabricated, I-V measurements will be obtained in order to relate the

island size to the threshold voltage and Coulomb blockade region. From these investigations, the capacitance, C_j, and threshold voltage, V_d, of the nano-islands can be determined using the following equations:

$$C_j = 2\pi d\varepsilon_r\varepsilon_0,$$

$$V_d = e/2C_j,$$

where ε_r is the relative dielectric constant (~ 2 – 3 for the porphyrin), ε_0 is the vacuum permittivity (8.854 x 10^{-12} F/m), d is the diameter of the nano-island, and e is the electric charge. With the diameter of the of the nano-islands fabricated thus far varying from ~ 5 – 20 nm, the capacitance of the island varies from approximately 5.56 x 10^{-19} F for the smallest porphyrin islands to ~ 2.23 x 10^{-18} F for the larger islands and threshold voltages from ~ 144 mV to ~ 36 mV, respectively. It has been noted that in order for a single electron transistor (SET) to function at room temperature, islands of ~ 5 nm would be required with attofarad capacitance.[420] Single electron tunneling has been achieved using Au nanoparticles which have shown large Coulomb gaps (1 eV) and Coulomb staircases at room temperature.[421] According to our approximations, the zinc porphyrin fabricated nano-islands should also display Coulomb blockade at room temperature and quantized conductance is being further investigated at smaller voltage ranges for the 5 nm islands.

7.4 Conclusions

Scanning probe lithography has been employed to create various nanostructures of zinc porphyrin thiol molecules arranged in shapes including circles, squares, frames as well as islands ranging from ~ 5 – 20 nm. Grafted ensemble arrays have been created

using lithography scripts to pattern micron size regions on Au(111) surfaces. It has been shown that the number of line scans by the AFM tip will affect the physical height of the grafted structures formed. By controlling the line speed and force in a DDT matrix, we have been able to show precise placement of the zinc porphyrin thiol molecules which is necessary for device applications and probing charge transport of the clusters. The ultimate goal to create Coulomb islands of the zinc porphyrin thiol molecule on the order of ~ 10 nm has been achieved. In previous studies, the self-assembled aggregates of the zinc metallated porphyrin have shown Coulomb blockade at low temperatures and bias-induced switching at room temperature. Further investigation of these nanografted islands with STM has shown the differences in assembly and apparent height of the 5 and 20 nm islands as well as the low current in the I-V curves of the 20 nm islands. Large arrays of nano-islands have been fabricated up to 18 x 18 for potential use of these molecules in any type of functioning device. Preliminary investigation of the 5 and 20 nm islands have shown differences in apparent height in the STM. Since the larger islands have a higher apparent height, we believe that as the island size increases, the molecular ensemble is capable of stabilizing more charge. Future studies of the electronic properties of arrays of 5, 20 and 40 nm size islands will be useful for determination of the capacitance of the islands at room temperature and verify the increase in charge stabilization.

CHAPTER VIII

SUMMARY AND FUTURE DIRECTIONS

8.1 Summary

The hype that molecules could function as active components of electronic devices has been around for decades since Aviram and Ratner first proposed the idea in 1974. Since then, research in molecular electronics has made significant progress but still has a lot of ground to cover. We now know that molecules do exhibit interesting properties from a fundamental standpoint where single molecules and aggregates can switch ON and OFF and display quantized conductance, but in order to be implemented into a device-type architecture, there are still inherent fabrication limitations and reproducibility issues that need to be overcome. In the work shown here, porphyrin molecules were investigated for use in molecularly-enhanced devices. Porphyrin derivatives have been fully characterized on Au surfaces, their charge transport behavior was investigated and ultimately Coulomb islands have been fabricated in arrays of patterns in areas up to ~ 8 μm^2. The first derivative characterized was a free base monopodal tri-pyridyl porphyrin compound. This molecule has been examined through attachment to Au surfaces by a thiol tether, through a tetrafluorophenyl linker. When inserted into a background matrix of dodecanethiol, the porphyrins are observed to tend to bind near the edges of defects within the alkanethiol layer as either single molecules or small ensembles (ca. 3-5 molecules). Based on the apparent height of the molecules relative to the dodecanethiol matrix, the tunneling efficiency was found to be low,

similar to that of a simple alkanethiol which is considered a molecular insulator. From DFT calculations, the low tunneling efficiency can be attributed to the lack of effective orbital overlap between the frontier orbitals of the porphyrin macrocycle and the thiol tether due to the orthogonal dihedral angle between the porphyrin ring and the perfluorophenyl linking group. In addition to the electronic effects on the phenyl ring, the 2,6 fluoro moieties increase the rotation barrier and diminish the dynamics of the aryl – porphyrin bond. Thus, this group introduces an effective tunneling barrier directly within the molecule reducing the tunneling efficiency, despite of the close proximity of the HOMO of the molecule to the Au Fermi level.

The monopodal zinc porphyrin thiol derivative when inserted into a background matrix of dodecanethiol would also bind near the edges of defects within the alkanethiol layer as larger ensembles due to π–π and zinc interactions. From DFT calculations, there was still a lack of effective orbital overlap after incorporation of the zinc metal center between the frontier orbitals of the porphyrin macrocycle and the thiol tether due to the orthogonal dihedral angle between the porphyrin ring and the perfluorophenyl linker group. Coordination of the porphyrin macrocycle with zinc lowers the proximity of the HOMO of the molecule by only a tenth of an electronvolt with respect to the Au Fermi level and does not induce a significant change in the electrostatic potential map of the molecule when compared with the free base analog. Although, the only change to the molecule was the incorporation of the zinc metal, there was a major difference in the behavior of the zinc coordinated molecule compared to the free base porphyrin thiol under an applied STM bias that leads to bias-induced switching and Coulomb blockade.

The switching was attributed to an ensemble size effect since the switching behavior was more evident in the 5 day mixed SAMs which contain larger clusters of porphyrins than the 1 day mixed SAMs. Non-linear I-V characteristics are exhibited at low temperatures with the incorporation of the zinc metal center suggesting that the molecule can be used in single electron tunneling devices where the Coulomb island was isolated and until a high enough potential was applied the current through the molecule will remain blocked.

When investigating the cis-bipodal porphyrin thiol derivatives, it was expected that these molecules would form large clusters reminiscent of the zinc monopodal porphyrin thiol islands. However, both the free base and zinc bipodal derivatives did not form large aggregates and did not exhibit any interesting electronic properties such as bias-induced switching. Since there are two tethers to anchor the porphyrin to the Au surface, the increased coverage of the molecules was also expected and was clearly evident in the pure monolayers on the surface, where complete coverage of the substrate was observed after 1 day of soaking a Au substrate in the free base bipodal porphyrin thiol. The free base bipodal derivatives were not stable in the mixed SAM since the molecules would disappear after imaging with the STM tip over time. Unlike the monopodal derivatives, the bipodal porphyrin thiol molecules are bulkier with two tethers in a cis orientation not allowing the molecules to insert into the defects of the pre-assembled DDT matrix to form the Coulomb islands.

Beyond characterization of the porphyrin thiol derivatives, fabrication of organic molecules was examined with 16-mercaptohexadecanoic acid (16-MHA). Nanografting of 16-MHA in two different solvents, ethanol and 3-phenyl-1-propanol (3P1P), has been

compared. The results indicate that formation of well-defined nanostructures can be achieved in both solvents with differences regarding the integrity and packing of the nanografted assemblies. The 16-MHA molecules were found to assemble as bilayers when grafted into a DDT matrix, however, monolayer nanostructures can also be fabricated if the molecules naturally self-assemble into the preshaved wells in the DDT matrix. With the use of a more viscous solvent, 3P1P, 16-MHA assembled into more uniform structures with little to no undesirable insertion of the 16-MHA molecules into the background matrix SAM. It is a possibility that the 3P1P molecules stabilize the matrix and the nanografted structures by inserting into the DDT matrix SAM forming van der Waals interactions between the 3P1P and the DDT molecules. Since ethanol and 3P1P both have alcohol functional groups, the phenyl ring and the longer alkane chain on the 3P1P could be the reason for the higher degree of chemical interaction with the background DDT providing a lubricative protection layer. If the 3P1P molecules are inserted at the terminal end of the matrix, this could create a barrier hindering the 16-MHA molecules from inserting into the background DDT. The higher quality of patterned assemblies in 3P1P and the little to no insertion of the 16-MHA into the DDT matrix could also be due to the physical property of the 3P1P solvent having a higher viscosity than compared to ethanol. The higher viscosity of 3P1P not only creates a resistance for the 16-MHA molecules to penetrate into the DDT matrix but also forms a protective layer around the 16-MHA assemblies. Additional factors other than solvent choice must also be considered in order to reproduce the nanoscale assemblies on Au surfaces. The packing of the nanografted 16-MHA molecules was affected by the line

spacing of the AFM tip inside the patterned region and therefore the physical heights of the bilayer formation. A more densely packed structure will lead to a nanografted ensemble that is physically higher, and using a CRLS analysis can provide a more precise control over the molecular assemblies. In order to create well-defined nanostructures for use in molecularly-enhanced electronic applications, the pattern consistency must be controlled using these methods.

By applying the knowledge of fabricating 16-MHA in different matrices and solvents, well-defined nanostructures of the monopodal zinc porphyrin thiol have been reproducibly created. Scanning probe lithography was employed to create various nanostructures of zinc porphyrin thiol molecules arranged in shapes including circles, squares, frames, and islands ranging from ~ 5 – 20 nm. Grafted ensemble arrays have been created using lithography scripts to pattern micron size regions on Au(111) surfaces. It has been shown that the number of line scans by the AFM tip will affect the physical height of the grafted structures formed. By controlling the line speed and force in a DDT matrix, we have been able to show precise placement of the zinc porphyrin thiol molecules which is necessary for device applications. The ultimate goal to create Coulomb islands of the zinc porphyrin thiol molecule on the order of ~ 10 nm has been achieved. In previous studies, the self-assembled aggregates of the zinc metallated porphyrin have shown Coulomb blockade at low temperatures and bias-induced switching at room temperature. Further investigation of these nanografted islands with STM has shown the differences in assembly and apparent height of the 5 and 20 nm islands as well as the low current in the I-V curves of the 20 nm islands and the sharp

turn-on in current for the 5 nm islands above ~ 1.6 V. Large arrays of nano-islands have been fabricated up to 18 x 18 for potential use of these molecules in any type of functioning device.

Overall, the derivatives of the porphyrin thiol molecule show interesting electronic properties as aggregates. These islands or aggregates show Coulomb blockade at low temperature and bias-induced switching at room temperature using an STM tip and sweeping above the threshold voltage. In order to use these molecules as active components in a device, the islands must be reproducibly fabricated in large areas on a surface. It has been shown that different patterned arrays of the porphyrin and other organic molecules can be made using scanning probe lithography. Specifically, nanografting has been used to fabricate circle, squares, frames, and small islands circa 10 nm of the zinc porphyrin thiol which has been shown as the optimal size for bias-induced switching of these molecules into a higher conductance state. The orientation and organization of the porphyrin derivatives in confined geometries has shown to be important factors when fabricating molecularly-enhanced devices. For example, only the lower apparent height islands of the self-assembled aggregates exhibit bias-induced switching and I-V curves with a current blocking region and sharp turn on voltage. Also, when fabricating 5 and 20 nm islands using SPL, the 5 nm islands were in a lower conductance state in stable configurations, while the 20 nm islands were very unstable when imaging with an STM tip and exhibited I-V curves with a very low current range. All of these factors must be considered when investigating and creating molecular ensembles for electronics.

8.2 Future Directions

The immediate future of this project will be to further investigate the electronic properties of the nanografted assemblies using CP-AFM. With SPL, arrays of different size islands including 5, 20 and 40 nm will be created in a DDT matrix, so that immediately after creation of the assembled islands, the I-V curves will be obtained using a conducting probe with the AFM setup. This will allow for determination of the current blocking range and threshold voltage as a function of island size to further elucidate the capacitance of these zinc porphyrin molecular ensembles.

Other derivatives to be characterized and investigated for potential use in electronic devices would be the porphyrin thiol without an alkanethiol tether as well as the porphyrin thiol with a hydrogenated phenyl coupling group. Removing the fluorine atoms from the phenyl group will afford more orbital overlap between the macrocycle and linker group to the surface. A phenyl group with hydrogens replacing the fluorine atoms will allow control of the coupling and remove the internal barrier located within the molecule which will allow easier transport of the electrons through the molecule and should increase the conductance of the porphyrin thiol. Further temperature dependent charge transport studies will be necessary to elucidate the electron transport mechanism of tunneling or hopping for the each of the porphyrin thiol derivatives and more in depth analysis of the electronic states of the aggregated porphyrins will be required to accurately determine the mechanism for switching and charge stabilization.

In regards to the broad future of this project, I expect that the mass production of the zinc porphyrin thiol islands will be carried out using a multi-pen array system similar

to that of DPN techniques. By nanografting with a multi-pen array, the 8 μm^2 patterned areas can be scaled up even further to produced hundreds if not thousands of the islands on a single platform. Beyond the fabrication of these Coulomb islands on Au surfaces, the zinc porphyrin thiol can be derivatized for attachment onto Si surfaces. The hybrid nanoelectronics field, combining CMOS with molecular electronics, is ideally the next step. Characterizing the identical zinc metallated macrocycle with a tether for attaching to a Si surface is the future of this project to progress to something more meaningful for the next technology for the continuation of Moore's Law.

REFERENCES

(1) Abruña, H. D.; Ratner, M. A.; Zee, R. D. v.; González, C. A.; Kagan, C. R.; Stewart, D. R.; Walker, A. V.; Batteas, J. D.; Chidsey, C. E. D.; Seideman, T. *Building Electronic Function into Nanoscale Molecular Architectures: Report of a National Science Foundation Workshop.*, National Science Foundation, 2007.

(2) Mirkin, C. A.; Ratner, M. A. *Annu. Rev. Phys. Chem.* **1992**, *43*, 719-754.

(3) Hille, B. *Ion Channels of Excitable Membranes;* 3 ed.; Sinauer Associates: Sunderland, 2001.

(4) Jin, Y.; Friedman, N.; Sheves, M.; He, T.; Cahen, D. *Proc. Natl. Acad. Sci.* **2006**, *103*, 8601-8606.

(5) Hong, F. T. *Molecular Electronics. Biosensors and Biocomputers*; Springer: New York, 1990.

(6) Aviram, A.; Ratner, M. A. *Chem. Phys. Lett.* **1974**, *29*, 277-283.

(7) Kushmerick, J. G.; Lazorcik, J.; Patterson, C. H.; Shashidhar, R.; Seferos, D. S.; Bazan, G. C. *Nano Lett.* **2004**, *4*, 639-642.

(8) Salomon, A.; Cahen, D.; Lindsay, S.; Tomfohr, J.; Engelkes, V. B.; Frisbie, C. D. *Adv. Mater.* **2003**, *15*, 1881-1890.

(9) Delamarche, E.; Schmid, H.; Bietsch, A.; Larsen, N. B.; Rothuizen, H.; Michel, B.; Biebuyck, H. *J. Phys. Chem. B* **1998**, *102*, 3324-3334.

(10) Engelkes, V. B.; Beebe, J. M.; Frisbie, C. D. *J. Am. Chem. Soc.* **2004**, *126*, 14287-14296.

(11) Wang, W. Y.; Lee, T.; Reed, M. A. *Physica E* **2003**, *19*, 117-125.

(12) Wold, D. J.; Frisbie, C. D. *J. Am. Chem. Soc.* **2000**, *122*, 2970-2971.

(13) York, R. L.; Slowinski, K. *J. Electroanal. Chem.* **2003**, *550*, 327-336.

(14) Kang, B. K.; Aratani, N.; Lim, J. K.; Kim, D.; Osuka, A.; Yoo, K.-H. *Mat. Sci. Eng. C* **2006**, *26*, 1023 - 1027.

(15) Kumaran, N.; Veneman, P. A.; Minch, B. A.; Mudalige, A.; Pemberton, J. E.; O'Brien, D. F.; Armstrong, N. R. *Chem. Mater.* **2010**, *22*, 2491-2501.

(16) Xu, M.; Endres, R. G.; Arakawa, Y. *Small* **2007**, *3*, 1539-1543.

(17) Rampi, M. A.; Whitesides, G. M. *Chem. Phys.* **2002**, *281*, 373-391.

(18) Grave, C.; Risko, C.; Shaporenko, A.; Wang, Y. L.; Nuckolls, C.; Ratner, M. A.; Rampi, M. A.; Zharnikov, M. *Adv. Funct. Mater.* **2007**, *17*, 3816-3828.

(19) Majumdar, N.; Gergel-Hackett, N.; Bean, J. C.; Harriott, L. R.; Pattanaik, G.; Zangari, G.; Yao, Y.; Tour, J. M. *J. Electron. Mater.* **2006**, *35*, 140-146.

(20) Fages, F.; Wytko, J. A.; Weiss, J. *C. R. Chim.* **2008**, *11*, 1241-1253.

(21) McCreery, R. L.; Bergren, A. J. *Adv. Mater.* **2009**, *21*, 4303-4322.

(22) Pognon, G.; Boudon, C.; Schenk, K. J.; Bonin, M.; Bach, B.; Weiss, J. *J. Am. Chem. Soc.* **2006**, *128*, 3488-3489.

(23) Stoddart, J. F. *Chem. Soc. Rev.* **2009**, *38*, 1802-1820.

(24) Suslick, K. S.; Rakow, N. A.; Kosal, M. E.; Chou, J.-H. *J. Porphyrins Phthalocyanines* **2000**, *4*, 407-413.

(25) Kubatkin, S.; Danilov, A.; Hjort, M.; Cornil, J.; Bredas, J.-L.; Stuhr-Hansen, N.; Hedegard, P.; Bjornholm, T. *Nature* **2003**, *425*, 698-701.

(26) Lafferentz, L.; Ample, F.; Yu, H.; Hecht, S.; Joachim, C.; Grill, L. *Science* **2009**, *323*, 1193-1197.
(27) Boyle, N. M.; Rochford, J.; Pryce, M. T. *Coord. Chem. Rev.* **2010**, *254*, 77-102.
(28) Burrell, A. K.; Officer, D. L.; Plieger, P. G.; Reid, D. C. *Chem. Rev.* **2001**, *101*, 2751-2796.
(29) Burrell, A. K.; Wasielewski, M. R. *J. Porphyrins Phthalocyanines* **2000**, *4*, 401-406.
(30) Lindsey, J. S. *New J. Chem.* **1991**, *15*, 153-180.
(31) Wu, W.; Liu, Y.; Wang, Y.; Xi, H.; Gao, X.; Di, C.; Yu, G.; Xu, W.; Zhu, D. *Adv. Funct. Mater.* **2008**, *18*, 810-815.
(32) Campbell, W. M.; Burrell, A. K.; Officer, D. L.; Jolley, K. W. *Coord. Chem. Rev.* **2004**, *248*, 1363–1379.
(33) Shea, P. B.; Pattison, L. R.; Kawano, M.; Chena, C.; Chend, J.; Petroff, P.; Martin, D. C.; Yamadac, H.; Onoc, N.; Kanicki, J. *Synth. Met.* **2007**, *157*, 190-197.
(34) Chan, Y.-H.; Schuckman, A. E.; Perez, L. M.; Vinodu, M.; Drain, C. M.; Batteas, J. D. *J. Phys. Chem. C* **2008**, *112*, 6110-6118.
(35) El-Khouly, M. E.; Ito, O.; Smith, P. M.; D'Souza, F. *J. Photochem. Photobiol., C* **2004**, *5*, 79-104.
(36) Hasobe, T.; Fukuzumi, S.; Kamat, P. V. *Interface* **2006**, *15*, 47-51.
(37) Li, Q. L.; Mathur, G.; Gowda, S.; Surthi, S.; Zhao, Q.; Yu, L. H.; Lindsey, J. S.; Bocian, D. F.; Misra, V. *Adv. Mater.* **2004**, *16*, 133-137.
(38) Liang, W.; Shores, M. P.; Bockrath, M.; Long, J. R.; Park, H. *Nature* **2002**, *417*, 725-729.
(39) *The Porphyrin Handbook*; Kadish, K.; Smith, K. M.; Guiard, R., Eds.; Academic Press: New York, 2000, 2003; Vol. 1-20.
(40) *Phthalocyanine. Properties and Applications*; Leznoff, C.; Lever, A., Eds.; VCH publications: New York, 1993; Vol. 3.
(41) Smith, K. M. *Porphyrins and Metaloporphyrins*; Elsevier: Amsterdam, 1972.
(42) Drain, C. M.; Christensen, B.; Mauzerall, D. C. *Proc. Natl. Acad. Sci. USA* **1989**, *86*, 6959-6962.
(43) Drain, C. M.; Mauzerall, D. *Bioelectrochem. Bioenerg.* **1990**, *24*, 263-266.
(44) Drain, C. M.; Mauzerall, D. C. *Biophys. J.* **1992**, *63*, 1556-1563.
(45) Mauzerall, D. C.; Drain, C. M. *Biophys. J.* **1992**, *63*, 1544-1555.
(46) Drain, C. M. *Proc. Natl. Acad. Sci. U. S. A.* **2002**, *99*, 5178-5182.
(47) Liu, C.-y.; Pan, H.-l.; Fox, M. A.; Bard, A. J. *Science* **1993**, *261*, 897-899.
(48) Liu, C.-y.; Pan, H.-l.; Fox, M. A.; Bard, A. J. *Chem. Mater.* **1997**, *9*, 1422-1429.
(49) Bai, Y.; Liu, X.; Chen, L.; Khizar-ul-Haq; Khan, M. A.; Zhu, W. Q.; Jiang, X. Y.; Zhang, Z. L. *Microelectronics J.* **2007**, *38*, 1185-1190.
(50) Grätzel, M. *J. Photochem. Photobiol. C: Photochem. Rev.* **2003**, *4*, 145-153.
(51) Guldi, D. M. *Chem. Soc. Rev.* **2002**, *31*, 22-36.
(52) Sgobba, V.; Giancane, G.; Conoci, S.; Casilli, S.; Ricciardi, G.; Guldi, D. M.; Prato, M.; Valli, L. *J. Am. Chem. Soc.* **2007**, *129*, 3148-3156.
(53) Yang, F.; Forrest, S. R. *ACS Nano* **2008**, *2*, 1022-1032.

(54) Ambroise, A.; Kirmaier, C.; Wagner, R.; Loewe, R.; Bocian, D.; Holten, D.; Lindsey, J. *J. Org. Chem.* **2002**, *67*, 3811-3826.
(55) Iengo, E.; Zangrando, E.; Minatel, R.; Alessio, E. *J. Am. Chem. Soc.* **2002**, *124*, 1003-1013.
(56) Koepf, M.; Trabolsi, A.; Elhabiri, M.; Wytko, J. A.; Paul, D.; Albrecht-Gary, A. M.; Weiss, J. *Org. Lett.* **2005**, *7*, 1279-1282.
(57) Ozawa, H.; Kawao, M.; Tanaka, H.; Ogawa, T. *Chem. Lett.* **2009**, *38*, 542-543.
(58) Sedghi, G.; Sawada, K.; Esdaile, L. J.; Hoffmann, M.; Anderson, H. L.; Bethell, D.; Haiss, W.; Higgins, S. J.; Nichols, R. J. *J. Am. Chem. Soc.* **2008**, *130*, 8582-8583.
(59) Li, C.; Ly, J.; Lei, B.; Fan, W.; Zhang, D.; Han, J.; Meyyappan, M.; Thompson, M.; Zhou, C. *J. Phys. Chem. B* **2004**, *108*, 9646-9649.
(60) Gouterman, M. In *The Porphyrins*; Dolphin, D., Ed.; Academic Press: New York, 1978; Vol. 3, p 1-153.
(61) Waluk, J.; Michl, J. *J. Org. Chem.* **1991**, *56*, 2729-2735.
(62) Drain, C. M.; Batteas, J. D.; Smeureanu, G.; Patel, S. In *Encyclopedia of Nanoscience and Nanotechnology*; Marcel Dekker: New York, 2004, p 3481-3502.
(63) Drain, C. M.; Bazzan, G.; Milic, T.; Vinodu, M.; Goeltz, J. C. *Isr. J. Chem.* **2005**, *45*, 255–269.
(64) Drain, C. M.; Chen, X. In *Encyclopedia of Nanoscience & Nanotechnology*; Nalwa, H. S., Ed.; American Scientific Press: New York, 2004; Vol. 9, p 593-616.
(65) Drain, C. M.; Goldberg, I.; Sylvain, I.; Falber, A. *Top. Curr. Chem.* **2005**, *245*, 55–88.
(66) Medforth, C. J.; Wang, Z.; Martin, K. E.; Song, Y.; Jacobsen, J. L.; Shelnutt, J. A. *Chem. Commun.* **2009**, 7261-7277.
(67) Bazzan, G.; Smith, W.; Francesconi, L.; Drain, C. M. *Langmuir* **2007**, *24*, 3244 - 3249.
(68) Nishiyama, F.; Yokoyama, T.; Kamikado, T.; Yokoyama, S.; Mashiko, S. *Appl. Phys. Lett.* **2006**, *88*, 253113.
(69) Lee, S. J.; Mulfort, K. L.; O'Donnell, J. L.; Zuo, X.; Goshe, A. J.; Wesson, P. J.; Nguyen, S. T.; Hupp, J. T.; Tiede, D. M. *Chem. Commun.* **2006**, 4581-4583.
(70) Liu, B.; Qian, D. J.; Huang, H. X.; Wakayama, T.; Hara, S.; Huang, W.; Nakamura, C.; Miyake, J. *Langmuir* **2005**, *21*, 5079-5084.
(71) Muniappan, S.; Lipstman, S.; George, S.; Goldberg, I. *Inorg. Chem.* **2007**, *46*, 5544-5554.
(72) Wang, Z.; Lybarger, L. E.; Wang, W.; Medforth, C. J.; Miller, J. E.; Shelnutt, J. A. *Nanotechnology* **2008**, *19*, 395604.
(73) Wang, Z.; Medforth, C. J.; Shelnutt, J. A. *J. Am. Chem. Soc.* **2004**, *126*, 15954-15955.
(74) Wang, Z.; Medforth, C. J.; Shelnutt, J. A. *J. Am. Chem. Soc.* **2004**, *126*, 16720-16721.
(75) Lee, S. J.; Hupp, J. T.; Nguyen, S. T. *J. Am. Chem. Soc.* **2008**, *130*, 9632-9633.

(76) Drain, C. M.; Smeureanu, G.; Patel, S.; Gong, X.; Garno, J.; Arijeloye, J. *New J. Chem.* **2006**, *30*, 1834-1843.
(77) Gong, X.; Milic, T.; Xu, C.; Batteas, J. D.; Drain, C. M. *J. Am. Chem. Soc.* **2002**, *124*, 14290-14291.
(78) Ozawa, H.; Tanaka, H.; Kawao, M.; Unoa, S.; Nakazato, K. *Chem. Commun.* **2009**, 7411-7413.
(79) Zhang, Y.; Chen, P.; Ma, Y.; He, S.; Liu, M. *Appl. Mater. Interfaces* **2009**, *1*, 2036-2043.
(80) Haino, T.; Fujii, T.; Watanabe, A.; Takayanagi, U. *Proc. Natl. Acad. Sci. USA* **2009** *106*, 10477-10481.
(81) Lu, G.; Zhang, X.; Cai, X.; Jiang, J. *J. Mater. Chem.* **2009**, *19*, 2417-2424.
(82) Radivojevic, I.; Likhtina, I.; Shi, X.; Singh, S.; Drain, C. M. *Chem. Commun.* **2010**, 1643.
(83) Sooambar, C.; Troiani, V.; Bruno, C.; Marcaccio, M.; Paolucci, F.; Listorti, A.; Belbakra, A.; Armaroli, N.; Magistrato, A.; Zorzi, R. D.; Geremia, S.; Bonifazi, D. *Org. Biomol. Chem.* **2009**, *7*, 2402-2413.
(84) Scandola, F.; Chiorboli, C.; Prodi, A.; Iengo, E.; Alessio, E. *Coord. Chem. Rev.* **2006**, *250*, 1471-1496.
(85) Drain, C. M.; Shi, X.; Milic, T.; Nifiatis, F. *Chem. Commun.* **2001**, 287–288.
(86) Cheng, K. F.; Drain, C. M.; Grohmann, K. *Inorg. Chem.* **2003**, *42*, 2075-2083.
(87) Drain, C. M.; Lehn, J.-M. *Chem. Commun.* **1994**, 2313-2315.
(88) Drain, C. M.; Batteas, J. D.; Flynn, G. W.; Milic, T.; Chi, N.; Yablon, D. G.; Sommers, H. *Proc. Natl. Acad. Sci. USA* **2002**, *99 Suppl 2*, 6498-6502.
(89) Drain, C. M.; Nifiatis, F.; Vasenko, A.; Batteas, J. D. *Angew. Chem.* **1998**, *37*, 2344-2347.
(90) Cheng, K. F.; Thai, N. A.; Grohmann, K.; Teague, L. C.; Drain, C. M. *Inorg. Chem.* **2006**, *45*, 6928-6932.
(91) Cheng, K. F.; Thai, N. A.; Teague, L. C.; Grohmanna, K.; Drain, C. M. *Chem. Commun.* **2005**, 4678–4680.
(92) Koepf, M.; Trabolsi, A.; Elhabiri, M.; Wytko, J. A.; Paul, D.; Albrecht-Gary, A. M.; Weiss, J. *Organic Letters* **2005**, *7*, 1279-1282.
(93) Kobuke, Y. *Struct. Bond.* **2006**, *121*, 49-104.
(94) Reimers, J. R.; Lü, T. X.; Crossley, M. J.; Hush, N. S. *Chem. Phys. Lett.* **1996**, *256*, 353-359.
(95) Tagami, K.; Tsukada, M.; Matsumoto, T.; Kawai, T. *Phys. Rev. B* **2003**, *67*, 245324.
(96) Long, M. Q.; Wang, L.; Chen, K. Q. *Mod. Phys. Lett. B* **2008**, *22*, 661-670.
(97) Tagami, K.; Tsukada, M. *Thin Solid Films* **2004**, *464-465*, 429-432.
(98) Wasielewski, M. R. *J. Org. Chem.* **2006**, *71*, 5051-5066.
(99) Hayes, R. T.; Wasielewski, M. R.; Gosztola, D. *J. Am. Chem. Soc.* **2000**, *122*, 5563-5567.
(100) Wang, Y.; Wang, X.; Ghosh, S. K.; Lu, H. P. *J. Am. Chem. Soc.* **2009**, *131*, 1479-1487.

(101) Drain, C. M.; Gentemann, S.; Roberts, J. A.; Nelson, N. Y.; Medforth, C. J.; Jia, S.; Simpson, M. C.; Smith, K. M.; Fajer, J.; Shelnutt, J. A.; Holten, D. *J. Am. Chem. Soc.* **1998**, *120*, 3781-3791.
(102) Drain, C. M.; Kirmaier, C.; Medforth, C. J.; Nurco, D. J.; Smith, K. M.; Holten, D. *J. Phys. Chem.* **1996**, *100*, 11984-11993.
(103) Retsek, J. L.; Drain, C. M.; Kirmaier, C.; Nurco, D. J.; Medforth, C. J.; Smith, K. M.; Sazanovich, I. V.; Chirvony, V. S.; Fajer, J.; Holten, D. *J. Am. Chem. Soc.* **2003**, *125*, 9787-9800.
(104) Kottas, G. S.; Clarke, L. I.; Horinek, D.; Michl, J. *Chem. Rev.* **2005**, *105*, 1281-1376.
(105) Jiao, J.; Schmidt, I.; Taniguchi, M.; Lindsey, J. S.; Bocian, D. F. *Langmuir* **2008**, *24*, 12047-12053.
(106) Xiao, J.; Dowben, P. *J. Mater. Chem.* **2009**, *19*, 2172–2178.
(107) Adler, A. D.; Longo, F. R.; Finarelli, J. D.; Goldmacher, J.; Assour, J.; Korsakoff, L. *J. Org. Chem.* **1967**, *32*, 476.
(108) Lindsey, J. S.; Schreiman, I. C.; Hsu, H. C.; Kearney, P. C.; Marguerettaz, A. M. *J. Org. Chem.* **1987**, *52*, 827-836.
(109) Lindsey, J. S. *New J. Chem.* **1991**, *15*, 153–180.
(110) Lindsey, J. S. In *The Porphyrin Handbook*; Kadish, K., Smith, K. M., Guiard, R., Eds.; Academic Press: New York, 2000; Vol. 1, p 45-118.
(111) Loewe, R. S.; Ambroise, A.; Muthukumaran, K.; Padmaja, K.; Lysenko, A. B.; Mathur, G.; Li, Q.; Bocian, D. F.; Misra, V.; Lindsey, J. S. *J. Org. Chem.* **2004**, *69*, 1453-1460.
(112) Drain, C. M.; Singh, S. In *The Handbook of Porphyrin Science with Applications to Chemistry, Physics, Materials Science, Engineering, Biology and Medicine*; World Scientific Publisher: Singapore, 2010, p 485-540.
(113) Sharghi, H.; Nejad, A. H. *Tetrahedron* **2004**, *60*, 1863-1868.
(114) *Phthalocyanine Properties and Applications*; Leznoff, C.; Lever, A., Eds.; Wiley VCH: New York, 1993; Vol. 1-4.
(115) Reed, M. A.; Zhou, C.; Muller, C. J.; Burgin, T. P.; Tour, J. M. *Science* **1997**, *278*, 252-254.
(116) Li, X.; He, J.; Hihath, J.; Xu, B.; Lindsay, S. M.; Tao, N. *J. Am. Chem. Soc.* **2006**, *128*, 2135-2141.
(117) Park, J.; Pasupathy, A. N.; Goldsmith, J. I.; Chang, C.; Yaish, Y.; Petta, J. R.; Rinkoski, M.; Sethna, J. P.; Abruna, H. D.; McEuen, P. L.; Ralph, D. C. *Nature* **2002**, *417*, 722-725.
(118) Venkataraman, L.; Klare, J. E.; Nuckolls, C.; Hybertsen, M. S.; Steigerwald, M. L. *Nature* **2006**, *442*, 904-907.
(119) Dunbar, T. D.; Cygan, M. T.; Bumm, L. A.; McCarty, G. S.; Burgin, T. P.; Reinerth, W. A.; Jones, L., II; Jackiw, J. J.; Tour, J. M.; Weiss, P. S.; Allara, D. L. *J. Phys. Chem. B* **2000**, *104*, 4880-4893.
(120) Kushmerick, J. G.; Naciri, J.; Yang, J. C.; Shashidhar, R. *Nano Lett.* **2003**, *3*, 897-900.
(121) Chen, J.; Reed, M. A. *Chem. Phys.* **2002**, *281*, 127.

(122) Weiss, E. A.; Chiechi, R. C.; Kaufman, G. K.; Kriebel, J. K.; Li, Z.; Duati, M.; Rampi, M. A.; Whitesides, G. M. *J. Am. Chem. Soc.* **2007**, *129*, 4336-4349.
(123) Yoshimoto, S.; Itaya, K. *J. Porphyrins Phthalocyanines* **2007**, *11*, 313-333.
(124) Liu, Z.; Yasseri, A. A.; Lindsey, J. S.; Bocian, D. F. *Science* **2003**, *302*, 1543-1545.
(125) Morita, T.; Lindsay, S. *J. Am. Chem. Soc.* **2007**, *129*, 7262-7263.
(126) Wold, D. J.; Frisbie, C. D. *J. Am. Chem. Soc.* **2001**, *123*, 5549-5556.
(127) Samor´ı, P.; Rabe, J. P. *J. Phys.: Condens. Matter* **2002**, *14*, 9955-9973.
(128) Donhauser, Z. J.; Mantooth, B. A.; Kelly, K. F.; Bumm, L. A.; Monnell, J. D.; Stapleton, J. J.; Price, D. W.; Rawlett, A. M.; Allara, D. L.; Tour, J. M.; Weiss, P. S. *Science* **2001**, *292*, 2303-2307.
(129) Chen, F.; Tao, N. J. *Acc. Chem. Res.* **2009**, *42*, 429-438.
(130) Chen, F.; Hihath, J.; Huang, Z.; Li, X.; Tao, N. J. *Annu. Rev. Phys. Chem.* **2007**, *58*, 535-564.
(131) Lu, X.; Hipps, K. W.; Wang, X. D.; Mazur, U. *J. Am. Chem. Soc.* **1996**, *118*, 7197-7202.
(132) Lu, X.; Hipps, K. W. *J. Phys. Chem. B* **1997**, *101*, 5391-5396.
(133) Ogunrinde, A.; Hipps, K. W.; Scudiero, L. *Langmuir* **2006**, *22*, 5697-5701.
(134) Scudiero, L.; Hipps, K. W.; Barlow, D. E. *J. Phys. Chem. B* **2003**, *107*, 2903-2909.
(135) Deng, W.; Hipps, K. W. *J. Phys. Chem. B* **2003**, *107*, 10736-10740.
(136) Scudiero, L.; Barlow, D. E.; Hipps, K. W. *J. Phys. Chem. B* **2002**, *106*, 996-1003.
(137) Hipps, K. W.; Scudiero, L.; Barlow, D. E.; Cooke, M. P. *J. Am. Chem. Soc.* **2002**, *124*, 2126-2127.
(138) Scudiero, L.; Barlow, D. E.; Hipps, K. W. *J. Phys. Chem. B* **2000**, *104*, 11899-11905.
(139) Visser, J.; Katsonis, N.; Vicario, J.; Feringa, B. L. *Langmuir* **2009**, *25*, 5980-5985.
(140) Nikiforov, M. P.; Zerweck, U.; Milde, P.; Loppacher, C.; Park, T.-H.; Uyeda, H. T.; Therien, M. J.; Eng, L.; Bonnell, D. *Nano Lett.* **2007**, *8*, 110-113.
(141) Scudiero, L.; Hipps, K. W. *J. Phys. Chem. C* **2007**, *111*, 17516-17520.
(142) Scudiero, L.; Barlow, D. E.; Mazur, U.; Hipps, K. W. *J. Am. Chem. Soc.* **2001**, *123*, 4073-4080.
(143) Grill, L.; Dyer, M.; Lafferentz, L.; Persson, M.; Peters, M. V.; Hecht, S. *Nat. Nanotechnol.* **2007**, *2*, 687-691.
(144) Garno, J. C.; Xu, C.; Bazzan, G.; Batteas, J. D.; Drain, C. M. In *Metal-Containing and Metallosupramolecular Polymers and Materials*; Schubert, U. S., Newkome, G. R., Manners, I., Eds.; American Chemical Society: 2006, p 168-183.
(145) Drain, C. M.; Varotto, A.; Radivojevic, I. *Chem. Rev.* **2009**, *109*, 1630-1658.
(146) Beletskaya, I.; Tyurin, V. S.; Tsivadze, A. Y.; Guilard, R.; Stern, C. *Chem. Rev.* **2009**, *109* 1659-1713.

(147) Ha, S.; Kaafarani, B.; Barlow, S.; Marder, S.; Kahn, A. *J. Phys. Chem. C* **2007**, *111*, 10493-10497.
(148) Hipps, K.; Scudiero, L.; Barlow, D.; Cooke, M. *J. Am. Chem. Soc.* **2002**, *124*, 2126.
(149) Barlow, S.; Raval, R. *Surf. Sci. Rep* **2003**, *50*, 201-341.
(150) Smith, R.; Lewis, P.; Weiss, P. *Progr. Surf. Sci.* **2004**, *75*, 1-68.
(151) Li, J. Z.; Gryko, D.; Dabke, R. B.; Diers, J. R.; Bocian, D. F.; Kuhr, W. G.; Lindsey, J. S. *J. Org. Chem.* **2000**, *65*, 7379-7390.
(152) Balakumar, A.; Lysenko, A. B.; Carcel, C.; Malinovskii, V. L.; Gryko, D. T.; Schweikart, K. H.; Loewe, R. S.; Yasseri, A. A.; Liu, Z. M.; Bocian, D. F.; Lindsey, J. S. *J. Org. Chem.* **2004**, *69*, 1435-1443.
(153) Wei, L. Y.; Padmaja, K.; Youngblood, W. J.; Lysenko, A. B.; Lindsey, J. S.; Bocian, D. F. *J. Org. Chem.* **2004**, *69*, 1461-1469.
(154) Yasseri, A. A.; Syomin, D.; Malinovskii, V. L.; Loewe, R. S.; Lindsey, J. S.; Zaera, F.; Bocian, D. F. *J. Am. Chem. Soc.* **2004**, *126*, 11944-11953.
(155) Kang, B.; Aratani, N.; Lim, J. K.; Kim, D.; Osuka, A.; Yoo, K.-H. *Chem. Phys. Lett.* **2005**, *412*, 303-306.
(156) Vaughan, O. P. H.; Turner, M.; Williams, F. J.; Hille, A.; Sanders, J. K. M.; Lambert, R. M. *J. Am. Chem. Soc.* **2006**, *128*, 9578-9579.
(157) Ulman, A. *Chem. Rev.* **1996**, *96*, 1533-1554.
(158) Love, J. C.; Estroff, L. A.; Kriebel, J. K.; Nuzzo, R. G.; Whitesides, G. M. *Chem. Rev.* **2005**, *105*, 1103-1169.
(159) Xu, S.; Cruchon-Dupeyrat, S. J. N.; Garno, J. C.; Liu, G. Y.; Jennings, G. K.; Yong, T. H.; Laibinis, P. E. *J. Chem. Phys.* **1998**, *108*, 5002-5012.
(160) Poirier, G. E. *Chem. Rev.* **1997**, *97*, 1117-1128.
(161) Poirier, G. E.; Pylant, E. D. *Science* **1996**, *272*, 1145-1148.
(162) Poirier, G. E.; Tarlov, M. J. *Langmuir* **1994**, *10*, 2853-2856.
(163) Carroll, R. L.; Gorman, C. B. *Angew. Chem. Int. Ed.* **2002**, *41*, 4378-4400.
(164) David, I. G.; Donald, B.; David, J. S.; Richard, J. N. *Nature* **2000**, *408*, 67-69.
(165) James, D. K.; Tour, J. M. *Chem. Mater.* **2004**, *16*, 4423-4435.
(166) Metzger, R. M. *Chem. Rev.* **2003**, *103*, 3803-3834.
(167) Adams, D. M.; Brus, L.; Chidsey, C. E. D.; Creager, S.; Creutz, C.; Kagan, C. R.; Kamat, P. V.; Lieberman, M.; Lindsay, S.; Marcus, R. A.; Metzger, R. M.; Michel-Beyerle, M. E.; Miller, J. R.; Newton, M. D.; Rolison, D. R.; Sankey, O.; Schanze, K. S.; Yardley, J.; Zhu, X. Y. *J. Phys. Chem. B* **2003**, *107*, 6668-6697.
(168) Venkataraman, L.; Klare, J. E.; Nuckolls, C.; Hybertsen, M. S.; Steigerwald, M. L. *Nature* **2006**, *442*, 904-907.
(169) Song, H.; Lee, C.; Kang, Y.; Lee, T. *Colloids Surf., A* **2006**, *284*, 583-588.
(170) Su, G. J. J.; Aguilar-Sanchez, R.; Li, Z. H.; Pobelov, I.; Homberger, M.; Simon, U.; Wandlowski, T. *ChemPhysChem* **2007**, *8*, 1037-1048.
(171) Kushmerick, J. G.; Pollack, S. K.; Yang, J. C.; Naciri, J.; Holt, D. B.; Ratner, M. A.; Shashidhar, R. In *Molecular Electronics III* 2003; Vol. 1006, p 277-290.
(172) Dholakia, G. R.; Fan, W.; Meyyappan, M. *Appl. Phys. A-Mater.* **2005**, *80*, 1215-1223.

(173) Arena, G.; Deretzis, I.; Forte, G.; Giannazzo, F.; La Magna, A.; Lombardo, G.; Raineri, V.; Sgarlata, C.; Spoto, G. *New J. Chem.* **2007**, *31*, 756-761.
(174) Wang, D. W.; Tian, F.; Lu, J. G. *J. Vac. Sci. Technol., B* **2002**, *20*, 60-64.
(175) Moore, A. M.; Dameron, A. A.; Mantooth, B. A.; Smith, R. K.; Fuchs, D. J.; Ciszek, J. W.; Maya, F.; Yao, Y.; Tour, J. M.; Weiss, P. S. *J. Am. Chem. Soc.* **2006**, *128*, 1959-1967.
(176) Lussem, B.; Muller-Meskamp, L.; Karthauser, S.; Waser, R.; Homberger, M.; Simon, U. *Langmuir* **2006**, *22*, 3021-3027.
(177) Ramachandran, G. K.; Hopson, T. J.; Rawlett, A. M.; Nagahara, L. A.; Primak, A.; Lindsay, S. M. *Science* **2003**, *300*, 1413-1416.
(178) Jung, K. H.; Hase, E.; Yasutake, Y.; Shin, H. K.; Kwon, Y. S.; Majima, Y. *Jpn. J. Appl. Phys., Part 2* **2006**, *45*, L840-L842.
(179) Seferos, D. S.; Blum, A. S.; Kushmerick, J. G.; Bazan, G. C. *J. Am. Chem. Soc.* **2006**, *128*, 11260-11267.
(180) Forrest, S. *Chem. Rev.* **1997**, *97*, 1793-1896.
(181) Liu, M.; Amro, N. A.; Liu, G.-y. *Annu. Rev. Phys. Chem.* **2008**, *59*, 367-386.
(182) Perrine, T. M.; Smith, R. G.; Marsh, C.; Dunietz, B. D. *J. Chem. Phys.* **2008**, *128*, 154706-154707.
(183) Thanopulos, I.; Paspalakis, E.; Yannopapas, V. *Nanotechnology* **2008**, *19*, 445202.
(184) Liu, H.; Duclairoir, F.; Fleury, B.; Dubois, L.; Chenavierb, Y.; Marchon, J.-C. *Dalton Trans.* **2009**, 3793-3799.
(185) Roth, K. M.; Yasseri, A. A.; Liu, Z.; Dabke, R. B.; Malinovskii, V.; Schweikart, K.-H.; Yu, L.; Tiznado, H.; Zaera, F.; Lindsey, J. S.; Kuhr, W. G.; Bocian, D. F. *J. Am. Chem. Soc.* **2003**, *125*, 505-517.
(186) Teague, L. C.; Boland, J. J. *J. Phys. Chem. B.* **2003**, *107*, 3820-3823.
(187) Teague, L. C.; Chen, D.; Boland, J. J. *J. Phys. Chem. B.* **2004**, *108*, 7827-7830.
(188) Teague, L. C.; Boland, J. J. *Thin Solid Films* **2004**, *464-465*, 1-4.
(189) Yerushalmi, R.; Scherz, A.; van der Boom, M. E. *J. Am. Chem. Soc.* **2004**, *126*, 2700-2701.
(190) Muthukumaran, K.; Loewe, R. S.; Ambroise, A.; Tamaru, S.-i.; Li, Q.; Mathur, G.; Bocian, D. F.; Misra, V.; Lindsey, J. S. *J. Org. Chem.* **2003**, *69*, 1444-1452.
(191) Hurley, P. T.; Ribbe, A. E.; Buriak, J. M. *J. Am. Chem. Soc.* **2003**, *125*, 11334.
(192) Hacker, C. A.; Anderson, K. A.; Richter, L. J.; Richter, C. A. *Langmuir* **2005**, *21*, 882-889.
(193) Schmidt, I.; Jiao, J.; Bocian, D. F.; Lindsey, J. S. *J. Nanosci. Nanotechnol.* **2008**, *8*, 4813-4817.
(194) Anariba, F.; Tiznado, H.; Diers, J. R.; Schmidt, I.; Muresan, A. Z.; Lindsey, J. S.; Zaera, F.; Bocian, D. F. *J. Phys. Chem. C* **2008**, *112*, 9474-9485.
(195) Holten, D.; Bocian, D. F.; Lindsey, J. S. *Acc. Chem. Res.* **2002**, *35*, 57-69.
(196) Padmaja, K.; Youngblood, W. J.; Wei, L.; Bocian, D. F.; Lindsey, J. S. *Inorg. Chem.* **2006**, *45*, 5479-5492.
(197) Ng, D.; Jiang, J. *Chem. Soc. Rev.* **1997**, *26*, 433.

(198) Carcel, C.; Laha, J.; Loewe, R.; Thamyongkit, P.; Schweikart, K.; Misra, V.; Bocian, D.; Lindsey, J. *J. Org. Chem.* **2004**, *69*, 6739-6750.
(199) Roth, K. M.; Lindsey, J. S.; Bocian, D. F.; Kuhr, W. G. *Langmuir* **2002**, *18*, 4030-4040.
(200) Roth, K. M.; Dontha, N.; Dabke, R. B.; Gryko, D. T.; Clausen, C.; Lindsey, J. S.; Bocian, D. F.; Kuhr, W. G. *J. Vac. Sci. Tech. B* **2000**, *18*, 2359-2364.
(201) Wiberg, J.; Guo, L.; Pettersson, K.; Nilsson, D.; Ljungdahl, T.; Martensson, J.; Albinsson, B. *J. Am. Chem. Soc.* **2006**, *129*, 155.
(202) Ghirotti, M.; Chiorboli, C.; You, C.; Wurthner, F.; Scandola, F. *J. Phys. Chem. A* **2008**, *112*, 3376-3385.
(203) D'Souza, F.; Chitta, R.; Gadde, S.; Islam, D.; Schumacher, A.; Zandler, M.; Araki, Y.; Ito, O. *J. Phys. Chem. B* **2006**, *110*, 25240-25250.
(204) Albinsson, B.; Martensson, J. *J. Photochem. Photobio. C* **2008**, *9*, 138-155.
(205) Ozawa, H.; Kawao, M.; Tanaka, H.; Ogawa, T. *Chem. Lett.* **2009**, *38*.
(206) Miyachi, M.; Ohta, M.; Nakai, M.; Kubota, Y.; Yamanoi, Y.; Yonezawa, T.; Nishihara, H. *Chem. Lett.* **2008**, *37*, 404.
(207) Madru, R.; Guillaud, G.; Al Sadoun, M.; Maitrot, M.; André, J. J.; Simon, J.; Even, R. *Chem. Phys. Lett.* **1988**, *145*, 343-346.
(208) Sedghi, G.; Sawada, K.; Esdaile, L. J.; Hoffmann, M.; Anderson, H. L.; Bethell, D.; Haiss, W.; Higgins, S. J.; Nichols, R. J. *J. Am. Chem. Soc.* **2008**, *130*, 8582-8583.
(209) Ambroise, A.; Wagner, R. W.; Rao, P. D.; Riggs, J. A.; Hascoat, P.; Diers, J. R.; Seth, J.; Lammi, R. K.; Bocian, D. F.; Holten, D.; Lindsey, J. S. *Chem. Mater.* **2001**, *13*, 1023-1034.
(210) Wagner, R.; Lindsey, J.; Seth, J.; Palaniappan, V.; Bocian, D. *J. Am. Chem. Soc.* **1996**, *118*, 3996-3997.
(211) Noguchi, Y.; Kubota, T.; Mashiko, S.; Wakayama, Y. *J. Appl. Phys.* **2005**, *97*, 073513.
(212) Noguchi, Y.; Nagase, T.; Kubota, T.; Kamikado, T.; Mashiko, S. *Thin Solid Films* **2006**, *499*, 90-94.
(213) Noguchi, Y.; Ueda, R.; Kubota, T.; Kamikado, T.; Yokoyama, S.; Nagase, T. *Thin Solid Films* **2008**, *516*, 2762-2766.
(214) Wakayama, Y.; Kubota, T.; Suzuki, H.; Kamikado, T.; Mashiko, S. *J. Appl. Phys.* **2003**, *94*, 4711-4713.
(215) Wakayama, Y.; Kubota, T.; Suzuki, H.; Kamikado, T.; Mashiko, S. *Nanotechnology* **2004**, *15*, 1446-1449.
(216) Wakayama, Y.; Ogawa, K.; Kubota, T.; Suzuki, H.; Kamikado, T.; Mashiko, S. *Appl. Phys. Lett.* **2004**, *85*, 329-331.
(217) Roth, K.; Gryko, D.; Clausen, C.; Li, J.; Lindsey, J.; Kuhr, W.; Bocian, D. *J. Phys. Chem. B* **2002**, *106*, 8639-8648.
(218) Turek, P.; Petit, P.; Andre, J. J.; Simon, J.; Even, R.; Boudjema, B.; Guillaud, G.; Maitrot, M. *J. Am. Chem. Soc.* **1987**, *109*, 5119-5122.

(219) Dunbar, T. D.; Cygan, M. T.; Bumm, L. A.; McCarty, G. S.; Burgin, T. P.; Reinerth, W. A.; Jone, L., II; Jackiw, J. J.; Tour, J. M.; Weiss, P. S.; Allara, D. L. *J. Phys. Chem. B* **2000**, *104*, 4880-4893.
(220) Li, X.; He, J.; Hihath, J.; Xu, B.; Lindsay, S. M.; Tao, N. *J. Am. Chem. Soc.* **2006**, *128*, 2135-2141.
(221) Reed, M. A.; Zhou, C.; Muller, C. J.; Burgin, T. P.; Tour, J. M. *Science* **1997**, *278*, 252-254.
(222) Venkataraman, L.; Klare, J. E.; Nuckolls, C.; Hybertsen, M. S.; Steigerwald, M. L. *Nature* **2006**, *442*, 904-907.
(223) Kushmerick, J. G.; Naciri, J.; Yang, J. C.; Shashidhar, R. *Nano Lett.* **2003**, *3*, 897 -900.
(224) Chen, J.; Reed, M. A. *Chem. Phys.* **2002**, *281*, 127-145.
(225) Weiss, E. A.; Chiechi, R. C.; Kaufman, G. K.; Kriebel, J. K.; Li, Z.; Duati, M.; Rampi, M. A.; Whitesides, G. M. *J. Am. Chem. Soc.* **2007**, *129*, 4336-4349.
(226) Beebe, J. M.; Moore, H. J.; Lee, T. R.; Kushmerick, J. G. *Nano Lett.* **2007**, *7*, 1364-1368.
(227) Troisi, A.; Beebe, J. M.; Picraux, L. B.; van Zee, R. D.; Stewart, D. R.; Ratner, M. A.; Kushmerick, J. G. *Proc. Natl. Acad. Sci. U. S. A.* **2007**, *104*, 14255-14259.
(228) Kramer, S.; Fuierer, R. R.; Gorman, C. B. *Chem. Rev.* **2003**, *103*, 4367-4418.
(229) Liu, G. Y.; Xu, S.; Qian, Y. L. *Acc. Chem. Res.* **2000**, *33*, 457-466.
(230) Selzer, Y.; Salomon, A.; Cahen, D. J. *J. Am. Chem. Soc.* **2002**, *124*, 2886-2887.
(231) Schoch, K. F.; Kundalkar, B. R.; Marks, T. J. *J. Am. Chem. Soc.* **1979**, *101*, 7071-7073.
(232) Diel, B. N.; Inabe, T.; Lyding, J. W.; Schoch, K. F.; Kannewurf, C. R.; Marks, T. J. *J. Am. Chem. Soc.* **1983**, *105*, 1551-1567.
(233) Dirk, C. W.; Inabe, T.; Schoch, K. F.; Marks, T. J. *J. Am. Chem. Soc.* **1983**, *105*, 1539-1550.
(234) Coe, B. J.; Curati, N. R. M. *Comments Inorg. Chem.* **2004**, *25*, 147-184.
(235) McCreery, R. L. *Chem. Mater.* **2004**, *16*, 4477-4496.
(236) Binnig, G.; Rohrer, H.; Gerber, C.; Weibel, E. *Phys. Rev. Lett.* **1982**, *49*, 57-61.
(237) Binnig, G.; Quate, C. F.; Gerber, C. *Phys. Rev. Lett.* **1986**, *56*, 930-933.
(238) Amro, N. A.; Xu, S.; Liu, G. Y. *Langmuir* **2000**, *16*, 3006-3009.
(239) Piner, R. D.; Zhu, J.; Xu, F.; Hong, S. H.; Mirkin, C. A. *Science* **1999**, *283*, 661-663.
(240) Allara, D. L.; Nuzzo, R. G. *Langmuir* **1985**, *1*, 52-66.
(241) Roy, D.; Fendler, J. *Adv. Mater.* **2004**, *16*, 479-508.
(242) Anariba, F.; Viswanathan, U.; Bocian, D. F.; McCreery, R. L. *Anal. Chem.* **2006**, *78*, 3104-3112.
(243) Wang, W. Y.; Lee, T.; Kretzschmar, I.; Reed, M. A. *Nano Lett.* **2004**, *4*, 643-646.
(244) Klein, J.; Leger, A.; Belin, M.; Defourne.D; Sangster, M. J. *Phys. Rev. B* **1973**, *7*, 2336-2348.
(245) Yu, L. H.; Keane, Z. K.; Ciszek, J. W.; Cheng, L.; Stewart, M. P.; Tour, J. M.; Natelson, D. *Phys. Rev. Lett.* **2004**, *93*.

(246) Tkachenko, N. V.; Vuorimaa, E.; Kesti, T.; Alekseev, A. S.; Tauber, A. Y.; Hynninen, P. H.; Lemmetyinen, H. *J. Phys. Chem. B* **2000**, *104*, 6371-6379.
(247) Li, X.; He, J.; Hihath, J.; Xu, B.; Lindsay, S. M.; Tao, N. J. *J. Am. Chem. Soc.* **2006**, *128*, 2135-2141.
(248) Park, J.; Pasupathy, A. N.; Goldsmith, J. I.; Chang, C.; Yaish, Y.; Petta, J. R.; Rinkoski, M.; Sethna, J. P.; Abruna, H. D.; McEuen, P. L.; Ralph, D. C. *Nature* **2002**, *417*, 722-725.
(249) Reed, M. A.; Zhou, C.; Muller, C. J.; Burgin, T. P.; Tour, J. M. *Science* **1997**, *278*, 252-254.
(250) Bumm, L. A.; Arnold, J. J.; Dunbar, T. D.; Allara, D. L.; Weiss, P. S. *J. Phys. Chem. B* **1999**, *103*, 8122-8127.
(251) Ishida, T.; Mizutani, W.; Aya, Y. O., H.; Sasaki, S. T., H. *J. Phys. Chem. B* **2002**, *106*, 5886-5892.
(252) Rawlett, A. M.; Hopson, T. J.; Nagahara, L. A.; Tsui, R. K.; Ramachandran, G.; Lindsy, S. M. *Appl. Phys. Lett.* **2002**, *81*, 3043-3045.
(253) Holmlin, R. E.; Ismagilov, R. F.; Haag, R.; Mujica, V.; Ratner, M. A.; Rampi, M. A.; Whitesides, G. M. *Angew. Chem. Int. Ed.* **2001**, *40*, 2316-2320.
(254) Ng, M.-K.; Lee, D.-C.; Yu, L. *J. Am. Chem. Soc.* **2002**, *124*, 11862-11863.
(255) Ng, M.-K.; Yu, L. *Angew. Chem. Int. Ed.* **2002**, *41*, 3598-3601.
(256) Yasuda, S.; Yoshida, S.; Sasaki, J.; Okutsu, Y.; Nakamura, T.; Taninaka, A.; Takeuchi, O.; Shigekawa, H. *J. Am. Chem. Soc.* **2006**, *128*, 7746-7747.
(257) Chen, J.; Reed, M. A.; Asplund, C. L.; Cassell, A. M.; Myrick, M. L.; Rawlett, A. M.; Tour, J. M.; Van Patten, P. G. *Appl. Phys. Lett.* **1999**, *75*, 624-626.
(258) Hacker, C. A.; Batteas, J. D.; Garno, J. C.; Marquez, M.; Richter, C. A.; Richter, L. J.; Zee, R. D. v.; Zangmeister, C. D. *Langmuir* **2004**, *20*, 6195-6205.
(259) Yang, G.; Qian, Y.; Engtrakul, C.; Sita, L. R.; Liu, G. *J. Phys. Chem. B* **2000**, *104*, 9059-9062.
(260) Blum, A. S.; Yang, J. C.; Shashidar, R.; Ratna, B. *Appl. Phys. Lett.* **2003**, *82*, 3322-3324.
(261) Nazin, G. V.; Qiu, X. H.; Ho, W. *Science* **2003**, *302*, 77-81.
(262) Arima, V.; Fabiano, E.; Blyth, R. I. R.; Sala, F. D.; Matino, F.; Thompson, J.; Cingolani, R.; Rinaldi, R. *J. Am. Chem. Soc.* **2004**, *126*, 16951-16958.
(263) Elemans, J. A. A. W.; Hameren, R. v.; Nolte, R. J. M.; Rowan, A. E. *Adv. Mater.* **2006**, *18*, 1251-1266.
(264) She, C.; Guo, J.; Irle, S.; Morokuma, K.; Mohler, D. L.; Zabri, H.; Odobel, F.; Youm, K.-T.; Liu, F.; Hupp, J. T.; Lian, T. *J. Phys. Chem. A* **2007**, *111*, 6832-6842.
(265) Chen, I.-W. P.; Fu, M.-D.; Tseng, W.-H.; Yu, J.-Y.; Wu, S.-H.; Ku, C.-J.; Chen, C.-h.; Peng, S.-M. *Angew. Chem. Int. Ed.* **2006**, *45*, 5814-5818.
(266) Lin, S.-Y.; Chen, I.-W. P.; Chen, C.-h.; Hsieh, M.-H.; Yeh, C.-Y.; Lin, T.-W.; Chen, Y.-H.; Peng, S.-M. *J. Phys. Chem. B* **2004**, *108*, 959-964.
(267) Jiao, J.; Anariba, F.; Tiznado, H.; Schmidt, I.; Lindsey, J. S.; Zaera, F.; Bocian, D. F. *J. Am. Chem. Soc.* **2006**, *128*, 6965-6974.

(268) Ssenyange, S.; Anariba, F.; Bocian, D. F.; McCreery, R. L. *Langmuir* **2005**, *21*, 11105-11112.
(269) Wei, J. J.; Schafmeister, C.; Bird, G.; Paul, A.; Naaman, R.; Waldeck, D. H. *J. Phys. Chem. B* **2006**, *110*, 1301-1308.
(270) Yamada, H.; Imahori, H.; Nishimura, Y.; Yamazaki, I.; Ahn, T. K.; Kim, S. K.; Kim, D.; Fukuzumi, S. *J. Am. Chem. Soc.* **2003**, *125*, 9129-9139.
(271) Chou, J.-H.; Kosal, M. E.; Nalwa, H. S.; Rakow, N. A.; Suslick, K. S. In *The Porphyrin Handbook*; Kadish, K. M., Smith, K. M., Guilard, R., Eds.; Academic Press: New York, 2000; Vol. 6, p 43-131.
(272) Amao, Y.; Asai, K.; Miyakawa, K.; Okura, I. *J. Porphyr. Phthalocya.* **2000**, *4*, 19-22.
(273) Imahori, H.; Fukuzumi, S. *Adv. Mater.* **2001**, *13*, 1197-1199.
(274) Yasseri, A. A.; Syomin, D.; Loewe, R. S.; Lindsey, J. S.; Zaera, F.; Bocian, D. F. *J. Am. Chem. Soc.* **2004**, *126*, 15603-15612.
(275) Hutchison, J. E.; Postlethwaite, T. A.; Murray, R. W. *Langmuir* **1993**, *9*, 3277-3283.
(276) Zak, J.; Yuan, H. o.; Ho, M.; Woo, L. K.; Porter, M. D. *Langmuir* **1993**, *9*, 2772-2774.
(277) Drain, C. M.; Batteas, J. D.; Flynn, G. W.; Milic, T.; Chi, N.; Yablon, D. G.; Sommers, H. *Proc. Natl. Acad. Sci. U. S. A.* **2002**, *99 Suppl 2*, 6498-6502.
(278) Drain, C. M.; Nifiatis, F.; Vasenko, A.; Batteas, J. D. *Angew. Chem. Int. Ed.* **1998**, *37*, 2344-2347.
(279) Shirley, D. A. *Phys. Rev. B* **1972**, *5*, 4709.
(280) Parr, R. G.; Yang, W. *Density Functional Theory of Atoms and Molecules*; Oxford University Press: New York, 1989.
(281) Frisch, M. J.; G. W. Trucks; H. B. Schlegel; G. E. Scuseria; M. A. Robb; J. R. Cheeseman; J. A. Montgomery, J.; T. Vreven; K. N. Kudin; J. C. Burant; J. M. Millam; S. S. Iyengar; J. Tomasi; V. Barone; B. Mennucci; M. Cossi; G. Scalmani; N. Rega; G. A. Petersson; H. Nakatsuji; M. Hada; M. Ehara; K. Toyota; R. Fukuda; J. Hasegawa; M. Ishida; T. Nakajima; Y. Honda; O. Kitao; H. Nakai; M. Klene; X. Li; J. E. Knox; H. P. Hratchian; J. B. Cross; C. Adamo; J. Jaramillo; R. Gomperts; R. E. Stratmann; O. Yazyev; A. J. Austin; R. Cammi; C. Pomelli; J. W. Ochterski; P. Y. Ayala; K. Morokuma; G. A. Voth; P. Salvador; J. J. Dannenberg; V. G. Zakrzewski; S. Dapprich; A. D. Daniels; M. C. Strain; O. Farkas; D. K. Malick; A. D. Rabuck; K. Raghavachari; J. B. Foresman; J. V. Ortiz; Q. Cui; A. G. Baboul; S. Clifford; J. Cioslowski; B. B. Stefanov; G. Liu; A. Liashenko; P. Piskorz; I. Komaromi; R. L. Martin; D. J. Fox; T. Keith; M. A. Al-Laham; C. Y. Peng; A. Nanayakkara; M. Challacombe; P. M. W. Gill; B. Johnson; W. Chen; M. W. Wong; C. Gonzalez; Pople, J. A.; Gaussian, Inc.: Wallingford, CT, 2004.
(282) Staroverov, V. N.; Scuseria, G. E.; Tao, J. M.; Perdew, J. P. *J. Chem. Phys.* **2003**, *119*, 12129-12137.
(283) Dunlap, B. I. *J. Mol. Struct. (Theochem)* **2000**, *529*, 37-40.

(284) Francl, M. M.; Pietro, W. J.; Hehre, W. J.; Binkley, J. S.; Gordon, M. S.; Defrees, D. J.; Pople, J. A. *J. Chem. Phys.* **1982**, *77*, 3654-3665.
(285) Hehre, W. J.; Ditchfie.R; Pople, J. A. *J. Chem. Phys.* **1972**, *56*, 2257-2261.
(286) Clark, T.; Chandrasekhar, J.; Spitznagel, G. W.; Schleyer, P. V. *J. Comput. Chem.* **1983**, *4*, 294-301.
(287) Krishnan, R.; Binkley, J. S.; Seeger, R.; Pople, J. A. *J. Chem. Phys.* **1980**, *72*, 650-654.
(288) Becke, A. D. *J. Chem. Phys.* **1993**, *98*, 5648-5652.
(289) Lee, C. T.; Yang, W. T.; Parr, R. G. *Phys. Rev. B* **1988**, *37*, 785-789.
(290) Senge, M. O. In *The Porphyrin Handbook*; Kadish, K. M., Smith, K. M., Guilard, R., Eds.; Academic Press: New York, 2000; Vol. 10, p 1-218.
(291) Eastman, D. E. *Phys. Rev. B* **1970**, *2*, 1-2.
(292) Schonenberger, C.; Sondaghuethorst, J. A. M.; Jorritsma, J.; Fokkink, L. G. J. *Langmuir* **1994**, *10*, 611-614.
(293) Sondaghuethorst, J. A. M.; Schonenberger, C.; Fokkink, L. G. J. *J. Phys. Chem.* **1994**, *98*, 6826-6834.
(294) Chan, Y. H.; Lin, J. T.; Chen, I. W. P.; Chen, C. H. *J. Phys. Chem. B* **2005**, *109*, 19161-19168.
(295) Varsanyi, G. *Assignments for Vibrational Spectra of Seven Hundred Benzene Derivatives*; Wiley: New York, 1974.
(296) Chabal, Y. J. *Surf. Sci. Rep.* **1988**, *8*, 211-357.
(297) Laibinis, P. E.; Whitesides, G. M.; Allara, D. L.; Tao, Y. T.; Parikh, A. N.; Nuzzo, R. G. *J. Am. Chem. Soc.* **1991**, *113*, 7152-7167.
(298) Picraux, L. B.; Zangmeister, C. D.; Batteas, J. D. *Langmuir* **2006**, *22*, 174-180.
(299) Yang, G. H.; Liu, G. Y. *J. Phys. Chem. B* **2003**, *107*, 8746-8759.
(300) Bumm, L. A.; Arnold, J. J.; Cygan, M. T.; Dunbar, T. D.; Burgin, T. P.; Jones, L.; Allara, D. L.; Tour, J. M.; Weiss, P. S. *Science* **1996**, *271*, 1705-1707.
(301) Cygan, M. T.; Dunbar, T. D.; Arnold, J. J.; Bumm, L. A.; Shedlock, N. F.; Burgin, T. P.; Jones, L.; Allara, D. L.; Tour, J. M.; Weiss, P. S. *J. Am. Chem. Soc.* **1998**, *120*, 2721-2732.
(302) Moth-Poulsen, K.; Patrone, L.; Stuhr-Hansen, N.; Christensen, J. B.; Bourgoin, J.-P.; Bjørnholm, T. *Nano Lett.* **2005**, *5*, 783-785.
(303) Zangmeister, C. D.; Picraux, L. B.; van Zee, R. D.; Yao, Y. X.; Tour, J. M. *Chem. Phys. Lett.* **2007**, *442*, 390-393.
(304) Wassel, R. A.; Fuierer, R. R.; Kim, N.; Gorman, C. B. *Nano Lett.* **2003**, *3*, 1617-1620.
(305) Cornil, J.; Karzazi, Y.; Bre´das, J. L. *J. Am. Chem. Soc.* **2002**, *124*, 3516-3517.
(306) Di Ventra, M.; Kim, S. G.; Pantelides, S. T.; Lang, N. D. *Phys. Rev. Lett.* **2001**, *86*, 288 - 291.
(307) Lang, N. D.; Avouris, P. *Phys. Rev. B* **2000**, *62*, 7325 - 7329.
(308) Seminario, J. M.; Zacarias, A. G.; Tour, J. M. *J. Am. Chem. Soc.* **2000**, *122*, 3015-3020.
(309) Hallbäck, A.-S.; Poelsema, B.; Zandvliet, H. J. W. *ChemPhysChem* **2007**, *8*, 661-665.

(310) Tao, Y.-T.; Wu, C.-C.; Eu, J.-Y.; Lin, W.-L.; Wu, K.-C.; Chen, C.-h. *Langmuir* **1997**, *13*, 4018-4023.
(311) Akkerman, H. B.; de Boer, B. *J. Phys.: Condens. Matter* **2008**, *20*, 20.
(312) Chen, F.; Hihath, J.; Huang, Z. F.; Li, X. L.; Tao, N. J. *Annu. Rev. Phys. Chem.* **2007**, *58*, 535-564.
(313) Vulillaume, D. *C. R. Phys.* **2008**, *9*, 78-94.
(314) Cheng, X. Y.; Noh, Y. Y.; Wang, J. P.; Tello, M.; Frisch, J.; Blum, R. P.; Vollmer, A.; Rabe, J. P.; Koch, N.; Sirringhaus, H. *Adv. Funct. Mater.* **2009**, *19*, 2407-2415.
(315) Stoliar, P.; Kshirsagar, R.; Massi, M.; Annibale, P.; Albonetti, C.; de Leeuw, D. M.; Biscarini, F. *J. Am. Chem. Soc.* **2007**, *129*, 6477-6484.
(316) Campbell, I. H.; Kress, J. D.; Martin, R. L.; Smith, D. L.; Barashkov, N. N.; Ferraris, J. P. *Appl. Phys. Lett.* **1997**, *71*, 3528-3530.
(317) Heimel, G.; Romaner, L.; Zojer, E.; Bredas, J. L. *Nano Lett.* **2007**, *7*, 932-940.
(318) Balaban, T. S.; Berova, N.; Drain, C. M.; Hauschild, R.; Huang, X. F.; Kalt, H.; Lebedkin, S.; Lehn, J. M.; Nifaitis, F.; Pescitelli, G.; Prokhorenko, V. I.; Riedel, G.; Smeureanu, G.; Zeller, J. *Chem. Eur. J.* **2007**, *13*, 8411-8427.
(319) Imahori, H. *J. Phys. Chem. B* **2004**, *108*, 6130-6143.
(320) Yong, Y. J.; Li, Y. L.; Liu, H. B.; Wang, S.; Wang, N.; Zhuang, J. P.; Li, X. F.; He, X. R.; Zhu, D. B. *Nanotechnology* **2005**, *16*, 1899-1904.
(321) Huijser, A.; Savenije, T. J.; Kotlewski, A.; Picken, S. J.; Siebbeles, L. D. A. *Adv. Mater.* **2006**, *18*, 2234-2239.
(322) Mantooth, B. A.; Weiss, P. S. *P. IEEE* **2003**, *91*, 1785-1802.
(323) Blum, A. S.; Kushmerick, J. G.; Long, D. P.; Patterson, C. H.; Yang, J. C.; Henderson, J. C.; Yao, Y. X.; Tour, J. M.; Shashidhar, R.; Ratna, B. R. *Nat. Mater.* **2005**, *4*, 167-172.
(324) Grabert, H.; Devoret, M. H. *Single Charge Tunneling: Coulomb Blockade Phenomena in Nanostructures;* Plenum: New York, 1992.
(325) Feldheim, D. L.; Keating, C. D. *Chem. Soc. Rev.* **1998**, *27*, 1-12.
(326) Noguchi, Y.; Nagase, T.; Kubota, T.; Kamikado, T.; Mashiko, S. *Thin Solid Films* **2006**, *499*, 90-94.
(327) Noguchi, Y.; Ueda, R.; Kubota, T.; Kamikado, T.; Yokoyama, S.; Nagase, T. *Thin Solid Films* **2008**, *516*, 2762-2766.
(328) Wakayama, Y.; Kubota, T.; Suzuki, H.; Kamikado, T.; Mashiko, S. *J. Appl. Phys.* **2003**, *94*, 4711-4713.
(329) Kim, B.; Beebe, J. M.; Olivier, C.; Rigaut, S.; Touchard, D.; Kushmerick, J. G.; Zhu, X. Y.; Frisbie, C. D. *J. Phys. Chem. C* **2007**, *111*, 7521-7526.
(330) Park, J. W.; Pasupathy, A. N.; Goldsmith, J. I.; Soldatov, A. V.; Chang, C.; Yaish, Y.; Sethna, J. P.; Abruna, H. D.; Ralph, D. C.; McEuen, P. L. *Thin Solid Films* **2003**, *438*, 457-461.
(331) Yu, L. H.; Zangmeister, C. D.; Kushmerick, J. G. *Nano Lett.* **2006**, *6*, 2515-2519.
(332) Baerends, E. J.; J. Autschbach; A. Bérces; F.M. Bickelhaupt; C. Bo; P.M. Boerrigter; L. Cavallo; D.P. Chong; L. Deng; R.M. Dickson; D.E. Ellis; M. van Faassen; L. Fan; T.H. Fischer; C. Fonseca Guerra; S.J.A. van Gisbergen; A.W.

Götz; J.A. Groeneveld; O.V. Gritsenko; M. Grüning; F.E. Harris; P. van den Hoek; C.R. Jacob; H. Jacobsen; L. Jensen; G. van Kessel; F. Kootstra; M.V. Krykunov; E. van Lenthe; D.A. McCormack; A. Michalak; J. Neugebauer; V.P. Nicu; V.P. Osinga; S. Patchkovskii; P.H.T. Philipsen; D. Post; C.C. Pye; W. Ravenek; J.I. Rodriguez; P. Ros; P.R.T. Schipper; G. Schreckenbach; J.G. Snijders; M. Solà; M. Swart; D. Swerhone; G. te Velde; P. Vernooijs; L. Versluis; L. Visscher; O. Visser; F. Wang; T.A. Wesolowski; E.M. van Wezenbeek; G. Wiesenekker; S.K. Wolff; T.K. Woo; A.L. Yakovlev; Ziegler, a. T.; ADF 2008.01 ed.; SCM: Amsterdam, The Netherlands, 2008.

(333) Perdew, J. P.; Chevary, J. A.; Vosko, S. H.; Jackson, K. A.; Pederson, M. R.; Singh, D. J.; Fiolhais, C. *Phys. Rev. B* **1992**, *46*, 6671-6687.

(334) Jiao, J.; Anariba, F.; Tiznado, H.; Schmidt, I.; Lindsey, J. S.; Zaera, F.; Bocian, D. F. *J. Am. Chem. Soc.* **2006**, *128*, 6965-6974.

(335) Ssenyange, S.; Anariba, F.; Bocian, D. F.; McCreery, R. L. *Langmuir* **2005**, *21*, 11105-11112.

(336) Anariba, F.; Viswanathan, U.; Bocian, D. F.; McCreery, R. L. *Anal. Chem.* **2006**, *78*, 3104-3112.

(337) Hutchison, J. E.; Postlethwaite, T. A.; Murray, R. W. *Langmuir* **1993**, *9*, 3277-3283.

(338) Cotton, C.; Glidle, A.; Beamson, G.; Cooper, J. M. *Langmuir* **1998**, *14*, 5139-5146.

(339) Laibinis, P. E.; Bain, C. D.; Whitesides, G. M. *J. Phys. Chem.* **1991**, *95*, 7017-7021.

(340) Lamont, C. L. A.; Wilkes, J. *Langmuir* **1999**, *15*, 2037-2042.

(341) Imahori, H.; Hasobe, T.; Yamada, H.; Nishimura, Y.; Yamazaki, I.; Fukuzumi, S. *Langmuir* **2001**, *17*, 4925-4931.

(342) Hunter, C. A.; Sanders, J. K. M. *J. Am. Chem. Soc.* **1990**, *112*, 5525-5534.

(343) Bumm, L. A.; Arnold, J. J.; Dunbar, T. D.; Allara, D. L.; Weiss, P. S. *J. Phys. Chem. B* **1999**, *103*, 8122-8127.

(344) Seferos, D. S.; Blum, A. S.; Kushmerick, J. G.; Bazan, G. C. *J. Am. Chem. Soc.* **2006**, *128*, 11260-11267.

(345) Lewis, P. A.; Inman, C. E.; Maya, F.; Tour, J. M.; Hutchison, J. E.; Weiss, P. S. *J. Am. Chem. Soc.* **2005**, *127*, 17421-17426.

(346) Cheng, J. Y.; Ross, C. A.; Thomas, E. L.; Smith, H. I.; Vancso, G. J. *Appl. Phys. Lett.* **2002**, *81*, 3657-3659.

(347) Cavallini, M.; Stoliar, P.; Moulin, J. F.; Surin, M.; Leclere, P.; Lazzaroni, R.; Breiby, D. W.; Andreasen, J. W.; Nielsen, M. M.; Sonar, P.; Grimsdale, A. C.; Mullen, K.; Biscarini, F. *Nano Lett.* **2005**, *5*, 2422-2425.

(348) Barth, J. V. *Annu. Rev. Phys. Chem.* **2007**, *58*, 375-407.

(349) Lopinski, G. P.; Wayner, D. D. M.; Wolkow, R. A. *Nature* **2000**, *406*, 48-51.

(350) Zhang, S. G. *Nat. Biotechnol.* **2003**, *21*, 1171-1178.

(351) Lowe, C. R. *Curr. Opin. Struct. Biol.* **2000**, *10*, 428-434.

(352) Hyun, J.; Ahn, S. J.; Lee, W. K.; Chilkoti, A.; Zauscher, S. *Nano Lett.* **2002**, *2*, 1203-1207.

(353) Niemeyer, C. M. *Curr. Opin. Chem. Biol.* **2000**, *4*, 609-618.
(354) Wang, C.; Xia, Q. F.; Li, W. D.; Fu, Z. L.; Morton, K. J.; Chou, S. Y. *Small* **2010**, *6*, 1242-1247.
(355) Hamley, I. W. *Nanotechnology* **2003**, *14*, R39-R54.
(356) Sharpe, R. B. A.; Titulaer, B. J. F.; Peeters, E.; Burdinski, D.; Huskens, J.; Zandvliet, H. J. W.; Reinhoudt, D. N.; Poelsema, B. *Nano Lett.* **2006**, *6*, 1235-1239.
(357) Barth, J. V.; Costantini, G.; Kern, K. *Nature* **2005**, *437*, 671-679.
(358) Chen, Y.; Ohlberg, D. A. A.; Li, X. M.; Stewart, D. R.; Williams, R. S.; Jeppesen, J. O.; Nielsen, K. A.; Stoddart, J. F.; Olynick, D. L.; Anderson, E. *Appl. Phys. Lett.* **2003**, *82*, 1610-1612.
(359) Noy, A.; Miller, A. E.; Klare, J. E.; Weeks, B. L.; Woods, B. W.; DeYoreo, J. J. *Nano Lett.* **2002**, *2*, 109-112.
(360) Lee, S.; Saito, N.; Takai, O. *Appl. Surf. Sci.* **2009**, *255*, 7302-7306.
(361) Seo, K.; Borguet, E. *Langmuir* **2006**, *22*, 1388-1391.
(362) Fang, T. H.; Chang, W. J. *Physica B* **2004**, *352*, 190-199.
(363) Sugimura, H.; Hanji, T.; Hayashi, K.; Takai, O. *Adv. Mater.* **2002**, *14*, 524-+.
(364) Garno, J. C.; Yang, Y. Y.; Amro, N. A.; Cruchon-Dupeyrat, S.; Chen, S. W.; Liu, G. Y. *Nano Lett.* **2003**, *3*, 389-395.
(365) Lee, H.; Jang, Y. K.; Bae, E. J.; Lee, W.; Kim, S. M.; Lee, S. H. *Curr. Appl. Phys.* **2002**, *2*, 85-90.
(366) Liu, G. Y.; Xu, S.; Qian, Y. L. *Acc. Chem. Res.* **2000**, *33*, 457-466.
(367) Liu, M.; Amro, N. A.; Liu, G. Y. *Annu. Rev. Phys. Chem.* **2008**, *59*, 367-386.
(368) Liu, J. F.; Cruchon-Dupeyrat, S.; Garno, J. C.; Frommer, J.; Liu, G. Y. *Nano Lett.* **2002**, *2*, 937-940.
(369) Garno, J. C.; Batteas, J. D. In *Applied Scanning Probe Methods IV*; Bhushan, B., Fuchs, H., Eds.; Springer: Germany, 2006, p 105-135.
(370) Smith, R. K.; Lewis, P. A.; Weiss, P. S. *Prog. Surf. Sci.* **2004**, *75*, 1-68.
(371) Tang, Q.; Shi, S. Q.; Zhou, L. M. *J. Nanosci. Nanotechnol.* **2004**, *4*, 948-963.
(372) Gannon, G.; Larsson, J. A.; Greer, J. C.; Thompson, D. *Langmuir* **2009**, *25*, 242-247.
(373) Barrena, E.; Ocal, C.; Salmeron, M. *J. Chem. Phys.* **1999**, *111*, 9797-9802.
(374) Xu, S.; Miller, S.; Laibinis, P. E.; Liu, G. Y. *Langmuir* **1999**, *15*, 7244-7251.
(375) Liang, J.; Scoles, G. *Langmuir* **2007**, *23*, 6142-6147.
(376) Ngunjiri, J. N.; Kelley, A. T.; Lejeune, Z. M.; Li, J. R.; Lewandowski, B. R.; Serem, W. K.; Daniels, S. L.; Lusker, K. L.; Garno, J. C. *Scanning* **2008**, *30*, 123-136.
(377) Sader, J. E.; Chon, J. W. M.; Mulvaney, P. *Rev. Sci. Instrum.* **1999**, *70*, 3967-3969.
(378) Hazel, J. L.; Tsukruk, V. V. *J. Tribol. Trans. ASME* **1998**, *120*, 814-819.
(379) Gotsmann, B.; Fuchs, H. *Phys. Rev. Lett.* **2001**, *86*, 2597-2600.
(380) Helt, J. M.; Batteas, J. D. *Langmuir* **2006**, *22*, 6130-6141.
(381) Xu, S.; Laibinis, P. E.; Liu, G. Y. *J. Am. Chem. Soc.* **1998**, *120*, 9356-9361.
(382) Ryu, S.; Schatz, G. C. *J. Am. Chem. Soc.* **2006**, *128*, 11563-11573.

(383) Yu, J. J.; Tan, Y. H.; Li, X.; Kuo, P. K.; Liu, G. Y. *J. Am. Chem. Soc.* **2006**, *128*, 11574-11581.
(384) Dameron, A. A.; Charles, L. F.; Weiss, P. S. *J. Am. Chem. Soc.* **2005**, *127*, 8697-8704.
(385) Bain, C. D.; Troughton, E. B.; Tao, Y. T.; Evall, J.; Whitesides, G. M.; Nuzzo, R. G. *J. Am. Chem. Soc.* **1989**, *111*, 321-335.
(386) Jung, L. S.; Campbell, C. T. *J. Phys. Chem. B* **2000**, *104*, 11168-11178.
(387) Liang, J.; Rosa, L. G.; Scoles, G. *J. Phys. Chem. C* **2007**, *111*, 17275-17284.
(388) Kelley, A. T.; Ngunjiri, J. N.; Serem, W. K.; Lawrence, S. O.; Yu, J. J.; Crowe, W. E.; Garno, J. C. *Langmuir* **2010**, *26*, 3040-3049.
(389) Garno, J. C.; Zangmeister, C. D.; Batteas, J. D. *Langmuir* **2007**, *23*, 7874-7879.
(390) Goss, C. A.; Brumfield, J. C.; Irene, E. A.; Murray, R. W. *Langmuir* **1993**, *9*, 2986-2994.
(391) Xu, S.; Amro, N. A.; Liu, G. Y. *Appl. Surf. Sci.* **2001**, *175*, 649-655.
(392) Castronovo, M.; Radovic, S.; Grunwald, C.; Casalis, L.; Morgante, M.; Scoles, G. *Nano Lett.* **2008**, *8*, 4140-4145.
(393) Wu, W. P.; Liu, Y. Q.; Zhu, D. B. *Chem. Soc. Rev.* **2010**, *39*, 1489-1502.
(394) Gaweda, S.; Podborska, A.; Macyk, W.; Szacilowski, K. *Nanoscale* **2009**, *1*, 299-316.
(395) Chung, A.; Deen, J.; Lee, J. S.; Meyyappan, M. *Nanotechnology* **2010**, *21*.
(396) Otsuki, J. *Coord. Chem. Rev.* **2010**, *254*, 2311-2341.
(397) Placencia, D.; Wang, W.; Shallcross, R. C.; Nebesny, K. W.; Brumbach, M.; Armstrong, N. R. *Adv. Funct. Mater.* **2009**, *19*, 1913-1921.
(398) Brumbach, M.; Placencia, D.; Armstrong, N. R. *J. Phys. Chem. C* **2008**, *112*, 3142-3151.
(399) Alloway, D.; Armstrong, N. *Appl. Phys. A: Mater. Sci. Process.* **2009**, *95*, 209-218.
(400) Armstrong, N. R.; Wang, W.; Alloway, D. M.; Placencia, D.; Ratcliff, E.; Brumbach, M. *Macromol. Rapid Commun.* **2009**, *30*, 717-731.
(401) Takami, T.; Clark, A.; Caldwell, R.; Mazur, U.; Hipps, K. W. *Langmuir* **2010**, *26*, 12709-12715.
(402) Mazur, U.; Hipps, K. W.; Riechers, S. L. *J. Phys. Chem. C* **2008**, *112*, 20347-20356.
(403) Gyarfas, B.; Wiggins, B.; Hipps, K. W. *J. Phys. Chem. C* **2010**, *114*, 13349-13353.
(404) Jiao, J.; Nordfund, E.; Lindsey, J. S.; Bocian, D. F. *J. Phys. Chem. C* **2008**, *112*, 6173-6180.
(405) Lysenko, A. B.; Thamyongkit, P.; Schmidt, I.; Diers, J. R.; Bocian, D. F.; Lindsey, J. S. *J. Porphyr. Phthalocya.* **2006**, *10*, 22-32.
(406) Roth, K. M.; Dontha, N.; Dabke, R. B.; Gryko, D. T.; Clausen, C.; Lindsey, J. S.; Bocian, D. F.; Kuhr, W. G. *J. Vac. Sci. Technol. B* **2000**, *18*, 2359-2364.
(407) Li, X.; He, J.; Hihath, J.; Xu, B.; Lindsay, S. M.; Tao, N. *J. Am. Chem. Soc.* **2006**, *128*, 2135-2141.

(408) Xu, B. Q.; Li, X. L.; Xiao, X. Y.; Sakaguchi, H.; Tao, N. J. *Nano Lett.* **2005**, *5*, 1491-1495.
(409) Xu; Xiao; Yang, X.; Zang, L.; Tao *J. Am. Chem. Soc.* **2005**, *127*, 2386-2387.
(410) Mullen, T. J.; Dameron, A. A.; Andrews, A. M.; Weiss, P. S. *Aldrichim. Acta* **2007**, *40*, 21-31.
(411) Amro, N. A.; Xu, S.; Liu, G.-y. *Langmuir* **2000**, *16*, 3006-3009.
(412) Xu, S.; Liu, G.-y. *Langmuir* **1997**, *13*, 127-129.
(413) Salaita, K.; Wang, Y.; Fragala, J.; Vega, R. A.; Liu, C.; Mirkin, C. A. *Angew. Chem.* **2006**, *118*, 7378-7381.
(414) Xu, S.; Laibinis, P. E.; Liu, G.-y. *J. Am. Chem. Soc.* **1998**, *120*, 9356-9361.
(415) Yu, J. H.; Ngunjiri, J. N.; Kelley, A. T.; Gano, J. C. *Langmuir* **2008**, *24*, 11661-11668.
(416) Liu, J. F.; Von Ehr, J. R.; Baur, C.; Stallcup, R.; Randall, J.; Bray, K. *Appl. Phys. Lett.* **2004**, *84*, 1359-1361.
(417) Bano, F.; Fruk, L.; Sanavio, B.; Glettenberg, M.; Casalls, L.; Niemeyer, C. M.; Scoles, G. *Nano Lett.* **2009**, *9*, 2614-2618.
(418) Schuckman, A. E.; Pérez, L. M.; Vinodu, M.; Tomé, J. P. C.; Yu, L. H.; Drain, C. M.; Kushmerick, J. G.; Batteas, J. D. *to be submitted to J. Am. Chem. Soc.*
(419) Gorman, C. B.; Carroll, R. L.; Fuierer, R. R. *Langmuir* **2001**, *17*, 6923-6930.
(420) *Nano and Molecular Electronics Handbook*; Lyshevski, S. E., Ed.; CRC: Boca Raton, FL, 2007.
(421) Yang, G. H.; Tan, L.; Tang, Y. Y.; Chen, S. W.; Liu, G.-Y. *Surf. Sci.* **2005**, *589*, 129-138.

VITA

Amanda Eileen Schuckman
Intel Corporation
Assembly & Test Technology Development
5000 West Chandler Boulevard,
Chandler, AZ 85226
aschuckman@chem.tamu.edu

EDUCATION

May 2011	**Ph.D. Chemistry** Texas A&M University, College Station, TX Thesis Advisor: Professor James D. Batteas
December 2005	**B.S. Chemistry, Math Minor** Texas Lutheran University Research Advisor: Professor Jonathan Bohmann

EXPERIENCE

2009 – 2010	**Graduate Student Intern**, Polyurethanes, Huntsman Advanced Technology Center
2006 – 2010	**Graduate Research Assistant**, Department of Chemistry, Texas A&M University
2008 – 2009	**NSF GK-12 Teaching Fellow**, Department of Chemistry, Texas A&M University
2006 – 2007	**Graduate Teaching Assistant**, Department of Chemistry, Texas A&M University
2005	**Undergraduate Research Assistant**, Department of Chemistry, Texas Lutheran University
2003 – 2005	**Undergraduate Teaching Assistant**, Department of Chemistry, Texas Lutheran University

SELECTED PUBLICATIONS

1. Yang-Hsiang Chan, Amanda E. Schuckman, Lisa M. Pérez, Mikki Vinodu, Charles M. Drain and James D. Batteas, "Characterization of a Thiol-Tethered Tripyridyl Porphyrin on Au(111)," *J. Phys. Chem. C*; **2008**; 112(15); 6110-6118.

2. Amanda E. Schuckman, Lisa M. Pérez, Mikki Vinodu, João P.C. Tomé, Lam H. Yu, Charles M. Drain, James G. Kushmerick and James D. Batteas, "Coulomb Blockade and Bias-Induced Switching in Nanoscale Porphyrin Islands on Au(111)" (to be submitted to *Journal of the American Chemical Society*).